Experimental Realization of Improved Magnetic Sensing and Imaging in Ensembles of Nitrogen Vacancy Centers in Diamond

A thesis presented

by

Connor A. Hart

to

The Graduate School of Arts and Sciences

in partial fulfillment of the requirements

for the degree of

Doctor of Philosophy

in the subject of

Physics

Harvard University

Cambridge, Massachusetts

August 2020

Dissertation Advisors:

Hongkun Park

Ronald Walsworth

Author

Connor A. Hart

Experimental Realization of Improved Magnetic Sensing and Imaging in Ensembles of Nitrogen Vacancy Centers in Diamond

Abstract

Nitrogen-vacancy (NV) color centers in diamond constitute a leading quantum sensing platform, with particularly diverse applications in magnetometry. The negatively-charged NV center (NV^-) exhibits a long-lived electronic spin-triplet ground state with magnetically sensitive sublevels under ambient conditions. The NV^- spin state can be prepared optically and readout via spin-state-dependent fluorescence. Additionally, it is possible to engineer ensembles of NV^- at suitably high densities in favorable geometries. Together, these properties make NV^- ensembles particularly advantageous for magnetic sensing and imaging applications spanning condensed matter physics, the life sciences, nuclear magnetic resonance, Earth and planetary science, and magnetic navigation and mapping. Despite the broad range of demonstrated applications, the magnetic sensitivities achieved using NV^- ensemble magnetometers remain orders of magnitudes from fundamental limits. Optical readout fidelities much less than unity, typical ensemble dephasing times over two orders of magnitude shorter than the spin lifetime, and ionization under strong optical illumination all contribute to limiting

the NV^- ensemble magnetic sensitivity. Furthermore, the strength of NV^- centers as multi-modal sensors of magnetic and electric fields, temperature, crystal stress, and external pressure can become a vulnerability, resulting in poor magnetic specificity (the ability to isolate magnetic signals from non-magnetic sources) and inhibiting the scalable production of diamond material with reproducible properties.

This work pursues two complementary avenues towards improved NV-ensemble magnetic sensitivity and specificity. First, the development of a characterization toolbox using NV^- centers as probes of their local environment provides feedback and informed metrics for the production of synthetic diamond material tailored to NV^- ensemble applications. This work is conducted in close collaboration with diamond manufacturers. Sources of heterogeneity are of particular concern; for example, the introduction of non-uniform crystal stress during synthesis results in pernicious NV^- ensemble dephasing. This crystal stress heterogeneity varies dramatically within and between samples, preventing the scalable production of material with consistent properties. Iterative efforts to characterize NV-diamond material and feedback on the synthesis methods provides a path toward improved NV^- ensemble magnetometer performance via material engineering. Second, this thesis reports the experimental realization of measurement protocols designed to simultaneously ameliorate the deficits of existing diamond material and relax requirements on diamond material under development. Double quantum coherence magnetometry is employed to mitigate the consequences of crystal stress inhomogeneity as well as temperature drift. Meanwhile, NV^- ensemble dephasing induced by dipolar interactions between the paramagnetic diamond spin bath and NV^- sensor spins is suppressed using resonant control of the

constituent bath spins. These techniques provide improved magnetic sensitivity and specificity, including the demonstration of record volume-normalized magnetic sensitivity for a wide-field quantum diamond microscope (QDM).

Contents

List of Figures

List of Tables

Citations to previously published work

Parts of this dissertation cover research reported in the following articles:

1. **C. Hart***, J. Schloss*, M. Turner, P. Schiedegger, E. Bauch, and R. Walsworth, "NV-Diamond Magnetic Microscopy using a Double Quantum 4-Ramsey Protocol" *arXiv 2009.02371,* 2020.

2. A. Edmonds, **C. Hart**, M. Turner, P.O. Colard, J. Schloss, K. Olsson, R. Trubko, M. Markham, A. Rathmill, B. Horne-Smith, W. Lew, A. Manickam, S. Bruce, P. Kaup, J. Russo, M. DiMario, J. South, J. Hansen, D. Twitchen, and R. Walsworth, "Characterisation of CVD Diamond with High Concentrations of Nitrogen for Magnetic-Field Sensing Applications," *arXiv 2004.01746,* 2020.

3. J. Barry, J. Schloss, E. Bauch, M. Turner, **C. Hart**, L. Pham, and R. Walsworth, "Sensitivity optimization for NV-diamond magnetometry," *Rev. Mod. Phys.,* 2020.[1]

4. D.P.L. Aude Craik, P. Kehayias, A. Greenspon, X. Zhang, M. Turner, J. Schloss, E. Bauch, **C. Hart**, E. Hu, and R. Walsworth, "Microwave-Assisted Spectroscopy Technique for Studying Charge State in Nitrogen-Vacancy Ensembles in Diamond,"*Phys. Rev. Applied,* 2020.[2]

5. E. Levine, M. Turner, P. Kehayias, **C. Hart**, N. Langellier, R. Trubko, D. Glenn, R. Fu, and R. Walsworth, "Principles and Techniques of the Quantum Diamond Microscope," *Nanophotonics,* 2019.[3]

[1] © 2020 American Physical Society
[2] © 2020 American Physical Society
[3] ©2019 Edlyn V. Levine et al., published by De Gruyter, Berlin/Boston. This work is licensed under the Creative Commons Attribution 4.0 Public License. BY 4.0

6. P. Kehayias, M. Turner, R. Trubko, J. Schloss, **C. Hart**, and R. Walsworth, "Imaging Crystal Stress in Diamond using Ensembles of Nitrogen-Vacancy Centers," *Phys. Rev. B,* 2019.[4]

7. E. Bauch, S. Singh, J. Lee, **C. Hart**, J. Schloss, M. Turner, J. Barry, L. Pham, N. Bar Gill, S. Yelin, and R. Walsworth, "Decoherence of dipolar spin ensembles in diamond," *arXiv 1904.08763,* 2019.

8. E. Bauch*, **C. Hart***, J. Schloss, M. Turner, J. Barry, P. Kehayias, S. Singh, R. Walsworth, "Ultralong Dephasing Times in Solid-State Spin Ensembles via Quantum Control," *PRX,* 2018.[5]

[4] © 2019 American Physical Society
[5] © 2018 American Physical Society

Acknowledgments

I am grateful for everyone who contributed to my Ph.D experience and made this work possible. I want to first acknowledge my research advisor, Prof. Ronald Walsworth, for his guidance and support. I particularly appreciate and value his efforts to nurture a friendly, collaborative group culture, which has been an invaluable asset. In the years since Ron warmly welcomed me into the group five years ago, I have benefited immensely as a scientist and person – learning about science, collaboration, and scientific communication. I wish to thank my committee members, Professors Hongkun Park, Evelyn Hu, and Amir Yacoby, for their time and encouragement of my growth as a scientist. I also wish to acknowledge the incredible support and opportunities my undergraduate research advisor and mentor, Professor Luis Orozco, provided. I would not be writing these words today without him.

I have been fortunate to work closely with an incredible collection of scientists and people. Much of the work in this thesis emerged from the efforts of our "T_2^*" taskforce: Erik Bauch, Matthew Turner, Jennifer Schloss, and John Barry. I owe Erik an enormous debt of gratitude for taking me under his wing as a young graduate student and playing a major role in positively shaping my graduate work and experience. I deeply admire both Erik's extensive technical understanding as well as impeccable intuition. I am persistently inspired by Matthew's work ethic, critical thinking, and experimental rigor. He is the person everyone goes to in the group when they have a technical challenge for a reason. I am grateful for the opportunity to work closely with him. I have learned the most about scientific communication from Jenny, who is as gifted writer as she is physicist. Last but not least, I would like to acknowledge John Barry for instilling some serious, AMO-experimental rigor. I am also grateful

for the opportunity to work with Patrick Scheidegger, a Masters student from ETH at the time and now a doctoral student. His technical strength, critical insights, and determined work ethic in the face of complex challenges enabled much of this work. I also learned a thing or two about cheese. More recently, I have had the honor of working closely with both Kevin Olsson, who brings impressive focus, and JJ Oon, who has made phenomenal progress understanding many formerly-outstanding mysteries. I look forward to continuing our efforts down at UMD.

I consider myself fortunate to have been part of such a friendly, encouraging, supportive, and talented research group. I have had the honor of learning and working with Keigo Arai, Nithya Arunkumar, Mikael Backlund, Oren Ben Dor, Willa Dworschack, Dominik Bucher, Francesco Casola, Johannes Cremer, David Glenn, J.C. Jaskula, Pauli Kehayias, Mark Ku, Nick Langellier, Junghyun Paul Lee, Rebecca Li, Mason Marshall, Tim Milbourne, Ben Moss, JJ Oon, David Phillips, Diana Prado Lopes Aude Craik, Aakash Ravi, Emma Rosenfeld, Raisa Trubko, Marie Wesson, Huiliang Zhang, Yuan Zhu, and others. I am also immensely thankful for our newest group members (Emma Huckestein, Jiashen Tang, Shantam Ravan , Zechuan Yin) who provided valuable feedback and comments on this thesis. I have also benefitted from the vibrant diamond community at Harvard and MIT, especially Elana Urbach, Hengyun Zhou, Joonhee Choi, Soonwon Choi, Alex Xingyu Zhang and Andy Greenspon. Farther afield, this work would be impossible without our close collaboration with Element Six, which manufactured the diamond samples discussed in this work. I especially want to thank Andrew Edmonds, Matthew Markham, Pierre-Olivier Collard, and Dan Twitchen for their support, curiosity, expertise, and for

always entertaining our many diamond material questions. I am also indebted to our collaborators at Lockheed Martin, including Wilbur Lew, Micheal DiMario, John Stetson, Arul Manickam, Scott Bruce for their support of this work and excellent technical discussions.

Next, I wish to thank the Harvard physics department, especially Lisa Cacciabaudo who has been an unrivaled and critical resource for all things throughout my graduate career. I am also grateful to have had the support and friendship of so many incredible fellow Harvard physics graduate students and Boston friends. The "farm share" crew has helped keep me sane: Abby, Albert, Scott, Sam, Delilah, Grey, and Ellen. I want to include a special shout out to my G1 officemates Abby and Albert for the many hours and meals shared together. I am also eternally grateful to Tim Milbourne, who hosted me during my G0 visit, convinced me to join the Walsworth group, and has been a steadfast and immensely generous friend, colleague, and housemate over the last five years. Thank you, Team Little Wolf, for teaching me a thing or two about good coffee.

Finally, I wish to thank my family and Sarah for their unwavering love, support, as well as the many plane flights and airport departures/arrivals over the last five years. I owe you all more than I could put into words here, but that will not stop me from trying. To my parents - you are my first and greatest role models. I strive in everything I do to be as patient, hardworking, brave, and kind as you both. Your perseverance has always inspired me. I owe everything I accomplish to the warm, supportive environment you have always created and your (nearly) boundless wisdom. I am so very thankful and proud to have you as parents. To my sister – I will never

admit to this again, but between the two of us, you are the better sibling. Your dedication and bravery astound me and inspire me to always work that much harder. I consider myself quite fortunate to get to have such a kind, smart, and quick-witted sister as a partner in crime. To my grandmother – your generosity and love have always been a critical foundation in my life, but especially so over the last few years. I look forward to delivering on a long-promised culinary tour of Cambridge and Boston. Sarah – I could not have done any of this without you. You are my anchor and greatest ally. Time has never gone by faster than during our many video calls over the past five years. Thank you for taking the time each day to talk through our accomplishments, dissect our trials, and entertain lively discussions about science. I look forward to many more years to come!

Connor Hart

August 31, 2020

Acknowledgements of Financial Support

This thesis is based on work funded by, or in part by, the U.S. Army Research Laboratory and the U.S. Army Research Office under Grant No. W911NF-15-1-0548; the Army Research Laboratory MAQP program under Contract No. W911NF-19-2-0181; the DARPA DRINQS program (Grant No. D18AC00033); the National Science Foundation (NSF) Physics of Living Systems (PoLS) program under Grant No. PHY-1504610; the Air Force Office of Scientific Research Award No. FA9550-17-1-0371; the Department of Energy (DOE) Quantum Information Science Enabled Discovery (QuantISED) program under Award No. DE-SC0019396; Lockheed Martin under Contract No. A32198; and the University of Maryland Quantum Technology Center.

Chapter 1

Introduction

Quantum sensing is an emergent pillar of quantum science and technology research which employs quantum mechanical systems as probes of physical quantities such as magnetic and electric fields, temperature, pressure, and rotation in real-world applications [1]. Current quantum sensing research builds upon many decades of work spanning atomic physics and magnetic resonance, including nuclear magnetic resonance (NMR), atomic clocks, atomic vapor magnetometers, and superconducting quantum interference devices (SQUID). In recent decades neutral atoms, trapped ions, superconducting circuits, and, more recently, solid state defects have emerged as promising platforms for quantum sensing. Solid state defects, in particular nitrogen-vacancy (NV) centers in diamond, offer key technological advantages, such as operation under ambient conditions, which make them well suited for real-world applications [2].

The NV center in diamond consists of a substitutional nitrogen adjacent to a vacancy in the carbon lattice. Although NV centers can exist in three charge states (NV^-, NV^0, NV^+), only the negatively-charge state, NV^-, with two unpaired elec-

trons, is conventionally used for sensing. Well protected inside the diamond lattice, NV^- centers possess a spin triplet (S=1) electronic ground state with millisecond long spin lifetimes at room temperature and sublevels which sensitive to magnetic fields, electric fields, temperature, and pressure. Crucially, the NV^- spin state can be optically initialized and readout via a spin-dependent inter-system crossing (ISC) and primarily non-radiative decay pathway. Additionally, the spin state can be coherently manipulated by applying resonant GHz-scale microwave fields. NV^--based sensors offer these attractive attributes while also not requiring bulky cryogenics, vacuum equipment, or large, Tesla-scale bias magnetic fields - a key advantage over many competing platforms [3]. Room-temperature operation makes them well suited for integration into compact, robust devices and enables the standoff distance between a source of interest and the sensor to be dramatically reduced (down to nanometer length-scales for single NV measurements) [4].

Quantum sensors using NV^- centers are particularly promising as magnetometers. Although the optically-active NV center had been characterized in diamond for multiple decades [5–8], single NV^- centers as well as NV^- ensembles were first proposed [9, 10] and demonstrated as magnetic field sensors around 2008 [11–13]. Since then, research in this direction has expanded rapidly, leading to applications in the life sciences [14, 15], Earth and planetary science [16], condensed matter systems [4], nuclear magnetic resonance [15], magnetic navigation and communication [3], and integrated circuits [17].

Experiments employing single NV centers have leveraged the angstrom-scale of the defect for high-resolution spectroscopy, including, for example, demonstrations of

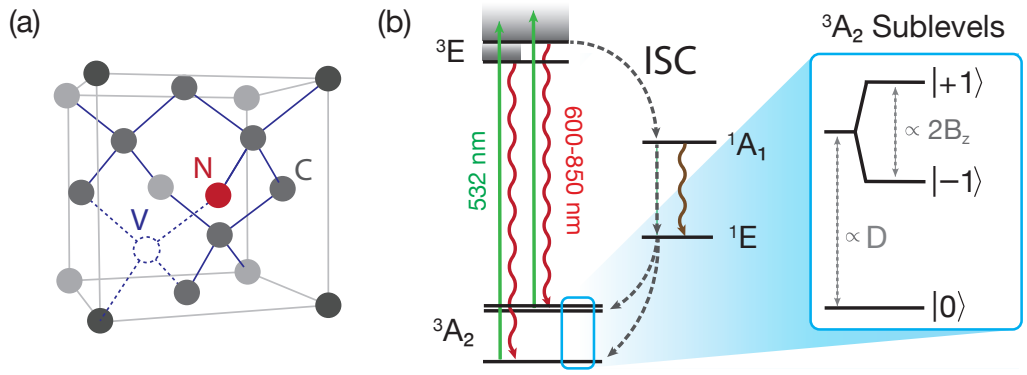

Figure 1.1: **Crystal Structure and Energy Diagram. (a)** Model of the carbon diamond lattice with a subsitutional nitrogen adjacent to a vacancy in the lattice. The NV symmetry axis is aligned with the crystallographic axis. **(b)** Energy level diagram for the negatively-charged NV center. The ground state ^{3}A$_2$ spin triplet exhibits a zero field splitting between the $m_s = 0$ ($|0\rangle$) and $m_s = \pm 1$ ($|\pm 1\rangle$) of approximately 2.87 GHz. Optical illumination (<637 nm, green arrows) excites NV$^-$ into the first excited state ^{3}E from which the defect can radiatively decays back to the ground state in a largely spin-conserving process that emits fluorescence in the 650-800 nm band (red arrows) at room temperature. NV$^-$ in $m_s = \pm 1$ can also decay to ^{3}A$_2$ from ^{3}E through an alternative pathway (^{1}A$_1$ $\rightarrow$^{1}E, black dashed arrows) via a spin-selective inter-system-crossing (ISC) which does not fluorescence in the visible (fluorescence in the IR is produced, brown arrow). Expanded view: ^{3}A$_2$ sublevels with the $|0\rangle$ split from $|\pm 1\rangle$ states splitting by a zero-field-splitting D. Meanwhile the $|\pm 1\rangle$ sublevels also exhibit a Zeeman splitting proportional to the projection of the bias magnetic field onto the NV-axis, B_z.

single protein NMR [18] and magnetic imaging of condensed matter systems using AFM-like scanning tip techniques [4]. Ensembles of NV^- centers have also found a wide range of applications which are amenable to trading spatial resolution for improved sensitivity (by virtue of averaging over many sensor spins) [2]. NV^- ensemble experiments can be broadly categorized by their fluorescence collection modality: single-channel versus multi-channel. Single-channel sensors, such as photodiodes, integrate the fluorescence from a micron to millimeter scale ensemble. Demonstrations include sensing the magnetic field produced by a firing neuron action potential [19], NV-NMR of pico-liter volumes with Hertz-scale linewidths [20, 21], and magnetic navigation using variations in the Earth's magnetic field [3, 22, 23].

Meanwhile, the second set of applications focus on magnetic microscopy, collecting fluorescence from a dense layer of NV^- centers onto a camera or similar device [24]. This modality, referred to as a quantum diamond microscope (QDM), enables imaging of magnetic sources with potentially diffraction-limited spatial resolution and millimeter-scale fields of view. QDM applications to-date include imaging magnetic fields from remnant magnetization in geological specimens [16], domains in magnetic memory [25], iron mineralization in chiton teeth [26], current flow in graphene devices [27,28] and integrated circuits [17], populations of living magnetotactic bacteria [29], and cultures of immunomagnetically labeled tumor cells [30]. QDMs take full advantage of the room-temperature operation and high spatial resolution provided by NV-based measurements.

In addition, both single-channel and imaging applications commonly utilize the full vector magnetometry capabilities of NV^- ensemble-based sensors to provide three

dimensional magnetic field reconstruction [31–33]. Typical NV^- ensemble diamond material contains NV^- centers with quantization axes (defined by the line between the substitutional nitrogen and vacancy) distributed along all four tetrahedral crystallographic axes of the diamond lattice. Thus, each class of NV^- centers, with a fixed orientation in the diamond lattice, is sensitive to a different projection of the applied magnetic field. In comparison, other vector magnetometers such as SQUID, Hall probes, and flux-gate magnetometers are only sensitive to a single projection of the magnetic field. While multiple single-axis vector magnetometers can be assembled together, this approach commonly suffers from heading errors and dead zones [34,35], which do not occur for NV-based magnetometers.

Despite the demonstrated utility of NV^- ensembles for magnetometry, many envisioned applications, such as imaging dynamic, natural magnetic activity in networks of mammalian cells, remain out of reach due to the magnetic sensitivity limits of current experiments [2, 19]. State-of-the-art NV^- ensemble experiments achieve sensitivities $\sim$pT Hz$^{-1/2}$ [2, 20], whereas established magnetometer technologies such as SQUID and spin-exchange relaxation-free atomic magnetometers provide magnetic sensitivities of $\sim$fT Hz$^{-1/2}$ or better [36] for a similar sensor size $\sim$ 1 mm. Though these other magnetometers cannot provide the combination of high-resolution and wide-field imaging of the QDM, the 1000-fold poorer volume-normalized NV-diamond sensitivity corresponds to a million times longer averaging time for the same signal-to-noise ratio (SNR). However, a number to comments are in order: (1) The readout fidelity F of current NV^- ensemble experiments ($F \sim 0.01$) are a factor of about 100 from the spin projection limit such that significant improvements are likely pos-

sible [2]; (2) similarly, typical NV ensemble dephasing times T_2^* of approximately 1 µs are over 100× shorter than the longest single NV T_2^* reported [37] and far from the theoretical maximum of twice the electronic spin state lifetime, $2T_1$ [2]. As we will develop further in the following sections, a primary focus of this dissertation is identifying and then experimentally implementing the most promising routes toward improved NV^- ensemble magnetometer sensitivity, especially when sensing broadband or static magnetic signals which account for a majority of demonstrated applications in recent years.

Beyond magnetic sensitivity, magnetic specificity and scalability are also critical metrics for NV^- ensemble magnetometry. Here, magnetic specificity refers to the ability to isolate the desired magnetic signals from other non-magnetic shifts in the electronic spin energy levels. In this regard, the potential of NV^- centers as multimodal sensors of electric fields, temperature, crystal stress, and pressure in addition to magnetic fields becomes a weakness - temperature drifts and stress-induced dephasing and resonance shifts are particularly harmful. Fortunately, proper choice of the sublevels ($m_s = \{+1, 0, -1\}$) used for sensing provides opportunities to suppress vulnerability to non-magnetic sources as will be discussed further in Sec. 1.4 and Chapter 3.

Scalability refers to achieving consistent performance independent of a specific diamond sample or location on a sample by controlling heterogeneities in the diamond material, in particular crystal strain and defect density. For example, spatial variations in the stress environment across an interrogated volume of NV^- sensor spins to due crystal strain heterogeneity degrades the ensemble dephasing time T_2^* and

reduces magnetic sensitivity inhomogeneously across a diamond. The magnitude of stress-gradient-induced dephasing in NV-diamond material is often comparable to or dominates other dephasing mechanisms and may vary dramatically between locations on the same diamond as well as between diamonds. Variations in the density of nitrogen incorporated during growth or NV centers themselves present similar challenges. As a consequence, small changes in the region used for measurements (or exchanging one diamond for another) can result in order of magnitude differences in the achieved magnetic sensitivity [38]. This reality makes producing NV-based devices at scale an outstanding challenge for the community [39]. However, exciting recent progress toward this goal is summarized in Chapter 6.

This dissertation will describe efforts to improve all three of these criteria: magnetic sensitivity, magnetic specificity, and scalabiltity (or reproducibility) - by pursuing two related research directions. First, much of the work presented in the following chapters contributes to an NV-diamond characterization toolbox. The goal of these efforts is to provide feedback and informed metrics to diamond growers, aiding in the development of diamond material tailored for NV ensemble applications. In parallel, measurement techniques that ameliorate the deficits of existing diamond material are implemented in order to enable immediate progress and relax requirements on the underlying diamond material.

1.1 NV^- Center Physics

The NV^- electronic ground state is an $^3A_2$ spin triplet state with quantum number S = 1, C_{3v} point-group symmetry, and a quantization axis defined along the N-V axis and

co-linear with the associated crystallographic axis [40]. The optical transition between the NV$^-$ $^3A_2$ ground state and the first excited state, ^3E, which is also a spin triplet, can be excited non-resonantly using wavelengths shorter than the NV$^-$ center's 637 nm zero-phonon-line due to the phonon-side-band at room temperature [40]. Irradiation with 532 nm laser light, which is commonly employed due to commercial availability, produces fluorescence in the 650-800 nm band when the excited population decays directly back to the ground state (see Fig. 1.1).

However, the excited state is also coupled to a spin-selective, alternative decay pathway which does not produce fluorescence in the 650-800 nm band. NV$^-$ centers in the excited triplet state $m_s = \pm 1$ sublevels can also decay back to the ground state via a spin-selective inter-system-crossing (ISC), passing through an excited singlet state and a lower meta-stable singlet state before finally decaying back to the $^3A_2$ ground state via a lower ISC [41, 42]. While the upper ISC is highly spin-selective, population traversing the lower ISC decays roughly equally into the $m_s = 0$ and $m_s = \pm 1$ sublevels [43] (see fig. 1.1). Nonetheless, this spin-selective process results in the accumulation of population in the $m_s = 0$ ground state sublevel, crucial for optical initialization. Additionally, since this alternative pathway does not fluoresce in the 650-800 nm band, NV$^-$ centers in the ground state $m_s = \pm 1$ sublevels will produce less fluorescence than those in the $m_s = 0$ upon optical excitation. This spin-state dependent fluorescence forms the basis of conventional optical NV$^-$ spin-readout.

The ground state $^3A_2$ Hamiltonian exhibits fine, hyperfine, and quadrupolar structure,

$$H_{\text{gs}}/h = S \cdot \mathbf{D} \cdot S + S \cdot \mathbf{A} \cdot I + I \cdot \mathbf{Q}, \tag{1.1}$$

where h is Planck's constant and $S = \{S_x, S_y, S_z\}$ and $I = \{I_x, I_y, I_z\}$ are the dimensionless electronic and nitrogen nuclear spin operators. The first, second, and third terms correspond to the electron spin-spin interaction with fine structure tensor $\mathbf{D}$, the electron-nuclear interaction with hyperfine tensor $\mathbf{A}$, and nuclear electric quadruple interaction with quadrupole tensor $\mathbf{Q}$ (relevant to the ^{14}N isotope with $I = 1$ and thus having an electric quadrupole moment). The tensors $\mathbf{D}$, $\mathbf{A}$, $\mathbf{Q}$ are diagonal as a result of the NV C_3v symmetry such that the ground state Hamiltonian can be expressed as,

$$H_{\text{gs}}/h = D(T)\hat{S}_z^2 + A_{||}\hat{S}_z\hat{I}_z + A_{\perp}(\hat{S}_x\hat{I}_x + \hat{S}_y\hat{I}_y) + P\hat{I}_z^2 \tag{1.2}$$

where the $m_s = 0$ ($|0\rangle$) ground state magnetic sublevel is separated from the $m_s = \pm 1$ ($|\pm 1\rangle$) sublevels by the zero-field-splitting $D(T)$ *approx* 2.87 GHz with temperature dependence $dD/dT = -74\,\text{kHz/C}$ [44]. The electronic states exhibit an additional splitting $A_{||}S_zI_z$ due to the hyperfine interaction between the NV electronic spin and the nitrogen nuclear spin ($I = 1$, $A_{||} \approx -2.14\,\text{MHz}$ for ^{14}N and $I = 1/2$, $A_{||} \approx 3.03\,\text{MHz}$ for ^{15}N) [45, 46]. The transverse hyperfine couplings $A_{\perp}$ for ^{14}N and ^{15}N are similar in magnitude with $A_{\perp} = -2.70\,\text{MHz}$ and $A_{\perp} = 3.65\,\text{MHz}$, respectively. While ^{14}N has an axial quadrupole coupling $P_{||} = -5.01\,\text{MHz}$, the ^{15}N isotope does not [45, 46].

In an external magnetic field $\vec{B} = \{B_z, B_x, B_y\}$, the ground state $|\pm 1\rangle$ sublevels are split via a Zeeman interaction term in the NV Hamiltonian,

$$H_{\text{zee}}/h = \frac{g_e\mu_B}{h}(B_z\hat{S}_z + B_x\hat{S}_x + B_y\hat{S}_y) \tag{1.3}$$

where $g_e \approx 2.003$ is the NV$^-$ electronic g-factor and $\mu_B = 9.24 \times 0^{-24}\,\mathrm{J/T}$ is the Bohr magneton, leading to an NV$^-$ gyromagnetic ratio $\gamma = 28.04\,\mathrm{GHz/T}$. Electric fields ($\vec{E} = \{E_z, E_x, E_y\}$ and crystal stress also contribute to the electronic ground state Hamiltonian with terms,

$$\begin{aligned} H_{\mathrm{stress}}/h \; &= M_z S_z^2 + M_x(S_x^2 - S_y^2) + M_y(S_x S_y + S_y S_x) \\ &\quad + N_x(S_x S_z + S_z S_x) + N_y(S_y S_z + S_z S_y), \end{aligned} \tag{1.4}$$

and

$$H_{\mathrm{elec}}/h = d_{||} E_z S_z^2 - d_\perp E_x(S_x^2 - S_y^2) + d_\perp E_y(S_x S_y + S_y S_x), \tag{1.5}$$

where M_z, M_x, M_y, N_x, and N_y are spin-strain coupling parameters, $d_{||} = 3.5 \times 10^{-3}\,\mathrm{Hz/(V/m)}$ is the axial electric dipole moment, and $d_\perp = 0.17\,\mathrm{Hz/(V/m)}$ is the transverse electric dipole moment [47–50].

Expressing these contributions to the ground state Hamiltonian together yields,

$$\begin{aligned} H_{\mathrm{total}}/h \; &\approx D(T) S_z^2 \\ &\quad + A_{||} \hat{S}_z \hat{I}_z + A_\perp(\hat{S}_x \hat{I}_x + \hat{S}_y \hat{I}_y) + P \hat{I}_z^2 \\ &\quad + \frac{g_e \mu_B}{h}(B_z \hat{S}_z + B_x \hat{S}_x + B_y \hat{S}_y) \\ &\quad + M_z S_z^2 + M_x \left(S_y^2 - S_x^2\right) + M_y \left(S_x S_y + S_y S_x\right) \\ &\quad + N_x \left(S_x S_z + S_z S_x\right) + N_y \left(S_y S_z + S_z S_y\right) \\ &\quad + d_{||} E_z S_z^2 - d_\perp E_x(S_x^2 - S_y^2) + d_\perp E_y(S_x S_y + S_y S_x). \end{aligned} \tag{1.6}$$

As discussed in detail in Chapter 3, the transverse magnetic coupling terms ($\propto B_x, B_y$) as well as the spin-strain coupling terms ($\propto N_x, N_y$) are suppressed by D and typically

negligible. Furthermore, when an external bias magnetic field $\vec{B}$ is applied with a non-zero projection along the NV axis, shifts in the ground state energy levels related to the transverse electric field components (E_x,E_y) and spin-strain parameters (M_x, M_y) are suppressed proportional to the projection B_z. The transitions between the $|0\rangle$ and $|\pm1\rangle$ sublevels of this simplified Hamiltonian (additionally dropping the hyperfine and quadrupole structure) become,

$$f_{\pm} = |E_{\pm1}\rangle - |E_0\rangle = (D(T) + M_z + d_{||}E_z) \pm \frac{g_e \mu_B}{h} B_z, \tag{1.7}$$

where $|E_{m_s}\rangle$ are the energy eigenstates of the $|m_s\rangle$ sublevels. The $|\pm1\rangle$ sublevels are split in common ($\propto S_z^2$) from $|0\rangle$ by the zero-field-splitting as well as axial crystal stress and electric fields. Meanwhile, the Zeeman term shifts the $|\pm1\rangle$ sublevels differentially (in opposite directions). As a consequence, axial stress and electric field induced shifts in the transitions can be deconvolved from magnetic-field-induced shifts either by making separate measurements of the $|0\rangle \rightarrow |+1\rangle$ and $|0\rangle \rightarrow |-1\rangle$ transitions or in a single measurement using multi-tone driving techniques such as double quantum magnetometry (see Chapter 3).

Finally, the NV ground state spin can be coherently manipulated using microwave (MW) irradiation resonant with the $f_{\pm}$ transitions which are non-degenerate when $B_z \neq 0$. Application of resonant or near-resonant MW control fields in combination with continuous wave or pulsed optical excitation forms the basis of NV-based multi-modal quantum sensing: shifts in the NV ground state spin resonances, $f_{\pm}$, will result in changes in the detected NV fluorescence. For small changes (relative to the dynamic range of the measurement), the shift in $f_{\pm}$ with respect to the frequency of

the applied MW control field can be linearly mapped to changes in magnetic field, electric field, crystal stress, or temperature.

1.2 Production of Synthetic NV-Diamond Material

Fabricated diamonds used for NV experiments can be produced using two methods: high pressure and high temperature (HPHT) synthesis [51] and plasma-enhanced chemical vapor deposition (PE-CVD or simply CVD) [52]. HPHT synthesis mimics the formation of natural diamond by compressing and heating a carbon source material. In addition to a diamond seed crystal, metal solvents are added to increase the growth rate and decrease the required temperature and pressure [51]. The density of incorporated nitrogen can be controlled (from $\sim$100 parts-per-million (ppm) down to a few parts-per-billion (ppb)) by tailoring the composition of the metal solvent [51,53].

In CVD synthesis, single-crystal diamond is grown on top of a diamond seed crystal using a hydrocarbon plasma. Methane is introduced as a carbon source. The addition of nitrogen both increases the growth rate and incorporates into the diamond lattice, replacing a carbon. The total nitrogen concentration [N] in CVD diamonds can be finely controlled and ranges from a few ppb up to tens of ppm. CVD synthesis upon a high-purity substrate (few ppb [N]) lends itself to producing the nitrogen-rich layers desired for many NV experiments including wide-field magnetic imaging applications, e.g., using a QDM [54, 55]. Typical layer thicknesses for such samples span from a few nanometers to tens of microns.

However, CVD synthesis suffers two primary deficiencies. First, the incorporation of unwanted vacancy-related defects, especially vacancy clusters and chains, is

common in many CVD diamonds [56–59]. These defect can act as charge acceptors and may decrease the optically detected measurement contrast by degrading the NV charge fraction $[NV^-]/[NV^0+NV^-]$ (see Chapter 6 for further discussion) [39]. These vacancy-related defects are also typically paramagnetic and therefore may contribute to NV ensemble dephasing [60]. Second, CVD diamonds often display crystal strain inhomogeneities which induce NV ground state spin resonance shifts on the order of typical NV ensemble linewidths (0.01-1 MHz) [38]. Exhibiting a diverse zoology, strain inhomogeneity may be present across a broad range of length-scales (sub-microns to millimeters) and is unique to each diamond [38]. The quality of the underlying diamond substrate used, especially any imperfections in the substrate surface, plays a major role in the resulting strain inhomogeneity [61, 62].

While diamond material produced using HPHT synthesis offers low crystal strain inhomogeneity and minimal incorporation of vacancy-related defects compared to most CVD diamonds [63], HPHT diamonds suffer several disadvantages for NV-based applications. First, single crystal HPHT diamond has different sectors with varying nitrogen incorporation. As a result, HPHT diamonds must first be processed into plates containing a single sector and it is not practical to produce the NV-rich, micron-scale surface layers favored for many NV applications [64]. Second, it remains to be demonstrated if the composition of HPHT diamond can be sufficiently well-controlled: attaining reproducible nitrogen densities, limiting the incorporation of ferromagnetic metal solvents (Fe, Co, Ni), and isotopically enriching the solid carbon and nitrogen sources similar to the purity available with the gaseous sources used in CVD synthesis. For example, isotopically purified methane with $>99.995\%$ ^{12}C is

common and favorable compared to natural abundance carbon sources which have 1.1% ^{13}C with nuclear spin $I = 1/2$ (^{12}C has nuclear spin $I = 0$).

Independent of the fabrication method, the concentration of NV defects in nitrogen-doped diamonds can be increased by irradiating the material (typically with electrons) to produce vacancies and annealing above 800 °C such that the vacancies becomes mobile and migrate to form NV [2]. The conversion efficiency E_{conv} of $N \rightarrow NV$ is used to indicate the fraction of [N] converted into [NV_{tot}]. In as-grown CVD diamonds (before irradiation and annealing), there exists approximately one NV for every three hundred nitrogen (300:1 [N]:[NV]) [65]. After irradiation and annealing (often referred to as post-treatment), conversion efficiencies ranging from $E_{conv} \sim 1 - 30\%$ have been reported [2]. The increased density of sensor spins is generally favorable for NV^- ensemble measurements (see Sec. 1.4).

For the work presented in this dissertation, nitrogen-doped, CVD-grown diamond material is used exclusively and both as-grown and post-treatment material is studied. While Chapters 2-5 describe, at least in part, techniques to characterize NV^- ensemble properties in CVD-grown material and improve NV-based magnetometer performance, Chapter 6 summarizes recent progress addressing the remaining weaknesses of CVD material (strain inhomogeneity and vacancy incorporation) achieved in collaboration with Element Six, Ltd.

1.3 Magnetic Sensing using NV^- Centers

The diverse set of magnetic sources studied using NV-based magnetometers can be divided into three regimes based on the signal's characteristic time-scale. In this section,

two of these three regimes are described along with the associated NV measurement protocols: static or broadband magnetic signals (DC-100 kHz) and narrowband, oscillating magnetic signals (1 kHz−10 MHz). For a review of techniques to measure GHz-scale magnetic signals, the reader is referred to Refs. [2, 24].

1.3.1 Static or broadband signals: DC−100 kHz

Three protocols are conventionally used to sense static, slowly-varying, or broadband magnetic signals using NV ensembles: continuous-wave optically detected magnetic resonance (CW-ODMR), pulsed-ODMR, and Ramsey magnetometry. The temporal characteristics of the magnetic signals that can be sensed using these protocols vary dramatically. Static signals, such as those produced by magnetic grains in geological samples [16, 66], domains in magnetic hard-disk memory [25], or the ferritin nanoparticles found in fixed magnetotactic bacteria [30] typically do not change on an experimentally relevant timescales and are amenable to signal averaging. In contrast, the broadband, millisecond-duration magnetic pulses produced by firing neurons require rapid measurements of the magnetic field, reconstructing the time-domain magnetic signals analogous to an oscilloscope. Meanwhile, magnetic navigation applications, which record slow changes in Earth's magnetic field while traveling relative to the Earth's surface, fall between these two timescales.

The technical simplicity of CW-ODMR has lead to it's broad implementation by the NV community. In a CW-ODMR protocol, the NV ensemble is optical illuminated while simultaneously applying microwave fields (as depicted in Fig. 1.2). A decrease in NV fluorescence is observed when the MW control field is resonant or near-resonant

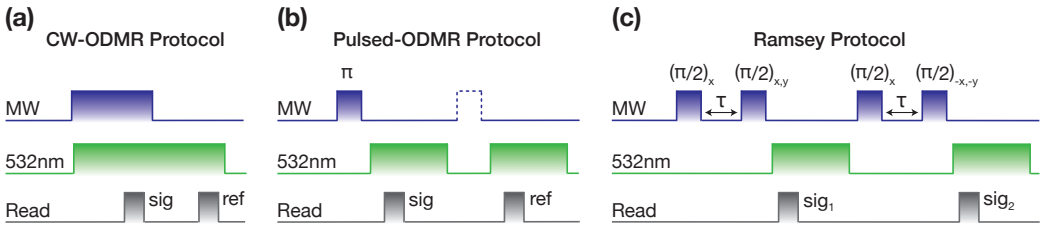

Figure 1.2: **Example DC Magnetometry Protocols (a)** CW-ODMR measurement protocol in which the optical (green) and MW fields (blue) are applied simultaneously. Acquisitions without MW control applied are used as reference such that the measurement contrast is given by $C = \text{sig}/\text{ref}$. **(b)** Pulsed-ODMR measurement protocol in which a MW π pulse is applied before optical readout. Again, acquisitions without MW control applied are used as reference such that the measurement contrast is given by $C = \text{sig}/\text{ref}$. (c) Ramsey measurement protocol consisting of two consecutive Ramsey sequences. For optimal sensitivity, the free precession interval, τ, is typically $\approx T_2^*$. Alternating the phase of the final $\pi/2$ pulse in successive sequences is used to modulate the NV$^-$ fluorescence and cancel low-frequency noise, such as $1/f$ noise. The measurement contrast is calculated as $C = (\text{sig}_1 - \text{sig}_2)/(\text{sig}_1 + \text{sig}_2)$ where sig_1 and sig_2 both contain information about the magnetic field sensed.

and drives population from the $|0\rangle$ to $|\pm 1\rangle$ sublevels, which is then pumped back into the $|0\rangle$ sublevel by the optical field. By sweeping the frequency of the applied MW control fields, an ODMR spectrum is produced exhibiting resonance features with line-centers dependent upon the external magnetic field, among other sources. For optimal sensitivity and temporal resolution, the NV$^-$ fluorescence is monitored while applying a MW field composed of a single or few frequencies at the point or point(s) of maximum slope for the resonance feature(s). Multi-frequency control can be used to operate on the point of maximum slope for each of the hyperfine-split resonances simultaneously and recover the "full" ODMR contrast and isolate resonance shifts from broadening or temperature drifts [19, 67, 68].

Despite the wide adoption of CW-ODMR techniques, their sensitivity is im-

paired by competing effects of the optical and microwave (MW) control fields applied during the sensing interval, leading to resonance broadening and a reduction in the maximum slope. Pulsed-ODMR techniques partially address this limitation by applying the optical and MW field sequentially [69]. After an optical pulse initializes the spin state into $|0\rangle$, a MW π-pulse transfers the population from $|0\rangle$ to either of the $|\pm1\rangle$ sublevels. The spin state is then readout and re-initialized via another optical pulse. If the NV spin resonances shift with respect to the frequency of the applied MW pulse, then the MW pulse will no longer completely transfer population to the $|\pm1\rangle$ sublevels as it would on resonance and results in a change in the NV fluorescence. Although an improvement compared to CW-ODMR, the observed resonance linewidth in pulsed-ODMR protocols remains a product of both the natural, T_2^*-limited linewidth and the NV spin's response to the fixed-duration MW pulse. Under optimal conditions for magnetic sensitivity, these two contributions are approximately equivalent.

Ramsey-based magnetometry protocols offer superior magnetic sensitivity compared to CW and pulsed-ODMR protocols by temporally separating the sensing interval from both the optical and MW pulses [70]. Among other advantages, Ramsey sequences enable increased optical intensity and MW field amplitude, yielding more photons per readout and sensing interval limited solely by the ensemble dephasing time T_2^*. In a Ramsey sequence, a MW pulse creates a superposition state of two sublevels which, in the simplest case, accumulate relative phase $\phi = 2\pi\gamma|\Delta m|B_z$ while evolving in the presence of a magnetic field for free precession interval, τ. Note that Δm accounts for the difference between the sublevels in the superposition state

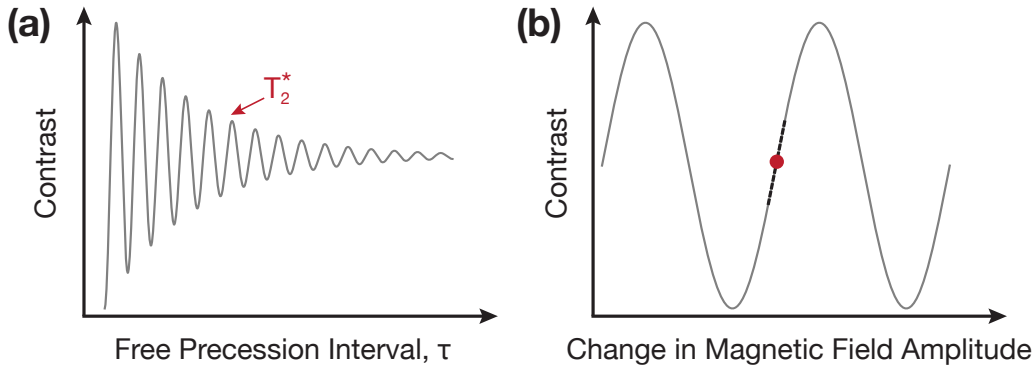

Figure 1.3: **Ramsey Free Induction Decay and Magnetometry Curve** **(a)** Ramsey signal as a function of free precession interval, τ. Ramsey fringes oscillate as a result of a detuning between the NV$^-$ spin resonances and applied MW pulse. The Ramsey fringes decay on the characteristic timescale T_2^* (when the signal amplitude is $\sim 1/e$ of its initial amplitude). (b) Ramsey signal as a function of a change in magnetic field magnitude, which results in a shift in the NV- spin resonance(s), commonly referred to as a DC magnetometry curve. For this measurement, the free precession interval remains fixed with $\tau \approx T_2^*$. The red circle indicates the point of maximum slope of optimal magnetic sensitivity. For small field changes, the NV response can be linearized about this point (black, dashed line). Note that a 2π phase ambiguity complicates magnetic sensing in the presence of large field changes.

($|\Delta m| = 2$ for a double quantum superposition of $|+1\rangle$ and $|-1\rangle$). Finally, a second MW pulse is applied to map the accumulated phase information into the relative populations of $|0\rangle$ and $|\pm 1\rangle$, which is subsequently readout using an optical pulse.

Sweeping the duration of the free precession interval produces Ramsey fringes which oscillate at a frequency determined by the detuning between the NV resonance and applied MW pulse and decay with a characteristic timescale T_2^* ($\sim$1/e of the initial amplitude). This dephasing time T_2^* is related to the natural linewidth Γ by $T_2^* = (\pi\Gamma)^{-1}$, assuming a Lorentzian lineshape. In a magnetometry measurement, the duration of the free precession interval, τ, is typically fixed to be approximately T_2^* for optimal magnetic sensitivity. With fixed τ, changes in the magnetic field, produce an oscillating response in the detected NV^- fluorescence referred to as a DC magnetometry curve. The point of maximum slope is indicated by the red point in Fig. 1.3. The calibration of a Ramsey-based magnetometer accounting for the impact of the NV hyperfine splitting and other factors is presented in Appendix A. Similar to sweeping the frequency in CW or pulsed-ODMR, Ramsey magnetometry protocols can also offer increased dynamic range at the cost of sensitivity by varying τ. The relevant parameters effecting the sensitivity of a Ramsey-based NV magnetometer are discussed in detail in the following section (Sec. 1.4).

1.3.2 Narrowband, AC magnetic signals: 1 kHz−10 MHZ

A prototypical example of an AC magnetic signal in NV applications is the NMR magnetic field produced by a thermally polarized nuclear spin ensemble precessing in an external, static magnetic field [18,20]. The Hahn echo sequence depicted in Fig. 1.4

builds upon the Ramsey sequence by adding an additional π-pulse in the middle of the free precession interval to refocus NV$^-$ ensemble dephasing, while making the sequence sensitive to narrow-band, oscillating (AC) magnetic fields (see Fig. 1.4). The MW pulses act as a narrow-band filter in frequency space with width given by the filter response function [71]. The rotation axes of the final $\pi/2$ pulses are chosen such that the sequence is either linearly sensitive to the magnetic field amplitude ({y,-y} in Fig. 1.4) or quadratically sensitive to magnetic noise with zero mean, but non-zero variance (corresponding to {x,-x}).

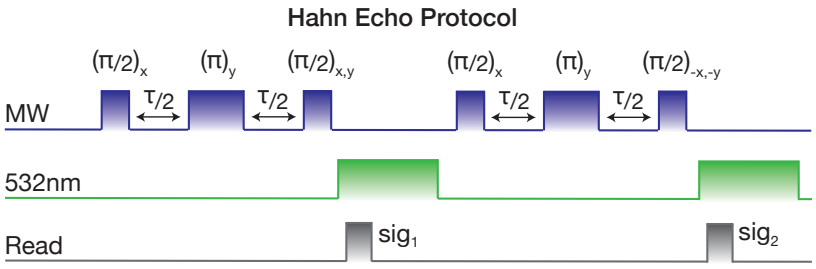

Figure 1.4: **Example Hahn Echo Measurement Protocol (a)** Each Hahn echo sequence includes a refocusing π-pulse, enabling phase-sensitive measurements of narrowband, AC magnetic signal. Alternating the phase of the final $\pi/2$ pulse in successive sequences is used to modulate the NV$^-$ fluorescence and cancel low-frequency noise, such as $1/f$ noise. The measurement contrast is calculated as $C = (\text{sig}_1 - \text{sig}_2)/(\text{sig}_1 + \text{sig}_2)$. When the phases of the final $\pi/2$ pulse are chosen to be {x, -x} ({y, -y}), the response to magnetic field amplitude changes is quadratic (linear). The full evolution period τ is chosen to match the period of the narrow-band, AC magnetic signal to be sensed.

Since the heterogeneous phase accumulated due to a stress-gradient or dipolar interactions with the diamond spin bath is cancelled by the Hahn echo sequence, the relevant timescale becomes the decoherence time, T_2. This decoherence time is typically at least an order of magnitude longer than T_2^* and determined by dynamic changes in the local magnetic environment of each NV$^-$ sensor spin, predominantly

arising from intra-bath interactions (see Chapter 2 and Ref. [72]). For optimal sensitivity, the total free precession interval τ (the time between $\pi/2$ pulses) should be $\sim T_2$. However, this condition is not typically satisfied for Hahn echo sequences since the duration between pulses ($\tau/2$) must be matched to the period of the AC magnetic field [9]. Multiple refocusing pulses (dynamical decoupling) can be employed to extend the decoherence time by narrowing the filter response function and subsequently increasing the duration of the total free precession. A wide range of dynamical decoupling sequences developed for NMR, such as CPMG-n and XY8-n, have been adopted for NV applications [71].

In this dissertation, AC magnetometry protocols are primarily used for characterization. For example, comparison of the ratio between the ensemble dephasing time T_2^* and Hahn echo decoherence time T_2 is a useful metric for elucidating underlying dephasing mechanisms. Additionally, the double electron electron resonance (DEER) spectroscopy techniques employed in Chapter 5 to study the diamond spin bath apply Hahn echo sequences to the NV ensemble while manipulating the bath spins [73].

1.4 Sensitivity of a Ramsey-based Magnetometer

Ramsey measurement protocols are anticipated to be favored over CW and pulsed-ODMR protocols for applications demanding the utmost magnetic sensitivity possible. In addition, unlike ODMR-based protocols, Ramsey sensing is compatible with techniques such as double quantum magnetometry (see Chapter 3). As discussed in Refs. [2], the magnetic field sensitivity of a Ramsey-based NV ensemble magnetometer

including spin projection noise and photon shot noise is:

$$\eta_{\text{ramsey}} = \frac{\hbar}{g_e \mu_B} \underbrace{\left(\frac{1}{\Delta m_s \sqrt{N\tau}}\right)}_{\text{Spin Projection Noise}} \underbrace{\left(\frac{1}{e^{-(\tau/T_2^*)^p}}\right)}_{\text{Dephasing}} \underbrace{\sqrt{1 + \frac{1}{C^2 n_{\text{avg}}}}}_{\text{Readout}} \underbrace{\sqrt{\frac{\tau + t_O}{\tau}}}_{\text{Overhead Time}} \tag{1.8}$$

where N is the number of non-interacting NVs, τ is the free precession interval between MW pulses, Δm_s accounts for the difference in m_s states used for sensing (at most $\Delta m_s = 2$), T_2^* is the ensemble dephasing time, p is the decay shape parameter ($p = 1$ for exponential decay), C is the measurement contrast, n_{avg} is the average number of photons collected per readout, and t_O is the measurement overhead time including the durations of the optical initialization, readout, and MW pulses.

As depicted in Eqn. 1.8, the ensemble magnetic sensitivity η_{ramsey} contains contributions related to spin projection noise, imperfect readout fidelity, ensemble dephasing, and measurement overhead time (any time not spent accumulating phase). However, NV$^-$ ensemble-based magnetometers are not typically limited by spin-projection-noise since instead of measuring S_z directly, the conventional NV$^-$ optical readout method indirectly probes the spin state by monitoring NV$^-$ fluorescence. As a consequence, photon shot noise on the measured fluorescence must also be incorporated into the sensitivity.

In Eqn. 1.8, the "readout" term, denoted σ_{R} hereafter, accounts for the addition of photon-shot-noise:

$$\sigma_R = \sqrt{1 + \frac{1}{C^2 n_{\text{avg}}}}, \tag{1.9}$$

and is the inverse of the measurement fidelity, $F \equiv 1/\sigma_{\text{R}}$. In Eqn. 1.9, the measurement contrast is defined using the fringe visibility $C = (a - b)/(a + b)$ where a (b)

is the number of photons collected when all NV$^-$ sensor spins are in the $|0\rangle$ sublevel ($|\pm1\rangle$ sublevels). The parameter σ_{R} is a useful metric for quantifying how far the sensitivity is from the standard quantum limit: as the measurement contrast C or average number of photons n_{avg} increases, the contribution of photon-shot-noise decreases and approaches $\sigma_{\mathrm{R}} \approx 1$ (the standard quantum limit or spin-projection-noise limit). However, this regime is uncommon for NV$^-$ ensemble magnetometers due to the limited measurement contrast of between the $|0\rangle$ and $|\pm1\rangle$ spin sublevels (typically $\lesssim 15\%$) and number of photons collected per NV$^-$ (typically $n_{\mathrm{avg}} \ll 1$). As a result, the product $C^2 n_{\mathrm{avg}}$ is usually much less than one and photon-shot-noise dominates.

The dephasing and measurement-overhead-related contributions to Eqn. 1.8 impact both the photon-shot-noise and spin-projection-noise sensitivities. The dephasing term accounts for the Ramsey fringe amplitude decay with increasing τ characterized by the ensemble dephasing time, T_2^* and decay profile parameter, p. An exponential decay profile, $p = 1$, is expected when dephasing is dominated by dipolar interactions with the diamond spin bath [74]. The measurement overhead time factor accounts for the fraction of each acquisition spent on optical initialization, optical readout, and MW control. Assuming M measurements, each with a free precession interval τ, are collected for a total measurement time of t_{meas} the sensitivity factor is $\sqrt{1/M} = \sqrt{(\tau + t_O)/t_{\mathrm{meas}}}$. The relative durations of t_O and T_2^* impact the optimal free precession interval τ in a Ramsey sequence. When measurement overhead time t_{O} is negligible compared to T_2^*, the optimal duration for τ corresponds to $\tau = T_2^*/2$. However, for typical NV$^-$ ensemble dephasing times ($T_2^* \approx 1\mu$s), the measurement overhead time dominates ($t_O \gtrsim 5\mu$s) such that the optimal free precession interval is

$\tau \approx T_2^*$.

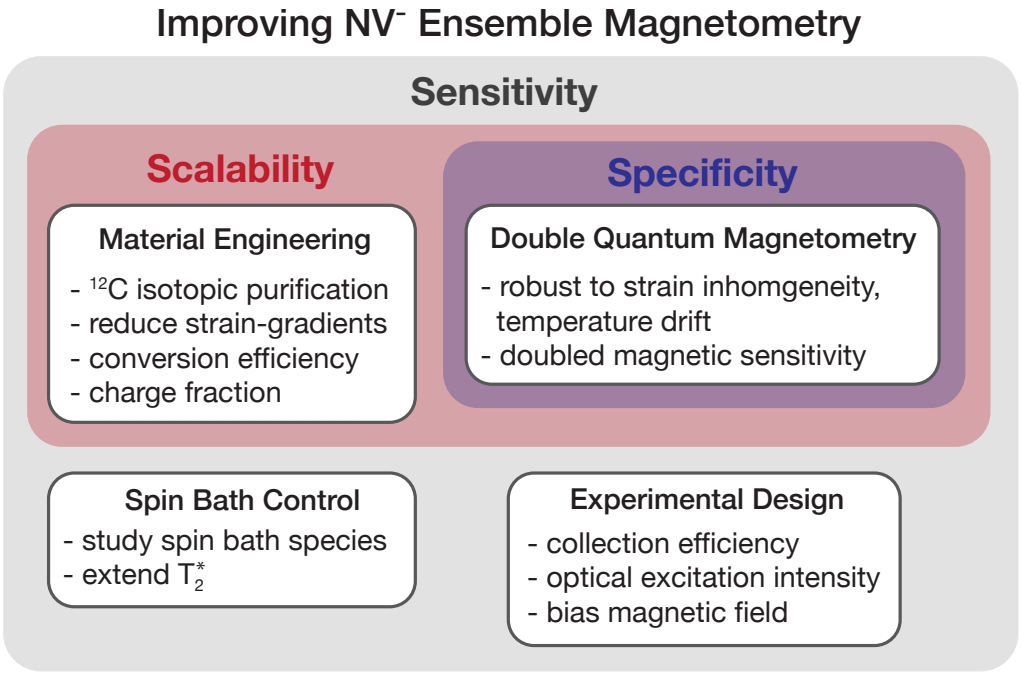

Figure 1.5: **Avenues Toward Improved NV-based Magnetometry.** Four directions are highlighted to enable improved magnetic sensitivity, magnetic specificity, and scalability for NV ensemble measurements based on Eqn. 1.8: material engineering, double quantum coherence magnetometry, spin bath control, and experimental design considerations. These directions are inter-related and work together synergistically. For example, spin bath driving while using the double quantum coherence can significantly extend the dephasing time T_2^* by mitigating multiple sources of dephasing simultaneously.

Inspecting Eqn. 1.8, it becomes apparent that increasing the measurement contrast C, the free precession interval τ, the dephasing time T_2^*, the number of NV$^-$ sensor spins N, and average number of photons n_{avg}) are all favorable for magnetic sensitivity (reducing η_{ramsey}). However, in practice, the inter-dependence of these quantities complicates efforts and requires considering the impact of changing any one parameter on the others. Addressing this challenge, the following discussion

introduces four promising avenues towards successfully improving the sensitivity of Ramsey magnetometry: material engineering, double quantum coherence magnetometry, spin bath control, and experimental design. Comments on the benefits of these directions for scalability and magnetic specificity are also included.

Of the parameters relevant for magnetic sensitivity, measurement contrast and dephasing time are particularly crucial to consider. The magnetic sensitivity scales inverse linearly with measurement contrast, such that improving contrast (or harming it while increasing other parameters) has a significant impact. Less obviously, in the experimentally common limit where the measurement overhead time exceeds T_2^*, changes in the dephasing time also scales near inverse-linearly with magnetic sensitivity [2]. Extending the dephasing time T_2^* is also promising because typical values for ensemble dephasing times reported in the literature are order of magnitudes shorter than both T_2 and T_1, suggesting significant improvements may be possible. With sufficient extensions in T_2^* ($\approx 20\mu$s), alternative readout techniques, which come with an additional overhead time penalty, such as repetitive ancilla-assisted readout or charge-state readout could yield further sensitivity improvements (see Ref. [2, 75] for further discussion).

Material Engineering – While tailoring NV-rich diamond material properties is application dependent, several guiding principles can be established here, with extensive further discussion in Chapters 2 and 6. In the context of increasing T_2^*, reducing the density of the ^{13}C ($I = 1/2$) nuclear spin bath and resulting NV-^{13}C dipolar interactions is broadly advantageous. In material with a natural abundance of ^{13}C nuclear spins (1.1% or 10700 ppm), the NV$^-$ ensemble T_2^* is limited to approximately 1μs;

similar to the electron spin bath contribution from $\approx 10\,\text{ppm}$ of nitrogen. However, CVD synthesis using isotopically purified methane (>99.995% ^{12}C purity is available) largely mitigates dephasing due to the nuclear spin bath, as ^{12}C has $I = 0$, without negatively impacting any other parameters - making this a straightforward win when working with material with $\lesssim 100\,\text{ppm}$ of nitrogen [39].

Reducing the magnitude of stress inhomogeneity is also commonly beneficial for T_2^* as well as measurement contrast, especially with decreasing concentrations of incorporated nitrogen and ^{12}C isotopic purification. Conversely, while increasing the concentration of incorporated nitrogen, [N] ultimately increases the number of NV sensor spins and average number of photons per readout, often this approach degrades T_2^* , which scales inverse-linearly with [N] (see Chapter 2). Instead, it is more rewarding to increase the conversion efficiency of incorporated nitrogen into NV$^-$, which is beneficial for N, n_{avg}, and T_2^*. The creation of NV$^-$ is typically assumed to consume two substitutional nitrogen defects (S=1/2) for every NV$^-$ created, reducing the effective spin bath density. Furthermore, NV$^-$ centers not actively employed for sensing, such as those oriented along the other crystal axes, are initialized into $m_s = 0$ and do not contribute to dephasing [40, 76].

Meanwhile, the measurement contrast, number of sensor spins, and average number of detected photons are also intimately related to the NV charge fraction,

$$\phi \equiv \frac{[\text{NV}^-]}{[\text{NV}^-] + [\text{NV}^0]}, \tag{1.10}$$

which can vary dramatically with sample properties, but typically degrades with increasing optical illumination intensity [77, 78]. Beyond the direct impact of the

NV charge fraction on the number of sensor spins and amount of NV^- fluorescence (N and n_{avg}), NV centers in the neutral charge state (NV^0) do not exhibit spin-state-dependent optical properties; thus they are not used in conventional NV-based magnetic sensing or optical readout and merely contribute background fluorescence, which decreases measurement contrast. As highlighted in Chapter 6, methods to improve the NV charge fraction via material engineering include reducing the density of vacancy-related defects incorporated during growth, which can act as charge acceptors.

Double Quantum Magnetometry – Coherent superpositions of the $|\pm 1\rangle$ sublevels (referred to as the double quantum or DQ coherence) during the sensing interval of a Ramsey sequence are immune to sources which shift the $|\pm 1\rangle$ sublevels in common-mode such as crystal stress and temperature drift, while also effectively doubling the NV^- gyromagnetic ratio ($\Delta m_s = 2$ in Eqn. 1.8) [73,79–81]. When stress-gradients dominate the ensemble dephasing, DQ Ramsey measurements can lead to extensions in T_2^* as well as suppress stress-gradient-induced T_2^* variations across a diamond sample or between samples.

In the absence of stress inhomogeneity, the DQ basis is twice as vulnerable to magnetic spin bath induced dephasing such that $T_2^*\{\mathrm{SQ}\} \approx T_2^*\{\mathrm{DQ}\}/2$. Nonetheless, even in this regime, magnetic sensitivity can be improved by using the DQ sensing basis. The effectively doubled gyromagnetic ratio of the DQ sensing basis accumulates magnetic phase twice as rapidly such that the same amount of phase can be accumulated in half the free precession interval compared to a SQ measurement. In the limit of negligible overhead, this doubles the measurement bandwidth and im-

proves magnetic sensitivity by a factor of $\sqrt{2}$. Additionally, as will be emphasized in Chapters 3, 4 and 6, the robustness of DQ measurements to common-mode shifts is also critical for magnetic specificity and scalability.

Spin Bath Control – After mitigating dephasing due to the ^{13}C nuclear spin bath and stress-gradients, the DQ T_2^* is typically limited by static dipolar interactions with the electronic spin bath. AC magnetometry protocols decouple the NV$^-$ sensor spins from the electronic spin bath (predominantly neutral substitutional nitrogen [N_s^0]) by applying MW π-pulses resonant with the NV sensor spins to refocus spin-bath-induced dephasing. However, this approach is incompatible with sensing static or broadband magnetic signals. Instead, resonant MW control of the bath spins can be used to decouple the bath from the NV$^-$ sensor spins, while retaining sensitivity to static or broadband magnetic signals [73, 82, 83]. In low-[NV$^-$], as-grown material, spin bath decoupling enables order-of-magnitude scale improvements in the NV T_2^*. For irradiated and annealed, NV-rich material, spin bath control enables dephasing times limited by NV-NV dipolar interactions (see Chapter 5).

Experimental Design – Eqn. 1.8 also suggests experimental design choices favorable for Ramsey-based magnetometry. First, pulsed protocols in general favor increasing the optical excitation intensity toward saturation intensity of the NV$^-$ (1–3 mWμm^{-2} [84]) to decrease the re-initialization time required between sensing intervals as well as increase n_{avg}. However, this must be balanced by the degradation of the NV charge fraction with increasing optical intensity and associated consequences. Second, optical collection efficiency in NV ensemble experiments is typically quite poor (less than a few percent [2]), making light-guides and similar optical devices

attractive when spatial information is not important [20]. Although noting their relevance, this dissertation does not discuss these application-specific experimental design choices in detail.

1.5 This Work

1.5.1 Organization of this Dissertation

Chapter 2 describes NV^- ensemble properties relevant for magnetometry applications as motivated in the preceding section (Sec. 1.4). Sec. 2.2 summarizes the sources of NV ensemble dephasing, including stress-inhomogeneity as well as dipolar interactions between NV sensors and the paramagnetic spin bath. As part of this discussion, ensemble dephasing is contrasted with decoherence. Sec. 2.3 then discusses crystal stress inhomogeneity in diamond, providing examples to emphasize the zoology of imperfections which arise. Sec. 2.4 describes the impact of NV charge fraction on measurement contrast and the number of sensor spins, especially under intense green illumination.

Chapter 3 introduces double quantum (DQ) coherence magnetometry, highlighting the benefits of using superpositions of the $|\pm 1\rangle$ sublevels for NV-based magnetometry, which simultaneously offers improved magnetic sensitivity, magnetic specificity, and scalability (reproducibility) in the presence of stress-gradient across an NV ensemble. The experimental methods required to implement DQ magnetometry along with a comparison of DQ and SQ Ramsey free induction decay measurements in multiple samples are discussed in the context of single-channel, photodiode based

experiments.

Chapter 4 applies DQ techniques to magnetic imaging applications, demonstrating record volume-normalized magnetic sensitivity for an NV-diamond imaging modality. The consequences of stress-gradients on varying length-scales for magnetic imaging are discussed in detail.

Chapter 5 describes methods to characterize and control the paramagnetic electronic spin bath in diamond. Double electron-electron resonance techniques are introduced to identify and quantify the contribution of different spin bath species to NV^- ensemble dephasing. Experiments using spin bath control to decouple spin bath dephasing to extend T_2^* and improve magnetic sensitivity are also described.

Chapter 6 summarizes recent progress toward diamond material tailored for NV^- ensemble magnetometry applications in collaboration with Element Six Ltd. and Lockheed Martin Corporation. Reducing the density of charge acceptors in as-grown diamond material is shown to produce final material (after irradiation and annealing) with favorable N to NV^- conversion efficiency, NV charge fraction, dephasing times T_2^*, measurement contrast, and stress inhomogeneity.

Finally, Chapter 7 provides a brief outlook highlighting the most promising directions for further advances in NV-based quantum sensing.

1.5.2 Coworker Contributions

I have been fortunate to work with a wonderful group of colleagues and collaborators. Much of the motivation for the results presented in this dissertation emerged from the efforts of the "T_2^* task-force" which included Jennifer Schloss, Matthew Turner, Erik

Bauch, John Barry, and myself. In particular, Jennifer Schloss, Matthew Turner, and John Barry initially identified the promise of double quantum (DQ) coherence (Chapter 3) and spin bath control (Chapter 4) in improving NV^- ensemble DC magnetic sensitivity. I have spent the intervening years realizing this promise and developing the technical innovations required to fully leverage their potential, including the DQ 4-Ramsey measurement protocol to mitigate the consequences of microwave pulse errors. Erik Bauch was an equal contributor to a significant fraction of the work reported in Chapters 3 and 4. The data collection and analysis establishing the contribution of the electronic and nuclear spin baths to NV ensemble dephasing and decoherence was collected jointly with Erik Bauch.

The discussion of stress inhomogeneity and NV charge state in Chapter 2 is the result of close collaboration with Matthew Turner, who pioneered the use wide-field magnetic imaging for crystal stress characterization along with Pauli Kehayias, and Kevin Olsson, who collected the NV charge fraction measurement presented.

Jennifer Schloss, Matthew Turner, Patrick Schiedegger, and I worked closely together realizing Ramsey-based wide-field imaging. Jennifer Schloss pioneered the initial motivation and characterization of the camera employed in Chapter 4. Patrick Schiedegger developed experimental control software and GPU-based fitting methods under my guidance on a setup originally configured by Erik Bauch and myself. Using this setup, I collected, analyzed, and documented the results presented in Chapter 4. Matthew Turner led the development of bio-compatible experimental components for a high sensitivity magnetic imager with Jennifer Schloss and me.

The development and characterization of improved diamond material described

in Chapter 6 is the result of collaboration with Element Six Ltd. Dr. Andrew Edmonds conceived the project, led the material growth, and oversaw the absorption-based characterization measurements. Kevin Olsson, Matthew Turner, and I jointly collected the NV-based characterization measurements. The results were documented and written up by Andrew Edmonds and me.

Chapter 2

NV-Diamond Material Properties Relevant for Magnetometry

Building upon the discussion in Sec. 1.4, this Chapter describes select material properties relevant for improving NV^- magnetometer performance: sources of ensemble dephasing, crystal stress inhomogeneity, and NV charge fraction. NV-based methods to characterize these properties are contrasted with existing techniques employed by the diamond growth community. Additionally, examples of the current state-of-the-art are provided for context and to motivate the need for further material development and exploration of measurement protocols robust to the described weaknesses.

After highlighting the difference between single NV^- and NV^- ensemble dephasing in Sec. 2.1, Sec. 2.2 introduces typical NV^- ensemble dephasing mechanisms, providing a brief summary of each before providing further discussion in subsequent sections. Experimental determinations of the scaling of T_2^* with the density of incorporated nitrogen [N] and other paramagnetic defects are presented and compared to

expectations from literature. In addition, while introducing Hahn echo decoherence measurements as a useful characterization metric, the distinction between ensemble dephasing and decoherence is emphasized.

Sec. 2.3 is dedicated to discussing the impacts of crystal stress inhomogeneity in CVD-grown, nitrogen-doped layer diamond material on NV magnetometry, including as a source of ensemble dephasing. The established method to characterize stress using birefringence measurements is compared to NV-based measurements which provides more direct measurements of the local stress in the nitrogen-doped layer and avoids the high-strain-induced, "$\pi/2$" phase ambiguity which complicates the interpretation of birefringence-based measurements.

Finally, the mechanisms impacting NV charge fraction are summarized while highlighting the need for improved understanding, especially in-situ under optical illumination. A method to determine the NV charge fraction from photo-luminescence (PL) measurements is used to study the NV charge state of an irradiated and annealed, nitrogen-doped layer ($\mathrm{N} \approx 8\,\mathrm{ppm}$) exhibiting poor "native" charge fraction which further decays with increasing optical illumination intensity. The effect of this charge fraction degradation on the ODMR contrast is presented as well.

2.1 NV^- Ensemble Dephasing

Single NV^- Ramsey fringe decay occurs due to the NV^- electronic spin effectively dephasing with itself across multiple measurements as a result of temporal variations in the local environment, such as magnetic fluctuations induced by the paramagnetic spin bath or temperature drift. Single NV^- T_2^* within the same diamond can vary

dramatically because of the random distribution of paramagnetic spins: NV^- spins that happen to be arranged to other paramagnetic spins nearby will exhibit a shorter T_2^* relative to NV^- spins which are more isolated in the lattice.

Although temporal variations in the environment also contribute to NV^- ensemble dephasing, the ensemble T_2^* is additionally limited by static heterogeneities across the interrogated volume of diamond, including spatially-varying crystal stress-gradients as well as magnetic dipolar interactions with other paramagnetic spins. These sources shift the resonance frequencies of constituent NV^- centers in the ensemble with respect to each other (in addition to the temporal dephasing experienced by each spin). Averaging over these distributions of resonance frequencies and T_2^* results in broadening of the NV^- ensemble resonance feature or, equivalently, an enhanced dephasing rate. Due to the role of spatially varying NV^- resonance shifts in ensemble dephasing, determining the ensemble T_2^* from the typical single NV^- T_2^* value in a sample is misleading and comparisons of single NV^- experiments or theory to NV^- ensembles should be made with care. For example, while a single NV^- Ramsey free induction signal exhibits Gaussian decay, the ensemble decay profile is exponential when limited by dipolar interactions with the diamond spin bath. This difference in decay profile arises from averaging over the less probable "bad apples", e.g., single NV^- centers with particularly large resonance shifts or short T_2^* due to a nearby bath spin [74].

2.2 NV$^-$ Ensemble Dephasing Mechanisms

The contributions of different dephasing sources to NV$^-$ ensemble T_2^* can be represented schematically as,

$$\begin{aligned}\frac{1}{T_2^*} \approx & \frac{1}{T_2^*\{\text{electronic spin bath}\}} + \frac{1}{T_2^*\{\text{nuclear spin bath}\}} \\ & + \frac{1}{T_2^*\{\text{stress gradients}\}} + \frac{1}{T_2^*\{\text{electric field noise}\}} \\ & + \frac{1}{T_2^*\{\text{magnetic field gradients}\}} + \frac{1}{T_2^*\{\text{temperature drift}\}} \\ & + \frac{1}{T_2^*\{\text{unknown}\}} + \frac{1}{T_2^*\{2T_1\}}\end{aligned} \tag{2.1}$$

where $T_2^*\{\text{X}\}$ refers to the limit on T_2^* imposed by mechanism X in the absence of any other dephasing mechanism. Note that Eqn. 2.1 assumes all terms are independent and the associated dephasing rates add linearly. However, this second assumption is only exactly true for dephasing induced by dipolar interactions with the diamond spin bath where the expected decay is exponential. For other sources, Eqn. 2.1 is in general only an approximation. Nonetheless, the form of Eqn. 2.1 motivates the proper approach towards extending T_2^*: The dominant source of dephasing should be reduced until another source becomes dominant. At which point, it is more productive to focus on the new dominant source then continue to suppress the original mechanism.

We now briefly discuss each term in Eqn. 2.1 and then go into more detail in following sections. As a note, the $1/T_2^*\{\text{unkown}\}$ term is included to emphasize that while we believe the following contributions are the major sources of dephasing in CVD diamond, other to-be-identified sources may play a role.

The term $1/T_2^*\{\text{electronic spin bath}\}$ accounts for dephasing induced by mag-

netic dipolar coupling of the electronic paramagnetic bath spins to constituent NV$^-$ centers. The individual dephasing contributions of different electronic spin species in the spin bath can be divided as,

$$\frac{1}{T_2^*} \approx \frac{1}{T_2^*\{\mathrm{N}_s^0\}} + \frac{1}{T_2^*\{\mathrm{NV}^-\}} + \frac{1}{T_2^*\{\mathrm{NV}^0\}} + \frac{1}{T_2^*\{\text{other electronic spins}\}}. \tag{2.2}$$

The term $1/(T_2^*\{\mathrm{N}_s^0\})$ corresponds to the dephasing induced by neutral substitutional nitrogen defects ($S = 1/2$), or P1 centers, with concentration $[\mathrm{N}_s^0]$. As result of the nitrogen-doping required to produce NV$^-$ ensemble diamond material, N_s^0 is typically the dominant species in the diamond electronic spin bath in as-grown diamonds. Sec. 2.2.1 describes the scaling of $T_2^*\{\mathrm{N}_s^0\}$ with $[\mathrm{N}_s^0]$. Following irradiation and annealing, dipolar interactions between NV$^-$ defects become a non-negligible source of ensemble dephasing as discussed further in Sec. 2.2.3. Although a term associated with NV^0 ($S = 1/2$) is included for completeness, NV^0 is not visible in EPR [85] and the present understanding is that it is a diminished contribution to NV$^-$ ensemble dephasing. The final term in Eqn. 2.2 accounts for dephasing due to dipolar interactions with other paramagnetic species. For CVD diamond, this includes mono-vacancies, multi-vacancy cluster or chains, and hydrogen-related defects such as NVH$^-$ [59,65,86].

The term $1/T_2^*\{\text{nuclear spin bath}\}$ in Eqn. 2.1 encompasses NV$^-$ ensemble dephasing due to dipolar interactions with the nuclear spin bath. In samples produced with natural abundance carbon sources, the contribution of 1.1% ^{13}C ($I = 1/2$) dominates over any other nuclear species. Although the dipolar coupling with the nuclear bath is $2000\times$ weaker than that of the electronic spin bath, the higher density of ^{13}C

spins compensates; 1.1% ^{13}C is equivalent to $[^{13}\mathrm{C}] \approx 10700\,\mathrm{ppm}$, which vastly exceeds the typical $[\mathrm{N}] \approx 1 - 20\,\mathrm{ppm}$. In CVD-grown diamond material, this ^{13}C contribution can be readily mitigated using isotopically purified methane. Sec. 2.2.4 discusses the scaling of T_2^* with $[^{13}\mathrm{C}]$. Beyond the ^{13}C nuclear spin bath, hydrogen (with the dominant ^{1}H isotope possessing I=1/2) is plentiful during CVD growth and can readily incorporate into the diamond lattice at concentrations comparable to [N], forming defects such as NVH^- and VH^- [87, 88]. While the role of hydrogen in NV^- dephasing remains unclear, it is a potential additional source of nuclear spin bath noise to investigate further, especially because of the about $4\times$ larger gyromagnetic ratio compared to ^{13}C.

Inhomogeneity in the crystal stress environment is another major source of NV^- ensemble dephasing. The typical magnitudes of stress-induced shifts of the NV^- spin resonances are comparable to, or dominate, the spin bath-related contributions (especially for ^{12}C isotopically-purified material with $[\mathrm{N}] \approx 1 - 20\,\mathrm{ppm}$). In addition, commonly observed crystal stress features can span a wide range of the length-scales from sub-micron to millimeters [38]. As noted in Sec. 1.4, the distribution of crystal stress varies within a sample as well as between samples, presenting challenges for attaining uniform magnetic sensitivity and scalability. Example measurements imaging the typical stress environments in CVD-grown, nitrogen-doped diamond layers are provided in Sec. 2.3 along with the corresponding impact on NV^- ensemble dephasing.

Eqn. 2.1 also includes terms accounting for dephasing mechanisms external to the diamond such as magnetic field gradients and temperature drift. These sources must be mitigated before dephasing intrinsic to the diamond material can be studied.

The bias magnetic fields applied throughout the experiments presented in this dissertation were engineered to suppress unwanted, magnetic field gradients (see App. B for additional discussion). Temperature drifts, which induce changes in the NV$^-$ zero-field-splitting ($dD/dT \approx 74\,\mathrm{kHz}/^\circ\mathrm{C}$), can manifest as ensemble dephasing. In addition, the permanent magnets or current carrying coils used to apply a bias magnetic field can exhibit temperature-dependent magnetic field strength which similarly result in extraneous ensemble dephasing (see Appendix B for discussion of the permanent magnet geometry used throughout this work).

Finally, NV$^-$ electronic spin depolarization places a fundamental limit on T_2^* of $2T_1$ [2, 89]. While achieving T_1-limited ensemble dephasing times may be unattainable, the orders of magnitude difference between typical $T_2^* \approx 1\,\mu\mathrm{s}$ compared to NV$^-$ $\mathrm{T}_1 \approx 5\,\mathrm{ms}$ suggests room for significant improvements. In particular, mitigating spatially inhomogeneous mechanisms, such as stress-gradients, which contribute to NV$^-$ ensemble T_2^* but not single NV$^-$ T_2^* is a promising avenue toward extending ensemble T_2^* [2] and improving magnetic sensitivity.

2.2.1 Nitrogen Limit to T_2^*

In nitrogen-rich diamond material, electronic spins predominately acquire charges from neutral substitutional nitrogen which can donate its electron to another defect [58]. As a result, the resulting contribution of the electronic spin bath to dephasing is coupled to the total nitrogen concentration, [N]. In as-grown material with low-[NV], the paramagnetic electronic spin bath is typically assumed to consist largely of [N_s^0] [72]. When other sources of dephasing are mitigated, an inverse linear scaling

is expected for the ensemble T_2^* as a function of $[N_s^0]$ according to,

$$\frac{1}{T_2^*\{N_s^0\}} = A_{N_s^0}[N_s^0] \tag{2.3}$$

This scaling is confirmed experimentally in Fig. 2.1(a) with T_2^* measurements for five as-grown diamond samples grown by Element Six [72, 73]. A linear fit to the data yields an estimate for $A_{N_s^0}$ of $101(12)\,\mathrm{ms}^{-1}\mathrm{ppm}^{-1}$. For these measurements, only isotopically-purified samples with >99.995% ^{12}C were studied using the stress-immune double quantum sensing basis to ensure non-nitrogen-related dephasing mechanisms were negligible. The extracted value for $A_{N_s^0}$ agrees reasonably well with the value of $A_{N_s^0} = 101(12)\,\mathrm{ms}^{-1}\mathrm{ppm}^{-1}$ derived from EPR-based measurements [90] as well as with separate numerical simulations [72]. In arriving at the experimental estimate for $A_{N_s^0}$, we have explicitly assumed that the total paramagnetic electronic spin bath density is well approximated by the total nitrogen [N] and that $[N_s^0] \approx [N]$. This assumption will be revisited in Chapter 6 when considering the potential role of charge acceptors such as vacancy clusters and chains on the NV$^-$ ensemble spin properties.

2.2.2 Nitrogen Limit to T_2

Hahn echo measurements, with structure $\pi/2-\tau/2-\pi-\tau/2-\pi/2$, mitigate static and slowly-varying heterogeneities. As a result of the π-pulse inserted halfway through the free precession interval, phase accumulated during the first half the sequence due to static, or quasi-static compared to the duration τ, sources is canceled by phase accumulated with opposite sign in the second free precession interval. As introduced in Sec. 1.3.2, the echo signal decays as a function of τ on the timescale of

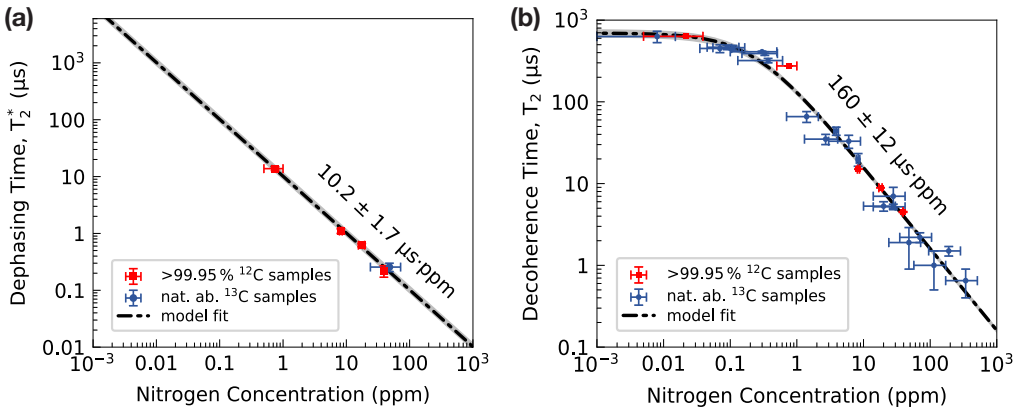

Figure 2.1: **Substitutional nitrogen spin-bath contribution to T_2^* and T_2.** **(a)** Measured spin-bath contribution to T_2^* versus nitrogen concentration as measured using secondary ion mass spectroscopy (SIMS). Fit yields $A_{\mathrm{N}_s^0} = 101(12)\,\mathrm{ms}^{-1}\mathrm{ppm}^{-1}$. Gray band indicates 95% confidence interval for fit. **(b)** Measured Hahn Echo T_2 for 25 diamond samples. The linear contribution to the fit yields $B_{\mathrm{N}_s^0} = 6.25(47)\,\mathrm{ms}^{-1}\mathrm{ppm}^{-1}$. Gray band indicates 95% confidence interval for fit. The nitrogen-independent contribution to the fit is 694(82) µs.

the decoherence time, T_2, due to temporal variations in the local environment.

It is critical to emphasize the different physical origins of dephasing and decoherence. While dephasing can be undone using refocusing pulses, decoherence cannot. An analogy using clocks is useful for intuitively distinguishing between the two processes: two clocks dephase when both initially read the same time, but one clock runs faster than the other by a fixed amount, such that at some interval later the two clocks disagree. Despite this disagreement, a known relationship between the two clocks remains; meaning one can determine the time indicated by one clock using the other. In contrast, NV$^-$ spin decoherence is analogous to the case where the rates of the two clocks do not have a fixed relationship, e.g., one runs faster for a while and then slows down or hops discretely relative to the other clock. At some interval later,

the time of one clock has no relationship with the time of the other clock. In the echo sequence, this translates to when phases accumulated on each half of the free precession interval are not equal and no longer cancel.

Similar to T_2^*, the NV ensemble decoherence time T_2 can depend on the nitrogen concentration $[\mathrm{N}_s^0]$, which determines both the dipolar coupling strength between NV^- and nitrogen spins as well as intra-bath dipolar coupling between nitrogen bath spins. These intra-bath interactions drive temporal changes in the magnetic environment, primarily though energy conserving flip-flop processes [72, 91, 92]. In nitrogen-doped diamond material with $[\mathrm{N}] \gtrsim 0.1\,\mathrm{ppm}$, the Hahn echo T_2 scales inverse linearly with the density of incorporated nitrogen,

$$\frac{1}{T_2\{\mathrm{N}_s^0\}} = \mathrm{B}_{\mathrm{N}_s^0}[\mathrm{N}_s^0]. \tag{2.4}$$

Fig. 2.1(b) depicts measurements of 25 as-grown, diamond samples which exhibits an inverse linear scaling across four decades in nitrogen concentration [72]. Fitting to this experimental data yields $\mathrm{B}_{\mathrm{N}_s^0} = 6.25(47)\,\mathrm{ms}^{-1}\,\mathrm{ppm}^{-1}$. For a 1-ppm-nitrogen sample this corresponds to a nitrogen-limited T_2 of 160(12) µs. For samples with $[\mathrm{N}] \lessapprox 0.1\,\mathrm{ppm}$, the saturation in measured T_2 is attributed to background magnetic noise external to the diamond [73]. As highlighted in Fig. 2.1(a) by differentiating between natural abundance and isotopically purified $^{13}\mathrm{C}$ samples (red and blue data points), the $^{13}\mathrm{C}$ nuclear spin bath does not play a significant role in the NV^- ensemble T_2 due to the six orders of magnitudes weaker intra-bath couplings [72] (for measurements with the magnetic field aligned with a single crystal axis [93, 94]).

Since the Hahn echo decoherence is not vulnerable to the static inhomogeneities

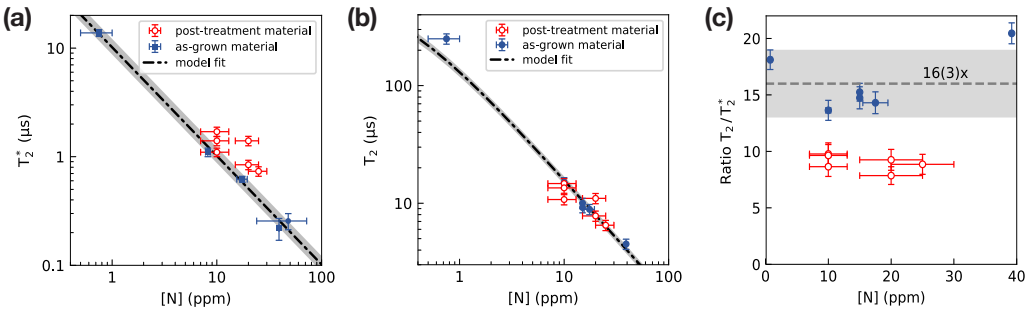

Figure 2.2: **Comparison of T_2 and T_2^* before and after electron irradiation and annealing.** **(a)** T_2^* measurements of as-grown diamond material shown in Fig. 2.1(a) are reproduced (blue, filled points) along with T_2^* measurements of electron-irradiated and annealed diamond material (red, open points). **(b)** Samples from Fig. 2.1(b) for which nitrogen-bath-limited T_2^* measurements also exist. **(c)** Comparison of T_2/T_2^* ratio for as-grown material with low-NV concentration ($T_2/T_2^* \approx 16(3)$) and post-treatment material with increased NV concentration ($T_2/T_2^* < 10$).

that dominate NV^- ensemble dephasing, comparing T_2^* and T_2 in a diamond sample is a useful characterization tool. For as-grown diamond material, we find that the nitrogen-limited Hahn echo T_2 exceeds the Ramsey ensemble T_2^* by a factor of 16(3). As shown in Fig. 2.2(c), this relationship between T_2 and T_2^* is consistent across samples with orders of magnitude difference in nitrogen concentration. However, after irradiation and annealing, we observe a decrease in the ratio, T_2/T_2^*, mostly as a result of extended dephasing times compared to the as-grown material (red data points in Fig. 2.2(a)). The contribution of NV^- to dephasing and an explanation for the decrease in the ratio T_2/T_2^* are presented in the following section (Sec. 2.2.3).

2.2.3 NV^- Limit to T_2^*

Like-spin dipolar interactions between NV^- defects can also contribute to dephasing. When considering their contribution to dephasing, the NV^- population can be divided

into two groups based upon their resonance frequency. NV^- centers with degenerate or nearly degenerate resonance frequencies are considered to be in the same group, while NV^- centers with non-degenerate resonance frequencies are considered to be in different groups. The magnitude and orientation of the bias magnetic field can be used to control the distribution of population between "same" and "different" groups by overlapping two or more spin resonances of NV^- centers along different crystal orientations. The contribution of these same-group ($NV^-_{\parallel}$) and different-group ($NV^-_{\nparallel}$) populations to dephasing can be decomposed as,

$$\begin{aligned}\frac{1}{T_2^*\{\mathrm{NV^-}\}} =& \frac{1}{T_2^*\{\mathrm{NV^-}\}_{\parallel}} + \frac{1}{T_2^*\{\mathrm{NV^-}\}_{\nparallel}} \\ =& \alpha_{\parallel}\mathrm{A}_{\mathrm{NV^-_{\parallel}}}[NV^-_{\parallel}] + \alpha_{\nparallel}\mathrm{A}_{\mathrm{NV^-_{\nparallel}}}[\mathrm{NV^-_{\nparallel}}]\end{aligned} \tag{2.5}$$

where $\alpha_{\nparallel}$ and $\alpha_{\nparallel}$ are dimensionless factors accounting for imperfect spin polarization for the $NV^-_{\parallel}$ population used for sensing and $NV^-_{\nparallel}$ population in the other group(s) [40]. When sensing with the $NV^-_{\parallel}$ spins, a majority of the $NV^-_{\nparallel}$ spins may be polarized into the $m_s = 0$ sublevel and therefore not contribute to dephasing. The exact fraction of $NV^-_{\nparallel}$ pumped into $m_s = 0$ depends on experimental choices for the laser polarization and duration of optical initialization.

A lack of published results for $T_2^*\{\mathrm{NV^-}\}$ as a function of $[\mathrm{NV^-}]$ makes determination of $\mathrm{A}_{\mathrm{NV^-_{\nparallel,\parallel}}}$ difficult. In particular, such measurements are complicated by the sensitivity of $\alpha_{\nparallel,\parallel}$ and $[\mathrm{NV^-_{\parallel,\parallel}}]$ to experimental choices for optical illumination (polarization, intensity, effects on NV charge fraction, etc.) and to bias magnetic field misalignment. However, $\mathrm{A}_{\mathrm{NV^-_{\nparallel,\parallel}}}$ can be estimated using the experimentally determined value for $\mathrm{A}_{\mathrm{N_s^0}}$ and consideration of the dipolar-dipolar spin Hamiltonian.

Flip-flop interactions between NV^- in different groups are off-resonant and therefore suppressed. Meanwhile, similar to the N_s^0 spin bath, resonant spin exchange is permitted between NV^- spins in the same group [76]. This additional flip-flop term in the dipole-dipole spin Hamiltonian results in increased dephasing and decoherence from $NV^-_{\parallel}$ spins compared to $NV^-_{\nparallel}$ spins such that $A_{NV^-_{\parallel}} \approx (3/2)A_{NV^-_{\nparallel}}$ [95].

Furthermore, assuming the NV^- and N_s^0 spin baths couples to NV^- sensor spins with similar strength, accounting for the difference in spin number (S), $A_{NV^-_{\nparallel}}$ is estimated to be,

$$A_{NV_{\nparallel}} \simeq \sqrt{\frac{S_{NV^-}(S_{NV^-}+1)}{S_{N_s^0}(S_{N_s^0}+1)}} A_{N_s^0} \tag{2.6}$$

such that $A_{NV^-_{\nparallel}} \approx \sqrt{8/3}A_{N_s^0} \approx 165\,\mathrm{ms^{-1}ppm^{-1}}$ and $A_{NV^-_{\parallel}} \approx 247\,\mathrm{ms^{-1}ppm^{-1}}$. For an ensemble with $[NV^-_{\parallel}] = 1$ ppm and all $NV^-_{\nparallel}$ spins pumped into $m_s = 0$, the anticipated NV-NV interaction-limited T_2^* is approximately $4\,\mu$s. These estimates are used to inform discussions in Chapters 5 and 6 considering the properties of NV-rich diamond material and methods to extend ensemble T_2^* via spin bath control.

We are now in a position to return to Fig. 2.2 and discuss the observed decrease in the ratio, T_2/T_2^*, for irradiated and annealed diamond material (see red data points). Inspecting Fig. 2.2(a,b), we find that the decrease in the ratio, T_2/T_2^* primarily results from an extended T_2^* compared to the as-grown material while T_2 remains similar both before and after treatment. Note that the increased spread in T_2^* for the post-treatment material is likely due to the varying irradiation and annealing recipes employed across the set of diamond samples. The increase in T_2^* post-treatment can be intuitively attributed to (a) the creation of NV^- spins which consumes two N_s^0 spins per NV^- formed, (b) optical pumping of the NV^- population

into the $m_s = 0$ sublevel (with no longitudinal magnetic moment), and (c) some of fraction of the NV spins existing in the neutral charge state. Together, these factors reduce the overall effective paramagnetic spin bath density. Meanwhile, the four times stronger intra-bath coupling between NV^- spins compared to N_s^0 spins [96] and the inability of Hahn echo-type sequences to decouple like-spin, NV-NV interactions between same group spins (referred to as instantaneous diffusion [97–100]) compensate for (a), (b), and (c) when considering their impact on T_2. In this proposed understanding, increasing conversion efficiency for N-to-NV^- leads to longer T_2^* and thus a lower T_2/T_2^* ratio.

2.2.4 ^{13}C Limit to T_2^*

Dipolar coupling between the NV^- sensor spins and the ^{13}C nuclear spin bath can also limit the NV^- ensemble T_2^*, especially for CVD material produced using natural abundance methane with 1.1% ^{13}C ($[^{13}C]$=10700(800) ppm). In the dilute limit ($\lesssim$ 1%) where the hyperfine contact term may be neglected, T_2^* scales inverse linearly with the concentration of ^{13}C nuclear spins:

$$\frac{1}{T_2^*\{^{13}C\}} = A_{^{13}C}[^{13}C]. \tag{2.7}$$

The scaling constant $A_{^{13}C}$ can be estimated using measurements of diamond samples with low nitrogen concentration and natural abundance $[^{13}C]$ in the stress-immune DQ sensing basis. Any residual contribution due to the electronic nitrogen spin bath is subtracted using the scaling established in Sec. 2.2.1 (see example data in Fig. 2.3(a) for Sample 2A and Chapter 3 for details of the double quantum Ramsey

measurement). This approach yields $A_{^{13}C} \approx 0.100\,\mathrm{ms^{-1}ppm^{-1}}$ such that a natural abundance carbon sample should exhibit a $T_2^*\{^{13}\mathrm{C}\} \approx 1\,\mu\mathrm{s}$ in the absence of other dephasing mechanisms. This limit is equivalent to the limit imposed by $[\mathrm{N}_s^0] \approx 10\,\mathrm{ppm}$.

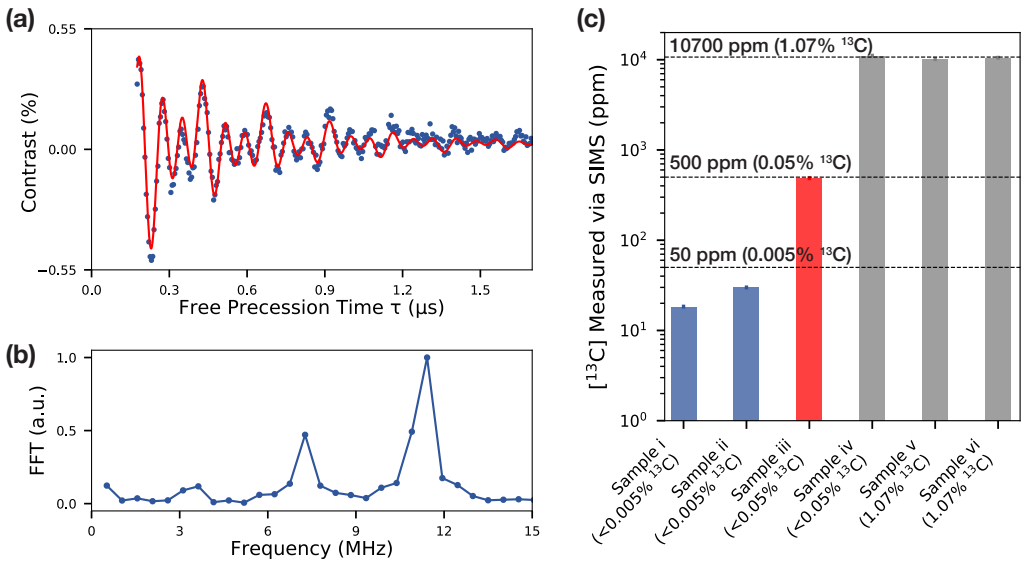

Figure 2.3: **^{13}C spins in diamond material.** **(a)** Double-quantum (DQ) Ramsey free induction decay for Sample 2A with natural abundance ^{13}C. Associated fit (red line) yields $T_2^*\{\mathrm{DQ}\} = 0.445(30)\,\mu\mathrm{s}$. With the known nitrogen contribution ($[\mathrm{N}] \approx 0.5\,\mathrm{ppm}$) subtracted, these data provide an estimate of $A_{^{13}\mathrm{C}} \approx 0.100\,\mathrm{ms^{-1}ppm^{-1}}$. **(b)** Fourier transform of the Ramsey FID signal. The three peaks arise from hyperfine interactions with the ^{14}N nuclear spin ($I = 1$) with inter-peak spacing double that of an equivalent single quantum Ramsey measurement ($\approx 2 \times 2.2\,\mathrm{MHz}$) **(C)** Secondary ion mass spectroscopy (SIMS) measurements of [^{13}C] in diamond samples grown with methane gas of varying isotopic purity (distinguished by the blue, red, and grey bars). The reported isotopic purity of the methane source gas used during growth is indicated within parentheses below the sample labels (i-vi) along the x-axis.

Isotopic purification of the carbon source is the most direct and effective approach to mitigate the contribution of the ^{13}C nuclear spin bath to dephasing. For diamond material with $[\mathrm{N}] \lesssim 100\,\mathrm{ppm}$, reducing the concentration [^{13}C] is beneficial for T_2^* (see Chapter 6). In the context of CVD-grown material, methane gas with up

to >99.995% ^{12}C is available, increasing the ^{13}C-induced limit on T_2^* to $\approx 200\mu s$. In Fig. 2.3(c), secondary ion mass spectroscopy (SIMS) measurements of the [^{13}C] in six samples (labelled samples i-vi in Fig. 2.3(c)) confirms that growth with isotopically purified methane translates into diamond material with similar purity.

2.3 Stress Inhomogeneity

Strain defects within a diamond induce spatially varying crystal stress which shifts the NV$^-$ ground state sublevels. Stress-gradients with magnitudes similar to spin-bath-related contributions to dephasing and characteristic length-scales spanning sub-micron to millimeters are common in CVD grown diamond material [38, 61]. As a consequence, the impacts of stress inhomogeneity on NV magnetometer performance are multi-fold and present a major technical challenge for NV$^-$ ensemble applications, especially for imaging applications where both stress-induced shifts across a field of view and resonance broadening (dephasing) are problematic (see Chapter 4). The following section introduces techniques for measuring crystal stress in diamond, including NV-based stress characterization and provides examples of typical stress distributions in CVD-grown diamond material.

Throughout the following discussion, we discuss the impacts of stress inhomogeneity when operating an NV$^-$ magnetometer in one of two modes of operation referred to as the full-sweep and few-point methods. In the full-sweep method, the entire ODMR feature is probed, providing large dynamic range at the cost of sensitivity since a large fraction of the measurement time is spent interrogating portions of the ODMR spectrum with little or no response to external magnetic fields. In

contrast, few-point methods offer optimal sensitivity because each of the discrete frequencies probed, possess optimal or near-optimal responses to changes in magnetic field. Typically, multiple locations on the ODMR feature are monitored to distinguish between magnetic shifts and temperature drift as well as resonance broadening. However, these few-point methods are inherently vulnerable to stress-induced shifts and broadening which ensure no single choice of frequencies (or free precession intervals, τ, for Ramsey measurements) are optimal for the entire field of view [19, 67, 68]. This degrades response to magnetic shifts and conflates magnetic and strain information.

2.3.1 Measuring Stress in Diamond

This section compares established techniques for imaging crystal stress in diamond to the NV-based crystal stress imaging method described in Ref. [38, 101]. Previous diamond strain imaging studies have employed x-ray tomography, Raman spectroscopy, cathodluminescence, and birefringence to characterize diamond strain [61, 102, 103]. Birefringence measurements, which are experimentally simple and provide rapid feedback, are particularly popular in the diamond growth community [39, 61, 104]. In a birefringent material, light with orthogonal polarization transmitted through a sample with thickness L accumulates a relative optical retardance phase $\delta = (2\pi\Delta nL)/\lambda$ where λ is the wavelength and Δn is the difference in refractive indices for the two polarizations. In a simple optical system where the sample is placed between two linear polarizers, the strain-dependent, accumulated phase can be converted to intensity variations. Using a rotating-linear-polarizer method, also known as Metripol, quantitative measurements of $|sin(\delta)|$ are possible [105]. An example im-

age of $sin^{-1}(|sin(\delta)|)$ is shown in Fig. 2.4(a) for a micron-scale, nitrogen-doped layer grown on top of an ultra-pure substrate (Sample 2B). Plastic deformation is visible as a stripe diagonal stretching across the upper left corner. Smaller length-scale petal-type defects are discernible scattered across the field of view.

Birefringence measurements suffer several drawbacks. First, since the optical retardance is integrated over the thickness of the sample it is difficult to isolate the location of the strain defect along the optical axis (e.g., differentiating between strain defects in the substrate versus a nitrogen-doped layer grown on top). Second, for micron-scale layers the sensitivity of birefringence-based techniques is insufficient (e.g., it is difficult to distinguish the small petal-type defects in Fig. 2.4(a)). Third, for high strain regions, the integrated phase may exceed $\pi/2$, resulting in an ambiguity when calculating stress.

For diamond material tailored to NV^- applications, measuring the crystal stress directly with the NV^- sensor spins as probes is an effective approach to map the crystal stress, leveraging the vulnerability of NV^- measurements to stress as a strength for characterization. Wide-field, quantum diamond microscopes (QDMs) can produce crystal stress maps with up to mm-scale fields of view and spatial resolution limited by the layer/sample thickness or optical diffraction limit (whichever is larger) [38]. For nitrogen-doped layer samples, this method is particularly advantageous since the NV^- spins are sensitive to stress locally in the layer.

CW-ODMR and Ramsey-based imaging are both suitable for extracting the resonance shifts and broadening induced by crystal stress and determining the impacts on NV^- magnetometer performance. Experimental setups designed for wide-field

magnetic imaging can be readily applied to stress characterization and are compatible with the integration of the optical elements required for birefringence imaging (see Ref. [38] and Chapter 4 for detailed descriptions). Fig. 2.4(b) illustrates the axial-stress-induced resonance shifts (proportional to M_z in the NV^- ground state Hamiltonian) across the same field of view as Fig. 2.4(a) to facilitate direct comparison with the birefringence-based method. The petal-type defects, originating from lattice dislocations that form during homo-epitaxial growth of the nitrogen-doped layer, are significantly more apparent in the M_z image. Furthermore, in the birefringence image, the magnitude of the diagonal-stripe feature misleadingly exhibits a valley between two higher-stress regions as a consequence of the $\pi/2$ phase ambiguity. Meanwhile, the M_z image correctly illustrates the stress environment within the stripe feature.

The ODMR spectra of three individual pixels from Fig. 2.4(b) are depicted in Fig. 2.4(c). In pixel (1), stress-gradients within the pixel broaden the resonance linewidth (Γ) and reduce the ODMR contrast (C), degrading achievable magnetic sensitivity ($\eta \propto \Gamma/C$). Although pixel (2) exhibits similar resonance frequencies, it suffers less from stress-gradients within the pixel and thus exhibits a narrower linewidth and improved contrast relative to pixel (1). In contrast, pixel (3) has a comparable linewidth to pixel (2), but the resonance frequencies are shifted by about 200 kHz. For the full-sweep method, pixels (2) and (3) would yield the same sensitivity. However, for few-point methods, the stress-induced shift between pixels (2) and (3) is problematic because it is no longer possible to simultaneously operate at the optimal set of points for both pixels.

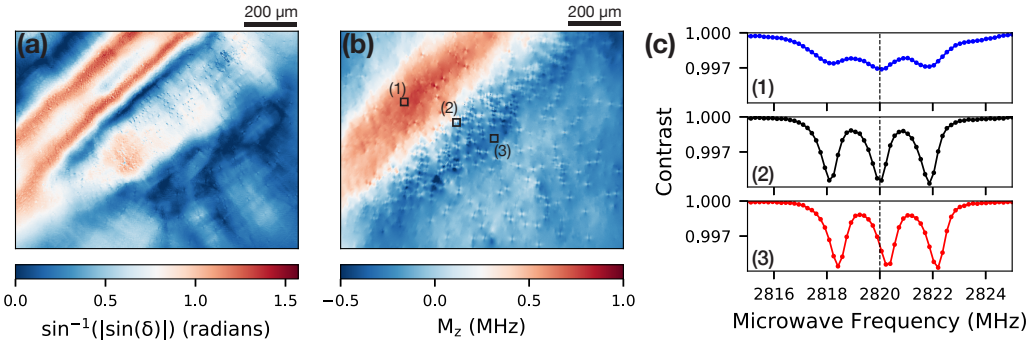

Figure 2.4: **Comparison of birefringence and NV-based stress imaging. (a)** Birefringence measurement using the Metripol method for an example region of a 25-ppm-nitrogen CVD layer grown on top of a low-nitrogen substrate (Sample 2B). A diagonal, stripe-like feature due to plastic deformation dominates the upper left-hand portion of the field of view. Additional, few-micron scale, petal-type stress features are poorly visible. **(b)** NV-based measurement of the axial-stress-induced, M_z, shifts for the same field of view as (a). The petal-type features are clearly visible. The plastic deformation feature appears qualitatively different due to the $\pi/2$ phase ambiguity which occurs for birefringence measurements in high-stress regions. The NV-based measurement is physically accurate. **(c)** ODMR spectra from selected pixels in (b) as indicated by black boxes and numbering. Pixel (1) exhibits excessive stress-induced broadening which is sufficient to degrade the ODMR contrast compared to low-stress-gradient pixels (2) and (3). The ODMR resonance features in pixel (2) and (3) are shifted by approximately 200 kHz with respect to each other.

Figure 2.5(a) presents a birefringence image for a 100 µm by 100 µm region of another nitrogen-doped layer with [N] ≈ 8 ppm and 40-micron thickness (Sample 2C). Note that this image does not use the Metripol method and is therefore only qualitative - with brighter regions corresponding to areas of higher relative strain. Fig. 2.5(b) illustrates the measured single quantum T_2^* for the same field of view as Fig. 2.5(a). Pixels with degraded T_2^* correlate strongly with the features in the birefringence image. Additional features that are challenging to identify in birefringence are readily apparent in the image of T_2^*. Additional discussion of Ramsey-based

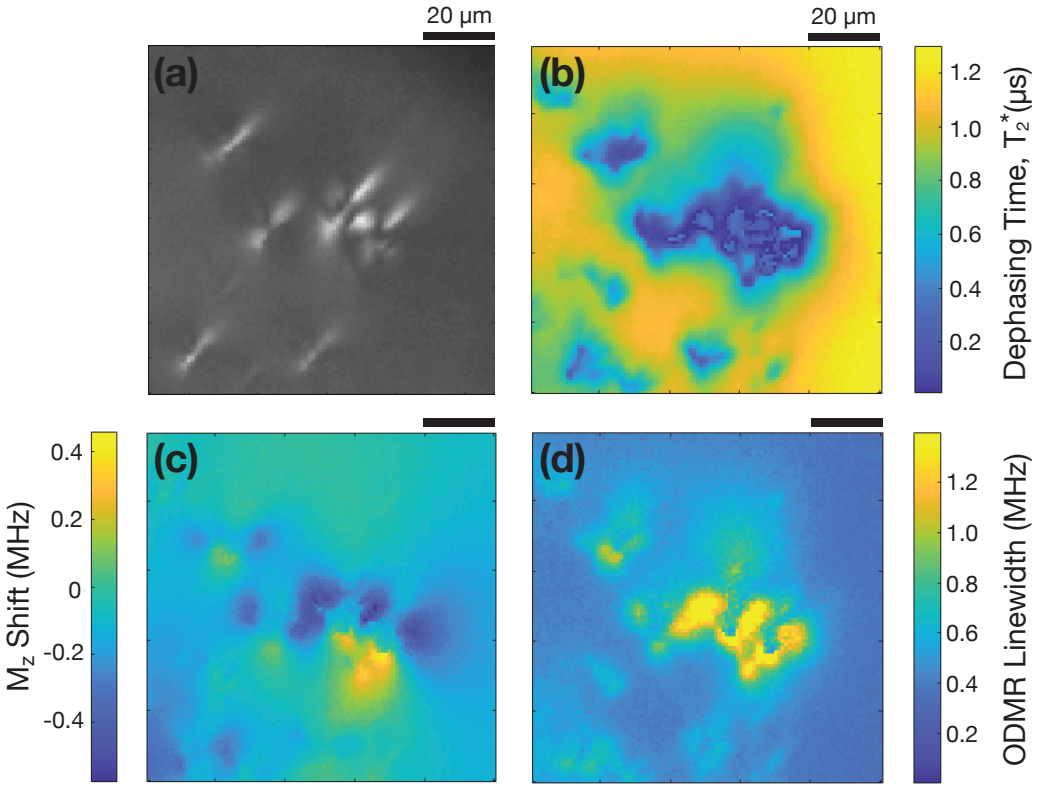

Figure 2.5: **Impact of stress on NV$^-$ spin properties (a)** Non-Metripol-based birefringence measurements of a dislocation bundle in an nitrogen-doped, layer grown on top of an ultra-pure substrate (Sample 2C). Brighter regions correspond to higher crystal stress. **(b)** QDM image of the T_2^* extracted from a single quantum Ramsey free induction decay (FID) across the same field of view as (a). In pixels with large-stress gradients, T_2^* decreases by about an order of magnitude compared to low stress-gradient pixels. The regions of shortened T_2^* correlate strongly with features in the birefringence image. **(c)** ODMR-based measurements (via QDM image) of the axial-stress-induced M_z shifts across the same field of view. Peak shift magnitudes are comparable to the NV$^-$ spin resonance linewidth. **(d)** Image of the ODMR resonance linewidths, which vary by about an order of magnitude within the field of view and are also highly correlated with features in (a) and (b) as expected.

imaging is available in Chapter 4.

The associated M_z and CW-ODMR linewidth images included in Fig. 2.5(c) and Fig. 2.5(d) provide complementary information. The M_z shifts of $\approx \pm 200\,\mathrm{kHz}$

occur across the tens of microns length-scale and are comparable to the NV^- ODMR linewidth even in low stress-gradient pixels away from the isolated petal defects. The order of magnitude variations in NV^- spin resonance frequency and linewidth (or equivalently dephasing) demonstrate the potential for stress inhomogeneity to impact NV^- magnetometer performance.

2.4 NV^- Charge State Fraction

As motivated in Sec. 1.4, increasing the NV^- charge state fraction,

$$\psi = [\mathrm{NV^-}]/[\mathrm{NV^0} + \mathrm{NV^-}] \tag{2.8}$$

is beneficial for magnetic sensitivity, providing both an increased number of sensor spins and improved measurement contrast due to reduced background fluorescence from NV^0 spins. This section summarizes the present understanding of NV^- ensemble charge state behavior and provides exemplary data for context when later describing efforts to improve the NV charge fraction, ψ, especially under optical illumination, in Chapter 6.

The conversion of nitrogen incorporated into the diamond lattice during growth into NV centers (with any charge state) is characterized by the conversion efficiency, $E_{\mathrm{conv}} = [NV]/[N]$. The conversion efficiency as defined here is invariant unless additional processing occurs, such as irradiation, implantation, high temperature, or high pressure. In contrast, the NV^- charge fraction depends intimately on the local conditions in the diamond and can be modified by external electric fields and optical

illumination.

In general, the steady-state NV^- charge fraction for a given sample and experimental procedure is difficult to predict due to the large number of relevant parameters, including the concentrations of charge acceptors and donor species, the characteristics of any optical illumination (intensity, wavelength, duty cycle) [106,107], the dynamics and concentrations of different species under such illumination, as well as irradiation dose [108] and annealing recipe [106]. Application of a bias electric field has also been demonstrated to impact the NV charge state fraction [109, 110]. Nonetheless, certain trends for the charge distribution in NV^- ensembles can be established. For example, the typical 532nm optical illumination employed in NV experiments ionizes NV^- via a two-photon process which results in degraded NV^- charge fraction with increasing intensity [77, 78]. Furthermore, increasing the density of donor species such as N_s^0 is favorable, as supported by the near unity NV charge fractions exhibited by high-N samples with $[N] \sim 100\,\text{ppm}$ [106, 111]. Similarly, reducing the concentration of charge acceptors such as vacancy cluster and chains is also expected to be beneficial (see Chapter 6 or Ref. [39] for experimental support of this claim).

Established techniques in the diamond community for studying NV charge state include UV-Vis absorption spectroscopy, Fourier transform infrared (FTIR) absorption spectroscopy, and electron paramagnetic resonance (EPR). In particular, cryogenic UV-Vis absorption-based measurements provide absolute measurements of $[NV^-]$ and $[NV^0]$ and therefore the charge fraction. However, all three of these methods are absorption-based and require the characterization of bulk material to provide sufficient SNR (e.g., material with thickness exceeding a few hundred microns or, in

the case of EPR, $\gtrsim 10^{11}$ spins). This precludes the study of micron-scale layer geometries which are useful for applications and more economical to produce. Also, these methods and associated experimental apparatuses do not usually lend themselves to studying the NV^- charge fraction as a function of optical illumination intensity - the most experimentally interesting regime. While EPR studies in combination with low intensity optical illumination have been reported reported [112], achieving optical intensities near the saturation intensity of the NV^- center (1-2 $mW\mu m^{-2}$ [84]) across a sufficient fraction of the required mm-scale diamond sample is technically demanding.

To address these shortcomings, we again turn to an NV-based characterization method which, in this case, utilizes the photo-luminescence (PL) emitted by the NV ensemble to determine the NV^- charge fraction in-situ under realistic experimental conditions. An exemplary PL-spectrum under 532 nm optical illumination is shown in Fig. 2.6. Two key observations are readily apparent. First, at room temperature, a majority of the NV^- and NV^0 PL is emitted into broad phonon sidebands. Second, these NV^- and NV^0 PL spectra are significantly overlapped. To calculate the NV^- charge fraction, it is necessary to decompose the emitted PL into NV^- and NV^0 contributions, preferably using a method that uses the large fraction of PL emitted into the phonon sidebands. Ref. [77] generates NV^- and NV^0 basis functions using samples previously established to contain predominately NV^- or NV^0 and decomposes a measured PL spectra into contributions from these two bases. Ref. [78] instead generates basis functions per sample by modulating the amount of NV^- PL using resonant microwave irradiation and thus isolating a portion of the NV^- spectrum. The details of this second method are described thoroughly in Ref. [78, 111]. To convert

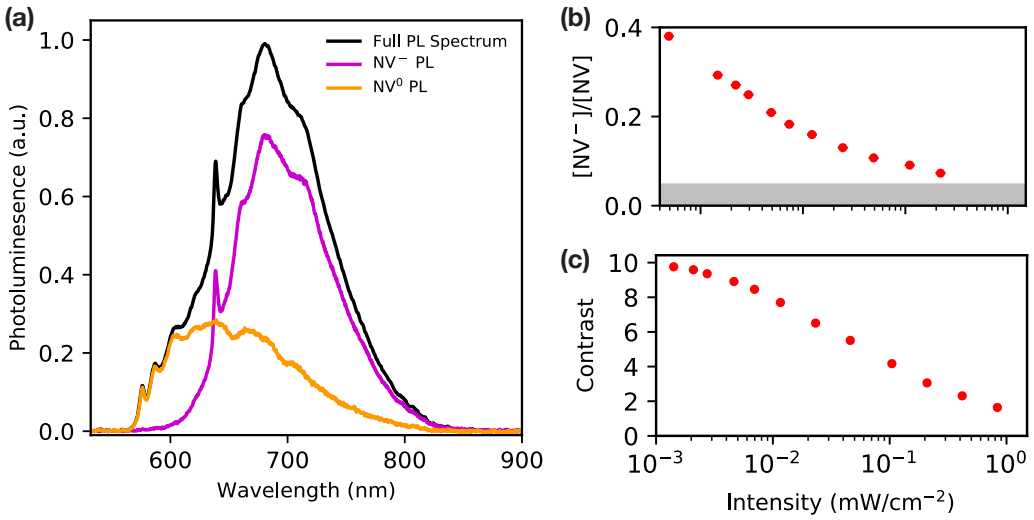

Figure 2.6: **PL-based NV- charge fraction and ODMR contrast measurements (a)** Example PL spectrum collected from a 10-ppm-nitrogen diamond sample after irradiation and annealing to increase [NV] (Sample 2D). The PL spectrum is decomposed into NV- (purple) and NV^0 (orange) contributions. **(b)** Measurement of NV- charge fraction as a function of optical illumination intensity for Sample 2D. **(c)** Measurement of the pulsed-ODMR contrast as a function of laser intensity for the same experimental conditions as (b). A strong π-pulse with a duration of < 50 ns was applied resonant with the $|0\rangle \rightarrow |+1\rangle$ transition to ensure high fidelity control of hyperfine-split populations.

from the calculated PL fraction to an NV charge fraction requires a wavelength-dependent scaling factor accounting for the NV- and NV^0 emission ratio. Ref. [77] determined $\kappa_{532} = 2.5(5)$ under low-intensity 532 nm optical illumination. This value is used in conjunction with the second method in the following discussion.

The PL spectrum in Fig. 2.6(a) is decomposed into the NV- and NV^0 PL contributions using the second, NV-modulation-based method. Fig. 2.6(b) demonstrates the study of the NV- charge fraction for an irradiated and annealed 10-micron layer sample with $[N] \approx 8$ ppm as a function of 532 nm optical illumination intensity (Sample 2D). A range of optical intensities spanning nearly three orders of magnitude

and approaching the NV saturation intensity are measured. For the lowest optical intensity recorded, Sample 2D exhibits a maximum charge fraction of less than 40% NV^-, which is substantially lower than the near unity charge fractions reported elsewhere for higher nitrogen material [111]. As the optical intensity increases, the charge fraction exhibits poor charge state stability, degrading further until approaching an experimental detection limit of around 5%. This rapid trend toward worse NV^- charge fraction is unfortunate because pulsed NV^- magnetometry protocols favor higher optical intensity to reduce the re-initialization duration and collect more fluorescence. Based on the measurements described above, Sample 2D was likely over-irradiated, producing superfluous charge acceptors and reducing the density of charge donors such as N_s^0 [113].

The degradation of the NV^- charge fraction with increasing optical illumination also hurts the measurement contrast - even with a 647 nm long-pass filter employed to partially remove the NV^0 PL contribution. The measured pulsed-ODMR contrast shown in Fig. 2.6(c), accounting for changes in optical initialization and optimal readout, decreases from nearly 10% to less than 2% as the optical intensity approaches saturation intensity of the NV^- center. While the low intensity ODMR contrast of 10% is reasonable ($\approx$14% is ideal for the epi-illumination with linearly-polarized optical illumination used in these measurements, see Chapter 6 or Ref. [39] for details), the magnetic sensitivity ultimately scales inverse linearly with the factor of five decrease in contrast at higher intensity. Together with the loss in $[NV^-]$, this contrast loss largely mitigates any potential sensitivity improvement from using increased optical intensity.

Building upon the challenges highlighted in this section, Chapter 6 revisits the topic of NV^- charge fraction and material-engineering-based progress to improve the native NV^- charge fraction (without illumination) and robustness of the NV^- charge fraction under optical illumination. In particular, diamond samples with varying densities of charge acceptors, in the form of grown-in vacancy clusters and chains, are compared.

Chapter 3

Double Quantum Coherence Magnetometry

While NV^- ensemble experimental work to date predominately treats the NV^- ground state as a pseudo-spin-1/2 system, operating in a single quantum (SQ) combination of the $|0\rangle$ and either $|+1\rangle$ or $|-1\rangle$ states,, this chapter describes progress in leveraging the full spin-1 nature of the NV^- for improved NV-ensemble magnetometry using the double quantum (DQ) coherence. In DQ coherence measurements, superpositions of the $|\pm 1\rangle$ states are used as the sensing basis. This DQ sensing basis, as discussed in detail in the following section, is doubly sensitive to magnetic fields as well as first-order insensitive to sources that shift the $|\pm 1\rangle$ magnetic sublevels in common-mode, such as axial-crystal-stress inhomogeneity and temperature drifts.

The enhanced magnetic sensitivity of the DQ coherence offers direct benefits to magnetic sensing and imaging. However, the robustness of the DQ sensing basis to non-magnetic shifts in the NV^- ground state spin resonances is equally critical

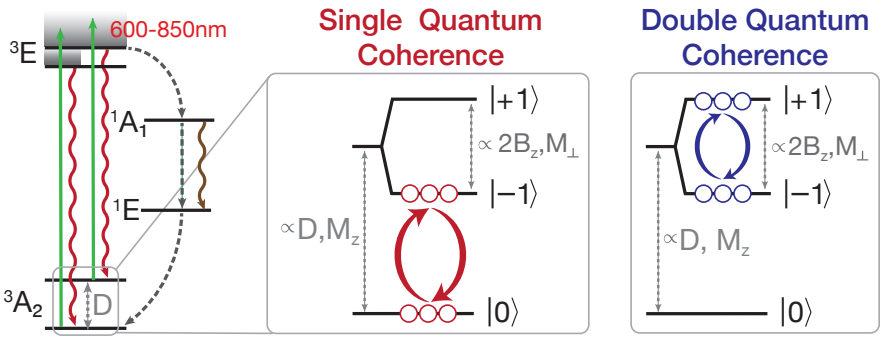

Figure 3.1: **Energy Level Diagram and Experimental Apparatus.** Energy level diagram for the negatively-charged nitrogen vacancy (NV^-) in diamond with zero field splitting D between the ground state spin levels $|m_s = 0\rangle$ and $|m_s = \pm 1\rangle$. The expanded views depict single (SQ) and double quantum (DQ) coherences. The zero-field-splitting, D, and axial crystal stress, M_z, shift the $|\pm 1\rangle$ sublevels in common-mode with respect to the $|0\rangle$ sublevel. Axial magnetic fields, B_z, and transverse crystal stress, $M_\perp$, shift the the $|\pm 1\rangle$ sublevels differentially, increasing the $|\pm 1\rangle$ splitting.

for NV^- ensemble applications. For example, as discussed in Sec. 2.3, lattice stress inhomogeneity is an outstanding material growth challenge for NV-ensemble sensing, inducing resonance shifts and broadening on the order of typical NV^- ensemble linewidths ($0.1 - 1\,\mathrm{MHz}$) over sub-micron to millimeter length-scales. The resulting stress-gradients across an interrogated NV^- ensemble are a significant source of dephasing, limiting the single quantum T_2^* (see Sec. 3.5). Meanwhile, the DQ T_2^* is unaffected by such stress-gradients, enabling longer free precession intervals in Ramsey measurements and improved magnetic sensitivity. While the present chapter focuses on the advantages DQ magnetometry affords photodiode-based measurements, Chapter 4 is dedicated to describing how DQ techniques address the additional challenges stress inhomogeneity presents for imaging applications.

After discussing the sensitivity of the NV^- ground state energy levels to both magnetic fields and crystal stress, the experimental details required to prepare and

utilize the DQ sensing basis for Ramsey-based magnetometry are described in Sec. 3.2 and Sec. 3.3. The successful implementation of such DQ control in ensemble experiments has conventionally been hindered by the technical challenge of producing DQ coherences with sufficient fidelity. Any MW pulse errors during the DQ pulses will generate residual SQ coherence, which reintroduces unwanted responses to common-mode shifts in the NV spin resonances, including axial-stress-induced resonance shifts and temperature drifts. To overcome this obstacle, a DQ 4-Ramsey measurement protocol is introduced in Sec. 3.4.1, which isolates the desired magnetic signal from residual SQ signals. This scheme is broadly applicable to both NV^- ensemble imaging and bulk sensing modalities, where robustness to temperature-induced drifts is often critical [19, 31, 114]. A demonstration of the 4-Ramsey protocol is described using photodiode-based measurements. The protocol is then used throughout the remainder of the work presented in this thesis, especially in Chapter 4.

In addition to the benefits of the DQ coherence for magnetometry applications, comparing the DQ and SQ ensemble dephasing times is also a valuable characterization tool for quantitatively understanding the ensemble dephasing mechanisms in a sample. Section 3.5 compares the SQ and DQ dephasing times for three samples with varying densities of incorporated nitrogen, elucidating the underlying dephasing mechanisms for each.

3.1 Sensitivity of the Double Quantum Sensing Basis to Magnetic Fields and Crystal Stress

Double quantum (DQ) coherence magnetometry was first demonstrated using single NV$^-$ centers by Fang *et al.* [80], highlighting the suppression of temperature-induced shifts in the NV$^-$ spin resonances. Mamin *et al.* [79] expanded upon this work, achieving improved magnetic sensitivity to narrow-band, AC fields using the DQ coherence. However, DQ coherence magnetometry is particularly advantageous for NV-ensembles, suppressing the resonance shifts and ensemble dephasing induced by spatial heterogeneity in crystal stress. This section examines the sensitivity of SQ and DQ measurements to magnetic fields and crystal stress by considering several limiting cases.

The NV$^-$ ground-state Hamiltonian in the presence of crystal stress and a static magnetic field aligned arbitrarily with respect to a particular NV$^-$ orientation is given by [49, 50, 115]:

$$\begin{aligned} H/h \approx & \left(D(T) + M_z\right) S_z^2 + \frac{\gamma}{2\pi}\vec{B}\cdot\vec{S} \\ & + M_x\left(S_y^2 - S_x^2\right) \\ & + M_y\left(S_xS_y + S_yS_x\right) \\ & + N_x\left(S_xS_z + S_zS_x\right) \\ & + N_y\left(S_yS_z + S_zS_y\right). \end{aligned} \tag{3.1}$$

Here, $D(T) \approx 2.87\,\text{GHz}$ is the temperature-dependent zero-field splitting, S_i are the dimensionless spin-1 projection operators, $\frac{g\mu_B}{h} = \frac{\gamma_{NV}}{2\pi} \approx 28.04\,\text{GHz/T}$ is the NV$^-$

gyromagnetic ratio, $\vec{B} = (\mathrm{B}_z, \mathrm{B}_x, \mathrm{B}_y)$ is the magnetic field in the NV$^-$ coordinate system, and M_i and N_i are terms related to crystal stress.

We refer to M_z as the axial crystal stress (aligned with the NV$^-$ symmetry axis) and define the transverse crystal stress, $M_\perp \equiv -(M_x + iM_y)$. Using this definition of $M_\perp$ and similarly introducing $B_\perp \equiv \frac{1}{\sqrt{2}}(B_x + iB_y)$ and $N_\perp \equiv \frac{1}{\sqrt{2}}(N_x + iN_y)$, Eqn. 3.1 can be rewritten, in matrix form, as:

$$H/h = \begin{pmatrix} D(T) + M_z + \frac{\gamma_{NV}}{2\pi}B_z & \frac{\gamma_{NV}}{2\pi}B_\perp^* + N_\perp^* & M_\perp \\ \frac{\gamma_{NV}}{2\pi}B_\perp + N_\perp & 0 & \frac{\gamma_{NV}}{2\pi}B_\perp^* - N_\perp \\ M_\perp^* & \frac{\gamma_{NV}}{2\pi}B_\perp - N_\perp^* & D(T) + M_z - \frac{\gamma_{NV}}{2\pi}B_z \end{pmatrix}. \quad (3.2)$$

If the applied magnetic field is aligned with the NV symmetry axis ($\mathrm{B}_\perp = 0$) and stress contributions are neglected, then the Hamiltonian in Eqn. 3.2 is diagonal and the energy levels are given by the zero-field splitting $D(T)$ and Zeeman splitting $\frac{\gamma_{NV}}{2\pi}B_z$,

$$E_{|\pm1\rangle}/h = D(T) \pm (\frac{\gamma_{NV}}{2\pi}B_z) \quad (3.3)$$

$$E_{|0\rangle}/h = 0. \quad (3.4)$$

During the free precession interval of a sequence, the SQ coherence accumulates phase proportional to the energy difference between the $|0\rangle$ and either of the $|\pm1\rangle$ magnetic sublevels. Figure 3.1 highlights the dependence of the energy difference, $\mathrm{E}_{|0\rangle}$-$\mathrm{E}_{|\pm1\rangle}$, on both the zero-field-splitting and Zeeman contributions.

Conversely, the DQ coherence accumulates net phase proportional to the energy

difference between the $|\pm 1\rangle$ sublevels ($E_{|+1\rangle} - E_{|-1\rangle}$). Terms in the NV$^-$ Hamiltonian such as the zero-field field splitting, which are proportional to S_z^2 in Eqn. 3.1 and shift the $|\pm 1\rangle$ sublevels in common-mode, cancel. Meanwhile, terms which add differentially ($\propto S_z$), such as the Zeeman term, constructively add to effectively double the gyromagnetic ratio and accumulate phase in a magnetic field at a rate twice that of the SQ coherence.

3.1.1 Non-Zero Transverse Magnetic Field Contribution

The transverse magnetic field, $B_\perp$, and crystal-stress-related $N_\perp$ couple into to the NV$^-$ ground state Hamiltonian similarly. As a consequence, although the following discussion explicitly considers the transverse magnetic field contribution, similar results are obtained for the $N_\perp$ contribution.

Assuming a non-zero transverse magnetic field ($B_\perp \neq 0$), the energy values for the NV Hamiltonian (Eqn. 3.2) can be evaluated by treating $B_\perp$ as a small perturbation, with perturbation Hamiltonian $V \equiv H - H_0$ defined as,

$$V = \begin{pmatrix} 0 & \frac{\gamma_{NV}}{2\pi} B_\perp^* & M_\perp \\ \frac{\gamma_{NV}}{2\pi} B_\perp + N_\perp & 0 & \frac{\gamma_{NV}}{2\pi} B_\perp^* - N_\perp \\ M_\perp^* & \frac{\gamma_{NV}}{2\pi} B_\perp - N_\perp^* & 0 \end{pmatrix}. \tag{3.5}$$

To simplify the analysis, $M_z = M_\perp = N_\perp = 0$. Using time-independent perturbation theory (see for example Ref. [116]), the corrected energy levels are given by: $E_{|\pm 1,0\rangle} \approx E^{(0)}_{|\pm 1,0\rangle} + E^{(1)}_{|\pm 1,0\rangle} + E^{(2)}_{|\pm 1,0\rangle} + \dots$, where $E^{(0)}_{|\pm 1,0\rangle}$ are the bare energies as given in Eqn.

3.4 and $E^{(k)}_{|\pm1,0\rangle}$ for $k > 0$ are the k-th order corrections. The energy corrections at first and second order are:

$$E^{(1)}_{|\pm1,0\rangle} = \langle \pm1, 0|\mathbf{V}|\pm1, 0\rangle = 0 \tag{3.6}$$

$$E^{(2)}_{|\pm1\rangle} = \frac{\|\langle \mp1|\mathbf{V}|\pm1\rangle\|^2}{E_{|\pm1\rangle} - E_{|\mp1\rangle}} + \frac{\|\langle 0|\mathbf{V}|\pm1\rangle\|^2}{E_{|\pm1\rangle}} = \frac{\|\frac{\gamma_{NV}}{2\pi}B_\perp\|^2}{D \pm \frac{\gamma_{NV}}{2\pi}B_z} \approx \frac{\|\frac{\gamma_{NV}}{2\pi}B_\perp\|^2}{D}, \tag{3.7}$$

$$\begin{aligned} E^{(2)}_{|0\rangle} = \frac{\|\langle +1|\mathbf{V}|0\rangle\|^2}{-E_{|+1\rangle}} + \frac{\|\langle -1|\mathbf{V}|0\rangle\|^2}{-E_{|-1\rangle}} &= -\left(\frac{\|\frac{\gamma_{NV}}{2\pi}B_\perp\|^2}{D + \frac{\gamma_{NV}}{2\pi}B_z} + \frac{\|\frac{\gamma_{NV}}{2\pi}B_\perp\|^2}{D - \frac{\gamma_{NV}}{2\pi}B_z}\right) \\ &\approx -\frac{2\|\frac{\gamma_{NV}}{2\pi}B_\perp\|^2}{D}, \end{aligned} \tag{3.8}$$

where the last two lines leverage the fact that $\frac{\gamma_{NV}}{2\pi}B_z \ll D(T)$ in typical NV$^-$ ensemble experiments ($1 - 10\,\mathrm{mT}$). The new transition frequencies $f_{\pm1}$ for $E_{|0\rangle} \rightarrow E_{|\pm1\rangle}$ are therefore:

$$f_{\pm1} \approx D \pm \frac{\gamma_{NV}}{2\pi}B_z + \frac{3\|\frac{\gamma_{NV}}{2\pi}B_\perp\|^2}{D}. \tag{3.9}$$

From Eqn. 3.9 it follows that energy level shifts due to transverse magnetic fields are mitigated by the large zero-field splitting $D(T)$; and are further suppressed in the DQ basis, as they add (approximately) in common-mode. Consequently, transverse magnetic fields and gradients in the transverse magnetic field can be neglected in the experiments presented in this chapter, especially when considering sources of ensemble dephasing. Similar analysis demonstrates that the crystal-stress-related $N_\perp$ contribution is also suppressed by the zero-field-splitting and therefore neglected in

the remainder of this dissertation.

3.1.2 Non-Zero Crystal Stress Contributions

Next, the effect of non-zero axial M_z and transverse $M_\perp$ crystal stress terms are considered, while assuming $N_\perp = 0$ and a bias magnetic field aligned along the NV symmetry axis with magnitude B_z such that $B_\perp = 0$. Under these conditions, the energy eigenvalues of the NV^- Hamiltonian (3.2) for the $|\pm1\rangle$ sublevels become,

$$E_{|\pm1\rangle}/h = D + M_z \pm \sqrt{(\frac{\gamma_{NV}}{2\pi}B_z)^2 + ||M_\perp||^2} \tag{3.10}$$

$$\approx D + M_z \pm \left[\frac{\gamma_{NV}}{2\pi}B_z + \frac{||M_\perp||^2}{2\frac{\gamma_{NV}}{2\pi}B_z} + \mathcal{O}\left(\frac{(||M_\perp||^4}{B_z^2}\right)\right]. \tag{3.11}$$

To first order, crystal stress shifts the energies of the $|\pm1\rangle$ states in common-mode by the axial stress term M_z. SQ measurements, which probe the difference between $E_{|0\rangle}$ and either $E_{|\pm1\rangle}$, are vulnerable to this axial-stress-induced shift. Conversely, DQ measurements which probe the difference between the $E_{|+1\rangle}$ and $E_{|-1\rangle}$ energies, are insensitive to axial stress. At second order, the transverse crystal stress term $M_\perp$ induces magnetic-like, differential shifts in the $E_{|\pm1\rangle}$ energies, which are not mitigated in either the SQ or DQ sensing bases. However, these transverse-stress-induced shifts are suppressed by a factor $||M_\perp||/(\gamma_{NV}B_z/\pi)$. For variations in $M_z \approx M_\perp \approx 100\,\text{kHz}$, an aligned bias magnetic field of 5 mT provides a suppression of $\approx 450\times$.

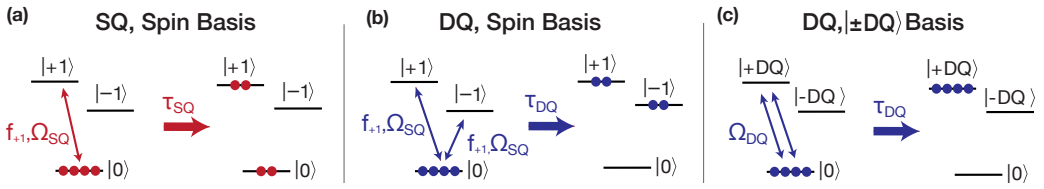

Figure 3.2: **SQ and DQ pulses for Ramsey experiments.(a)** Depiction of a single-tone MW pulse with frequency f_{+1} resonant with the $|0\rangle \rightarrow |+1\rangle$ transition and Rabi frequency Ω_{SQ} in the $\{|0\rangle, |+1\rangle, |-1\rangle\}$ spin basis. The applied pulse, with duration τ_{SQ}, creates an equal superposition of the $|0\rangle$ and $|+1\rangle$ sublevels. **(b)** Depiction of a dual-tone MW pulse with frequencies f_{+1} and f_{-1} resonant with the $|0\rangle \rightarrow |+1\rangle$ and $|0\rangle \rightarrow |+1\rangle$ transitions in the $\{|0\rangle, |+1\rangle, |-1\rangle\}$ spin basis. Both transitions are driven with Rabi frequency Ω_{SQ}. The applied pulse, with duration $\tau_{\mathrm{DQ}} = \sqrt{2}\tau_{\mathrm{SQ}}$, creates an equal superposition of the $|-1\rangle$ and $|+1\rangle$ sublevels. **(c)** Depiction of a dual-tone MW pulse in the $\{|0\rangle, |+\mathrm{DQ}\rangle, |-\mathrm{DQ}\rangle\}$ basis with duration $\tau_{\mathrm{DQ}} = \pi/\Omega_{\mathrm{DQ}}$ (where $|\pm DQ\rangle = (|+1\rangle \pm |-1\rangle)/\sqrt{2}$). In this basis, the applied pulse behaves like a π-pulse transferring population from $|0\rangle$ into $|+\mathrm{DQ}\rangle$

3.2 Implementing Double Quantum Control

For single quantum (SQ) Ramsey magnetometry, a single-tone $\pi/2$-pulse addressing the $|0\rangle \rightarrow |+1\rangle$ or $|0\rangle \rightarrow |-1\rangle$ transitions with frequency f_{+1} or f_{-1}, Rabi frequency Ω_{SQ}, and duration $\tau_{\mathrm{SQ}} = \pi/(s\Omega_{\mathrm{SQ}})$ generates an equal superposition of the $|0\rangle$ and either $|\pm 1\rangle$ sublevels (see Fig. 3.2(a)).

In contrast, in the presence of an external magnetic field, preparation and control of the double quantum (DQ) coherence employs resonant excitation of both transitions to generate a superposition of the $|\pm 1\rangle$ sublevels. If each transition is driven with Ω_{SQ}, then the resulting on-resonance DQ Rabi frequency Ω_{DQ} is $\sqrt{2}\Omega_{\mathrm{SQ}}$ and the corresponding pulse duration τ_{DQ} to create a superposition of the $|\pm 1\rangle$ sublevels is (see Fig. 3.2(b)):

$$\tau_{\mathrm{DQ}} = \frac{\pi}{\Omega_{\mathrm{DQ}}} = \sqrt{2}\tau_{\mathrm{SQ}}. \tag{3.12}$$

For an equal superposition of the $|\pm 1\rangle$ states, the phase relationship $\Delta\phi$ in $(|+1\rangle + e^{-i\Delta\phi}|-1\rangle)/\sqrt{2})$ is determined by the relative phase between the two applied MW tones. In Fig. 3.2(c), the orthogonal states $|+DQ\rangle = (|+1\rangle + |-1\rangle)/\sqrt{2}$ and $|-DQ\rangle = (|+1\rangle - |-1\rangle)/\sqrt{2}$ are defined with $\Delta\phi = 0°, 180°$, respectively. Since neither $|\pm\text{DQ}\rangle$ are energy eigenstates of the system, population precesses between $|+\text{DQ}\rangle$ and $|-\text{DQ}\rangle$ while accumulating phase in a magnetic field. While it is possible to sequentially address these transitions using SQ (single-tone) pulses and generate the requisite superposition of the $|\pm 1\rangle$ sublevels [117], the discussion in this section focuses on two-tone pulses which address both transitions simultaneously because the required DQ rotations can be accomplished in a shorter amount of time compared to sequential single-tone pulses.

For the experiments described throughout this dissertation, dual-tone MW control fields are synthesized using two signal generators with independent amplitude and phase control on each tone. The synthesized MW signals are then combined either before or after passing through an amplifier and ultimately delivered to the diamond via a MW delivery structure (commonly a fabricated planar gold wave-guide or shorted coaxial loop). Fig. 3.3(a) depicts an exemplary DQ Ramsey pulse sequence, including the optical pulse used for initialization and readout as well as a TTL pulse which triggers DAQ readouts on the rising edge (or another device such as a camera).

A schematic of the MW control hardware is included in Fig. 3.3(b)). However, this configuration is not unique and other hardware configurations include (a) double side-band modulation of a single local oscillator as demonstrated by Mamin et al [79] or (b) directly synthesizing the GHz-scale MW control fields using an arbitrary wave-

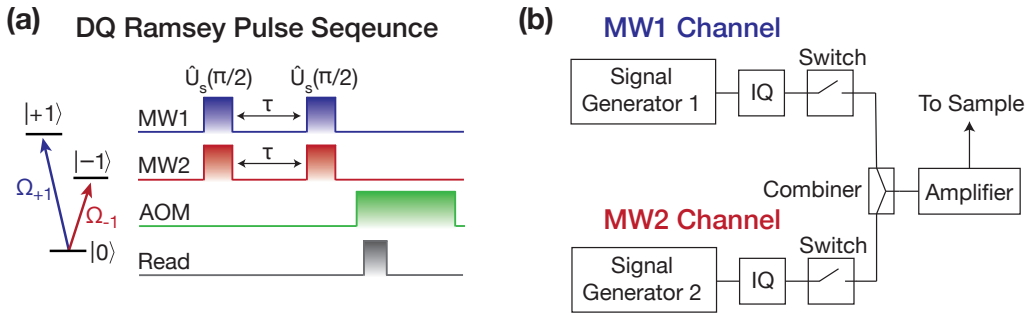

Figure 3.3: **DQ Microwave Control.** **(a)** Illustration of a DQ Ramsey pulse sequence with dual-tone MW pulses used to apply unitary spin-1 DQ rotations $\hat{U}_{s=1}(\pi/2)$. In a Ramsey free induction decay measurement, the duration between the MW pulses, τ is swept. An AOM is used to apply optical pulses for readout and re-initialization. The rising edge of the readout pulse triggers a DAQ to read the voltage from a photodiode or acquires from other hardware such as a camera. **(b)** Microwave generation and delivery schematic. For NV spin state control: Single and two-tone signals can be generated using two signal generators (e.g., SRS384). Both channels include IQ mixers to manipulate the phases of the synthesized signals. Minicircuits ZASWA-2-50DR+ switches are used to generate the NV control pulses before amplification with a Minicircuits ZHL-16W-43 amplifier. The NV control fields are delivered to the diamond sample using a fabricated microwave waveguide (500 μm diameter).

form generator with sufficient sampling rate. Independent of these details, control of the amplitude of each tone is critical in order to overcome the frequency-dependent couplings of the MW delivery structure, frequency-dependent gain in the MW amplifier, and losses which would otherwise produce unequal SQ Rabi frequencies for the two spins transitions.

3.3 DQ Pulse Calibration using State Tomography

This section describes a state tomography-based procedure to calibrate the amplitudes and duration of the dual-tone MW pulses used to produce and manipulate

equal superpositions of the $|\pm1\rangle$ sublevels. The calibration procedure begins with the two sets of measurements depicted schematically in Fig. 3.4(a,c). The objective of these measurements is to calibrate the relative amplitudes of the constituent MW tones, MW1 and MW2, which are resonant with the $|0\rangle \rightarrow |+1\rangle$ and $|0\rangle \rightarrow |-1\rangle$ spin transitions, respectively. Ideally, when the effective Rabi frequencies for both transitions are equivalent, a two-tone pulse with duration τ_{DQ} will create an equal superposition of the $|\pm1\rangle$ sublevels. However, frequency-dependent coupling of the MW delivery structure, amplification, or attenuation by other components can lead to unequal Rabi frequencies for the two transitions. If one transition is addressed with a faster Rabi frequency, then population will more rapidly accumulate in either of the $|\pm1\rangle$ sublevels. The procedure described below is intended to determine the proper amplitude A^{MW2} relative to A^{MW1} to ensure equal driving of both transitions. Here, the amplitudes A^{MW1} and A^{MW2} are reported in terms of the RF output power from each signal generator (in units of dBm) and initially estimated using SQ Rabi measurements on each transition independently (with the other MW tone absent). It is critical to note that when both MW tones are amplified using the same amplifier (as shown in Fig. 3.3), increasing A^{MW2} and thus the effective SQ Rabi frequency results in a commensurate decrease in the Rabi frequency observed on the other transition.

As illustrated in Fig. 3.4(a,c), a dual-tone MW pulse with duration τ_{DQ} and amplitudes A^{MW1} and A^{MW2} is applied to the NV^- ensemble. Then, a SQ Rabi measurement using a single-tone pulse on MW1 or MW2 is performed to probe the population distribution between the $|\pm\rangle$ sublevels. After recording the SQ Rabi oscillations when probing MW1 for a range of A^{MW2}, a second set of measurements

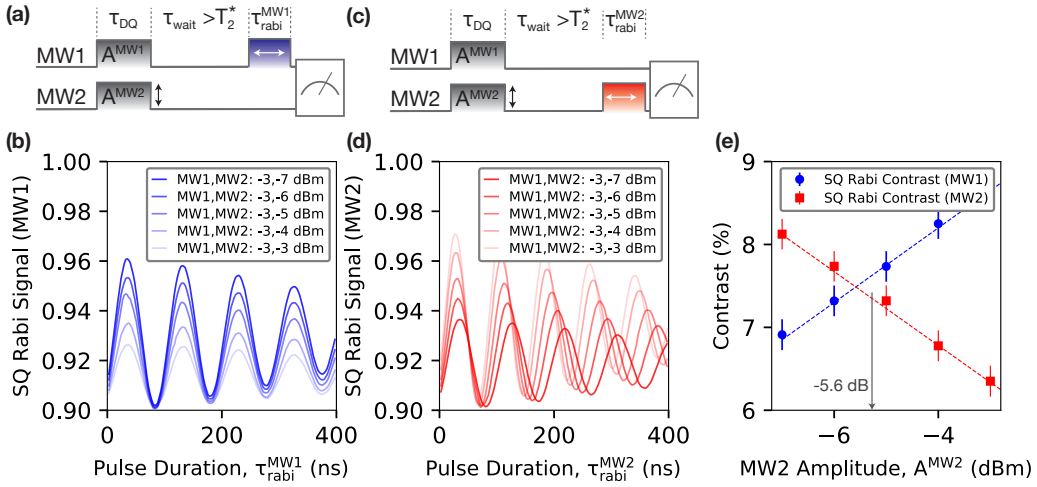

Figure 3.4: **MW Amplitude Calibration Procedure.** **(a)** Pulse sequence used to measure the SQ Rabi oscillation on the MW1 channel which is resonant with the $|0\rangle \rightarrow |+1\rangle$ transition as a function of the MW2 pulse amplitude A^{MW2}. A^{MW1} is fixed throughout. **(b)** Example data produced using the pulse sequence depicted in (a). The Rabi contrast decreases with in increasing A^{MW2}. **(c)** Pulse sequence used to measure the SQ Rabi oscillation on the MW2 channel which is resonant with the $|0\rangle \rightarrow |-1\rangle$ transition as a function of A^{MW2}. **(d)** Example data produced using the pulse sequence depicted in (c). The measured SQ Rabi contrast and frequency increases with increasing A^{MW2}. **(e)** The Rabi contrast values extracted from the measurements in (b,d) are shown as a function of A^{MW2}. The black arrow indicates the intersection at A^{MW2} = -5.6 dBm which corresponds to the amplitude required for the populations in $|-1\rangle$ and $|-1\rangle$ to be equivalent after the dual-tone pulse in (a,c) is applied. Note that the amplitude A^{MW2} depends in the initial choice for A^{MW1}.

is acquired addressing MW2. The recorded SQ Rabi contrasts are proportional to the population transferred into either of the $|\pm1\rangle$ sublevels. A wait interval τ_{wait} is introduced after the dual-tone MW pulse is applied. The wait interval must satisfy $\tau_{wait} \gg T_2^*$ in order to ensure that any coherences have dephased and the measured SQ Rabi contrast is only dependent on the population difference between the $|0\rangle$ and probed $|\pm1\rangle$ sublevels (diagonal terms of the density matrix).

Fig. 3.4(b) depicts the first set of measurements where SQ Rabi oscillations are

measured on the $|0\rangle \rightarrow |+1\rangle$ transition (MW1) while the amplitude of MW2, A^{MW2}, addressing the $|0\rangle \rightarrow |-1\rangle$ transition, is swept. When A^{MW2} is small compared to A^{MW1}, the applied dual-tone pulse mostly couples the $|0\rangle$ and $|+1\rangle$ sublevels and results in maximum contrast. As the relative amplitude of MW2 and the coupling of the dual-tone pulse to the other transition increases, the contrast of the $|0\rangle \rightarrow |+1\rangle$ Rabi oscillations decreases.

Meanwhile, Fig. 3.4(d) depicts the second set of measurements: SQ Rabi oscillations are measured on the $|0\rangle \rightarrow |-1\rangle$ transition (MW2) while the applied RF amplitude of MW2 is again swept. The SQ Rabi contrast and frequency increases as A^{MW2} increases as expected. The extracted Rabi contrasts for both data sets are then presented in Fig. 3.4(e). When the SQ Rabi contrasts are equivalent, the two populations are driven between the $|0\rangle$ and $|\pm 1\rangle$ sublevels at equal rates as desired.

With the amplitude calibration complete, the optimal dual-tone pulse duration τ_{DQ} can be determined by measuring the DQ Rabi oscillation (transferring spin population between the $|0\rangle$ and $|\pm \mathrm{DQ}\rangle$). Exemplary DQ Rabi oscillations are shown in Fig. 3.5 for two choices of applied MW tones on an ^{15}NV ensemble sample (Sample 2D, see App. C). Fig. 3.5(a) depicts DQ Rabi oscillations for the "equal-detuning" case in which the MW tones are symmetrically detuned from both hyperfine-split populations by about ($|\Delta_1| = |\Delta_2| \approx 1.55\,\mathrm{MHz}$) and the effective Rabi frequencies for each population are equivalent. It is immediately apparent from Fig. 3.5(a) that the DQ Rabi signal is not a simple mono-tone oscillation as observed in SQ Rabi measurements, but instead exhibits two oscillations at a frequency Ω_{DQ} and, as we will derive, its half-harmonic at $\Omega_{\mathrm{DQ}}/2$. Ultimately, this is a feature of vee-type three

level systems with the two higher energy states coupled through a single lower energy state. However, the case of differential, but equal magnitude detunings considered here is less commonly discussed.

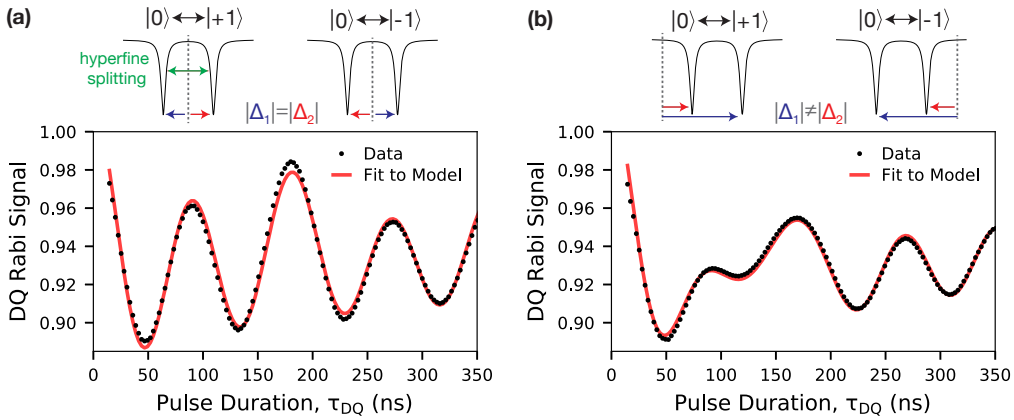

Figure 3.5: **DQ Rabi Oscillations. (a)** DQ Rabi oscillation measured by sweeping the duration of the dual-tone MW pulse. The applied MW tones are detuned symmetrically from both hyperfine populations in the ^{15}N-enriched diamond sample ($|\Delta_1| = |\Delta_2| \approx 1.55\,\text{MHz}$). The red line is a fit to the data using Eqn. 3.17 with an additional exponential decay envelope and overall scaling factor. **(b)** Similar to (a), but with an additional differential detuning of 3.5 MHz such that the detunings for both hyperfine populations are non-degenerate ($|\Delta_1| \neq |\Delta_2|$). The red line is a fit to the data using Eqn. 3.17 with an additional exponential decay envelope and overall scaling factor.

To obtain analytical expressions for the DQ Rabi signal, we begin with the ground state electronic Hamiltonian (Eqn. 3.1), neglecting stress and transverse magnetic field contributions, but including an external AC magnetic field to drive transitions between the $|0\rangle$ and $|\pm1\rangle$ magnetic sublevels,

$$H/h \approx (D(T) + M_z)\, S_z^2 + \frac{\gamma}{2\pi} B_z \cdot S_z + \frac{\gamma}{2\pi} B_{\text{AC}}[\cos(\omega_1 t) + \cos(\omega_2)t] \cdot \sqrt{2} S_x. \quad (3.13)$$

Using the rotation operator,

$$R(t) = \begin{pmatrix} e^{-i\omega_1 t} & 0 & 0 \\ 0 & 1 & 0 \\ 0 & 0 & e^{-i\omega_1 t} \end{pmatrix} \tag{3.14}$$

and rotating wave approximation, Eqn. 3.13 can be transformed into a rotating frame as,

$$\tilde{H}/h = \begin{pmatrix} D + \frac{\gamma}{2\pi}B_z - \omega_1 & \frac{1}{2}\frac{\gamma}{2\pi}B_{\mathrm{AC}} & 0 \\ \frac{1}{2}\frac{\gamma}{2\pi}B_{\mathrm{AC}} & 0 & \frac{1}{2}\frac{\gamma}{2\pi}B_{\mathrm{AC}} \\ 0 & \frac{1}{2}\frac{\gamma}{2\pi}B_{\mathrm{AC}} & D - \frac{\gamma}{2\pi}B_z - \omega_2 \end{pmatrix}, \tag{3.15}$$

which after defining the SQ Rabi frequency for each transition as $\Omega_{SQ} = \frac{\gamma}{2\pi}B_{\mathrm{AC}}$ and, for a differential detuning with magnitude $|\Delta|$, $w_{1,2} = (D \pm \frac{\gamma}{2\pi}B_z) \pm \Delta$, reduces to the form:

$$\tilde{H}/h = \begin{pmatrix} -\Delta & \frac{1}{2}\Omega_{SQ} & 0 \\ \frac{1}{2}\Omega_{SQ} & 0 & \frac{1}{2}\Omega_{SQ} \\ 0 & \frac{1}{2}\Omega_{SQ} & \Delta \end{pmatrix}. \tag{3.16}$$

If the system is initialized into $|0\rangle$ at time $t = 0$ with $|\tilde{c}_0(0)|^2 = 1$, then the population in the $m_s = 0$ state will evolve according to,

$$|\tilde{c}_0(t)|^2 = A\cos(2\pi\Omega_{\mathrm{DQ}}t) + B\cos(2\pi(\frac{\Omega_{\mathrm{DQ}}}{2})t) + C \tag{3.17}$$

where the coefficients A, B, and C are time-independent and only depend upon the detuning and SQ Rabi frequency Ω_{SQ},

$$A = \frac{2\Omega_{SQ}^4}{\Omega_{\mathrm{DQ}}^4},\ B = \frac{16\Omega_{\mathrm{SQ}}^2\Delta^2}{\Omega_{\mathrm{DQ}}^4},\ C = \frac{2\Omega_{SQ}^4 + 16\Delta^4}{\Omega_{\mathrm{DQ}}^4}. \tag{3.18}$$

For a detuning Δ, Ω_{DQ} is defined as $\sqrt{4\Delta^2 + 2\Omega_{SQ}^2}$. Returning to the experimental data presented in Fig. 3.5(a), the red solid line was produced by fitting to Eqn. 3.17 for the equal-detuning case. The only free parameters used for fitting are the DQ Rabi frequency Ω_{DQ}, an additional exponential decay term, and an overall scaling factor. The magnitude of the detuning Δ from each hyperfine population was fixed to be $\Delta_{\mathrm{HF}}/2 = |\Delta_{1,2}| \approx 1.55\,\mathrm{MHz}$. The resulting fit shown in red in Fig. 3.5(a) captures the experimental data well.

In the limit of large Ω_{DQ} and Ω_{SQ}, the B term and the relative contribution of the half-harmonic is suppressed such that we recover a single oscillation with frequency Ω_{DQ}: $|\tilde{c}_0(t)|^2 = \cos(2\pi\Omega_{\mathrm{DQ}}t) + \frac{1}{2}$ where $C = 1/2$ and $A = 1$. The fractional contribution of the half-harmonic term to the resulting DQ Rabi signal decreases with increasing Ω_{SQ} according to a Lorentzian profile,

$$\frac{B}{A+B} = \frac{\Delta^2}{\Delta^2 + \frac{1}{8}(\Omega)^2}, \tag{3.19}$$

with width proportional to the detuning.

For the equal-detuning, ^{15}NV ensemble measurements shown in Figs. 3.5(a), SQ Rabi frequencies Ω_{SQ} in excess of 18 MHz on both the $|0\rangle \rightarrow |+1\rangle$ and $|0\rangle \rightarrow |+1\rangle$ transitions are required to suppress the fractional contribution of the half-harmonic

term to less than 10%. For reference, the measurement presented in Figs. 3.5(a) with $\Omega_{SQ} \approx 11\,\text{MHz}$, the fractional contribution of the half-harmonic is $\approx 24\%$.

While such SQ Rabi frequencies Ω_{SQ} (and even larger) can be readily attained in single NV experiments and confocal volumes, the competing requirements of spatial homogeneity and increasing SQ Rabi frequencies for ensemble measurements present an outstanding technical roadblock for many applications. The presence of the half-harmonic most dramatically effects DQ, dual-tone "swap"-pulses designed to exchange the populations in the $|+1\rangle$ and $|-1\rangle$ sublevels. These rotations are critical for echo-type DQ pulse sequences [79] as well as magnetically-insensitive variants used for thermometry [117] (Ref. [117] in fact uses sequential single-tone pulses instead of dual-tone pulses in part to avoid this challenge). Fortunately, for the DQ Ramsey sequences primarily considered here, the optimal pulse duration τ_{DQ} corresponds to the first minima in the DQ Rabi signal. When $\Omega_{SQ} > \Delta_{\text{HF}}$, the half-harmonic behavior does not significantly impact the contrast or duration τ_{DQ} of the first minima. However, it is important to note that as Ω_{SQ} decreases and becomes comparable to Δ_{HF}, the half-harmonic term can dramatically alter the DQ Rabi signal and optimal pulse duration.

Fig. 3.5(b) depicts the DQ Rabi signal resulting from non-degenerate detunings for each of the hyperfine-split populations ($\Delta_1 \neq \Delta_2$). In this case, the measured data is fit to an analytical form which includes terms for both hyperfine populations with detunings, $\Delta_1 \approx -1.95\,\text{MHz}$ and $\Delta_2 \approx 5.05\,\text{MHz}$. As with the equal-detuning case, the resulting fit exhibits reasonable agreement with the measured DQ Rabi signal. For both cases, the optimal DQ pulse duration is $\approx 50\,\text{ns}$.

3.4 The DQ 4-Ramsey Measurement Protocol

As alluded to in the previous section, generating strong and uniform MW control fields across an interrogated ensemble becomes an increasingly difficult technical challenge as the volume of the interrogated ensemble increases. A spatially varying Rabi frequency induces MW pulse errors because only one global pulse duration can be chosen for the entire field of view. In SQ measurements, MW pulse errors result in a loss of contrast. However, for DQ measurements such pulse errors additionally result in residual SQ coherence that remains sensitive to common-mode shifts of the $|\pm 1\rangle$ sublevels, degrading the robustness of DQ magnetometry to stress-induced shifts and temperature drifts.

This challenge is circumvented here by introducing a DQ 4-Ramsey protocol specifically designed to suppress residual SQ coherence. While further technical progress designing more efficient and uniform MW delivery structures remains critical, this 4-Ramsey protocol relaxes technical requirements such that presently existing solutions are sufficient. The protocol consists of four consecutive Ramsey sequences that, when combined, isolate the desired DQ magnetometry signal from residual SQ signal by modulating the MW pulse phases (see Fig. 3.6). SQ protocols commonly employ sets of two Ramsey sequences (2-Ramsey), alternating the phase of the final $\pi/2$ pulse in successive sequences by 180°, to modulate the NV^- fluorescence and cancel low-frequency noise, such as $1/f$ noise [118]. In such a SQ 2-Ramsey protocol, the magnetometry signal alternately maps to positive and negative changes in NV^- fluorescence, such that subtracting every second detection from the previous yields a rectified magnetometry signal.

An analogous DQ 2-Ramsey protocol exists: The two-tone MW pulses discussed earlier couple the $|0\rangle$ state to equal-amplitude superpositions of the $|\pm 1\rangle$ state, with a phase relationship $(|+1\rangle + e^{i\Delta\phi}|-1\rangle)/2$ determined by the relative phase $\Delta\phi$ between the two MW tones [79]. By modulating $\Delta\phi = \{0^\circ, 180^\circ\}$ between the tones in the final $\pi/2$ pulse, the $|0\rangle$ state can be alternately coupled to the orthogonal superposition states $|\pm\text{DQ}\rangle = (|+1\rangle \pm |-1\rangle)/\sqrt{2}$. Although this DQ 2-Ramsey protocol effectively mitigates noise at frequencies below the $\Delta\phi$ modulation frequency, it does not disentangle the desired DQ signal from unwanted SQ signal arising from MW pulse errors.

Fig. 3.6 illustrates the DQ rotations applied in the $\{|0\rangle, |-\text{DQ}\rangle, |+\text{DQ}\rangle\}$ basis for a particular implementation of the DQ 4-Ramsey protocol along with the expected sign of the contrast change produced by a magnetic signal. In this example, the choice of relative phases has been restricted to 0° or 180°. While the initial pulse in each Ramsey sequence prepares the $|+\text{DQ}\rangle$ state, the final pulse alternately couples to the $|+\text{DQ}\rangle$ and $|-\text{DQ}\rangle$ states, similar to the DQ 2-Ramsey protocol. If the signal from each of the four measurements $i = 1{-}4$ is denoted by S_i then the rectified DQ signal S_{4R} is given by:

$$S_{4R} = S_1 - S_2 + S_3 - S_4 \tag{3.20}$$

where, as shown in Fig. 3.6(a), S_2 and S_4 contain DQ signals with opposite sign compared to S_1 and S_3. When implementing these DQ rotations, we have flexibility in choosing the absolute phases of each tone. For example, {0°, 0°} and {180°, 180°} both couple to $|+\text{DQ}\rangle$ while {0°, 180°} and {0°, 180°} couple to $|-\text{DQ}\rangle$. We leverage this degree of freedom to ensure that residual SQ signals are canceled by Eqn. 3.20.

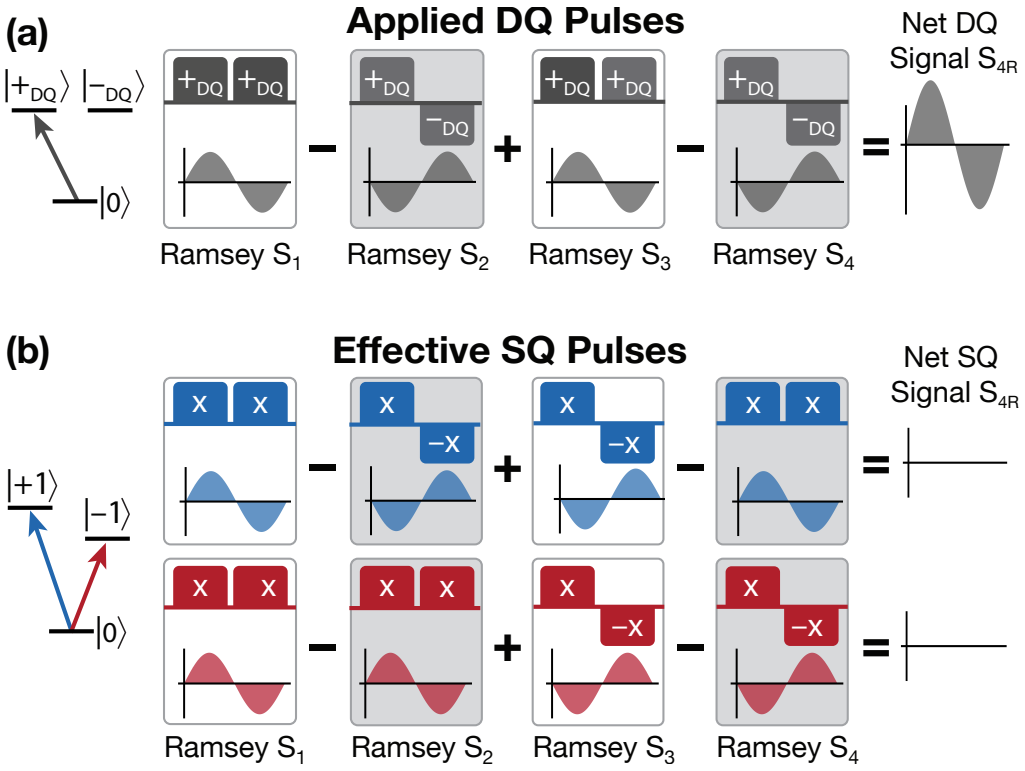

Figure 3.6: **4-Ramsey Measurement Protocol.** **(a)** Representation of the DQ 4-Ramsey measurement protocol to cancel residual single quantum (SQ) signals resulting from MW pulse errors. The two-tone DQ pulses applied during each Ramsey sequence are depicted above the DC magnetometry curve associated with that choice of phases. The net DQ magnetometry signal S_{4R} is shown on the right. **(b)** The applied MW pulses are decomposed into effective SQ rotations for each pseudo-two-level system. The resultant DC magnetometry signals for each Ramsey sequence are depicted and shown to produce no net SQ signal under Eqn. 3.20.

The effective SQ pulses applied to each two-level subsystem transition ($|0\rangle \rightarrow |+1\rangle$ and $|0\rangle \rightarrow |-1\rangle$) are illustrated in Fig. 3.6(c) as Bloch sphere rotations about the axes x and $-x$. Note that the phase shifts, $\{0°, 180°\}$, correspond to rotations about {x, -x}, respectively.

If pulse errors arise, leading to residual SQ coherence, then Eqn. 3.20 cancels the resultant SQ signal because the SQ signal contained in the summation S_2+S_4 is the

same as S_1+S_3, assuming the pulse error is constant over the measurement duration. For photodiode-based measurements, which provide access to S_{1-4} directly, the right hand side of Eqn. 3.20 can be divided by the sum of S_{1-4} to cancel the effects of noise sources such as laser intensity drift.

3.4.1 Experimental Demonstration of the 4-Ramsey Protocol

In this following, the 4-Ramsey protocol is demonstrated using a custom-built epi-fluorescence microscope (see Fig. 3.7). An approximately $100\,\mu m \times 100\,\mu m$ region of 1-micron-thick, nitrogen-doped CVD diamond layer ($[N] \approx 20\,ppm$, $^{12}C = 99.995\%$, natural abundance nitrogen) grown by Element Six (Sample 3A) is illuminated with 500 mW of 532nm laser light. Post-growth treatment via electron irradiation and annealing increased the NV^- concentration in the nitrogen-doped layer to $\sim 2\,ppm$. The emitted NV^- fluorescence is collected onto a single-channel photodiode detector (Hamamatsu C10508). An Aglient E9310A with built-in IQ modulation and a Windfreak SynthHD signal generator in combination with an external Marki-1545LMP IQ mixer provided the two-tone MW control fields and requisite phase control employed in this work. A Pulseblaster ESR-Pro with 500 MHz clock controlled the synchronization of applied MW pulses, optical pulses, and photodiode readouts. Samarium cobalt ring-shaped magnets (as described further in Ref. [73] and Appendix B) applied a 5 mT bias magnetic field used to split the $|0\rangle$ and $|\pm 1\rangle$ transitions.

Figs. 3.7(b-e) illustrate the benefit of the DQ 4-Ramsey protocol over SQ and DQ 2-Ramsey protocols by comparing the measured change in contrast in response to differential (magnetic-field-like) and common-mode (temperature, axial-stress-like)

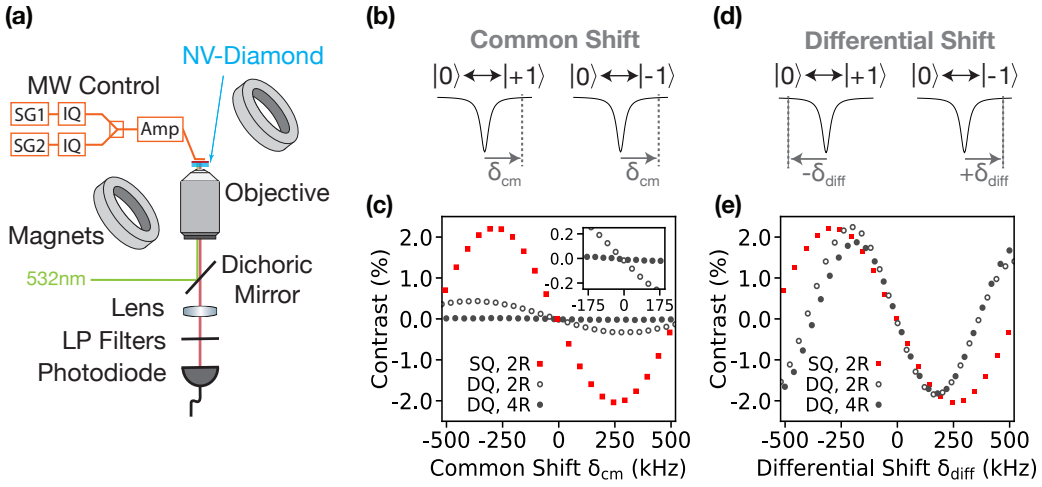

Figure 3.7: **Experimental demonstration of the 4-Ramsey protocol using Sample 3A. (a)** Apparatus overview including 532nm excitation of a micron-scale layer of NV centers in a macroscopic diamond chip, using a 20x objective and epi-illumination configuration. NV fluorescence is collected using the same objective onto a photodiode. 647 nm and 532 nm long-pass (LP) optical filters partially isolate NV^- fluorescence from NV^0 background fluorescence. MW control fields are synthesized using two signal generators with phase control on both tones and applied via a millimeter-scale shorted coaxial loop. A bias magnetic field of 5mT is aligned with NV centers oriented along a single crystallographic axis. **(b)** The applied two-tone MW field frequencies are detuned from the NV^- resonances in common-mode by δ_{cm} to emulate stress- and temperature-induced shifts. **(c)** Single-channel (photodiode) measurements of the NV^- response to common shifts of the $|0\rangle \rightarrow |+1\rangle$ and $|0\rangle \rightarrow |-1\rangle$ spin resonances. For each sensing protocol, $\delta_{\mathrm{cm}} = 0$ indicates the point of maximum slope after calibration (see Appendix A). The DQ 4-Ramsey response to common shifts is suppressed by 96× compared to the SQ 2-Ramsey response. **(d)** The applied two-tone MW field frequencies are detuned from the NV^- resonances differentially by $\pm\delta_{\mathrm{diff}}$ to emulate axial-magnetic-field induced shifts. **(e)** Single-channel measurements of the NV^- response to differential shifts of the $|0\rangle \rightarrow |+1\rangle$ and $|0\rangle \rightarrow |-1\rangle$ spin resonances. For each measurement protocol, $\delta_{\mathrm{diff}} = 0$ indicates the point of maximum slope after calibration, which determines the optimal magnetometer sensitivity.

shifts when operating with a free precession interval τ and detuning from the center hyperfine resonance optimized for magnetic sensitivity (see Appendix A). In these

measurements, the MW pulse errors are attributed approximately equally to a 10% Rabi gradient across the ensemble and the hyperfine-induced differences in effective Rabi frequency for each of the three hyperfine-split resonances. The sample used for this demonstration (Sample 3A) has a 1-micron-thick, ^{14}N-doped layer (nuclear spin $m_I = 1$).

By approximating the change in fluorescence about the optimal detuning ($\delta_{\mathrm{cm}} = \delta_{\mathrm{diff}} = 0$) using a linear fit, we find that DQ Ramsey measurements using the conventional 2-Ramsey protocol (with residual SQ signal) suppress the response to common shifts δ_{cm} compared to SQ 2-Ramsey measurements by a factor of 7. Although this suppression factor depends on both the particular setup and diamond, the factor of 7 reported in this work is similar to that in Ref. [80] for a single NV^-, which also attributes the residual observed response to MW pulse imperfections. Meanwhile, under the same experimental conditions, the DQ 4-Ramsey protocol suppresses the common shift response by about a factor of 100 compared to SQ Ramsey measurements. As depicted in Fig. 3.7(e), the DQ 4-Ramsey and DQ 2-Ramsey responses exhibit about a cumulative 25% increase in slope (and hence magnetometer sensitivity) compared to the SQ 2-Ramsey response, after accounting for the increased effective gyromagnetic ratio in the DQ basis and the loss of DQ contrast due to pulse errors.

Finally, although the 4-Ramsey protocol introduces a factor of 2 reduction in the temporal resolution compared to a 2-Ramsey DQ protocol (it takes 4 measurements to produce a rectified signal), there is no penalty on sensitivity or bandwidth because the rate of Ramsey measurements is unchanged and the DQ signals from

each measurement add constructively.

3.5 Comparing DQ and SQ T_2^* Measurements

This section discusses Ramsey fringe measurements in the SQ and DQ sensing bases for three as-grown CVD samples with varying concentrations of nitrogen doping (Samples 3B, 3C, 3D). Comparison of the SQ dephasing time $T_2^*\{\mathrm{SQ}\}$ and decay shape to the stress-gradient-immune $T_2^*\{\mathrm{DQ}\}$ and decay shape is a useful tool for identifying and quantifying the underlying dephasing mechanisms. After introducing the samples used in this section, Sec. 2.2 is summarized as relevant for the present discussion.

As summarized in Tab. 3.1, Samples 3B ($[N] \lesssim 0.05\,\mathrm{ppm}$) and 3C ($[N] = 0.75\,\mathrm{ppm}$) each consist of a ^{14}N-doped, 100- μm-thick CVD layer (99.99% ^{12}C) deposited on top of a diamond substrate. Sample 3D ($[N], = 10\,\mathrm{ppm}$) possesses a 40- μm-thick, ^{15}N-doped CVD layer (99.95% ^{12}C) on a diamond substrate. Since these samples have not been electron irradiated and annealed, they exhibit an N-to-NV conversion efficiency of much less than 1% [65] and therefore dephasing due to NV-NV dipolar interactions can be neglected.

The major remaining dephasing mechanisms to consider are dipolar interactions with the electronic substitutional nitrogen and ^{13}C nuclear spin baths as well as axial-stress-gradients M_z across the ensemble. Recall that transverse-stress-gradients, $M_\perp$, are suppressed by a modest aligned bias magnetic field of 2–8.5 mT in the following experiments, and neglected in the following analysis. The contribution of these three

dephasing mechanisms to the ensemble $T_2^*\{\mathrm{SQ}\}$ can be expressed as,

$$\frac{1}{T_2^*\{\mathrm{SQ}\}} \approx \frac{1}{T_2^*\{N_S^0\}} + \frac{1}{T_2^*\{^{13}C\}} + \frac{1}{T_2^*\{M_z\}}. \tag{3.21}$$

Eqn. 3.21 assumes the dephasing rates for all mechanisms add approximately linearly (i.e., that they lead to exponential decay in the Ramsey fringe envelope). While this assumption is true for purely spin-bath-limited dephasing where the NV$^-$ ensemble decay envelope exhibits a simple exponential decay (decay shape parameter, $p = 1$) [74, 92], stress-gradient-limited NV spin ensemble dephasing can exhibit a wide range of decay shapes ($p \neq 1$). Therefore, Eqn. 3.21 only provides an estimate for $T_2^*\{\mathrm{SQ}\}$ in the presence of stress-gradient-induced dephasing. For $T_2^*\{\mathrm{DQ}\}$, the contribution of magnetic-spin-bath-limited terms in Eqn. 3.21 ($T_2^*\{\mathrm{N}_s^0\}$ and $T_2^*\{^{13}\mathrm{C}\}$) should be doubled and the axial-stress-gradient contribution neglected,

$$\frac{1}{T_2^*\{\mathrm{DQ}\}} = 2 * \Big(\frac{1}{T_2^*\{N_S^0\}} + \frac{1}{T_2^*\{^{13}C\}}\Big). \tag{3.22}$$

This expression is now exact - the Ramsey decay should be exponential assuming the spin bath concentrations are uniform across the interrogated volume. As introduced Sec. 2.2.1 and Sec. 2.2.4, the contributions of dipolar interactions with the N_s^0 and ^{13}C spin baths to dephasing can be estimated using,

$$\frac{1}{T_2^*\{\mathrm{N}_{s0}\}} = \Delta m_s A_{\mathrm{N}_s^0} \cdot [\mathrm{N}_s^0], \tag{3.23}$$

$$\frac{1}{T_2^*\{^{13}\mathrm{C}\}} = \Delta m_s A_{^{13}\mathrm{C}} \cdot [^{13}\mathrm{C}], \tag{3.24}$$

where $|\Delta m_s|$ is the absolute value of the difference between the magnetic sublevels used for sensing ($\Delta m_s = 2$ for the DQ sensing basis).

In the following sections, we use the average dipolar coupling to estimate $A_{\mathrm{N}_s^0}$ instead of the scaling presented in Sec. 2.2.1 ($101 \pm 12\,\mathrm{ms^{-1}ppm^{-1}}$) since measurements of Sample 3C and Sample 3D were used to determine this value. Instead, the NV$^-$ ensemble T_2^* as a function of nitrogen concentration is estimated from the average dipolar coupling between electronic nitrogen spins, which is given by $\gamma_{\mathrm{e-e}} = a \times \frac{\mu_0}{4\pi} g^2 \mu_B^2 / \hbar \frac{1}{\langle r \rangle^3} \approx 2\pi \times 9.1 \cdot [\mathrm{N}_s^0]\,\mathrm{kHz/ppm}$, where μ_0 is the vacuum permeability, g is the electron g-factor, μ_B is the Bohr magneton, $\hbar$ is the reduced Planck constant, $\langle r \rangle = 0.55\,[\mathrm{N}_s^0]^{-1/3}$ is the average spacing between bath spins as a function of concentration (in parts-per-million), and a is a factor of order unity collecting additional factors that need to be considered in the dipolar estimate such as the angular dependence and spin resonance lineshape of the ensemble [95]. A sample with $[\mathrm{N}_s^0] = 1\,\mathrm{ppm}$ therefore has an estimated $T_2^*\{\mathrm{SQ}\} \approx 1/(2\pi \times 9.2\,\mathrm{kHz}) = 17.5\,\mu\mathrm{s}$.

This dipolar estimate is roughly a factor of two larger than the experimentally established scaling. This is qualitatively reasonable since the dipolar estimate does not appropriately capture the contribution of single NV$^-$ centers with a paramagnetic defect much closer than the average spacing to the overall ensemble T_2^* as described in Ref. [74] and supported by simulations of NV$^-$ ensemble T_2^* [72].

For the ^{13}C contribution, analytical and experimental measurements suggest $A_{^{13}\mathrm{C}} \approx 0.1\,\mathrm{ms^{-1}ppm^{-1}}$ such that the estimate for $T_2^*\{^{13}\mathrm{C}\}$ with $[^{13}\mathrm{C}] \approx 10700\,\mathrm{ppm}$ ($\approx$1.1%) is approximately 1µs. The dephasing times extracted for the three samples discussed will be compared to the expectations based on these estimates.

Sample	[N] (ppm)	^{13}C (%)	$T_2^*\{\text{SQ}\}$ (μs)	$T_2^*\{\text{DQ}\}$ (μs)	$T_2^*\{\text{N}_s^0\}$ (μs)	$T_2^*\{^{13}\text{C}\}$ (μs)	$T_2^*\{\text{N}_s^0,^{13}\text{C}\}$ (μs)
3B	$\lesssim 0.05$	0.01	$5-12$	34(2)	350	100	78
3C	0.75	0.01	$1-10$	6.9(5)	23	100	19
3D	10	$<$0.005	$0.3-1.2$	0.60(2)	2	20	2

Table 3.1: **Characteristics of Samples 3B, 3C, and 3D.** Estimated T_2^* values are calculated using the contributions of ^{13}C and N_s^0 as described in the main text. Reasonable agreement is found between the estimated $T_2^*\{\text{N}_s^0,^{13}\text{C}\}$ and twice the measured $T_2^*\{\text{DQ}\}$, consistent with the twice faster dephasing in the DQ basis for all three samples.

The measurements presented in this section utilized a setup similar to the one discussed previously (see Fig. 3.7(a)); however, the diameter of the optical excitation beam waist and input optical power were reduced to a diameter of about 10 μm and 250 mW, respectively. In addition, when measurements of the dephasing time and decay shape are used to study dephasing mechanisms internal to the diamond, careful attention must be paid to ensure T_2^* is not limited by external contributions such as applied magnetic field gradients or temperature drift while averaging a measurement. For this reason, the diametrically-opposed Samarium Cobalt ring magnets depicted in Fig. 3.7 were explicitly designed to sufficiently minimize magnetic field gradient contributions across the samples considered here. Appendix B provides further discussion and simulations of the magnetic field produced by these magnets.

3.5.1 Low Nitrogen Regime

Experiments on Sample 3B ($[N] \lesssim 0.05$ ppm, ^{14}N) probed the low nitrogen density regime where other dephasing mechanisms are significant contributions to the ob-

served Ramsey decay. In different regions of this diamond, the measured SQ Ramsey dephasing time varies between $T^*_{2,SQ} \simeq 5 - 12\,\mu$s, with $1 < p < 2$. Strikingly, even the longest measured $T^*_{2,SQ}$ is $\sim 30\times$ shorter than the estimated $T^*_2\{N^0_s\}$ calculated using the total nitrogen concentration, [N], of the sample ($\gtrsim 350\,\mu$s, see Table 3.1) and $\sim 10\times$ smaller than the expected SQ limit due to 0.01% ^{13}C spins ($\simeq 100(7)\,\mu s$). This discrepancy suggests that dipolar broadening due to paramagnetic spins is not the dominant NV$^-$ ensemble dephasing mechanism. Instead, the spatial variation in $T^*_2\{\mathrm{SQ}\}$, decay shape parameter $p \neq 1$, and low concentration of nitrogen and ^{13}C spins together suggest that crystal stress inhomogeneity is the main source of NV spin ensemble dephasing in this sample.

Measurements in the DQ basis further support this assessment. Fig. 3.8 shows data for T^*_2 in both the SQ and DQ bases for an example region of Sample 3B with SQ dephasing time $T^*_2\{\mathrm{SQ}\} = 5.8(2)\,\mu$s and $p = 1.7(2)$. In the DQ basis, we find $T^*_2\{\mathrm{DQ}\} = 34(2)\,\mu$s with $p = 1.0(1)$, which is a $\sim 6\times$ improvement over the measured $T^*_2\{\mathrm{SQ}\}$. We observed similar $T^*_2\{\mathrm{DQ}\}$ in other regions of this diamond; independent of the measured $T^*_2\{\mathrm{SQ}\}$. Furthermore, the decay shape parameter in the DQ sensing basis is consistently $p = 1$. The difference between the measured $T^*_2\{\mathrm{SQ}\}$ and $T^*_2\{\mathrm{DQ}\}$, yields an estimate for the typical axial-stress-gradient contribution of $\sim 0.15\,\mu\mathrm{s}^{-1}$ ($\sim$24 kHz). If using a Ramsey-based sequence for magnetic sensing (free precession interval $\tau \approx T^*_2$), the $\sim 6\times$ increase in $T^*_2\{\mathrm{DQ}\}$ compared to $T^*_2\{\mathrm{SQ}\}$ provides an expected relative sensitivity improvement of at least $5\times$ given $\sqrt{\mathrm{T}^*_2\{\mathrm{DQ}\}/T^*_2\{\mathrm{SQ}\}} \approx 2.5$ and twice faster phase accumulation in the DQ basis.

The measured $T^*_2\{\mathrm{DQ}\}$ and p values in Sample 3B are consistent with the com-

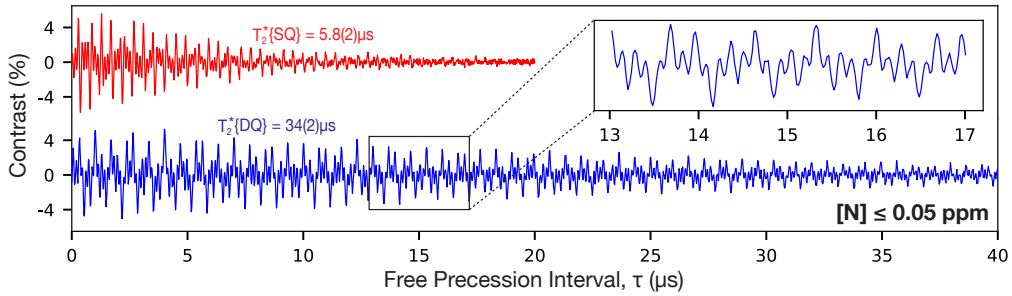

Figure 3.8: **SQ and DQ Ramsey free induction decay for Sample 3B.** Comparison of Ramsey fringe measurements for Sample 3B ([N]$\leq$ 0.05 ppm) in the SQ (red) and DQ (blue) sensing bases for a single location on the diamond sample. Inset: Zoomed view of the time-domain signals. Applied bias magnetic field is aligned with a single NV$^-$ orientation ($B_z = 2\,\mathrm{mT}$).

bined effect of NV dipolar interactions with (i) the 0.01 % concentration of ^{13}C nuclear spins ($T_2^*\{^{13}\mathrm{C}\}/2 \simeq 50\,\mu\mathrm{s}$) and (ii) residual nitrogen spins $[N] \sim 0.05\,\mathrm{ppm}$ ($T_2^*\{^{13}\mathrm{C}\}/2 \simeq 175\,\mu\mathrm{s}$). Using Eqn. 3.22 to estimate the combined electronic and nuclear spin bath T_2^*-limit, yields an expected $T_2^*\{\mathrm{DQ}\}$ of $\approx 39\,\mu\mathrm{s}$. These results suggest that in the low nitrogen density regime, dipolar interactions with the ^{13}C nuclear spin bath can be a major dephasing mechanism when DQ basis measurements are employed to remove strain and temperature effects. Consequently, diamond samples with greater isotopic purity (^{12}C$>$ 99.99%) would likely yield further enhancements in $T_2^*\{\mathrm{DQ}\}$ (in the absence of other dephasing mechanisms).

3.5.2 Intermediate Nitrogen Regime

Although Sample 3C ($[N] = 0.75\,\mathrm{ppm}$, ^{14}N) contains more than an order of magnitude higher nitrogen spin concentration than Sample 3B ($[N] \lesssim 0.05\,\mathrm{ppm}$), we observed SQ Ramsey dephasing times $T_{2,SQ}^* \simeq 1 - 10\,\mu\mathrm{s}$ in different regions of Sample 3C, which are similar to the results from Sample 3B. This suggests that, once again,

stress inhomogeneities contribute significantly to NV$^-$ ensemble dephasing in Sample 3C. However, comparative measurements of T_2^* in both the SQ and DQ bases yield a more moderate increase in $T_{2,DQ}^*$ for Sample 3C than for Sample 3B. Ramsey fringe measurements for a single location in Sample 3C are displayed in Fig. 3.9(a), showing $T_2^*\{\mathrm{SQ}\} = 1.80(6)\,\mu\mathrm{s}$ in the SQ basis increasing to $T_2^*\{DQ\} = 6.9(5)\,\mu\mathrm{s}$ in the DQ basis, a $\sim 4\times$ extension. For these measured values of $T_2^*\{SQ\}$ and $T_2^*\{\mathrm{DQ}\}$, magnetic sensing using the double quantum basis would yield modest improvements in the relative magnetic sensitivity of at least $4\times$. The observed $T_2^*\{\}$ in Sample 3C is approximately consistent with the expected limit set by the average dipolar coupling of NV spins to electronic nitrogen spins in the diamond ($T_2^*\{\mathrm{N}_s^0\}/2 \simeq 12(\,\mu\mathrm{s})$, but is still well below the expected DQ limit due to 0.01 % ^{13}C nuclear spins ($\simeq 50\,\mu\mathrm{s}$).

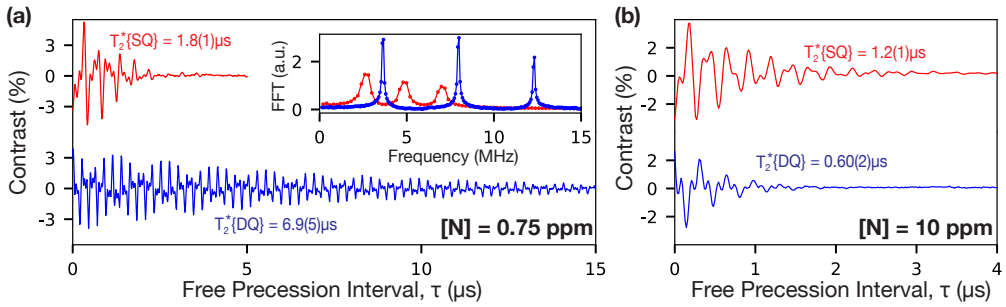

Figure 3.9: **SQ and DQ Ramsey free induction decay for Samples 3C and 3D. (a)** Comparison of Ramsey fringe measurements for Sample 3C ([N]= 0.75 ppm) using the SQ (red) and DQ (blue) sensing bases for a single location on the diamond sample. Inset: Fourier transform of time-domain signals. The doubled ^{14}NV hyperfine splitting in the DQ data is due to the effectively doubled gyromagnetic ratio. The applied bias magnetic field is aligned with a single NV orientation ($B_0 = 8.5\,\mathrm{mT}$). **(b)** Comparison of measurements for Sample 3D ([N]= 10 ppm) for the SQ (red) and DQ (blue) sensing bases for a single location on the diamond sample. The applied bias magnetic field is aligned with a single NV orientation ($B_0 = 8.5\,\mathrm{mT}$).

3.5.3 High Nitrogen Regime

Exemplary measurements of the Ramsey signal for Sample 3D are shown in Fig. 3.9(b). The observed values for $T_2^*\{\mathrm{SQ}\}$ across the sample range from $0.3 - 1.2\,\mu\mathrm{s}$ with $p = 0.9 - 2$; while $T_2^*\{\mathrm{DQ}\}$ was consistently $0.60(2)\,\mu\mathrm{s}$ with $p = 1.0(1)$. In this sample, the DQ dephasing time $T_2^*\{\mathrm{DQ}\}$ is approximately one-half the maximum observed $T_2^*\{\mathrm{SQ}\}$ as expected for magnetic spin-bath-dominated dephasing where the doubled effective gyromagnetic ratio of the DQ sensing basis results in twice the dephasing rate. Nonetheless, even in the regime where $T_2^*\{\mathrm{SQ}\}= T_2^*\{\mathrm{DQ}\}/2$, the DQ sensing basis offers an improvement in relative magnetic sensitivity of up to $\sqrt{2}$: In DQ sensing basis, the same amount of phase is accumulated in half the time compared to the SQ basis such that in the limit of $T_2^* \gg \tau_{\mathrm{read,init}}$ the measurement bandwidth is doubled.

3.5.4 Outlook

Although the concentration of incorporated nitrogen varies by over two order of magnitudes for the three samples evaluated, we find that stress-gradients across tens of microns dominate dephasing in the lower and intermediate [N] samples and, for many locations in the highest [N] sample, at least contribute similarly to the spin-bath-induced dephasing. This result emphasizes the outstanding need to minimize the introduction of crystal stress inhomogeneity during CVD synthesis - typically introduced by imperfections of the substrate surface upon which N-doped diamond is grown. The heterogeneity in $T_2^*\{\mathrm{SQ}\}$ both within a sample and between different samples also impacts reproducibility and scalabilty of NV-diamond technologies: If

the location of laser spot shifts on the sample or one sample is exchanged for another, ultimately the DC magnetic sensitivity can vary dramatically due to the non-uniform stress-gradient environment. Chapter 6 discusses recent advances to reliably produce material with low stress-inhomogeneity. In the meantime, by suppressing these stress-gradient contributions, the DQ sensing basis yields $T_2^*\{\mathrm{DQ}\} > T_2^*\{\mathrm{SQ}\}/2$ and the associated improvements in relative sensitivity. Crucially, this all enables consistent performance across a sample and between samples despite the underlying stress inhomogeneity.

The dominant role of the N_s^0 spin bath in determining $T_2^*\{\mathrm{DQ}\}$ for samples 3C and 3D is further supported in Chapter 5, where experiments controlling the N_s^0 baths spins, and the effect on the NV^- ensemble T_2^* are discussed. Based on these results, the $T_2^*\{\mathrm{DQ}\}$ measurements presented in this section for Samples 3C and 3D are used to determine the experimental scaling in Chapter 2 (in addition to similar measurements on other samples). Sample 3B is excluded since we believe the nuclear spin bath contributes significantly to the observed $T_2^*\{\mathrm{DQ}\}$.

Throughout this discussion, we have purposefully used samples with low concentrations of NV^- in order to simplify the underlying spin bath and avoid processing that would introduce additional variability in the sample properties such as electron irradiation and annealing. While Chapter 2 discusses how $[\mathrm{NV}^-]$ contributes to T_2^*, experimental results are presented in Chapters 5 and 6.

Chapter 4

Magnetic Microscopy using a Double Quantum 4-Ramsey Protocol

This chapter describes wide-field, Ramsey-based magnetic imaging experiments which leverage the double quantum (DQ) 4-Ramsey protocol introduced in the previous chapter to overcome multiple challenges hindering the performance of NV-diamond magnetic microscopes. First, as discussed in Chapter 3, Ramsey-based magnetometry, by separating the sensing interval from the NV control and readout steps, offers superior magnetic sensitivity compared to the continuous-wave (CW) and pulsed optically detected magnetic resonance (ODMR) techniques typically used in NV-diamond magnetic imaging applications.

Second, the robustness of DQ magnetometry to axial stress inhomogeneity in the host diamond crystal is particularly advantageous in imaging modalities. The pernicious effects of the micron to millimeter scale stress-gradients common in NV-diamond samples are multi-fold. These gradients result in degraded and inhomogeneous mag-

netic sensitivity across a field of view as well as conflate non-magnetic stress variations with the magnetic signals on interest, which impacts dynamic range requirements and complicates analysis. DQ-based magnetic imaging protocols addresses both of these challenges simultaneously.

The DQ 4-Ramsey protocol, which is implemented in hardware using a pixel-by-pixel lock-in camera, provides a homogeneous, median volume-normalized sensitivity of η^V of $38\,\mathrm{nT\mu m^{3/2}Hz^{-1/2}}$ per pixel across a $125\mu\mathrm{m} \times 125\,\mu\mathrm{m}$ field of view with sub-millisecond temporal resolution. The technical advances outlined in this chapter lay the foundation for future work imaging dynamic, broadband magnetic sources such as integrated circuits and electrically active cells.

4.1 Motivation

The combination of magnetically-sensitive spin resonances, all-optical spin-state preparation and readout under ambient conditions, and the ability to engineer dense nanometer to micron-scale layers of defects [2, 40] makes ensembles of NV^- centers particularly advantageous for wide-field magnetic microscopy of physical and biological systems with micrometer-scale spatial resolution — a modality known as the quantum diamond microscope (QDM) [24]. QDM applications to date include imaging magnetic fields from remnant magnetization in geological specimens [16], domains in magnetic memory [25], iron mineralization in chiton teeth [26], current flow in graphene devices [27, 28] and integrated circuits [17], populations of living magnetotactic bacteria [29], and cultures of immunomagnetically labeled tumor cells [30].

Despite this progress, QDM magnetic imaging applications have been largely

restricted to mapping of static magnetic fields exceeding several microtesla due to shortcomings of conventional single quantum (SQ) magnetometry. SQ schemes employ the $|0\rangle$ and either of the $|\pm1\rangle$ NV sublevels, e.g., optically-detected magnetic resonance (ODMR). In particular, the sensitivity of QDMs using continuous wave (CW) ODMR is impaired by competing effects of the optical and microwave (MW) control fields applied during the sensing interval [2, 24]. Pulsed-ODMR schemes, which separate the optical spin-state readout and preparation from the MW control and sensing interval, offer improved sensitivity, but cannot exceed the performance achievable with SQ Ramsey magnetometry [2].

Furthermore, any SQ magnetometry scheme is vulnerable to diamond crystal stress inhomogeneities and temperature variations, which shift and broaden the NV^- spin resonances. Stress-gradients are particularly pernicious for SQ QDM applications, with typical gradient magnitudes comparable to NV^- resonance linewidths $(0.1-1\,\mathrm{MHz})$ and spatial structure spanning from sub-microns to millimeters [38]. Stress-induced resonance shifts or broadening may be mistaken for magnetic signals of interest. Stress gradients can also degrade per-pixel sensitivity and sensitivity homogeneity across an image. While protocols such as sequentially sampling the ODMR spectrum at multiple frequencies [16] or employing four-tone MW control [67, 68] can separate magnetic and non-magnetic signals, the degraded, inhomogeneous magnetic sensitivity caused by stress-gradients remains unaddressed.

Here, we demonstrate a double quantum (DQ) Ramsey imaging protocol that overcomes the shortcomings of SQ CW- and pulsed-ODMR measurement techniques. By temporally separating the spin state control, optical readout, and sensing intervals,

Ramsey schemes are compatible with increased laser and MW intensity for improved measurement contrast and higher fluorescence count rates without broadening the NV^- spin resonances. Furthermore, by leveraging a DQ superposition of the m_s=$|\pm 1\rangle$ ground-state sublevels in combination with an applied bias magnetic field, DQ Ramsey-based magnetic imaging is immune to stress-induced resonance shifts and broadening [73, 79, 80, 119]. Therefore, DQ Ramsey-based schemes can disentangle magnetic and non-magnetic signals while also enabling improved, homogeneous per-pixel magnetic sensitivity across an image.

To date, the implementation of DQ Ramsey magnetic imaging has been hindered by the technical challenge of producing sufficiently uniform, strong MW fields to avoid spatially-varying errors in MW pulse duration and hence NV measurement protocol. Such pulse errors result in residual SQ coherence that remains sensitive to common-mode shifts of the $|\pm 1\rangle$ sublevels, degrading the robustness of DQ magnetometry to stress-induced shifts and temperature drifts.

In the present work, we circumvent this challenge by employing the DQ 4-Ramsey protocol described in Chapter 3 (Sec. 3.4.1), which suppresses residual SQ signal. By properly selecting the spin-1 rotations applied in four consecutive Ramsey measurements (4-Ramsey), the DQ signal from each Ramsey measurement is preserved while the residual SQ signals cancel. This scheme is broadly applicable to both NV^- ensemble imaging and bulk sensing modalities where robustness to temperature-induced drifts is often critical [19, 31, 114]. The 4-Ramsey measurement protocol is described in detail and demonstrated in a non-imaging modality in the previous chapter (Sec. 3.4.1)

The present chapter describes the experimental demonstration of Ramsey-based magnetic imaging utilizing the 4-Ramsey protocol. After describing the experimental apparatus in Sec. 4.2, SQ and DQ Ramsey fringe imaging is used to characterize, pixel by pixel, the reduced spatial variation in T_2^* and NV$^-$ resonance frequency when using the DQ sensing basis for a particular sample (Sample 3A) in Sec. 4.3. Using the same field of view, we then measure a 1.5× improved median per-pixel sensitivity and a 4.7× narrower spatial distribution of sensitivity using the the DQ sensing basis compared to the SQ basis (Sec. 4.4). Finally, in Sec. 4.5 next steps to further improve DC magnetic sensitivity and temporal resolution are highlighted along with a discussion of envisioned applications for high-sensitivity, broadband magnetic microscopy using the DQ 4-Ramsey protocol.

4.2 Experimental Methods

The measurement presented in this chapter employed a QDM to image spin-state-dependent fluorescence from a 1-micron-thick nitrogen-doped CVD diamond layer ($[\mathrm{N_{total}}] \approx 20\,\mathrm{ppm}$, $^{12}\mathrm{C} = 99.995\%$, natural abundance nitrogen) grown by Element Six on a $(2 \times 2 \times 0.5)\,\mathrm{mm}^3$ high purity diamond substrate (Sample 3A). Post-growth treatment via electron irradiation and annealing increased the NV$^-$ concentration in the nitrogen-doped layer to $\approx 2\,\mathrm{ppm}$. The magnitude and distribution of stress inhomogeneity in Sample 3A is representative of typical diamonds fabricated for NV-based magnetic imaging (see Refs. [38, 61] for additional examples).

An approximately 150µm by 300µm region of the NV layer is illuminated with 1 W of 532nm laser light in a total internal reflection (TIR) geometry (see Fig. 4.1(a,b));

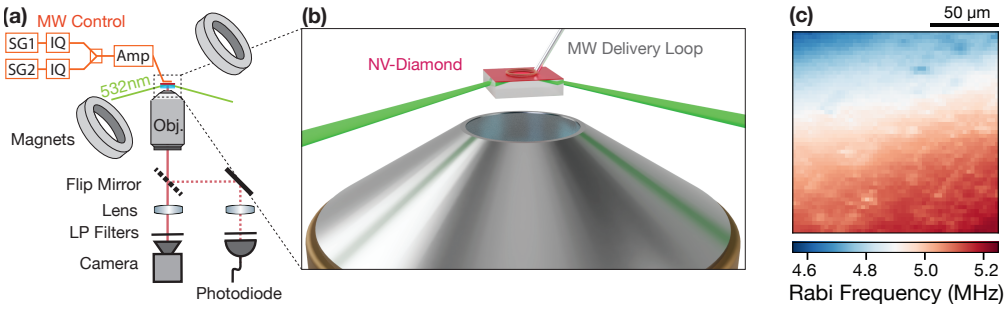

Figure 4.1: **Experimental Apparatus and Rabi Imaging. (a)** Apparatus overview including 532nm excitation of a micron-scale layer of NV centers in a macroscopic diamond chip, using total internal reflection (TIR). Fluorescence is collected using a 20x objective onto a camera or photodiode. 647 nm and 532 nm long-pass (LP) optical filters partially isolate NV^- fluorescence from background NV^0 fluorescence. MW control fields are synthesized using two signal generators with phase control on both tones and applied via a millimeter-scale shorted coaxial loop. A bias magnetic field of 5mT is aligned with NV centers oriented along a single crystallographic axis. **(c)** Image of the typical NV^- Rabi frequency variation across the 125μm×125μm field of view in this work. The effect of inhomogeneous, stress-induced NV^- resonance shifts on the Rabi frequency are visible in addition to a quasi-linear Rabi gradient due to spatial variation in the MW amplitude.

and the associated NV^- fluorescence is collected onto either a Heliotis heliCam C3 camera.

The heliCam C3 operates by subtracting alternating exposures in analog and then digitizing the background-subtracted signal, enabling the detected magnetic field information to fill each pixel's 10-bit dynamic range. Each frame from the camera contains the accumulated difference signal for multiple exposure pairs. The device is capable of operating at internal lock-in frequencies (exposure rates) of up to 250 kHz ($\approx$ 30 kHz in this work) and a maximum external frame rate of 3.8 kHz (1.25 kHz in this work). The lock-in frequency was defined by a user-input demodulation signal (square wave) with each demodulation cycle broken into four quarters. The exposures from the first and third quarters subtract to produce an in-phase signal on the camera's I channel. Similarly, the exposures from the second and fourth quarters subtract to produce a quadrature signal on the camera's Q channel. The output from the camera consists of these two images per frame.

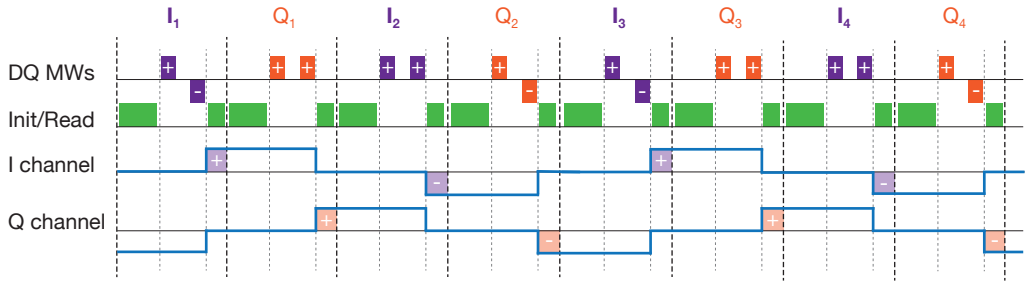

Figure 4.2: **Schematic of the DQ 4-Ramsey protocol** synchronized with the heliCam C3 lock-in camera. Two 4-Ramsey protocols (orange and purple pulses) are interwoven to generate images on the I and Q channels. The camera exposures (shaded regions on the I and Q channels) are chosen to be blind to fluorescence from the optical initialization pulses. The free precession interval duration is chosen to be approximately $T_2^* \approx 1\mu s$. The initialization and readout pulse durations are 4µs in total.

Figure 4.2 depicts the implementation of pulsed NV readout using the heliCam across two demodulation cycles (of the N demodulation cycles used to produce an I and Q image). The MW and optical control pulses are synchronized with the camera's I and Q exposures. Two 4-Ramsey protocols are interleaved such that both the I and Q channels produce images containing only DQ magnetic signal. The MW pulse phases for the Q channel are chosen such that the Q channel contains the negative magnetic signal compared to the I channel image. S_I is then subtracted from S_Q to yield a single image per frame.

To generate the MW control fields, two signal generators, an Aglient E9310A with built-in IQ modulation and a Windfreak SynthHD signal generator in combination with an external Marki-1545LMP IQ mixer, provide the two-tone MW control fields and requisite phase control employed in this work.

The DQ 4-Ramsey protocol is particularly critical in wide-field imaging applications where spatial gradients in the applied MW control fields result in varying Rabi frequencies and ultimately residual SQ coherence since only global MW pulses can be applied. Fig. 4.1(c) depicts the Rabi gradient for a mm-scale shorted coaxial loop. Although the spatial properties of the applied MW field depend upon setup-specific MW synthesis and delivery approaches, the $\pm 4\%$ ($\pm 200\,\mathrm{kHz}$ gradient on top of an average $\Omega_{\mathrm{avg}} = 5\,\mathrm{MHz}$) shown in Fig. 4.1(c) is typical.

The hyperfine splitting and stress-induced shifts of the NV^- resonances can also introduce MW pulse errors as a result of the detuning dependent effective Rabi frequency, particularly for the naturally abundant ^{14}N ($I = 1$) isotope where any single-tone MW field is detuned from at least two of the three hyperfine split resonances.

The effective Rabi frequency is given by $\Omega_{eff} = \sqrt{\Omega^2 + \Delta^2}$ where Ω is the on-resonance Rabi frequency and Δ is the detuning from a particular hyperfine resonance. In this work, the hyperfine splitting ($\Omega_{\text{avg}} = 5\,\text{MHz}$, $\Delta \approx 2.2\,\text{MHz}$) results in an effective Rabi frequency of $\Omega_{eff} = 5.46\,\text{MHz}$ for the two detuned hyperfine resonances ($m_I = \pm 1$). The resulting pulse error is approximately double that imposed by the Rabi gradient of $\pm 200\,\text{kHz}$. However, these hyperfine-induced pulse errors are uniform across the field of view. In addition, stress-induced shifts of the NV^- resonances can spatially modulate the effective Rabi frequency. The measured absolute pixel-to-pixel spread in the NV^- resonance frequencies due to stress-gradients is $\approx 300\text{kHz}$. However, the effective Rabi frequency resulting from a 300kHz stress-induced shift varies from $\Omega_{\text{avg}} = 5\,\text{MHz}$ by about 10 kHz, significantly smaller than the other two sources of errors described above.

Techniques to mitigate hyperfine- and stress-induced pulse errors include increasing the MW Rabi frequency, implementing pulse envelope shaping, or operating equally detuned from the two hyperfine split resonances of isotopically-purified ^{15}N ($I = 1/2$). All three of these directions present challenges, adding experimental complexity or requiring changes to the CVD synthesis process.

4.3 Ramsey Free Induction Decay Fringe Imaging

This section describes the use of SQ 2-Ramsey and DQ 4-Ramsey free induction decay (FID) measurements to image the NV^0 ensemble spin properties relevant for DC magnetic field sensitivity across a 125µm by 125µm field of view in Sample 3A. The photon-shot-noise-limited sensitivity of a Ramsey-based measurement η_{ramsey} depends

upon the NV$^-$ ensemble dephasing time T_2^*, the contrast C, and the average number of photons collected per measurement N [2]:

$$\eta_{\text{ramsey}} = \frac{1}{\gamma}\frac{1}{\Delta m}\frac{1}{C\mathrm{e}^{-(\tau/T_2^*)^p}\sqrt{N}}\frac{\sqrt{\tau + t_{r,i}}}{\tau} \tag{4.1}$$

where Δm accounts for the difference between the m_s states utilized for the sensing basis ($\Delta m = 1, 2$ for the SQ, DQ sensing bases), τ is the free precession interval per measurement, p describes the decay shape, and $t_{r,i}$ indicates the duration of time dedicated to readout/initialization per measurement. The optimal free precession interval is determined by the NV$^-$ dephasing time T_2^*, which is proportional to the inverse of the natural linewidth Γ ($T_2^* = 1/\pi\Gamma$ assuming a Lorentzian lineshape). Axial stress-gradients within a pixel degrades η_{ramsey} by decreasing T_2^*; while stress-induced resonance shifts between pixels worsen η_{ramsey} by shifting the optimal applied MW frequency for maximum magnetic sensitivity and introducing spatially-varying, non-magnetic offsets in the Ramsey signal that can complicate data analysis [38].

We imaged the NV$^-$ ensemble spin properties by sweeping the free precession time in the SQ and DQ Ramsey sequence and fitting the resulting fringes to a sum of oscillations with a common decay envelope:

$$S_{\text{ramsey}}(\tau) = \mathrm{e}^{-\tau/T_2^*}\sum_{i=m_I} A_i \sin(2\pi f_i + \delta_i) \tag{4.2}$$

where each oscillatory term, indexed by $m_I = \{-1, 0, 1\}$ (for an ^{14}N ensemble), has an amplitude A_i, frequency f_i, phase shift δ_i, and the decay shape is fixed to $p = 1$. A purposeful detuning of 3 MHz from the resonance corresponding to the $m_I = 0$

hyperfine population was introduced in order to more easily extract all three frequencies and the decay envelope. Eqn. 4.2 was rapidly fit to the data pixel-by-pixel using open source, GPU-accelerated non-linear least-squares fitting software, GPUfit [120].

Dephasing times – The extracted T_2^* values for the SQ and DQ sensing bases are shown in Fig. 4.3(a,b) as images and plotted as a histogram in Fig. 4.3(c). To quantify the spread in T_2^* values, we report the median value and the relative inter-decile range (RIDR):

$$\text{RIDR} = \frac{D_{90} - D_{10}}{(\text{median})} \tag{4.3}$$

where 80% of the measured values fall between the first decile D_{10} and ninth decile D_{90}. In Fig. 4.3(a), the extracted $T_2^*\{\text{SQ}\}$ values have a median of 0.910 (0.710,1.03)µs, where the values in parentheses correspond to the deciles (D_{10}, D_{90}). As shown in Tab. 4.1, the calculated RIDR for the extracted $T_2^*\{\text{SQ}\}$ values is 35%. We attribute the spatially-correlated variations in $T_2^*\{\text{SQ}\}$ to axial stress gradients within pixels [38, 73]. The observed stress features are likely due to polishing-induced imperfections in the substrate surface upon which the NV^- ensemble layer was grown [61].

Invulnerable to within-pixel stress gradients, the measured $T_2^*\{\text{DQ}\}$ values are 5.6× more uniform than the $T_2^*\{\text{SQ}\}$ values with a median of 0.620 (0.605,0.643) µs and an RIDR of 6.0%. Additionally, the median $T_2^*\{\text{DQ}\}$ is approximately one half the longest measured $T_2^*\{\text{SQ}\}$, 1.15(3) µs, as expected when stress-induced dephasing is negligible and the dominant contribution to T_2^* is dipolar coupling to an electronic spin bath (of predominantly neutral substitutional nitrogen) [73].

Fringe frequencies – Figures 4.3(d-f) display the extracted SQ and DQ Ramsey fringe frequencies associated with the detuning of the applied MW pulses from the

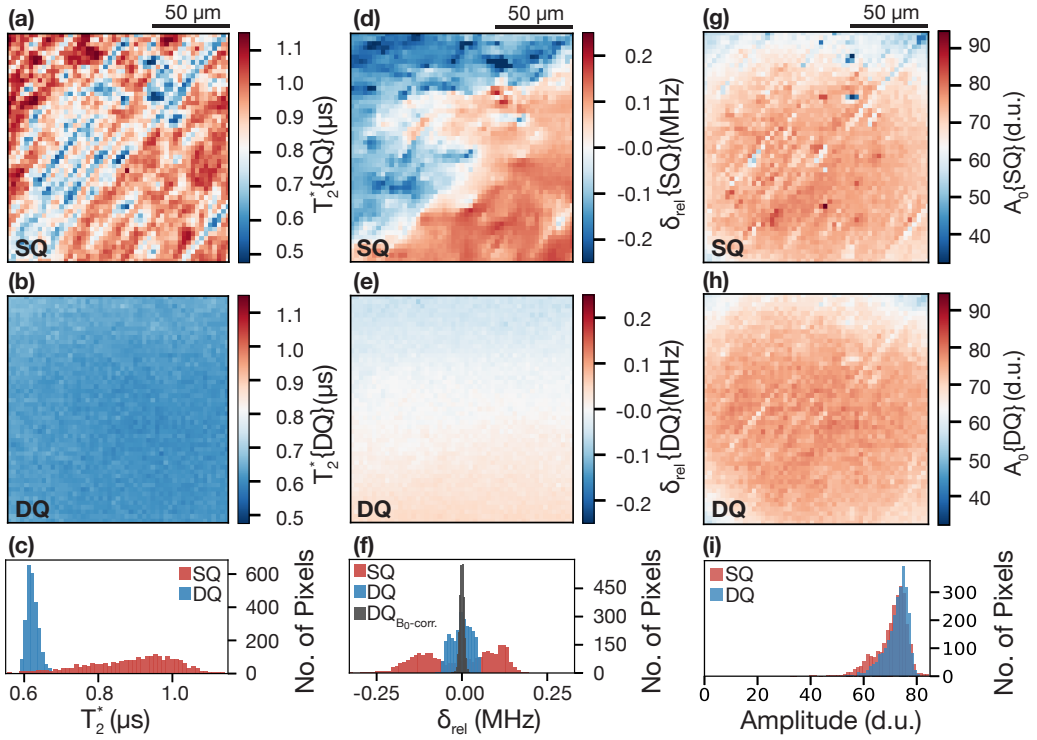

Figure 4.3: **Imaging NV⁻ Ensemble Spin Properties.** **(a)** Image of the single quantum (SQ) T_2^* extracted by fitting the SQ 2-Ramsey fringe decay to Eqn. 4.2. Spatial variations in $T_2^*\{\text{SQ}\}$ are due to stress-induced broadening of the NV⁻ resonances within the 3-dimensional volume imaged onto a pixel. **(b)** Image of $T_2^*\{\text{DQ}\}$ measured using the DQ 4-Ramsey protocol across the same field of view as shown in (a). In pixels with minimal stress-gradients, the $T_2^*\{\text{DQ}\}$ is half the $T_2^*\{\text{SQ}\}$ as expected. **(c)** Histogram of $T_2^*\{\text{SQ}\}$ and $T_2^*\{\text{DQ}\}$ values from the pixels in (a) and (b). **(d)** Image of the relative SQ resonance shifts $\delta_{\text{rel}}\{\text{SQ}\}$ from the median SQ Ramsey fringe frequency. Variations in $\delta_{\text{rel}}\{\text{SQ}\}$ are attributed to axial-stress-induced shifts of the NV⁻ resonance frequencies between pixels. **(e)** Image of the relative DQ detuning $\delta_{\text{rel}}\{\text{DQ}\}$ across the same field of view as (a, b, d). The axial-stress-induced shifts apparent in (c) are mitigated. Inhomogeneity in the magnitude of the applied bias magnetic field B_0 results in a residual gradient of less than 40kHz. **(f)** Histogram of the extracted SQ and DQ δ_{rel} values from the pixels in (d) and (e). The distribution of DQ δ_{rel} values with the setup-specific B_0-gradient contribution corrected is shown in grey. **(g)** Image of the SQ Ramsey fringe amplitude $A_0\{\text{SQ}\}$ corresponding to the spin transition associated with the $m_I = 0$ nuclear spin state in digital units (d.u.) as reported by the heliCam. **(h)** Image of the DQ Ramsey fringe amplitude $A_0\{\text{DQ}\}$ corresponding to the spin transition associated with the $m_I = 0$ nuclear spin state in digital units (d.u.) as reported by the heliCam. **(i)** Histogram of the extracted SQ and DQ Ramsey fringe amplitudes from the pixels in (g) and (h).

	SQ		DQ	
	$\tilde{x}$ (D_{10}, D_{90})	RIDR	$\tilde{x}$ (D_{10}, D_{90})	RIDR
Dephasing Time, T_2^* (µs)	0.907 (0.710, 1.03)	35%	0.621 (0.605, 0.643)	6.0%
Fringe Freq., f_0 (MHz)	3.09 (2.94, 3.22)	9.2%	6.00 (5.96, 6.04)	1.3%
Fringe Freq., f_0 (B_0-corr.) (MHz)	3.10 (2.95, 3.21)	8.2%	6.00 (5.99, 6.01)	0.27%
Fringe Amplitude, A_0 (d.u.)	72.1 (61.8, 76.6)	21%	73.5 (66.5, 77.0)	14%

Table 4.1: **Median extracted fit parameters ($\tilde{x}$) using Eqn. 4.2 for the SQ and DQ Ramsey images shown in Fig. 4.3.** The lower and upper deciles, D_{10} and D_{10} are given in parentheses (80% of the pixels exhibit values between D_{10} and D_{90}). The SQ and DQ relative inter-decile ranges (RIDR) calculated using Eqn. 4.3 are included.

spin transition frequency for the $m_I = 0$ hyperfine population. The relative detuning δ_{rel} from the median Ramsey fringe frequency f_0 is shown in Figures 4.3(d-f) to highlight the inhomogeneity across the field of view. The median SQ fringe frequency, $f_0\{SQ\}$, is 3.09 (2.94, 3.22) MHz with a relative spread of 9.2 %. The absolute spread in $f_0\{SQ\}$, $|D_{90}\text{-}D_{10}| = 280$ kHz, is comparable to the median NV^- resonance linewidth and attributed to stress-gradients spanning multiple pixels [38].

The DQ fringe frequencies exhibit a 7x narrower distribution about a median $f_0\{\text{DQ}\}$ of 6.00(5.96,6.04)MHz (RIDR = 1.3 %). Note that the factor of two between the median detunings $f_0\{\text{SQ}\}$ (≈ 3 MHz) and $f_0\{\text{DQ}\}$ (≈ 6 MHz) is consistent with the doubled effective gyromagnetic ratio for the DQ sensing basis. The absolute spread in $f_0\{\text{DQ}\}$ is 3.6× smaller than the spread in $f_0\{\text{SQ}\}$, with the remaining variation dominated by a quasi-linear ≈40 kHz gradient due to residual inhomogeneity in the 5mT applied bias magnetic field. In Fig. 4.3(f), a histogram of the relative shifts $\delta_{\text{rel}}\{DQ\}$ with a linear B_0-gradient contribution subtracted is included in grey and exhibits a reduced RIDR of 0.26%.

Contrast – In the present work, inhomogeneity in the measurement contrast C is largely independent of the choice of sensing basis and attributed to the Gaussian intensity profile of the excitation beam and fixed exposure duration. The extracted amplitudes A_i for the measured Ramsey fringes, which are proportional to C, are reported in digital units (d.u.) of accumulated difference as measured by the heliCam C3. The median amplitudes $A_0\{\mathrm{SQ}\}$ and $A_0\{\mathrm{DQ}\}$, 72.1 (61.8, 76.6) d.u. and 73.5 (66.5, 77.0) d.u., as well as the RIDR (21% and 14%) are comparable and included in Table 4.1 as well as depicted in Fig 4.3(g-i). The residual spread in $A_0\{\mathrm{SQ}\}$ and $A_0\{\mathrm{DQ}\}$ is a consequence of the Gaussian intensity profile of the excitation beam and fixed exposure duration. Shorter length-scale spatial variations (<50µm) in the extracted SQ amplitude $A_0\{\mathrm{SQ}\}$ exhibit a strong correlation with the $T_2^*\{\mathrm{SQ}\}$ and $\delta_{\mathrm{rel}}\{\mathrm{SQ}\}$ images due to strain-gradients decreasing the ODMR contrast and inducing variations in the effective Rabi frequency.

4.4 Magnetic Sensitivity Analysis

In this section, the magnetic sensitivity of the SQ 2-Ramsey and DQ 4-Ramsey protocols is compared across the same field of view imaged in the previous section. The narrower distribution of $T_2^*\{\mathrm{DQ}\}$ and resonance shifts $\delta_{\mathrm{rel}}\{\mathrm{DQ}\}$ for the DQ sensing basis translate into improved, more homogeneous magnetic sensitivity. For both sensing bases, an optimal free precession interval τ and applied MW frequency (or frequencies) f_{AC} was selected to maximize the median NV^- response to a change in magnetic field, dS/dB (see Appendix A). Under these conditions, a series of measurements was collected and used to calculate the magnetic sensitivity pixel-by-pixel.

The magnetic-field sensitivity is defined as $\delta B\sqrt{T}$, where T is the measurement duration and δB is the minimum detectable magnetic field, i.e., the field giving an signal-to-noise ratio (SNR) of 1 [9, 121–123]. A measurement with duration T and sampling frequency $F_s = 1/T$ has a Nyquist-limited single-sided bandwidth of $\Delta f = F_s/2$. When the measurement bandwidth is sampling-rate limited, the noise level of the magnetic-field sensor, σ_B, is given by the standard deviation of a series of measurements such that σ_B is equal to the minimum detectable field δB. Therefore, the sensitivity can be expressed as [31]:

$$\eta = \sigma_B\sqrt{T} = \frac{\sigma_B}{\sqrt{2\Delta f}} \tag{4.4}$$

In the present work, the sampling frequency was determined by the external frame rate of the camera such that $F_s \approx 1.25$kHz (the maximum external frame rate is 3.8kHz). Each frame contained the accumulated difference signal of multiple Ramsey sequences. The standard deviation of each pixel was calculated from 1250 consecutive frames (1s of acquired data) and converted to magnetic field units using the calibration dS/dB determined for each pixel. Although the fixed time required for data transfer from the heliCam (≈ 5 s, neglected in the above analysis) prevents continuous field monitoring at the calculated sensitivity for arbitrarily, the camera's 500-frame buffer still allows sets of high-bandwidth imaging data to be acquired over 0.4 s.

The resulting sensitivities η_{DQ} and η_{SQ} are plotted in Fig. 4.4(a,b). The median DQ 4-Ramsey magnetic per-pixel magnetic sensitivity $\eta_{\mathrm{DQ}} = 16\,(15, 17)\,\mathrm{nT\,Hz^{-1/2}}$ provides a factor of about 1.5× improvement compared to the SQ 2-Ramsey per-pixel magnetic sensitivity, $\eta_{\mathrm{SQ}} = 24\,(20, 36)\,\mathrm{nT\,Hz^{-1/2}}$ with voxel dimensions of $(2.5 \times 2.4 \times$

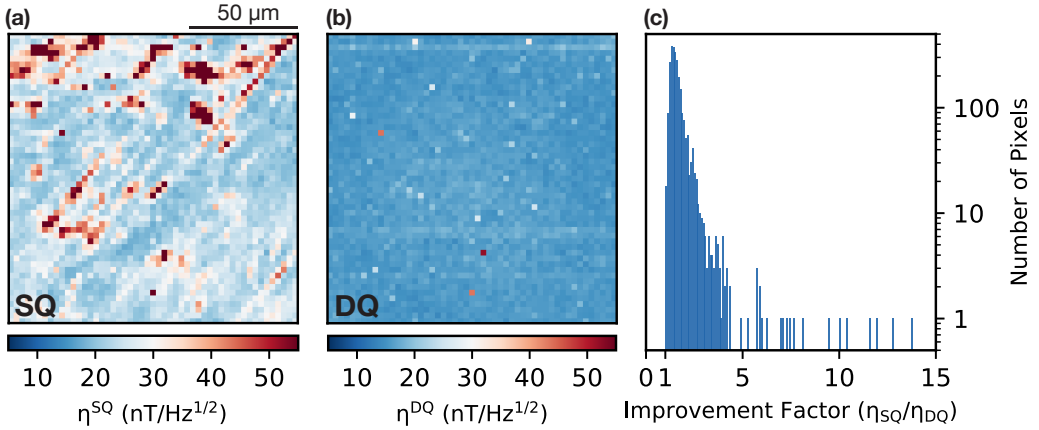

Figure 4.4: **Imaging DC Magnetic Sensitivity.** **(a)** Data acquired with SQ 2-Ramsey protocol when operating at an applied MW field f_{AC} and free precession interval τ that optimize the median per-pixel magnetic sensitivity. **(b)** Data acquired with DQ 4-Ramsey protocol with optimal f'_{AC} and τ, across the same field of view as (a). A few isolated, defective pixels with degraded sensitivity are visible. **(c)** Histogram of the relative sensitivity improvement $\eta_{\mathrm{SQ}}/\eta_{\mathrm{DQ}}$ per pixel.

1) 3μm. The upper and lower deciles, D_{10} and D_{90}, are reported in parentheses. The typical uncertainty in the calculated per-pixel magnetic sensitivity, about 6 %, is dominated by the uncertainty in determining the parameters extracted from fitting the DC magnetometry curve in each pixel. The median volume-normalized sensitivities are therefore $\eta^{\mathrm{V}}_{\mathrm{DQ}} = 38\,(35, 41)\,\mathrm{nT\,Hz^{-1/2}\,\mu m^{3/2}}$ and $\eta^{\mathrm{V}}_{\mathrm{SQ}} = 60\,(47, 85)\,\mathrm{nT\,Hz^{-1/2}\,\mu m^{3/2}}$. We observe about a 4.7× reduction in the RIDR for η_{DQ} ($\approx 14\%$) compared to the RIDR of η_{SQ} ($\approx 67\%$). The improved median sensitivity and reduced spread across the field of view are attributed to the elimination of axial-stress-induced dephasing and resonance shifts for the DQ 4-Ramsey protocol, such that it is possible to operate at the optimal τ and applied MW frequency f_{AC} for an increased fraction of pixels simultaneously.

As illustrated by the histogram in Fig. 4.4(c), all pixels exhibit improved mag-

netic sensitivity in the DQ sensing basis. Order-of-magnitude sensitivity improvements in the DQ basis are seen for the pixels corresponding to regions of diamond with higher stress gradients. In pixels with minimal stress-related effects, the effectively doubled gyromagnetic ratio in the DQ sensing basis enables faster measurements (increased F_s because $T_2^*\{\mathrm{DQ}\}$, and thus the optimal τ, is reduced) for the same phase accumulation, leading to improved magnetic sensitivity. The residual 14% spread in η_{DQ} is largely due to the Gaussian intensity profile of the excitation beam spot - highlighting the potential utility of optical beam-shaping techniques to enable further improvements.

Fig. 4.5(a,b) depict the SQ and DQ DC magnetometry curves measured for fifty pixels randomly sampled across the field of view shown in Fig. 4.4. The magnetometry curves were generated by sweeping the applied single or dual-tone MW pulse frequencies differentially to mimic the Zeeman splitting of the NV^- resonances. The SQ magnetometry curves exhibit dramatic variations in both the maximum slope achievable and the frequency at which the maximum slope occurs. These variations result in the degraded sensitivities depicted earlier in Fig. 4.4.

The Allan deviations calculated using SQ and DQ data from the same fifty pixels selected for Fig. 4.5(a,b) are shown in Fig. 4.5(c,d). While both the SQ and DQ Allan deviations scale with inverse square root of the measurement time as expected for photon-shot-noise-limited measurements, the SQ data exhibits a broader distribution across pixels as a result of inhomogeneous sensitivity to NV^- resonance shifts.

In addition to achieving homogeneous magnetic sensitivity, it is advantageous to produce magnetic images with minimal background features (especially non-magnetic

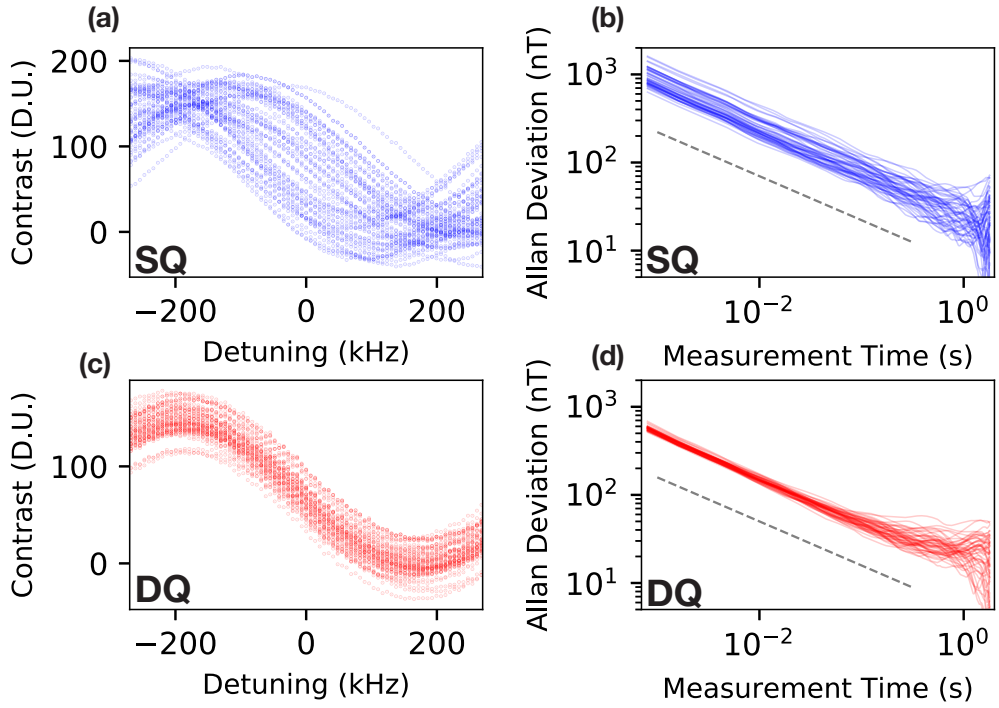

Figure 4.5: **Ramsey magnetometry curves and Allan deviations for 50 randomly selected pixels.** **(a)** SQ Ramsey magnetometry curves for each of the 50 pixels selected. The applied MW pulse frequency was detuned to mimic a magnetic-field-induced shift in the NV- resonance frequency. The variations pixel-to-pixel are a consequence of stress-gradient-induced resonance broadening and shifts. **b** DQ Ramsey magnetometry curves for each of the 50 pixels selected. The applied MW pulse frequencies were detuned differentially to mimic a magnetic-field-induced shift in the NV- resonance frequencies. **(c)** Plot of the Allan deviations calculated using a SQ 2-Ramsey sensing protocol for 50 randomly pixels across the same field of view as (a). **(d)** Plot of the Allan deviations calculated using the DQ 4-Ramsey sensing protocol for the same 50 pixels as depicted in (a). The free precession interval and detuning are optimized for each sensing basis to minimize the median per-pixel magnetic sensitivity. Dashed grey lines indicated a power law scaling proportional to $T^{-1/2}$ as a guide to the eye.

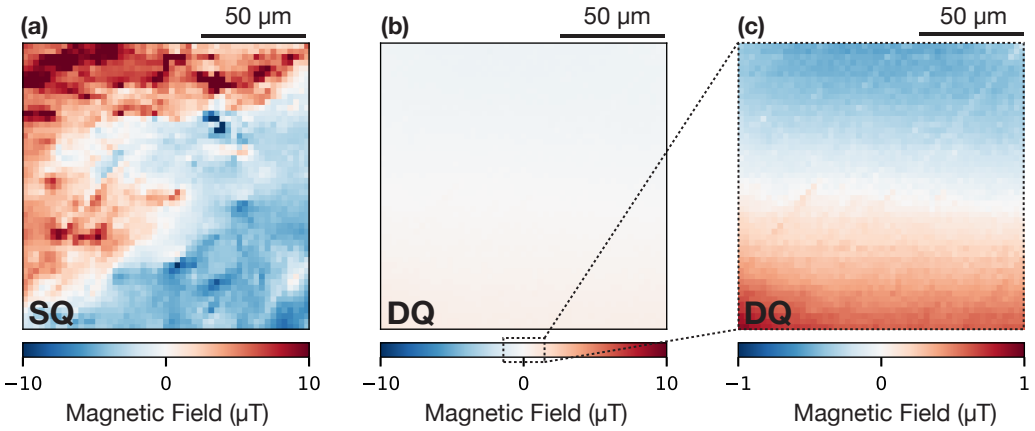

Figure 4.6: **Averaged SQ and DQ images. (a)** Averaged SQ 2-Ramsey and DQ 4-Ramsey images when operating at optimal sensing conditions across the same field of view as shown in Fig. 4.3 and 4.5. (a) SQ image exhibiting 10μT-scale spatial variations due to stress-induced NV resonance shifts. (b) DQ image with reduced spatial variations due to insensitivity to non-magnetic sources. (c) Same data as (b) but with a 10× reduced magnetic field scale to highlight residual spatial variation predominantly correlated with the bias magnetic field, which is aligned along one NV^- axis at an angle of 54.7° relative to the normal to the image plane. The images in (a-c) were produced by averaging 1 s of acquired data.

features) in order to more easily identify small changes in the desired fields on the desired length-scales. Fig. 4.6 compares the magnetic field image produced after acquiring 1 second of data using the SQ 2-Ramsey protocol and DQ 4-Ramsey protocol. No additional magnetic sources are applied beyond the 5mT bias magnetic field. However, the SQ image in Fig. 4.6(a) exhibits large non-magnetic spatial variations on the order of 10 µT due to lattice stress inhomogeneity. The inability of SQ measurements to distinguish lattice stress from magnetic fields complicates the analysis of such images. In particular, identifying sub-µT features on top of 10 µT background variations on the same spatial length-scale is a challenging analysis problem traditionally requiring multiple images and large dynamic range to tackle. In contrast, the pixels in the DQ image (Fig. 4.6(b)) respond only to magnetic-sources, such that the resulting DQ image exhibits an order of magnitude reduced variation (as highlighted by the reduced color-scale in Fig. 4.6(c)). Similar to the DQ Ramsey-based solution presented here, multi-frequency CW and pulsed-ODMR techniques have also been recently demonstrated to disentangle magnetic and non-magnetic signals without acquiring multiple images [68]. However, these techniques cannot also recover the stress-gradient-induced degradation in magnetic per-pixel sensitivity.

The residual variation in the DQ magnetic image (Fig. 4.6(c)) is predominantly correlated with the bias magnetic field, which can be further engineered to reduce residual magnetic gradients. However, subtle scratch-like features on the sub-100nT scale are also visible, stretching diagonally across the field of view. These features are attributed to scratches surface of the diamond substrate before growth of the nitrogen-doped layer. Similar features can be identified in the extracted Ramsey

fringe amplitudes in Fig. 4.3(c,d) for the SQ and, to a lesser extent, DQ sensing bases. The persistence of these features in both bases is illuminating and suggests that transverse stress inhomogeneity, which is not suppressed by either sensing basis, may contribute to the residual variation of the averaged DQ image shown in Fig. 4.6(b,c). As discussed in detail in Chapter 3, transverse crystal stress $M_\perp$ results in a differential, magnetic-field-like shift in the NV^- resonances which is suppressed by a factor proportional to $M_\perp/B_z$ where B_z is the projection of the bias magnetic field along the NV symmetry axis. An $M_\perp$ of ≈100kHz would induce a differential shift of about 0.2kHz or 8nT given the aligned 5mT bias magnetic field (a 450× suppression). While sufficiently small to be negligible compared to the axial-stress-induced shifts which dominate the SQ measurements, this estimate appears consistent with the scale of residual features visible in Fig 4.6(c).

4.5 Outlook

The median volume-normalized broadband magnetic sensitivity demonstrated in this work compares favorably to the est value to date for an NV^- ensemble $34\,\mathrm{nT\,Hz^{-1/2}\mu m^{3/2}}$ reported in Ref. [19], which used photodiode-based measurements to detect the single-neuron action potential from a living marine worm, *M. infundibulum*. Critically, the present work achieves a similar sensitivity while operating in an imaging modality, with degraded optical collection efficiency, and using NV^- centers along only a single axis whereas the non-imaging apparatus employed in Ref. [19] overlapped two NV^- axes and had ≈ 16× higher optical collection efficiency..

The demonstrated magnetic imaging method using the DQ 4-Ramsey protocol

enables uniform magnetic sensitivity across a field of view independent of inhomogeneity in the host diamond material and applied microwave control fields. In particular, the MW phase alternation scheme of the 4-Ramsey protocol (Fig. 3.6(a)), which isolates the double quantum magnetic signal from residual single quantum signal. These methods provide a path toward imaging a range of dynamic magnetic phenomena, including nanotesla-scale fields from single mammalian neurons or cardiomyocytes, as well as fields from integrated circuits and condensed matter systems. Increased optical excitation intensity and optimized material engineering can yield further improvements in volume-normalized magnetic sensitivity. Although many single-NV pulsed experiments operate near the NV^- center's saturation intensity (1-3 $\mathrm{mW\,\mu m^{-2}}$ [84]) to minimize the initialization and readout durations [2], this work achieved optimal sensitivity when operating at an average intensity $\sim 45\times$ below saturation. The lower intensity allowed the NV ensemble to maintain a favorable charge state ratio by reducing optical ionization of NV^- to NV^0 [77, 78]. For this reason, future material development improving and stabilizing the NV charge fraction, for example by reducing the density of other parasitic defects which can act as charge acceptors [39], is critical.

The high-sensitivity, pulsed imaging method demonstrated here also enables applications beyond broadband magnetic imaging such as parallelized, high-resolution NV^- ensemble NMR using AC magnetic field detection protocols. Additionally, the MW phase control utilized for the DQ 4-Ramsey protocol is sufficient to implement magnetically-insensitive measurement protocols [117, 124] as recently suggested by Ref. [125] for imaging the lattice damage induced by colliding weakly-interacting

massive particles (WIMPs).

Chapter 5

Characterization and Control of the Diamond Spin Bath

This chapter presents techniques to study and control the diamond spin bath. Sec. 5.1 describes double resonance measurement protocols to measure the magnetic noise produced by the diamond spin bath. As the dominant electronic spin bath constituent, the ground state Hamiltonian of the neutral substitutional nitrogen spins, N_s^0, is described in detail along with Double Electron-Electron Resonance (DEER) ODMR spectra of the ground state N_s^0 spin transitions. DEER ODMR measurements are also shown to be a valuable characterization technique for studying other defects in the bath and determining the nitrogen isotopic purity of ^{15}N-enriched diamond material. In Sec. 5.2, spin echo double resonance (SEDOR) protocols are used to quantitatively account for the contribution of dipolar couplings between the different spin bath species and NV sensor spins to NV^- ensemble dephasing.

Sec. 5.3 explores the use of resonant RF control to decouple the electronic spin

bath from the NV sensor spins and extend the NV$^-$ ensemble T_2^*. This is specifically intended for DC magnetometry applications where echo-type decoupling of the NV sensor spins directly is not applicable. By applying continuous-wave irradiation resonant with the spin bath transitions during an NV$^-$ Ramsey sequence, extensions of NV T_2^* by over an order of magnitude are achieved in as-grown diamond material. The scaling of NV T_2^* with spin bath Rabi frequency along with a phenomenological model of the intermediate decoupling regime are presented (for sufficiently strong control fields, the NV$^-$ T_2^* saturates due to the next dominant dephasing source). Similar results are attained using pulsed spin bath control. In both approaches, NV$^-$ Ramsey free induction decay (FID) measurements crucially leverage the DQ sensing basis in combination with bath decoupling in order to avoid stress-gradient-induced dephasing (see Chapters 3 and 4). Finally, the measured relative sensitivity improvements attained using spin bath decoupling in combination with DQ Ramsey control for Samples 3C and 3D with [N]≈ 0.75 ppm and [N]≈ 8 ppm are presented.

Sec. 5.3.6 discusses preliminary experiments decoupling the spin bath in NV-rich diamond material (post-irradiation and annealing). Initial results indicate that in such material, decoupling of the spin bath is sufficient to approach NV-NV interaction-limited T_2^*. With all other parameters constant, it is desirable for the NV$^-$ T_2^* to be limited by like-spin interactions between NV sensor spins (assuming NV spins not used for sensing are pumped into $m_s = 0$) instead of by other dephasing mechanisms such as the spin bath or stress-gradients. Barring the experimental realization of proposed sequences to decouple NV-NV interactions while retaining some sensitivity to DC magnetic fields, NV-NV-limited T_2^* is an optimal regime for NV$^-$ magnetometer

operation. However, operation in this regime has yet to be achieved regularly by DC magnetometry experiments using NV^- ensembles.

5.1 Double Resonance Measurements for Characterizing the Diamond Spin Bath

This section introduces double resonance techniques to study magnetic noise produced by the paramagnetic diamond spin bath. In these sequences, resonant control fields are applied to the diamond to drive transitions associated with the spin bath species in addition to the MW fields employed to control the NV sensor spins. Many of the techniques introduced here are adopted from conventional bulk NMR and EPR using inductive-detection (requiring $\gtrsim 10^{11}$ spins) [126]. Compared to these bulk methods, NV-based double resonance protocols leverage the proximity of the NV sensor spins to the diamond bath spins ($\sim$nanometers) to probe the dramatically larger magnetic fields produced by nearby bath spins. We begin by describing the ground state Hamiltonian of N_s^0 spins, which are commonly the dominant spin bath species and exhibit a complex resonance spectrum due to strong hyperfine couplings and Jahn-Teller distortions. Example measurements of the N_s^0 DEER ODMR spectrum for ^{14}N and ^{15}N-enriched material are presented in addition to example spectra of other species in the spin bath as function of irradiation and annealing.

5.1.1 Substitutional Nitrogen Electronic Spins

Substitutional nitrogen electronic spins constitute the dominant non-NV$^-$ paramagnetic spin species in the diamond spin bath. As a consequence, for both as-grown and post-treatment diamond material, magnetic dipolar interactions between the NV sensors and bath of N_s^0 defects contribute significantly to NV$^-$ ensemble dephasing, especially in ^{12}C isotopically-purified diamonds. Similar to NV centers, N_s^0 can be composed of either a ^{14}N ($I = 1$) or ^{15}N ($I = 1/2$) nuclear spins - determining the number of hyperfine-split resonances and magnitude of the associated splittings. N_s^0 defects also exhibit trigonal symmetry with axes co-linear with the [111] crystal lattice due to a Jahn-Teller distortion of the nitrogen nuclear spin towards one of the neighboring carbon atoms in the lattice [127].

The ground state N_s^0 Hamiltonian is given by,

$$H_{N_s^0}/h = \frac{\mu_B}{h}\vec{B}\cdot\mathbf{g}\cdot\vec{I} + \frac{\mu_N}{h}\vec{B}\cdot\mathbf{g}\cdot\vec{S} + \vec{S}\cdot\mathbf{A}\cdot\vec{I} + \vec{I}\cdot\mathbf{Q}\cdot\vec{I} \tag{5.1}$$

where μ_B is the Bohr magneton, μ_N is the nuclear magneton, h is Planck's constant, $\vec{B} = (B_x, B_y, B_z)$ is the magnetic field vector, $\vec{S} = (S_x, S_y, S_z)$ are the dimensionless spin-1/2 Pauli matrices, and $\vec{I} = (I_x, I_y, I_z)$ are the dimensionless Spin-1/2 (^{15}N) or Spin-1 (^{14}N) nuclear spin operators. In the following discussion, the nuclear Zeeman term (second term in Eqn. 5.1) is discarded since the contribution is negligible for the typical $\lesssim 10\,\mathrm{mT}$ magnetic field applied in this work.

The electronic g-factor tensor $\mathbf{g}$, the hyperfine tensor $\mathbf{A}$, and electric quadrupole tensor $\mathbf{Q}$ are diagonal in the N_s^0 coordinate system where the z-axis is aligned along

	$^{14}N_s^0$
g	2.0025 [128]
$A_\perp, A_\parallel$	114 MHz, 81.3 MHz [127–129]
$P_\parallel$	-3.97 MHz [129]

	$^{15}N_s^0$
$A_\perp, A_\parallel$	-159.7 MHz, -113.83 MHz [127]
P	0 (since I<1)

Table 5.1: **Summary of Hamiltonian parameters** used to simulate the N_s^0 resonance spectrum for both the ^{14}N and ^{15}N isotopes.

any one of the [111] crystal axes,

$$\mathbf{g} = \begin{pmatrix} g_\perp & 0 & 0 \\ 0 & g_\perp & 0 \\ 0 & 0 & g_\parallel \end{pmatrix}, \mathbf{A} = \begin{pmatrix} A_\perp & 0 & 0 \\ 0 & A_\perp & 0 \\ 0 & 0 & A_\parallel \end{pmatrix}, \mathbf{Q} = \begin{pmatrix} P_\perp & 0 & 0 \\ 0 & P_\perp & 0 \\ 0 & 0 & P_\parallel \end{pmatrix}. \tag{5.2}$$

Here, $g_\parallel$, $A_\parallel$, $P_\parallel$, $g_\perp$, $A_\perp$, and $P_\perp$ correspond to the gyromagnetic, hyperfine, and quadrupolar axial and transverse tensor components. Further simplifications are possible by noting that the g-factor tensor is nearly isotropic ($g_\perp \approx g_\parallel \equiv g_\mathrm{e}$) and that for axial symmetry the off-axis quadrupolar component vanishes. The simplified Hamiltonian for an N_s^0 defect aligned with a particular crystal axis has the form,

$$H_{\mathrm{N}_s^0}/h \approx \frac{g_\mathrm{e}\mu_B}{h}(B_z S_Z + B_x S_x + B_y S_y) + A_\parallel S_z I_z + A_\perp (S_x I_x + S_y I_y) + P_\parallel I_z^2, \tag{5.3}$$

with the hyperfine constants $A_\parallel$ and $A_\perp$ for ^{14}N and ^{15}N summarized in Tab. 5.1.

For $^{14}N_s^0$ defects with $S = 1$ and $I = 1$ there exist six energy eigenstates

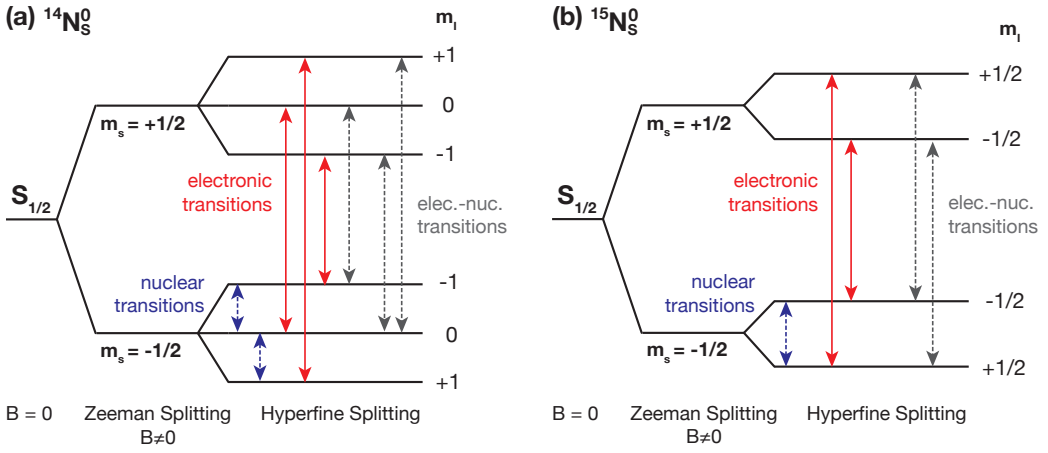

Figure 5.1: **N_s^0 energy level diagrams. (a)** Energy level diagram for $^{14}N_s^0$ defects with electronic spin $S = 1/2$ and nuclear spin $I = 1$. Dipole-allowed electronic transitions ($\Delta m_s = \pm 1$) are indicated by red, solid arrows. The dashed grey and blue arrows depict the first order forbidden ($\Delta m_s = \pm 1$, $\Delta m_I = \mp 1$) and nuclear spin transitions ($\Delta m_I = \pm 1$), respectively. **(b)** Same as (a) but for $^{15}N_s^0$ defects with $I = 1/2$.

$|m_s = \pm 1/2, m_I = \{0, \pm 1\}\rangle$. Fig. 5.1 depicts the three dipole-allowed transitions ($\Delta m_s = \pm 1$, $\Delta m_I = 0$, solid red arrows), the four first-order forbidden transitions ($\Delta m_s = \pm 1$, $\Delta m_I = \mp 1$, dashed grey arrows), as well as the nuclear-spin-related transitions ($\Delta m_s = 0$, $\Delta m_I = \pm 1$, dashed, blue arrows). As with NV$^-$, N_s^0 defects may be oriented along any of the four crystallographic directions, independent of the applied bias magnetic field vector. Considering the three driven electronic transitions for each population of $^{14}N_s^0$ defects along all four possible crystal lattice orientations, there are twelve possible spin transitions. However, with the bias magnetic field aligned with one of the crystal axes, as employed throughout this Chapter, N_s^0 defects along three of the orientations experience the same $B_\parallel$ and $B_\perp$ projections such that the spin transitions become degenerate. In this configuration, the twelve spin transitions collapse to six non-degenerate spectral groups (three of which contain three

overlapped N_s^0 spin resonances).

5.1.2 DEER ODMR Spectroscopy

N_s^0 defects do not exhibit spin-dependent fluorescence or optical polarization at arbitrary magnetic fields; therefore, the N_s^0 spin resonances cannot be readout optically via spin-state-dependent fluorescence as with NV^- defects. Instead, double resonance pulse protocols must be employed to determine the N_s^0 spin resonances indirectly using the NV defects as probes of the magnetic environment. A double electron-electron resonance (DEER) ODMR protocol used to identify bath-related spin resonances is illustrated in Fig. 5.2(a). A Hahn echo or multi-pulse decoupling sequence with free precession interval $\tau \approx T_2$ is applied to the NV sensor spins, canceling static sources of phase accumulation including bath-induced dephasing. Meanwhile, another pulse is applied to the bath spins concurrently with the NV^- π-pulse(s). The amplitude and duration of the bath pulse is calibrated such that, when resonant with a bath transition, the bath spins are inverted (i.e., a π-pulse), rendering the NV echo refocusing ineffective in a frequency-selective manner. As the frequency of the bath pulse is swept, the ODMR contrast decreases when the bath pulse is resonant with a bath resonance (see Fig. 5.2(b)). The DEER ODMR pulse sequence described above can alternatively be understood as entangling each NV sensor spin with the nearby bath spins.

Fig. 5.3(a) illustrates an example DEER ODMR spectrum for a ^{14}N diamond sample with an external $\approx$10 mT magnetic field aligned with a single [111]-crystal axis (Sample 3C). The strong axial and transverse hyperfine couplings result in

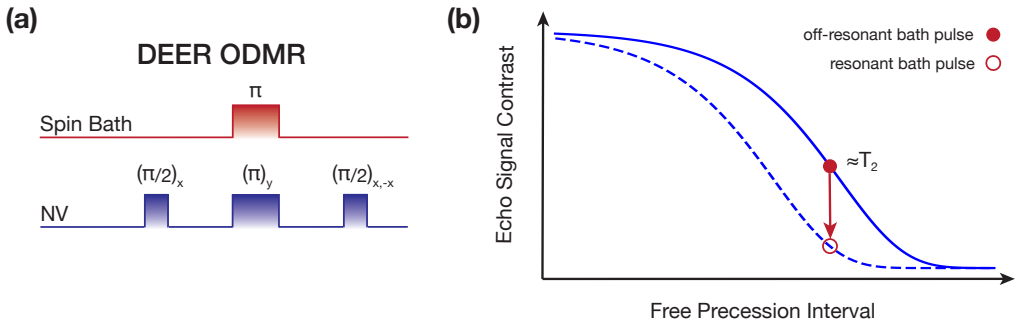

Figure 5.2: **DEER ODMR pulse protocol. (a)** Depiction of the double electron electron resonance ODMR protocol. The frequency of the bath π-pulse (red) is swept while an echo sequence is applied to the NV$^-$ sensor spins. The total free precession interval is chosen to be approximately the NV$^-$ Hahn echo coherence time, T_2. **(b)** Cartoon of the NV signal as a function of free precession interval. When the bath pulse is resonant with a bath-spin transition, the measured NV contrast decreases as a result of the reduced NV decoherence time, T_2.

groups which are split from the bare-electronic spin resonance frequency (denoted "g=2") on the order of 100 MHz. The six non-degenerate N_s^0 spectral groups due to electronic transitions ($\Delta m_s = \pm 1$, $\Delta m_I = 0$) are labelled 1-6. The Group 2, 4, and 5 resonances exhibit about three times the amplitude compared to Groups 1, 3, and 6 because the former correspond to three overlapped N_s^0 resonances. A subset of first-order forbidden transitions are also visible, albeit with reduced amplitude [95]. The simulated spectrum in Fig. 5.3(a) is obtained by considering the B_z, B_x, and B_y projections for each orientation of N_s^0 defects. The following parameters have been used in the simulation (see Tab. 5.1): $B_z = 95.5\,\mathrm{mT}$ (projection along aligned axis), $g_e\mu_B/h \approx 2.8025 \times 10^4\,\mathrm{MHz/T}$, $A_\parallel = 114\,\mathrm{MHz}$, $A_\perp = 81.3\,\mathrm{MHz}$, and $P_\parallel = -3.97\,\mathrm{MHz}$.

In Fig. 5.3(b), the simulated spectrum for a ^{15}N-enriched sample is shown together with experimental data from Sample 3D ([^{15}N]= 7.7(7) ppm measured via

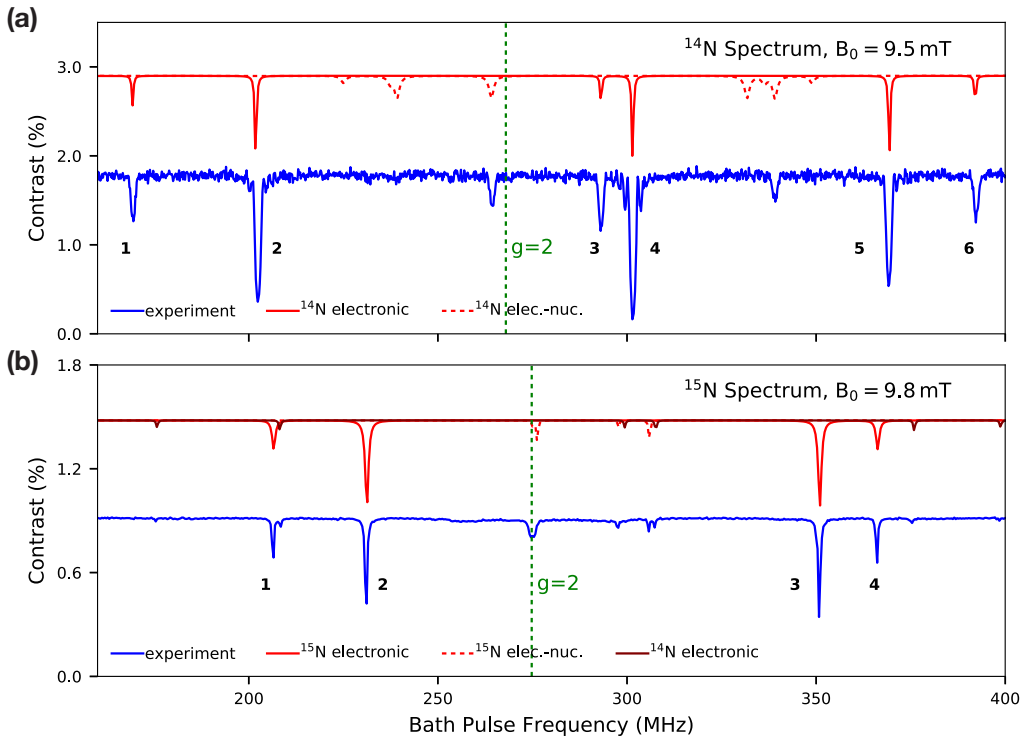

Figure 5.3: **$^{14}N_s^0$ and $^{15}N_s^0$ DEER ODMR spectra (a)** Simulated (red) and measured (blue) DEER spectrum for Sample 3C with natural abundance ^{14}N. Allowed electronic transitions ($\Delta m_s = \pm 1$) are labeled 1-6. Smaller amplitude peaks corresponding to first-order forbidden transitions ($\Delta m_I \neq 0$) are visible. Frequencies are simulated using Eqn. 5.3 and displayed as Lorentzian resonance features with widths and amplitudes chosen to reflect the experimental data. The Larmor frequency of an electronic spin without hyperfine shifts (g=2) is indicated by a dashed, green line. **(b)** Similar to (a), but the DEER spectrum for the ^{15}N-enriched, Sample 3D. Electronic transitions due to ≈6% residual ^{14}N incorporated during growth are also visible.

SIMS). With an aligned magnetic field, the $^{15}N_s^0$ defects exhibit four instead of six distinct resonance groups labelled 1-4. Groups 2 and 3 exhibit increased amplitude again due to three overlapped transitions. However, for the ^{15}N-isotope with $S = 1/2$ and $I = 1/2$ only eight dipole-allowed transitions exist compared to the twelve for $^{14}N_s^0$. Note that in Fig. 5.3(b), electronic $^{14}N_s^0$ resonances with reduced amplitude are also visible in addition to the $^{15}N_s^0$-related resonances due to residual contamination during growth yielding $[^{14}N] = 0.50(5)$ ppm (measured via SIMS).

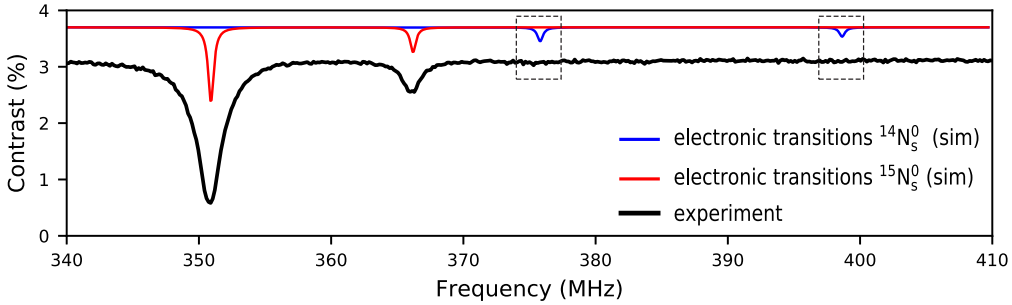

Figure 5.4: **^{15}N-enriched DEER spectrum without residual $^{14}N_s^0$.** Simulated $^{15}N_s^0$ (red) and $^{14}N_s^0$ (blue) DEER spectra shown alongside experimental data for a ^{15}N-enriched diamond material (Sample 5A) without observable ^{14}N contamination. The expected frequencies for the $^{14}N_s^0$ resonances are enclosed by dashed, black boxes.

The isotopic contamination fraction $[^{14}N]/([^{14}N]+[^{15}N])$ is reflected in the relative amplitudes between the well-isolated $^{14}N_s^0$ and $^{15}N_s^0$ groups, making this a useful characterization method for nitrogen isotopic purity. An example spectrum is shown in Fig. 5.4 for an additional ^{15}N isotopically-enriched layer sample (Sample 5A) with no detectable ^{14}N contamination in DEER ODMR or SIMS. While SIMS measurements have a detection limit for nitrogen of about 0.01 ppm, limit for DEER ODMR depends on numerous factors including the amount of NV^- fluorescence, the ODMR contrast, and number of refocusing pulses. For the data presented in Fig. 5.4 using

Sample 5A (as-grown, 1-micron-thick layer sample), the estimated detection limit for an SNR of unity is $[^{14}N_S^0] \approx 0.1\,\text{ppm}$. Interrogating larger collection volumes, increasing NV^- density, or using multi-pulse dynamical decoupling techniques are expected to yield detection limits competitive with SIMS measurements.

5.1.3 Other Electronic Species in DEER ODMR Spectra

NV-based double resonance techniques also provide insight into the composition of the diamond spin bath beyond N_s^0 electronic defects. For example, paramagnetic mono- and multi-vacancy defects which lack hyperfine interactions with constituent nuclear spins exhibit resonances commensurate with the Larmor frequency of bare electronic spins (i.e., "g=2"). Fig. 5.5(a) shows the DEER ODMR spectra for a sample (Sample 5B, $[N] \approx 8\,\text{ppm}$) at different stages of treatment intended to increase [NV]: as-grown, after electron irradiation to produce vacancies, and after subsequent annealing to mobilize the vacancies and form NV defects. After growth, only resonances associated with N_s^0-related are observable in DEER measurements of Sample 5A. However, after electron irradiation with a dose of $3 \times 10^{18}\,e^-/\text{cm}^2$ at 1 MeV, a prominent feature at the bare electronic frequency attributed to vacancy-related defects is apparent as expected (see expanded view in Fig. 5.5). Following annealing at 800° C for 12 hours, the "g=2" feature which dominates after irradiation is mitigated and only resonances likely attributable to first-order forbidden N_s^0 electron-nuclear transitions remain. This suggests that the annealing conditions were sufficient or nearly sufficient for the vacancies introduced during irradiation to mobilize and form other defects (predominantly NV^- centers).

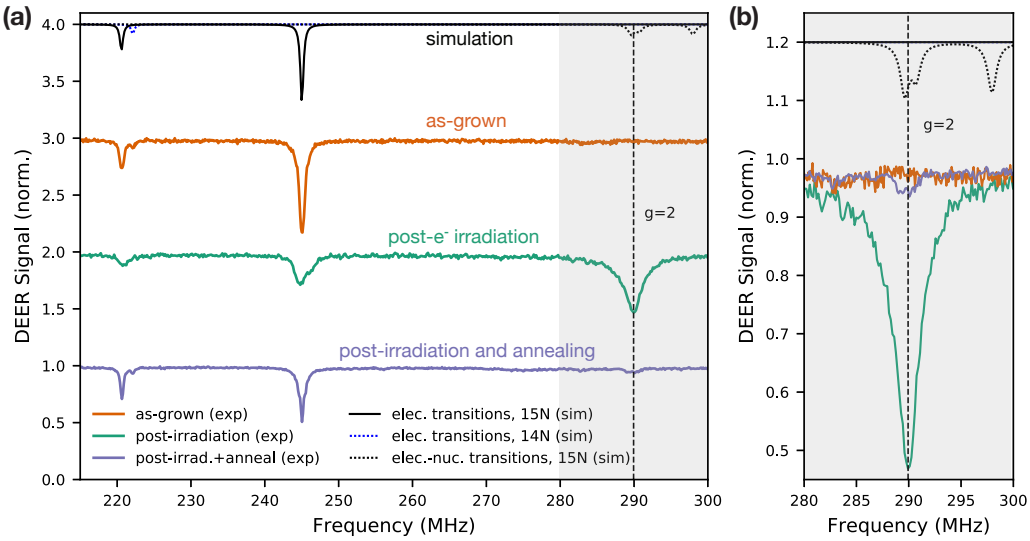

Figure 5.5: **DEER spectra at different treatment stages.** **(a)** DEER spectra for the same sample (Sample 5B) at three stages: as-grown (orange), after electron irradiation with a dose of $3 \times 10^{18} e^-/cm^2$ at 1 MeV to introduce vacancies (green), and after subsequent annealing at 800°C for 12 hours to mobilize vacancies and produce NV^- centers (purple). Experimental spectra were collected at a nominal bias magnetic field of 10 mT with bath pulse calibrated to a duration of 1 µs. An artificial offset of unity is added to separate the normalized data. The simulated N_s^0-related spectra is included for reference. **(b)** Expanded view of the spectral region around the bare electron Larmor frequency ("g=2", dashed black line).

5.1.4 Comparison of N_s^0 and NV$^-$ Resonance Linewidths

In this section, the natural N_s^0 and NV$^-$ resonance linewidths within the same samples (Samples 3C and 3D) are determined using pulsed-ODMR and DEER ODMR spectral measurements, respectively, as summarized in Fig. 5.6. Bath and NV π-pulses with decreasing Rabi frequency, and consequently increasing duration, are used to avoid Fourier broadening as described for pulsed-ODMR in Ref. [69].

Figs. 5.6(b,c) compare the $^{14}N_s^0$ Group 1 linewidths (single resonance) with that of Group 5 (three overlapped resonances) for different π_{bath}-pulse durations in Sample 3C. For shorter π_{bath}-pulse durations (larger applied AC magnetic field amplitudes), the observed spin resonances are Fourier-broadened, such that the extracted linewidth is a convolution of the natural linewidth and the inverse duration of the π_{bath}-pulse [69]. For increasing π_{bath}-pulse durations, however, the measured linewidth approaches its natural (Lorentzian) linewidth $\Gamma = (\pi T_2^*)^{-1}$. At the longest π_{bath}-pulse durations used in this work, Group 1 exhibits a single resonance with linewidth of approximately 25 kHz. In contrast, Group 5 reveals two peaks, consisting of two overlapped and one detuned resonance, which is attributed to imperfect magnetic field alignment. The splitting between the two peaks in Group 5 is ≈ 100 kHz and consistent with a misalignment of approximately 1° for the applied bias magnetic field of 10 mT. The linewidth of the isolated, detuned resonance in Group 5 (26.3 kHz) agrees with the linewidth extracted for Group 1.

Fig. 5.6(d) compares the determined NV$^-$ and N_s^0 Group 1 ensemble linewidths for Sample 3C as a function of (NV or bath) π-pulse duration. For both species, the linewidths narrow with increasing π-pulse durations, as discussed above, and saturate

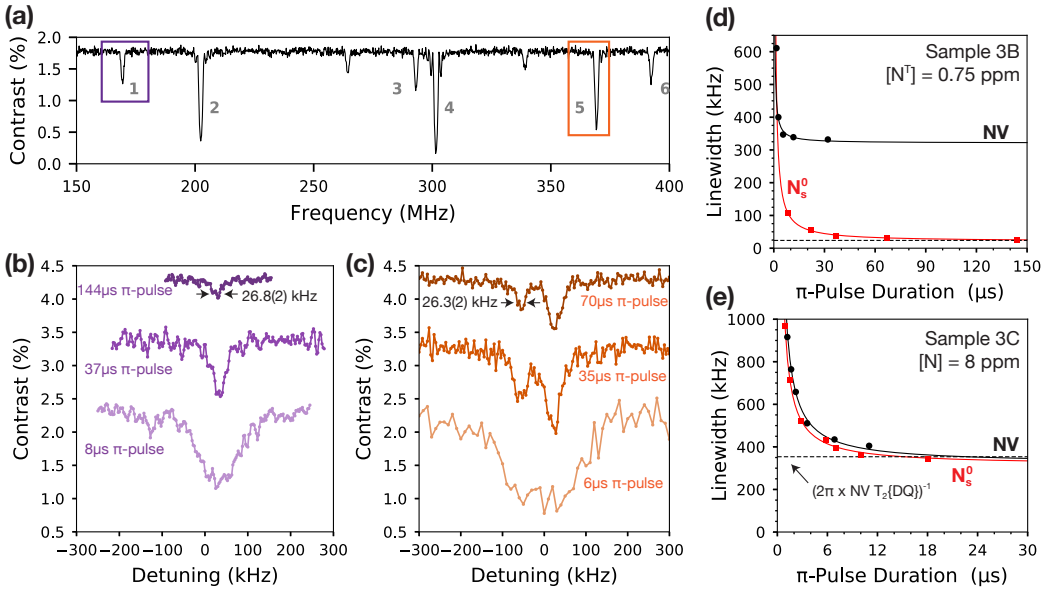

Figure 5.6: **Comparison of NV$^-$ and N_s^0 linewidths.** **(a)** DEER spectrum for Sample 3C with the spectral groups associated with the electronic $\Delta m_s = \pm 1$ transitions labeled 1-6. Groups 6 consists of a single resonance, while Group 5 corresponds to three, degenerate resonances. **(b)** DEER spectra for Group 1 in Sample 3C with three different bath π-pulse durations. The minimum extracted linewidth of 26.8 kHz is indicated. **(c)** DEER spectra for Group 5 in Sample 3C with three different bath π-pulse durations. For the longest pulses, it is possible to distinguish one imperfectly overlapped resonance from the other two resonances. **(d)** NV$^-$ (black, circles) and N_s^0 (red, squares) linewidths approaching their respective natural linewidths. The natural linewidth is extract by fitting to the function form, $y = A/x + B$, where B is the saturation linewidth. While the NV$^-$ linewidth becomes stress-gradient-limited, the N_s^0 linewidth is immune and saturates at 23(2) kHz. This value for the N_s^0 natural linewidth is consistent with $(2\pi \times T_2^*\{\mathrm{DQ}\})^{-1}$ (black, dashed line) as expected for a Lorenztian lineshape and the effectively doubled DQ gyromagnetic ratio. **(e)** Similar to (d), but for Sample 3D which contains an order of magnitude higher concentration of nitrogen. Stress-gradient contributions are negligible such that the NV$^-$ and N_s^0 linewidths converge.

at their respective natural linewidths. The saturation linewidth is extracted by fitting to the functional form, $y = A/x + B$, where the measured linewidth scales inverse linearly with the π-pulse duration and B corresponds to the natural linewidth without additional Fourier-broadening. In Sample 3C, the natural NV$^-$ linewidth is found to be significantly larger ($13\times$) than the natural N_s^0 linewidth of $20.6(1.2)\,\mathrm{kHz}$. This order-of-magnitude difference is a result of broadening induced by stress-gradients across the interrogated volume. Pulsed-ODMR measurements of the NV$^-$ ensemble linewidth (see Fig. 5.6a) performed in the SQ sub-bases ($\{0, +1\}$ and $\{0, -1\}$) are vulnerable to such stress-gradients. In contrast, N_s^0 defects in diamond do not couple to stress gradients or electric fields as apparent from the N_s^0 Hamiltonian in Eqn. 5.3. As a consistency check, note that NV$^-$ ensemble Ramsey measurements in Sample 3C, made in the DQ sensing basis, yield a stress-independent dephasing time $T^*_{2,DQ} = 6.9(5)\,\mu\mathrm{s}$. This dephasing time, presumably limited by the N_s^0 spin bath, implies a N_s^0 spin resonance linewidth given by $(2\pi \times T_2^*\{\mathrm{DQ}\})^{-1} = 23(2)\,\mathrm{kHz}$, which is in reasonable agreement with the DEER-based measurements of the natural N_s^0 linewidth. Similar consistency is found for measurements of the NV and N_s^0 ensemble resonance linewidths in Sample 3D, as shown in Fig. 5.6(e). Such agreement across multiple samples further suggests that the DQ T_2^* value for NV$^-$ ensembles is limited by the surrounding N_s^0 spin bath. Note that for these samples, $[\mathrm{NV}^-] \ll [N_s^0]$; therefore, we ignore the back action of NV$^-$ spins onto N_s^0 spins in the DEER readout. For denser NV$^-$ samples, however, this back action has to be taken into account [130].

5.2 Spin Echo Double Resonance Measurements

When spin bath resonance features are spaced by several linewidths, resonant pulses manipulating one spectral group at a time are possible. This section describes spin echo double resonance (SEDOR) schemes which can selectively measure the coupling of each group of bath spins to the NV sensor spins. The SEDOR protocol employs a sequence similar to DEER ODMR measurements. However, instead of sweeping the frequency of the applied bath pulse, the duration of the NV free precession interval is swept while the bath pulse frequency is fixed to be resonant with a single group of bath spins. This produces a spin echo signal which decays with characteristic time $T_2^i\{\text{SEDOR}\}$ when the i$^{\text{th}}$ spectral group is addressed. If no bath pulse or a non-resonant bath pulse is applied, then the bath spins are not manipulated and $T_2^i\{\text{SEDOR}\} = T_2$. However, with a resonant bath pulse applied, the dephasing induced by the resonant spectral group on the NV sensor spins can be probed quantitatively; while all other dephasing channels including other bath groups are refocused.

The ensemble spin echo signal without bath control exhibits a decay profile between a Gaussian and exponential with decay shape parameter, $p = 1.5$ (see Ref. [72]). However, with resonant control of a bath spectral group, the echo signal decays faster with a shape parameter approaching $p \approx 1$ corresponding to exponential decay. This change in decay shape is attributed to the quasi-static dephasing channel selectively turned on, resulting in Ramsey-like dephasing via dipolar interactions with the spin bath. The SEDOR decay time constant $T_2^i\{\text{SEDOR}\}$ yields the r.m.s interaction strength b_i between the NV sensor spins and i$^{\text{th}}$ bath group: $1/T_2^i\{\text{SEDOR}\}$. The

Sample	$[^{14}N]$ (ppm)	$[^{15}N]$ (ppm)	^{13}C (%)	$T_2^*\{\text{SQ}\}$ (μs)	$T_2^*\{\text{DQ}\}$ (μs)
3C	0.75	–	0.005	$1-10$	6.9(5)
3D	7.7(7)	0.50(5)	0.0030(3)	$0.3-1.2$	0.73(4)

Table 5.2: **Characteristics of Samples 3C and 3D.** Samples 3C and 3D were synthesized with 99.995% 12C. The $[^{14}\text{N}]$, $[^{15}\text{N}]$ and $[^{13}\text{C}]$ were measured via SIMS for Sample 3D which was grown using ^{15}N and ^{12}C-enriched source gases. The uncertainty for SIMS measured quantities is 10%. The $[^{14}\text{N}]$ and $[^{13}\text{C}]$ for Sample 3C are based on reported values from the manufacturer Element Six and confirmed with fluorescence-based measurements. The thicknesses of the CVD-grown nitrogen-doped layers were also reported by Element Six. The measured T_2^* in the SQ and DQ bases are included for reference.

measured b_i per group add inverse linearly (since the decay is exponential) such that the total dephasing $b_{tot} = \sum_{i=1}^{n} b_i = 1/T_2^*\{\text{SEDOR}\}$ where n is the nitrogen-isotope dependent number of spectral groups. If the NV T_2^* is limited solely by N_s^0 dipolar interactions, then $T_2^*\{\text{SEDOR}\}$, measured in the SQ sensing basis, should be equal to twice the rate extracted via Ramsey measurements ($2T_2^*\{\text{DQ}\}$). When $T_2^*\{\text{SEDOR}\}$ does not approach $2T_2^*\{\text{DQ}\}$, this suggests the contribution of an additional non-bath-related dephasing mechanism.

We now use SEDOR measurements to quantitatively study the ensemble dephasing sources for Samples 3C and 3D from Chapter 3. The material properties presented earlier are summarized in Tab. 5.2. By probing the spin-bath-induced dephasing directly, SEDOR measurements confirm the suspected role of NV-N_s^0 dipolar interactions in determining $T_2^*\{\text{DQ}\}$ for these samples and highlight the promise of extending T_2^* using the spin bath decoupling techniques described next in Sec. 5.3.

SEDOR-based measurements of the six N_s^0 allowed spectral groups are sum-

marized in Tab. 5.3 and yield a total measured dephasing rate b_{tot} from all groups of $56(3)\,\mathrm{ms}^{-1}$ ($T_2^*\{\mathrm{SEDOR}\} = 18(1)\,\mu\mathrm{s}$). Additionally, accounting for residual contributions of ^{13}C nuclear spins and the magnetic field gradient across the 40-micron layer thickness (see Tab. 5.3 and Appendix B), we estimate a T_2^* of about $14\,\mu\mathrm{s}$ ($b_{tot} \approx 71\,\mathrm{ms}^{-1}$) which compares favorably with twice the measured DQ Ramsey dephasing time, $2T_2^*\{\mathrm{DQ}\} = 14(1)$, which yields ($b_{meas} = 73(5)\,\mathrm{ms}^{-1}$).

SEDOR-based measurements of Sample 3D similarly suggest that dipolar coupling with the N_s^0 spin bath is the dominant NV$^-$ ensemble dephasing mechanism in the DQ sensing basis. In total, measurements of the dephasing induced by the four ^{15}N spectral groups in Fig. 5.3(b) and six spectral groups associated with the residual [$^{14}\mathrm{N}_s^0$] yields $b_{^{15}N} = 64(3)\,\mathrm{ms}^{-1}$ and $b_{^{14}N} = 3.8(2)\,\mathrm{ms}^{-1}$ (see Tab. 5.4). Together these channels suggest an estimated T_2^* of $1.5(1)\,\mu\mathrm{s}$ which agrees well with twice the measured DQ dephasing rate: $2T_2^*\{\mathrm{DQ}\} = 1.47(8)\,\mu\mathrm{s}$. In this sample, dephasing-induced by dipolar coupling to the ^{13}C spin bath and magnetic field gradients have a negligible effect compared to the N_s^0 contribution.

The above analysis suggests significant gains in T_2^* are possible for as-grown material if the N_s^0 spins were to be decoupled from the NV$^-$ sensor spins and no longer contribute to NV$^-$ dephasing. The next anticipated sources of dephasing: the residual ^{13}C spin bath and magnetic field gradients across the ensemble appear to set limits on T_2^* of $\approx 100\,\mu\mathrm{s}$ ($\approx 50\,\mu\mathrm{s}$) in the SQ (DQ) sensing basis. The following section explores spin bath decoupling approaches for extending T_2^* using Samples 3C and 3D. This is followed by similar measurements for irradiated and annealed, NV-rich diamond material where NV-NV dipolar interactions are no longer negligible.

Dephasing Mechanism	Magnitude	Dephasing Rate	T_2^*	Method
		1/ms	μs	
^{14}N (allowed)		56(3)	18(1)	SEDOR
^{13}C	<0.01%	≈ 10	≈ 100	reported by E6
B_0-gradient @ 85 G	0.056 kHz/G	≈4.7	≈210	estimated
total (b_{tot})		≈71	≈14	
observed (DQ Ramsey)		73(5)	14(1)	measured

Table 5.3: **NV ensemble dephasing mechanisms for Sample 3C.** Individual contributions to dephasing are accounted for using direct measurements (SEDOR) or estimated values. The estimated total dephasing rate is compared to the observed DQ Ramsey decay. The concentration, [^{13}C], is estimated according to the scaling in Sec. 2.2.4 and reported isotopic purity. See Appendix B for details of the magnetic field gradient estimate.

Dephasing Mechanism	Magnitude	Dephasing Rate	T_2^*	Method
		1/ms	μs	
^{15}N (allowed)		64(3)	1.6(1)	SEDOR
^{14}N (allowed)		3.8(2)	26(1)	SEDOR
^{13}C	30(3) ppm	3.0(3)	330(30)	SIMS
B_0-gradient @ 100 G	0.022 kHz/G	≈2.2	≈446	estimated
subtotal ($b_{^{14}N} + b_{^{15}N}$)		680(30)	1.5(1)	
total (b_{tot})		≈686	≈1.5	
observed (DQ Ramsey)		682(41)	1.47(8)	measured

Table 5.4: **NV ensemble dephasing mechanisms for Sample 3D.** Individual contributions to dephasing are accounted for using direct measurements (SEDOR) or estimated values. The estimated total dephasing rate is compared to the observed DQ Ramsey decay. The concentration, [^{13}C], is measured directly using SIMS and then the contribution to dephasing is estimated according to the scaling in Sec. 2.2.4. See Appendix B for details of the magnetic field gradient estimate.

5.3 Extending the NV$^-$ T_2^* with Spin Bath Decoupling Techniques

This section presents experimental results using spin bath control techniques to extend the NV$^-$ ensemble T_2^* by decoupling the NV-bath dipolar interactions. Performing these experiments in the DQ sensing basis is critical to significantly extending T_2^* since stress-gradients commonly contribute similarly to or dominate the ensemble dephasing (see Sections 2.3 and 3.5). Measurements using the stress-gradient-immune DQ basis ensure that, for the nitrogen-doped CVD diamond material considered here, magnetic dipolar interactions between the bath spins and NV sensor spins dominate the ensemble dephasing. In Sec. 5.3.2, the efficacy of spin bath decoupling in as-grown diamond material with negligible [NV] is explored using Samples 3C and 3D. A phenomenological model is introduced to describe the scaling of T_2^* with the magnitude of the spin bath control fields. In Sample 3C, spin bath decoupling during a DQ Ramsey free induction decay (FID) enables a factor sixteen extension in $T_2^*\{\text{DQ}\}$ compared to the native $T_2^*\{\text{SQ}\}$. The presented control techniques, and associated extensions in T_2^*, are purposefully compatible with Ramsey-based static/broadband magnetometry and provide improved magnetic sensitivity as demonstrated in Sec. 5.3.5.

The dipolar spin bath may be decoupled from the NV sensor spins using multi-tone resonant continuous-wave (CW) or pulsed protocols to manipulate the spin bath population associated with different spectral groups. Fig. 5.7 depicts typical pulse sequences for CW and pulsed spin bath decoupling. In pulsed spin bath protocols [82], a multi-frequency RF π-pulse is applied to each of the bath spin resonances

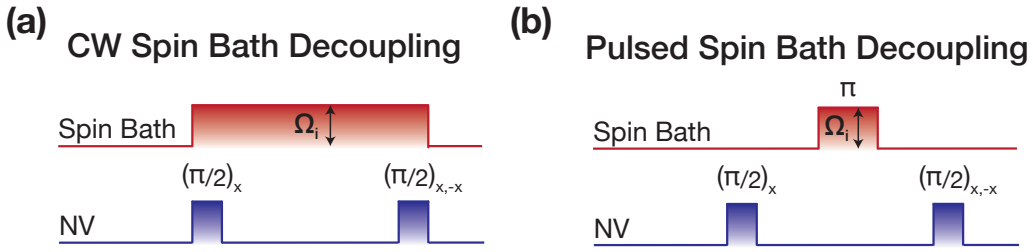

Figure 5.7: **Spin Bath Decoupling Protocols.** **(a)** Depiction of continuous-wave (CW) spin bath decoupling during a DQ or SQ Ramsey sequence. The bath control field typically contains multiple tones resonant with the spin bath resonances to be controlled. The i^{th} driven bath spectral group oscillates with Rabi frequency Ω_i. **(b)** Pulsed spin bath decoupling applies π-pulses resonantly with the bath spin resonances midway through the Ramsey free precession interval.

midway through the NV^- Ramsey sequence, decoupling the bath from the NV sensor spins analogous to a refocusing π-pulse in a spin echo sequence [131]. Alternatively, the bath spins can be driven continuously (CW) [82, 83]. In this case, the Rabi oscillation frequency Ω_{bath} induced by the resonant MW irradiation applied to each spectral group must significantly exceed the characteristic dipolar coupling strength γ between the bath spins and NV sensor spins, i.e., $\Omega_{bath}/\gamma \gg 1$, to achieve effective decoupling. Under this condition, the bath spins undergo many Rabi oscillations during the characteristic dipolar interaction time $1/\gamma$. As a result, the average dipolar-interaction with the bath is incoherently averaged and the NV^- spin dephasing time increases.

5.3.1 Experimental Methods

In the following experiments, the electronic spin bath is decoupled using multi-tone MW irradiation resonant with the electronic spectral groups identified using DEER

ODMR. Although the first-order forbidden resonances (corresponding to electronic-nuclear flip-flops) can also be controlled [95], this is not necessary or efficient when attempting to decouple the electronic spin bath contribution to dephasing.

For decoupling the N_s^0 spin bath in a diamond sample grown with natural abundance ^{14}N, the bath control field consists of six MW tones when the bias magnetic field is aligned with a single crystallographic axis. Under the same magnetic field alignment, only four spectral groups must be manipulated for ^{15}N-enriched diamond samples due to the reduced nuclear spin ($I = 1/2$ instead of $I = 1$). Meanwhile, for an arbitrarily aligned magnetic field, ^{14}N (^{15}N) material may require control of up to twelve (eight) spectrally-distinct resonances. More tenably, if the bias magnetic field has equal projections along all crystal axes, a minimum of three (two) tones are required. Additional tones resonant with other paramagnetic electronic species, such as lattice vacancies, can also be applied as necessary for the given sample.

We now describe the experimental details of generating and calibrating the multi-tone MW field used to control the bath spins. For bias magnetic fields with magnitude $B_0 \approx 5 - 10\,\mathrm{mT}$, the dipolar-allowed N_s^0 bath transitions occur between 100-500 MHz. For the experiments presented here, each tone in the bath control field is synthesized using a dedicated signal generator (see the schematic in Fig. 5.8). While economical signal generators such as the Windfreak SynthNV or TPI-1002-A are employed for the experiments in this section, other solutions, including using arbitrary waveform generators, are expected to be compatible. The multiple synthesized tones are then combined and amplified using a single Minicircuits ZHL-100W-52+ high-power amplifier. A dedicated shorted-loop or planar wave-guide structure delivers

the bath control field to the diamond sample. Due to the technical demands of combining after amplification and amplifier bandwidth constraints, the NV^- control fields are synthesised and delivered to the diamond sample separately.

Spin bath control field calibration – For measurements of the NV^- ensemble T_2^* as a function of the applied bath control field magnitude it is convenient for all spectral groups to be driven with the same bath Rabi frequency. For pulsed spin bath decoupling, calibration of the bath Rabi per group is critical to ensure that the selected pulse duration corresponds to a π-pulse on all bath spins (assuming all tones pass through the same switch as shown in Fig. 5.8). The bath Rabi frequency for each spectral group can be measured independently using a DEER Rabi scheme in which the duration of the bath pulse is swept while all other parameters remain fixed. To isolate the Rabi oscillations of a particular group while accounting for the inter-related distribution of power between the other tones in the amplifier, a single tone is resonant at a time, while the other tones are sufficiently detuned to not drive Rabi oscillation. Such DEER Rabi measurements are then performed iteratively, adjusting the output amplitude of one signal generator and measuring the resulting Rabi frequency for all spectral groups. A gradient-descent-based algorithm is used to approach a target Rabi frequency for all spectral groups. Residual variations in the Rabi frequency across groups are typically about 5% of the reported average bath Rabi $\Omega_{\text{bath}}^{\text{avg}}$.

AC Zeeman Shifts – The control field applied to one group of bath spins can shift the resonances of the other groups via the AC Zeeman effect (analogous to the AC Stark effect for systems sensitive to AC electric fields). As a consequence,

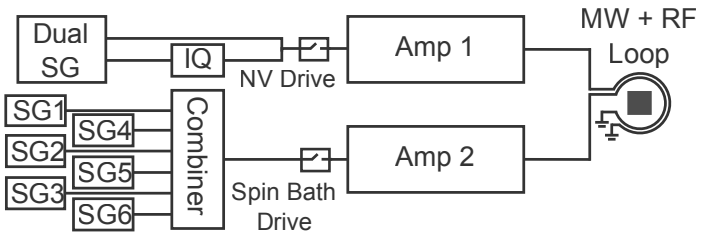

Figure 5.8: **Microwave synthesis and delivery schematic.** For NV spin state control: Single and two-tone signals are generated using a dual channel Windfreak Technology Synth HD signal generator. One channel includes a Marki IQ-1545 mixer to manipulate the relative phase between both channels. A single Minicircuits ZASWA-2-50DR+ switch is used to generate the NV control pulses before amplification with a Minicircuits ZHL-16W-43 amplifer. The NV control fields are delivered to the diamond sample using a fabricated microwave waveguide (diameter 500m). For spin bath control: Up to eight single channel Windfreak Technology Synth NV signal generators are combined before passing through a switch and a Minicircuits ZHL-100W-52 amplifier. The amplified field is delivered via a grounded cooper loop (1 mm diameter).

the applied tones no longer resonantly address the other, intended groups. The AC Zeeman shift $\Delta_{\text{AC Zee.}}$ induced by an off-resonant driving field scales approximately proportional to $\delta_{\text{AC Zee.}} \propto \Omega_{\text{res}}^2/\delta$ where Ω_{res} is the on-resonance Rabi frequency and δ is the detuning between the bath control field frequency and bath spectral group. For ^{15}N diamond material in a 10 mT bias field aligned with one of the for possible defect orientations, the nearest resonances are 15 MHz apart (see Fig. 5.3(b)) such that a detuned driving field with $\Omega_{\text{res}} = 5$ MHz produces a 1 MHz shift in the spectral group resonance frequency.

The AC Zeeman-induced shifts reduce the spin bath decoupling efficacy if not accounted for during calibration. The constituent spin bath control field frequencies can be crudely optimized by maximizing the measured T_2^* while dithering each driving tone iteratively, since the required corrections are typically small compared to the

overall detuning. Using the measured bath Rabi frequency and resonance frequency for each spectral group, the AC Zeeman-shifts can also be calculated via numerical simulations (the analytical result is only approximate since it assumes a far-detuned limit which is no longer valid for this system).

The AC Zeeman shifts induced by the spin bath control fields on the NV$^-$ spin resonances may also be of concern for high-sensitivity applications of the technique. The estimated shifts in NV$^-$ resonance frequencies from a bath field with $\Omega_0 = 5\,\text{MHz}$ detuned by about $\sim$2.87 GHz is a non-negligible $\approx$10 kHz. However, this is generally considered a minimal concern for magnetic sensing because (a) the shifts are largely common-mode and therefore suppressed in the DQ sensing basis and (b) for CW spin bath decoupling the shifts are static. Nonetheless, it is likely beneficial to operate with sufficient spin bath decoupling to saturate at the next dominant dephasing mechanism such that the NV$^-$ T_2^* is not vulnerable to fluctuations in the spin bath control field amplitude. This approach is also generally advantageous for robustness against other factors such as drift in the spin bath resonance frequencies.

5.3.2 Extending T_2^* in As-Grown Diamond Material

This section presents experimental results employing CW spin bath decoupling to extend the ensemble T_2^* of as-grown diamond Samples 3C and 3D. Fig. 5.9(a) depicts DQ and SQ Ramsey FID signal for Sample 3C ([N]$\approx$ 0.75 ppm) with and without multi-tone bath control applied. For these data, all six electronic N_s^0 spectral groups experience an average bath Rabi frequency of 1 MHz. The Ramsey FID decay signals

are fit to the functional form:

$$S(\tau) = \mathrm{e}^{-(\tau/T_2^*)^p} \sum_{i=1}^{n} A_i sin(2\pi f_i \tau + \phi_i) \tag{5.4}$$

where T_2^* is the familiar ensemble dephasing time, p is the decay shape parameter, A_i is the oscillation amplitude for the signal from each of the n hyperfine-split populations with detunings f_i and phases ϕ_i. In the following discussion the decay shape parameter is constrained to be $p = 1$ unless otherwise noted (see Sec. 5.3.3 for example). The $T_2^*\{\mathrm{SQ}\}$ extracted from the data in Fig. 5.9 doesn't respond significantly to the applied bath decoupling protocol because the ensemble dephasing is dominated by stress-gradients across the interrogated volume of diamond. However, in the DQ sensing basis, the $T_2^*\{\mathrm{DQ}\}$ exhibits a dramatic 16x increase compared to the observed "bare" $T_2^*\{\mathrm{SQ}\}$, leaping from 1.80(6) μs to 29.2(7) μs.

The transition between the bare $T_2^*\{\mathrm{DQ}\}$ without spin bath decoupling to the extended $T_2^*\{\mathrm{DQ, CW}\}$ demonstrated in Fig. 5.9(a) warrants further exploration in order to both elucidate the relevant physical parameters as well as determine the technical requirements placed on the experimental apparatus (e.g., what Ω_{bath} is required for decoupling). Therefore, we also characterized the efficacy of CW spin bath decoupling for extending T_2^* in both the SQ and DQ bases as a function of the average N_s^0 Rabi frequency $\Omega_{N_s^0}$. These data are shown in Fig. 5.9(b) for Sample 3C. As expected, the $T_2^*\{\mathrm{SQ}\}$, which is dominated by non-spin-bath-induced dephasing, does not depend on $\Omega_{N_s^0}$. In contrast, $T_2^*\{\mathrm{DQ}\}$ exhibits an initial, rapid increase and then saturates at $T_{2,DQ}^* \approx 27\,\mu\mathrm{s}$ for $\Omega_N \gtrsim 1\,\mathrm{MHz}$.

To explain the observed trend, we introduce a model that distinguishes between

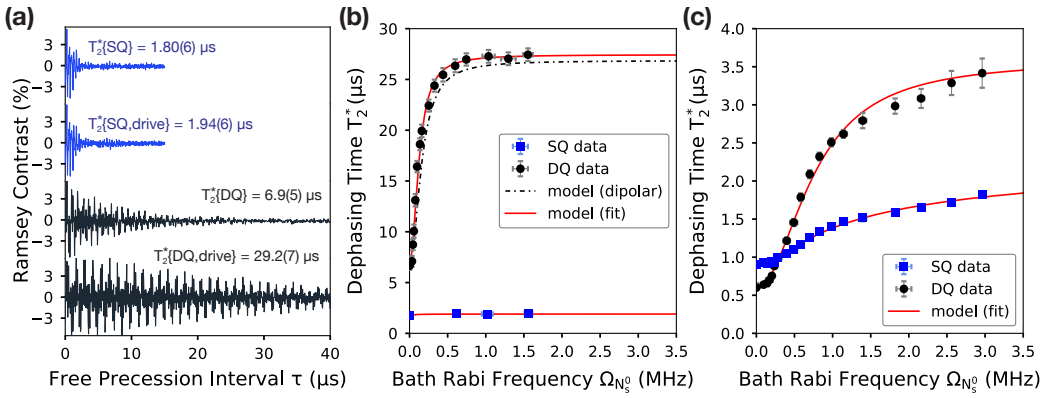

Figure 5.9: **CW spin bath decoupling in the SQ and DQ bases. (a)** NV Ramsey free induction decay (FID) measurements for Sample 3C ($B_0 = 8.5\,\mathrm{mT}$). Comparison of time-domain data and resulting fit values for the NV ensemble T2* for the SQ coherence (blue, first from top), the SQ coherence with spin-bath drive (blue, second from top), the DQ coherence with no drive (black, third from top), and the DQ coherence with spin-bath drive (black, fourth from top) reveals a 16.2× improvement of T_2^* with spin bath decoupling with the DQ sensing compared to SQ with no drive. **(b)** T_2^* extracted from Ramsey FID measurements in the SQ (blue) and DQ (black) bases for different average spin-bath drive Rabi frequencies (Sample 3C at $B_0 = 8.5\,\mathrm{mT}$). The black dashed-dotted line is calculated using the model presented in Eqn. 5.5 and Eqn. 5.6 with the values reported in the main text. The red solid line is a fit of the same model to the T_2^* data (see main text for details). **(c)** Same as (b) but for Sample 3D ($B_0 = 10.3\,\mathrm{mT}$).

(i) NV$^-$ ensemble dephasing due to the controlled N_s^0 bath spins, which depends upon bath drive strength $\Omega_{\mathrm{N}_s^0}$, and (ii) dephasing from other, bath-control-independent sources, including stress-gradients and ^{13}C nuclear spins:

$$\frac{1}{T_2^*} = \frac{1}{T_2^*\{\mathrm{N}_s^0\}(\Omega_{\mathrm{N}_s^0})} + \frac{1}{T_2^*\{other\}}. \tag{5.5}$$

Taking the coherent dynamics of the bath drive into account, the data is well described

by the functional form:

$$\frac{1}{T_2^*\{\mathrm{N}_s^0\}(\Omega_{\mathrm{N}_s^0})} = \Delta m \times \gamma_{NV-N} \frac{\delta_{\mathrm{N}_s^0}^2}{\delta_{\mathrm{N}_s^0}^2 + \delta_{\mathrm{N}_s^0}^2}, \tag{5.6}$$

where the effective magnetic field produced by the ensemble of N_s^0 spins is modeled as a Lorentzian line shape with spectral width $\delta_{N_s}{}^0$ (half width at half max) and a maximum γ_{NV-N} at zero drive frequency ($\Omega_{N_s}{}^0 = 0$). The parameter $\Delta m = 1(2)$ is the change in spin quantum number in the SQ (DQ) basis. Although we find that NV$^-$ and N_s^0 spins have comparable T_2^* ($\gamma_{NV-N} \approx \gamma_{N-N}$, see Sec. 5.1.4), the effective linewidth $\delta_{\mathrm{N}_s^0}$ relevant for bath decoupling is increased due to imperfect overlap of the N_s^0 spin resonances caused by a small misalignment angle of the applied bias magnetic field.

We define three spin bath decoupling regimes: (1) no bath decoupling, (2) an intermediate regime where the average dipolar coupling between bath and NV sensor spins, γ_{NV-N} is comparable to $\Omega_{\mathrm{N}_s^0}$, and (3) a strong-decoupling regime where $\Omega_{\mathrm{N}_s^0} \gg \delta_{\mathrm{N}_s^0}$. In the strong-driving regime, the N_s^0 spin ensemble is coherently driven and the resulting magnetic field noise spectrum is detuned away from the zero-frequency component, to which NV Ramsey measurements are maximally sensitive [71]. In this regime, the NV$^-$ ensemble T_2^* increases $\propto \Omega_{\mathrm{N}_s^0}^2/\delta_{\mathrm{N}_s^0}^2$. However, in the intermediate regime with $\Omega_N \lesssim \delta_N$, the N_s^0 spin ensemble is inhomogeneously driven and the dynamics of the spin bath cannot be described by coherent driving. Nonetheless, $1/T_2^*$ approaches γ_{NV-N} in the limit $\Omega_{\mathrm{N}_s^0} \to 0$, which is captured by the Lorentzian model.

Using the N_s^0-related dipolar estimate for Sample 3C, $\gamma_{NV-N} \approx 2\pi \times 7\,\mathrm{kHz}$,

$\delta_{N_s^0} \approx 80\,\text{kHz}$ extracted from DEER measurements (see Sec. 5.1.4), and a saturation value of $T^*_{2,other} \approx 27\,\mu\text{s}$, we combine Eqns. 5.5 and 5.6 and plot the calculated T_2^* as a function of $\Omega_{N_s^0}$ in Fig. 5.9(b) (black, dashed line). The reasonable agreement between the model and our data in the DQ basis suggests that Eqns. 5.5 and 5.6 capture the dependence of T_2^* on drive field magnitude (i.e., Rabi frequency). Alternatively, we fit the model to the DQ data (red, solid line) and extract $\gamma^{fit}_{NV-N} = 2\pi \times 9.3(2)$kHz and $\delta^{fit}_{N_s^0} = 60(3)\,\text{kHz}$, in reasonable agreement with our estimated parameters. In summary, the results from Sample 3C demonstrate that spin bath decoupling in the DQ basis suppresses inhomogeneous NV$^-$ ensemble dephasing due to both interactions with the N_s^0 spin bath and stress-gradients.

Fig. 5.9(c) presents similar measurements using Sample 3D with $[^{15}\text{N}] = 7.7(7)\,\text{ppm}$ and $[^{14}\text{N}] = 0.50(5)\,\text{ppm}$. With the increased nitrogen density, interactions with the N_s^0 bath dominate NV$^-$ ensemble dephasing, and $T_2^*\{SQ\}$ and $T_2^*\{DQ\}$ both exhibit a clear dependence on spin bath Rabi frequency $\Omega_{N_s^0}$. With no drive ($\Omega_{N_s^0} = 0$), $T_2^*\{DQ\} \approx T_2^*\{SQ\}/2$, as expected for dephasing dominated by a paramagnetic spin environment and the twice higher dephasing rate in the DQ basis [79, 80, 132]. Note that this result is in contrast to the observed DQ basis enhancement of T_2^* at lower nitrogen density for Sample 3C (Fig. 5.9(b)). While the T_2^* for both bases scales less quickly with $\Omega_{N_s^s}$ then for Sample 3C (due to the stronger dipolar interaction strength), we observe that T_2^* in Sample 3D increases more rapidly as a function of spin bath drive amplitude in the DQ basis than in the SQ basis, such that $T_2^*\{DQ\}$ surpasses $T_2^*\{SQ\}$ with sufficient $\Omega_{N_s^s}$. We attribute the T_2^* saturation in the SQ basis ($\simeq 1.8\,\mu\text{s}$) to stress inhomogeneities in this sample. Meanwhile, the longest observed

T_2^* in the DQ basis is $\simeq 3.4\,\mu s$, which is below the expected saturation of about $9\,\mu s$ due to the 30(3) ppm of ^{13}C spins and 0.50(5) ppm residual $[^{14}N_s^0]$ incorporated during growth (see Tab. 5.4). This difference between expected and observed saturation results in an unidentified $\approx 180\,ms^{-1}$ contribution to the dephasing rate. Further experimental and theoretical work is warranted to definitively account for this source of dephasing. Possible explanations include a technical limitation such as insufficient management of AC Zeeman effects, inaccurate SIMS measurements of $[^{13}C]$ or $[^{14}N_s^0]$, or an additional paramagnetic species we have not yet properly accounted for in the diamond spin bath.

5.3.3 Ramsey Decay Shape for the Intermediate Spin Bath Decoupling Regime

For the analysis in the previous section, the decay shape parameter was constrained to a mono-exponential profile ($p = 1$) when extracting T_2^* to better compare changes in the dephasing time despite additional changes in decay shape. While Eqns. 5.5 and Eqns. 5.6 capture the dependence of T_2^* with $\Omega_{N_s^s}$ reasonably well, the assumption of exponential decay profile in the intermediate decoupling regime is not valid. In this regime where $\Omega_{N_s^s} \approx \gamma_{NV-N}$, bath spins which are more weakly coupled to the NV$^-$ sensor spins (further away in the lattice) are decoupled, while dipolar interactions due to nearby bath spins remain. This results in a rapid initial decay in the Ramsey FID signal, followed by a slower-than-expected decay at longer times compared to simple exponential decay.

When fitting measured Ramsey FID data in this intermediate regime, the ex-

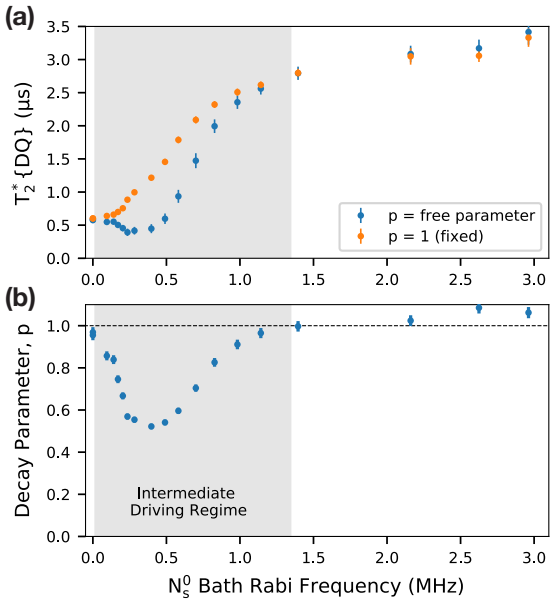

Figure 5.10: **Ramsey decay shape with spin bath decoupling.** **(a)** T_2^* extracted from NV Ramsey FID data (Sample 3D) as a function of average spin bath Rabi frequency. The extracted T_2^* values, when the decay shape parameter p is included in the fit as a free parameter, are shown in blue. The resulting T_2^* when p is fixed to $p = 1$ are shown in orange. **(b)** Extracted decay shape parameter p as a function of the average spin bath Rabi frequency when included as a free parameter in model. With increasing bath Rabi frequency, p decreases from unity towards a minimum of $p \sim 0.5$ before increasing back to $p \sim 1$ for spin bath Rabi frequencies exceeding 1 MHz.

tracted decay shape parameter is $p < 1$, as shown in Fig. 5.10(b). As a function of the average Rabi frequency $\Omega_{N_s^s}$, the decay shape parameter, p, decreases to a minimum value of approximately $p \approx 0.5$ around 400 kHz. The change in decay also modifies the extracted T_2^*. In the strong-decoupling regime, the decay shape parameter saturates at approximately $p \approx 1$ as even strongly interacting bath spins nearby to an NV sensor spin are decoupled. The sensitivity and dependence of the decay shape parameter highlights its value in understanding microscopic ensemble properties.

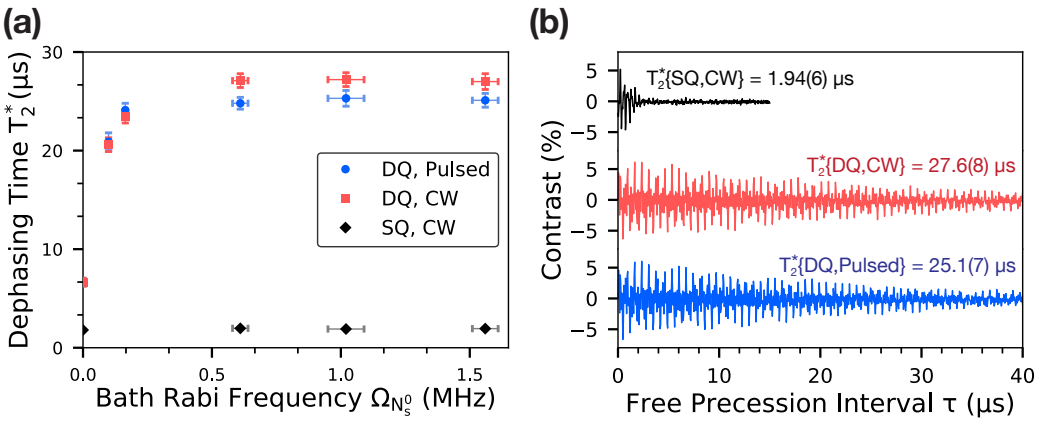

Figure 5.11: **Comparison of CW and pulsed spin bath decoupling experiments using Sample 3C. (a)** Measured T_2^* as a function of bath Rabi frequency for DQ CW (red squares) and DQ pulsed (blue circles) spin bath decoupling, with the SQ CW results (black diamonds) again included for reference. **(b)** Measured Ramsey FID decay in the DQ sensing basis for CW and pulsed driving ($\Omega_{N_s^0} = 1.5\,\text{MHz}$). The decay for CW driving in the SQ basis is included for reference.

5.3.4 Pulsed versus CW Spin Bath Decoupling

As noted earlier in this chapter, both continuous-wave (CW) and pulsed driving can decouple the electronic spin bath from the NV$^-$ sensor spins (see Fig. 5.7). In CW-decoupling, the bath spins are driven continuously such that they undergo many Rabi oscillations during the characteristic interaction time $1/\gamma_{NV-N}$, and thus the time-averaged NV-N dipolar interaction approaches zero. For pulsed-decoupling, π-pulses resonant with spin transitions in the bath are applied midway through the NV Ramsey free precession interval, to refocus bath-induced dephasing.

Fig. 5.11(a) illustrates the measured $T_2^*\{\text{DQ}\}$ as a function of $\Omega_{N_s^s}$ for Sample 3C using both methods. Pulsed-decoupling yields similar T_2^* improvements to CW-decoupling over the measured range of bath Rabi frequencies. Fig. 5.11(b) compares T_2^* for Sample 3C for both schemes at maximum bath drive strength $\Omega_N = 1.5\,\text{MHz}$

(for pulsed-decoupling, $\tau_\pi \equiv 1/2\Omega_{N_s^s}$). Both decoupling schemes result in comparable T_2^* improvements ($13-15\times$) over the non-driven SQ measurement, which is shown for reference. We attribute the slightly shorter $T_2^*\{\mathrm{DQ}\}$ achieved with pulsed-decoupling to decoherence caused by temporal variations in the magnetic environment which are not decoupled. In contrast, CW-decoupling protocols also mitigate decoherence sources and lead to extensions in T_2 when used in conjunction with echo-type pulse sequences suitable for AC magnetic field sensing.

Despite the similar improvements in T_2^* achieved using both methods, pulsed driving can reduce heating of the MW delivery loop and diamond sample - an important consideration for temperature sensitive applications. For this reason, pulsed driving may be preferable in such experiments despite the need for π-pulse calibration across multiple resonances and slightly reduced performance.

5.3.5 Sensitivity Improvement with Spin Bath Decoupling

This section demonstrates that the extended T_2^* achieved when combining spin bath decoupling techniques with DQ coherence magnetometry protocols translate to improved magnetic sensitivity without degrading any other sensitivity-relevant properties. Fig. 5.12(a) compares the accumulated phase for SQ, DQ, and DQ plus spin bath decoupling measurements in a tunable static magnetic field of amplitude B_{DC}, for Sample 3C. Sweeping B_{DC} leads to a characteristic observed oscillation of the Ramsey signal $S \propto C\sin(\phi)$, where C is the measurement contrast and $\phi = \Delta m \times \gamma_{NV} B_{DC} \tau$ is the accumulated phase during the free precession interval $\tau \approx T_2^*$. Choosing $\tau_{SQ} = 1.308\,\mu\mathrm{s}$ and $\tau_{DQ+Drive} = 23.99\,\mu\mathrm{s}$, we find a $36.3(1.9)\times$

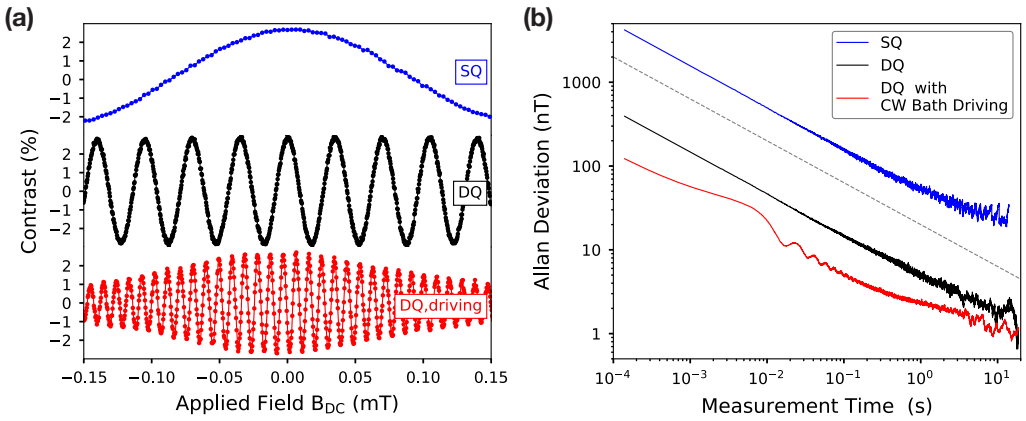

Figure 5.12: **DC magnetic field sensing and Allan deviation. (a)** DC magnetometry curves for SQ, DQ, and DQ with spin bath decoupling in Sample 3C, produced by sweeping the magnitude of a coil-generated applied magnetic field (in addition to the fixed bias field) while the free precession interval is set to $\tau_{\mathrm{SQ}} = 1.308\,\mu\mathrm{s}$ (blue, top), $\tau_{\mathrm{DQ}} = 6.436\,\mu\mathrm{s}$ (black, middle), and $\tau_{\mathrm{DQ,CW}} = 23.990\,\mu\mathrm{s}$ (red, bottom). The amplitude for the DQ+CW decoupling data (red) decays with increasing applied magnetic field B_{DC} because the spin bath transitions shift out of resonance with the control fields and T_2^* decreases. **(b)** Allan deviation using the same fixed values from (a) for measurements using SQ (blue), DQ (black), and DQ with CW decoupling (red). The external field strength was tuned to sit on a zero crossing of the respective DC magnetometry curves in (a) for sine magnetometry. The black dashed line is a guide to the eye indicating $T^{-1/2}$ scaling where T is the total measurement time.

faster oscillation period (at equal measurement contrast) when DQ and spin bath decoupling are both employed, compared to a SQ measurement. This enhancement in phase accumulation, and hence DC magnetic field sensitivity, agrees well with the expected improvement ($2 \times \tau_{DQ+Drive}/\tau_{SQ} = 36.7$).

Assuming a signal-to-noise ratio of unity, the minimum detectable magnetic field δB_{min} in a Ramsey measurement is given by [2, 80]

$$\delta B_{min} \approx \frac{\delta S}{\max|\frac{\partial S}{\partial B}|}, \tag{5.7}$$

where the Ramsey signal S is

$$S = C(\tau)\sin(\gamma_{NV} B_{DC} \tau). \tag{5.8}$$

Here, $C(\tau) = C\exp\left(-(\tau/T_2^*)^p\right)$ is the time-dependent measurement contrast defined via the NV spin-state-dependent fluorescence visibility, γ_{NV} is the NV gyromagnetic ratio, B_{DC} is the magnetic field to be sensed, and τ is the sensing time during which the NV^- sensor spins accumulate phase. The term $\max|\frac{\partial S}{\partial B}|$ is the maximum slope of the Ramsey signal:

$$\max|\frac{\partial S}{\partial B}| = C(\tau)\gamma_{NV}\tau. \tag{5.9}$$

Assuming uncorrelated, Gaussian noise, $\delta S = \sigma(t)/\sqrt{n_{meas}}$ is the standard error of the contrast signal, which improves with the number of measurements n_{meas}. Including a dead time τ_D that accounts for time spent during initialization of the NV ensemble and readout of the spin-state-dependent fluorescence during a single measurement, $n_{meas} = T/(\tau + \tau_D)$ measurements are made over the total measurement time T. δB_{min} is then found to be

$$\delta B_{min} = \frac{\sigma\sqrt{\tau + \tau_D}}{C(\tau)\gamma_{NV}\tau\sqrt{T}}, \tag{5.10}$$

and the sensitivity is given by multiplying δB_{min} by the bandwidth $\sqrt{T}$ and including

a factor $\Delta m = 1(2)$ for the SQ (DQ) basis:

$$\eta = \frac{\delta B_{min}\sqrt{T}}{\Delta m} = \frac{\sigma\sqrt{\tau+\tau_D}}{\Delta m \times C(\tau)\gamma_{NV}\tau}. \tag{5.11}$$

Note that in the ideal case of $\tau_D \ll \tau$, $\frac{\sqrt{\tau+\tau_D}}{\tau} \approx 1/\sqrt{\tau}$ and the sensitivity η scales $\propto \tau^{-1/2}\exp{(\tau/T_2^*)^p}$. The optimal sensing time in the Ramsey experiment is then $\tau_{opt} \approx T_2^*/2$ for p = 1-2. However, in the more realistic case, $t_D \sim \tau$, the improvement of η with increasing τ approaches a linear scaling and $\eta \propto \tau^{-1}\exp{(\tau/T_2^*)^p}$ for $t_D \gg \tau$. The optimal sensing time then becomes $\tau_{opt} \approx T_2^*$. Consequently, the measured increase in sensitivity may often exceed the enhancement estimated from the idealized case without accounting for overhead time.

With Eqn. 5.11 we calculate and compare the sensitivities for the three measurement modalities (SQ, DQ, and DQ + spin-bath-control) applied to Sample 3C. Using $C \approx 0.026$, which remains constant for the three schemes (see Fig.5.12(a)), sensing times $\tau_{SQ} = 1.308\,\mu s$, $\tau_{DQ} = 6.436\,\mu s$, and $\tau_{DQ+Drive} = 23.99\,\mu s$, standard deviations $\sigma_{SQ} = 0.0321$, $\sigma_{DQ} = 0.0324$, and $\sigma_{DQ+Drive} = 0.0325$ calculated from 1 s of data, fixed sequence duration of $\tau + \tau_D = 70\,\mu s$, and $\gamma_{NV} = 2\pi \times 28\,\mathrm{GHz/T}$, the estimated sensitivities for the SQ, DQ and DQ+Drive measurement schemes are $\eta = 70.7$, 6.65, and $1.97\,\mathrm{nT}/\sqrt{\mathrm{Hz}}$, respectively. In summary, we obtain an 10× improvement in DC magnetic field sensitivity in the the DQ basis, relative to the conventional SQ basis, and a 35× improvement using the DQ basis with spin bath decoupling. Note that this enhancement greatly exceeds the expected improvement when no dead time is present ($\tau_D \ll \tau$) and is attributed to the approximately linear increase in sensitivity with sensing times $\tau \lesssim \tau_D$. Lastly, we plot the Allan deviation for the three schemes

in Fig. 5.12(b) showing a $T^{-1/2}$ scaling for a measurement time of $\approx 1\,\mathrm{s}$ and the indicated enhancements in sensitivity.

5.3.6 Extending T_2^* in NV-Rich Diamond Material

This section discusses spin bath decoupling techniques applied to irradiated and annealed diamond material with non-negligible [NV$^-$]. After outlining a model for estimating the NV$^-$ ensemble T_2^* including dipolar interactions between NV$^-$ spins, initial measurements are presented. The following discussion is primarily intended to motivate the need for future experimental work to better understand T_2^* in NV-rich diamond material.

With the [N_s^0] concentration reduced post-irradiation and annealing, spin bath decoupling is expected to become easier, i.e., lower bath Rabi frequencies are required for CW decoupling. As will be explored in the following discussion, the next dominant dephasing source in NV-rich material after N_s^0 dipolar interactions are ideally dipolar interactions between the NV$^-$ sensor spins themselves. However, commonly operating DC NV$^-$ ensemble magnetometers in this NV-limited T_2^* regime remains an outstanding technical challenge.

As described in Sec. 2.2.3, the NV$^-$ population (and associated dephasing contributions) can be sub-divided into either same ($NV^-_{\parallel}$) or different spin groups ($NV^-_{\nparallel}$) based upon their resonance frequencies. NV$^-$ spins belonging to the same group are expected to exhibit stronger dipolar interactions ($A_{NV_{\parallel}} \sim 247\,\mathrm{ms^{-1}ppm^{-1}}$) compared to those in different groups ($A_{NV_{\nparallel}} \sim 165\,\mathrm{ms^{-1}ppm^{-1}}$) as motivated in Sec. 2.2.3. Assuming a bias magnetic field aligned with a single orientation of NV$^-$ spins, we refer

$[N_s]$ (ppm)	[NV] (ppm)	[NV$^-$] (ppm)	[NV^0] (ppm)	ψ ([NV$^-$]/[NV])
13.3(3)	2.8(2)	2.0(2)	0.80(1)	0.72(5)

Table 5.5: **Defect concentrations and NV$^-$ charge fraction** determined via FTIR and UV-Vis absorption measurements for a diamond sample grown using the same synthesis process as Sample 5C. Reported uncertainties indicate the standard deviation in measured values across 5 samples grown using the same synthesis process.

to these aligned-NV$^-$ spins as those in the same group ($NV_{\parallel}$). These spins, which account for one quarter of the total NV$^-$ population, will be used for sensing, while NV$^-$ spins along the other three orientations will not be used for sensing ($NV_{\nparallel}$).

The expected T_2^* assuming only dephasing mechanisms due to an electronic spin bath composed of N_s^0 and NV$^-$ can be estimated using a toy model as,

$$\begin{aligned}\frac{1}{T_2^*\{\text{elec. spin bath}\}} &\approx A_{N_s^0}\cdot[N_s^0] + A_{NV_{\parallel}^-}\cdot[NV_{\parallel}^-] + A_{NV_{\nparallel}^-}\cdot\zeta[NV_{\nparallel}^-] \\ &\approx A_{N_s^0}\cdot\chi[N_s] + A_{NV_{\parallel}^-}\cdot(\zeta_{\parallel})\psi_{\parallel}[NV_{\parallel}^-] + A_{NV_{\nparallel}^-}\cdot\zeta_{\nparallel}\psi_{\nparallel}[NV_{\nparallel}^-]\end{aligned} \tag{5.12}$$

where $A_{N_s^0} = 101(12)\,\text{ms}^{-1}\text{ppm}^{-1}$, χ is the N_s charge fraction, $\zeta_{\parallel}$ ($\zeta_{\nparallel}$) is the fraction of same (different) group NV$^-$ spins not in $m_s = 0$ during the DQ Ramsey measurement, and $\psi_{\parallel,\nparallel}$ are the same and different-group NV charge fractions ([NV$^-$]/(NV$^-$+NV^0)). Using Eqn. 5.12 to anticipate the T_2^* for an NV-rich sample is challenging because it requires knowledge of the fraction of NV spins along all four axes initialized into $m_s = 0$ by the 532 nm pump laser as well as the NV and N_s charge fractions across a typically inhomogeneous excitation profile (e.g., a Gaussian laser beam spot). These quantities depend strongly on experimental parameters such a optical illumination intensity and polarization due to the ionization of N_s^0 and NV$^-$.

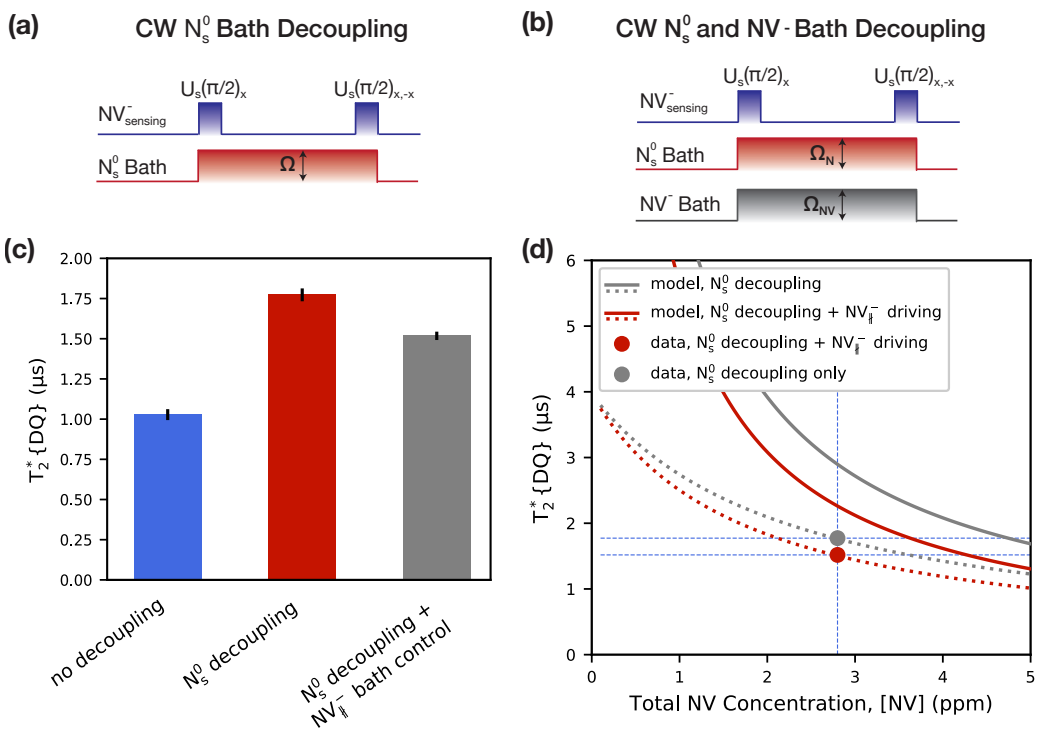

Figure 5.13: **Spin bath control in an NV-rich sample.** **(a)** Schematic representation of CW N_s^0 bath decoupling. **(b)** Schematic representation of CW N_s^0 bath decoupling in addition to CW driving of one of the $NV^-_{\nparallel}$ spectral groups not used for sensing. **(c)** Left to right: T_2^* extracted from Sample 5C without any spin bath control, with N_s^0 bath decoupling, and with N_s^0 bath decoupling as well as control of the $NV^-_{\nparallel}$ population. **(d)** Comparison of the measured $T_2^*\{\mathrm{DQ}\}$ with bath control to the model presented in Eqn. 5.12. The solid red and grey lines depict the estimate $T_2^*\{\mathrm{DQ}\}$ without $NV^-_{\nparallel}$ driving, $\psi_{\nparallel} = \psi_{\parallel} = 0.7$, and $\zeta_{\nparallel} = 0.3$ ($\zeta_{\parallel} = 0.7$). The dashed red and grey lines depict the estimate $T_2^*\{\mathrm{DQ}\}$ with $NV^-_{\nparallel}$ driving such that $\zeta_{\nparallel} = 0.5$. Solid lines indicate the estimated $T_2^*\{\mathrm{DQ}\}$ including dephasing contributions from the ^{13}C spin bath and residual magnetic field gradient. Dashed lines indicate the estimated $T_2^*\{\mathrm{DQ}\}$ including an additional unknown dephasing source of $\approx 0.1\,\mu\mathrm{s}^{-1}$. The dashed vertical blue line indicates $[\mathrm{NV}] = 2.8$ ppm.

To estimate $[N_s^0]$, $[NV^-_{\parallel}]$, and $[NV^-_{\nparallel}]$ under experimental conditions, we begin by considering diamond material synthesized using a well characterized process for which FTIR, UV-vis, and SIMS measurements are available (see Chapter 6 or Ref. [39] for further details). These data provide initial estimates for the concentrations and charge

distribution of different species in the absence of optical excitation. The estimated values for one such sample grown with a process yielding [N] $\approx$ 16 ppm and then irradiated and annealed to produce [NV]= 2.8(2) ppm are shown in Tab. 5.5 (Sample 5C).

To highlight the importance of accounting for dephasing in this NV-rich sample, we first consider the expected T_2^* for the as-grown material. With a total nitrogen concentration of about 16 ppm, we would expect Sample 5C to exhibit a $T_2^*\{\mathrm{SQ}\} \approx 600$ ns and $T_2^*\{\mathrm{DQ}\} \approx 300$ ns based on the scaling determined in Sec. 2.2.1. This estimate agrees reasonably well with measurements of Sample 5C before irradiation and annealing ($T_2^*\{\mathrm{DQ}\} \approx 200$ ns). However, this as-grown estimate for T_2^* is dramatically shorter than the measured value of $T_2^*\{\mathrm{DQ}\} \approx 1\,\mu$s for Sample 5C after irradiation and annealing. Thus, we explore must a refined estimate using Eqn. 5.12 to attempt to understand the post-treatment T_2^*.

The charge fractions noted in Tab. 5.5 are measured in the absence of optical illumination using FTIR and UV-Vis spectroscopy and should provide an upper-bound for our estimates since increasing optical intensities result typically in a degraded ensemble NV charge fraction [77, 78]. Experimentally determining the NV charge fraction per group, the fraction of NV^- pumped into $m_s = 0$, and the N_s charge fraction under optical illumination is a difficult task. In the case of the N_s charge fraction, direct NV-based measurements in-situ are not currently expected to be possible. In the following analysis, we crudely assume that the N_s charge fraction and NV charge fraction (for both groups) are all approximately the same, $\chi \approx \psi_{\|} \approx \psi$ and similar to the FTIR and UV-Vis values measured without illumination. We additionally

assume a 70% initialization fraction into $m_s = 0$ for both NV$^-$ groups after optical pumping [40]. This yields $\zeta_{\nparallel} \approx 0.7$ and $\zeta_{\parallel} \approx 0.3$.

Using these ζ estimate, along with $\chi \approx \psi_{\parallel} \approx \psi \approx 0.7$ from Tab. 5.5, Eqn. 5.12 yields an estimated $T_2^*\{\mathrm{DQ}\}$ of about 450 ns. Although this is modestly longer than the as-grown estimate, it is significantly shorter than the measured value of $T_2^*\{\mathrm{DQ}\} = 1.03(3)$ µs using an average illumination intensity multiple order of magnitude below saturation intensity (see Fig. 5.13(c)).

From this discrepancy, it is apparent that our toy model proposed in Eqn. 5.12, at least with the initial estimated parameters above, is insufficient. Evaluating the dependence of Eqn. 5.12 to changes in the $\psi_{\parallel}$, $\psi_{\parallel}$, ζ, and χ reveals that to achieve estimated T_2^* consistent with observations requires a reduction in $[\mathrm{N}_s^0]$, presumably by tuning the N_s^0 charge fraction. Decreasing the N_s^0 charge fraction estimate such that $\chi \approx 0.22$, while $\psi_{\parallel}$ and $\psi_{\nparallel}$ remain unchanged, yields an estimated $T_2^*\{\mathrm{DQ}\}$ which agrees with the observed value within uncertainty. Due to a lack of experimental data for the N_s^0 charge fraction under 532 nm in similar samples, it remains unclear whether this assumption is physically realistic. Tuning the NV charge fraction yields more modest changes and is not sufficient on its own to account for the observed $T_2^*\{\mathrm{DQ}\}$.

From the results above, it is apparent that without decoupling, dipolar interactions between the N_s^0 bath and NV$^-$ sensor spins remain a significant source of NV$^-$ ensemble dephasing for the present diamond sample (Sample 5C). In the following discussion, CW spin bath decoupling is employed to mitigate the N_s^0-related contribution to dephasing. Preliminary measurements of the change in $T_2^*\{\mathrm{DQ}\}$ under CW

spin bath decoupling are shown in Fig. 5.13(c) for an average bath Rabi frequency of 1 MHz. With decoupling of the N_s^0 bath spins using the protocol in Fig. 5.13(a), the $T_2^*\{\mathrm{DQ}\}$ increases from 1.03(3) μs to a value of 1.77(4) μs.

We can compare this result to the expected T_2^*-limit imposed by dipolar interactions between the NV$^-$ spins suggested by,

$$\frac{1}{T_2^*\{\mathrm{NV}\}} \approx \mathrm{A}_{\mathrm{NV}^-_{\parallel}} \cdot \zeta_{\parallel}\psi_{\parallel}[\mathrm{NV}_{\parallel}] + \mathrm{A}_{\mathrm{NV}_{\nparallel}} \cdot \zeta_{\nparallel}\psi_{\nparallel}[\mathrm{NV}_{\nparallel}] \tag{5.13}$$

which, assuming $\psi_{\parallel} \approx \psi_{\nparallel} \approx 0.7$, $\zeta_{\nparallel} = 0.3$, and $\zeta_{\parallel} = 0.7$, suggests a $T_2^*\{\mathrm{DQ}\}$ exceeding 3 μs. This estimate is nearly a factor of two longer than the observed value of 1.77(4) μs. The solid grey line in Figure 5.13(d) illustrates the estimated $T_2^*\{\mathrm{DQ}\}$ as a function of [NV] using Eqn. 5.13 and the assumptions above in addition to residual contributions from ^{13}C nuclear spin bath and magnetic field gradient ($\approx 0.02\,\mu\mathrm{s}^{-1}$ informed by Sec. 5.3.2 and Appendix B. However, consideration of these two sources is insufficient to explain the observed $T_2^*\{\mathrm{DQ}\}$. The grey dashed line depicts the inclusion of an additional, dephasing source of $0.1\,\mu\mathrm{s}^{-1}$ due to $[^{14}\mathrm{N}_s^0] \approx 5\%$ based upon DEER ODMR measurements. Including this contribution brings the estimated $T_2^*\{\mathrm{DQ}\}$ into agreement with the observed value. This result highlights the important of producing 15N-enriched diamond material with reduced $[^{14}\mathrm{N}_s^0]$ impurity as demonstrated in Sec. 5.1.2.

Although NV-NV interactions may not dominate the observed T_2^*-saturation of about 1.7 μs, they remain a relevant contribution. By resonantly driving the $\mathrm{NV}_{\nparallel}$ population not used for sensing, $\zeta_{\nparallel}$ can be modulated such that the $\mathrm{NV}_{\nparallel}$ spin bath is effectively in a mixed state of $|0\rangle$ and $|+1\rangle$ ($\zeta_{\nparallel} = 0.5$) instead of mostly pumped into

the non-interacting $m_s = 0$ sublevel. A decrease in $T_2^*\{\mathrm{DQ}\}$ is observed with $\mathrm{NV}_{/\!/}$ CW-driving applied ($T_2^*\{\mathrm{DQ}\} = 1.51(3)\,\mu\mathrm{s}$) as illustrated by Figs. 5.13(b,c). This outcome suggests that our assumption of an initialization fraction favoring NV^- $\zeta_{/\!/} = 0.7$ is reasonable. In Fig. 5.13(d), the red solid and dashed lines depict the estimated $T_2^*\{\mathrm{DQ}\}$ as a function of [NV] when both the N_s^0 and $\mathrm{NV}_{/\!/}$ populations are controlled. As with the N_s^0-decoupling-only case, the solid red line includes residual contributions from $^{13}\mathrm{C}$ nuclear spin bath and magnetic field gradient, while the dashed line reflects the introduction of dephasing due to residual $^{14}\mathrm{N}_s^0$ contamination of $0.1\,\mu\mathrm{s}^{-1}$). This again brings the estimated dephasing time into agreement with the experimentally observed value.

Chapter 6

Developing Diamond Material Tailored for NV^- Ensemble-based Magnetic Sensing Applications

Reproducible and scalable fabrication of NV^- ensembles with desired properties is crucial envisioned NV^- applications in academia and industry; as is an understanding of how those properties influence magnetometer performance. This chapter addresses these goals by characterizing nitrogen-doped diamond produced by the chemical vapor deposition (CVD) method across a range of synthesis conditions. This is shown to produce material with widely differing absorption characteristics, which are linked to the level of parasitic defects other than substitutional nitrogen (N_S) and NV. In such material, the achievable concentration of NV^- ($[NV^-]$) after irradiation and annealing is found to be influenced by the as-grown properties. At the 10–20 ppm level for $[N_S]$, the production of CVD-grown material with strain levels sufficient not

to limit achievable device sensitivity is demonstrated. The resulting diamond material exhibits a favorable product of [NV^-] and T_2^* - a key figure of merit when considering magnetic sensitivity - compared to other results published in the literature.

6.1 Material Considerations for NV^- Ensemble Magnetic Field Sensitivity

As motivated in Sec. 1.4 and discussed further in Chapter 2, material-related parameters including the number of NV^- sensor spins (N_{NV}), the ODMR measurement contrast (C), strain inhomogeneity, and dephasing time (T_2^*) influence the magnetic sensitivity of NVT--ensemble-based devices. Increasing N_{NV}, C, or T_2* (without degrading any other parameters) or decreasing the strainm inhomogeneity yields improved magnetic sensitivity. In contrast to earlier chapters, which employed active methods to improve the performance of a given sample, this chapter focuses on material-engineering efforts to develop diamond material with more favorable NV^- ensemble properties.

A typical approach to create NV centers in diamond is to start with a sample produced by high-pressure high-temperature (HPHT) or CVD synthesis containing substitutional nitrogen (N_S); to electron-irradiate to create vacancies (V); and then to anneal at temperatures $>600\,^{\circ}C$, where the V are mobile (see Fig. 6.1(c) for example images of material at different stages) [133]. The negative-charge state NV^-, which has the physical properties utilized in sensing, arises from the donation of an electron (typically from N_S^0) according to $NV^0 + N_S^0 \rightarrow NV^- + N_S^+$. Menawhile, the neutral

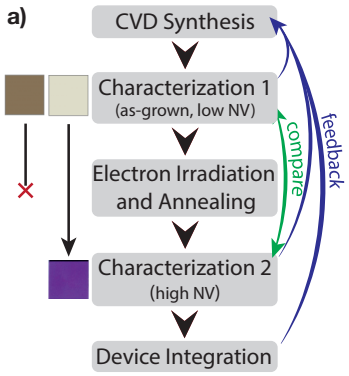

Figure 6.1: **Material development procedure.** Schematic summarising the development of a process for producing diamond material for NV-ensemble magnetometry. Evolution of sample color from a dull brown or yellow to an intense, uniform purple color after irradiation and annealing is a result of high [NV^-] with minimal unwanted other defects.

charge state NV^0 exhibits an optical luminescence spectrum that overlaps with that of NV^-; thus NV^0 will contribute to the background luminescence in a typical device, degrading the contrast (see Sec. 2.4). As a result, it is important to consider the fraction of NV^- compared to the total [NV]:

$$\psi = \frac{[NV^-]}{[NV^-] + [NV^0]} \tag{6.1}$$

Material-related factors influencing ψ include the starting level of [N_S] in the diamond material, which also acts as an upper limit of the possible level of [NV]; the irradiation dose (i.e., [V]); and the annealing recipe used to convert N_S and V present post-irradiation into NV. Other defects, X, present in the diamond, either post-growth (CVD-specific examples are discussed in section 6.1.1) or post-irradiation [134], may additionally act as donors/acceptors and influence ψ.

[NV^-], [NV^0] and [N_S^0] also influence the resulting ensemble NV- dephasing

time T_2^*, as they contribute to the electronic spin-bath. The concentration of other defects present in the diamond ([X]) may also contribute to T_2^*, if the defects are paramagnetic. Additionally, ^{13}C has a nuclear spin of $I = \frac{1}{2}$ and therefore contributes to the nuclear spin-bath and associated dephasing (sec Sec. 2.2.4). It is thus typical to produce diamond samples with depleted levels of [^{13}C] in order to maximize T_2^* [12]. The final major source of ensemble dephasing intrinsic to the diamond material is non-uniform strain across the area of the diamond sample being utilized [38, 135]. Considering these contributions, the material-related T_2^* can be approximated by the following expression following the discussion in Sec. 2.2.3 and Refs. [2, 73]:

$$\frac{1}{T_2^*(\text{material})} \approx \frac{1}{T_2^*(\text{N}_\text{S}^0)} + \frac{1}{T_2^*(\text{NV}^-)} + \frac{1}{T_2^*(\text{NV}^0)} + \frac{1}{T_2^*(\text{X})} \tag{6.2}$$

$$+ \frac{1}{T_2^*(^{13}\text{C})} + \frac{1}{T_2^*(\text{strain} - \text{gradient})} \tag{6.3}$$

Assuming sufficient strain uniformity, the N_S^0, NV^-, and ^{13}C contributions in Eqn 6.2 typically dominate the NV- ensemble dephasing. However, since [N_S^0] ultimately limits the [NV^-] that can be produced by irradiation and annealing, the key material-related decisions are the starting [N_S] and [^{13}C]. The expected T_2^*, assuming that [N_S^0] and [^{13}C] are the dominant contributors to the dephasing time, can be estimated as:

$$\frac{1}{T_2^*(^{13}\text{C}, \text{N}_\text{S}^0)} \approx A_{^{13}\text{C}} \times [^{13}\text{C}] + A_{\text{N}_\text{S}^0} \times [\text{N}_\text{S}^0] \tag{6.4}$$

where, from previous measurements (Secs. 2.2.1 and 2.2.4), $A_{^{13}\text{C}} \approx 0.100\,\text{ms}^{-1}\,\text{ppm}^{-1}$ and $A_{\text{N}_\text{S}^0} \approx 101\,\text{ms}^{-1}\,\text{ppm}^{-1}$ [72, 73]. The contribution from NV^- centers after irra-

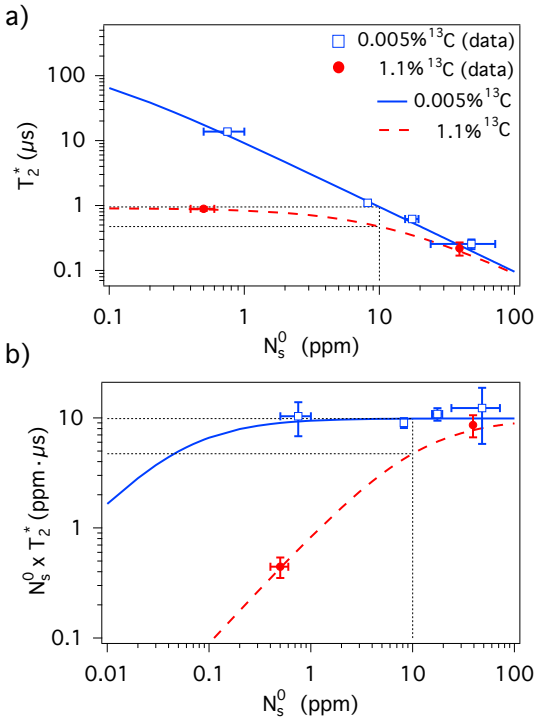

Figure 6.2: **Motivating the choice of [N_S] and [^{13}C] for NV$^-$ ensemble diamond material. (a)** Expected dependence of ensemble NV$^-$ T_2^* with varying [N_S^0] and [^{13}C], according to equation 6.4. (b) Product of [N_S^0] and T_2^* as a function of [N_S^0]. The [N_S^0] ~10–15 ppm regime, the focus of the present chapter, is indicated by the dashed, black lines. Measurements from Chapter 2 are included for reference.

diation and annealing is expected to be proportional to [N_S^0] and is thus not explicitly included in the subsequent analysis. The dependence of T_2^* on [N_S^0] for natural abundance ^{13}C (1.1%, 11000 ppm) and depleted ^{13}C (0.005%, 50 ppm) is illustrated in Fig. 6.2(a), including example measurements reported in Chapter 2 as well as Refs. [2, 72, 73]. Figure 6.2(b) depicts the product of [N_S^0] and T_2^* for both natural abundance ^{13}C (1.1%, 11000 ppm) and isotopically depleted ^{13}C (0.005%, 50 ppm). Across the range of [N_S^0] depicted, the concentration of ^{13}C ([^{13}C]) has a critical role in determining both the achievable magnetic sensitivity and optimal [N_S^0].

From Figs. 6.2(a,b) it is apparent that, for $[N_S^0]$ below $\sim 100\,\text{ppm}$, ^{13}C-isotopic depletion is advantageous, extending T_2^* and increasing the figure of merit $[N_S^0] \times T_2^*$. Furthermore, as discussed in Barry *et al.*, if nitrogen-related dephasing is a small contribution to T_2^*, then the nitrogen concentration should be increased until similar to the dominant dephasing source [2]. This is illustrated by the plateau in the product of $[N_S^0]$ and T_2^* for increasing $[N_S^0]$ in Fig. 6.2(b). While in natural abundance material $[N_S^0] \times T_2^*$ plateaus at $[N_S^0] \sim 100\,\text{ppm}$, ^{13}C-depletion reduces the optimal $[N_S^0]$ to approximately 1–20 ppm.

Since the figure of merit for ^{13}C-depleted material is largely constant in the range 1–20 ppm, additional factors should be considered when choosing a target $[N_S^0]$ within this regime. For pulsed magnetometry protocols such as Ramsey, lower $[N_S^0]$ and longer T_2^* may provide advantages such as improved measurement duty cycle. However, achieving longer T_2^* in practice requires better control of other dephasing sources such as magnetic-bias-field gradients and strain inhomogeneity across an interrogated NV^- ensemble. Consequently, $[N_S^0]$ of order 10–20 ppm is attractive, as it relaxes these material and sensor design requirements without degrading the figure of merit $[N_S^0] \times T_2^*$. These considerations are especially critical when increasing the sensing volume for bulk magnetometry and wide-field magnetic field imaging applications using NV- ensembles.

6.1.1 Development of CVD diamond for NV- ensemble magnetic-field sensors

The present efforts focus on tailoring CVD diamond material. CVD-based synthesis enables the introduction of controllable and reproducible levels of [N_S] and hence [NV^-] and is also amenable to creating diamonds with NV-ensemble surface layers for wide-field magnetic-imaging applications. These advantage make CVD-grown material more attractive compared to material grown using HPHT synthesis (see Sec. 1.2 for further comparison).

To produce material better suited for NV-based magnetic field sensing, we investigate two potential issues for the production of diamond for NV-ensemble magnetometry applications by the CVD method. First, a possible limitation of CVD synthesis of nitrogen-containing diamond is the incorporation of additional, undesired defects. In particular, diamond grown by the CVD method may exhibit a brown coloration, with strong correlations observed between the nitrogen concentration in the process gases during CVD growth (necessary to produce N_S in the material) and the level of broadband-absorption features that give rise to this brown color [53, 136]. Such features are thought to arise from vacancy chains and clusters [56–58, 137] that are incorporated during synthesis. These defects, as well as H-related defects in CVD diamond (e.g., the nitrogen-vacancy-hydrogen defect, NVH [87]), may exhibit charge states that are paramagnetic [87, 88] and thus act as a source of dephasing, contributing to the $1/T_2^*(\mathrm{X})$ term in equation 6.2. They may also influence the value of ψ and hence influence the achievable ODMR contrast. Understanding the links between material characteristics and charge fraction, as [N] is varied, is thus a key

challenge. Secondly, increasing [N] to the tens of ppm level in the CVD process gases has been observed to promote the formation of extended or non-epitaxial defects during growth [138, 139], thereby making it potentially challenging to achieve high-[N] material with homogeneous strain [61, 140].

With these aims in mind, this chapter reports the study of nitrogen-doped CVD processes across a range of synthesis conditions (Section 6.2), examining the resulting broadband-optical-absorption characteristics and level of charge acceptors in as-grown CVD material (Sec 6.3). Irradiated and annealed samples are then examined to assess the influences of strain and parasitic defects on key metrics relevant for NV^- ensemble sensors: defect concentration [NV^-], charge fraction ψ, and dephasing time T_2^* (Sec 6.4). In Sec. 6.4.2 the interplay between the as-grown charge balance (in terms of N_S) and NV^- charge state and spin-state readout contrast are explored. In addition, the prospects for producing batches of samples with controlled levels of strain, [NV], and T_2^* are discussed.

6.2 Sample Synthesis, Treatment and Characterization Methods

The samples examined in the following sections were produced by Element Six using CVD in a microwave-plasma-assisted reactor. {100}-oriented single-crystal CVD diamond plates containing $[N_S^0] \sim 0.1$ ppm acted as substrates during each deposition run. A wide range of synthesis conditions were utilized, in order to produce batches of samples with deliberately varying levels of [N_S] and optical-absorption characteris-

tics. Synthesis was stopped once the diamond layer thickness reached $\sim 1\,\text{mm}$ in each run, in order to permit the use of multiple characterization techniques to examine the $[N_S]$, optical absorption, and strain of the grown material.

The resulting samples were irradiated using an electron beam energy of 4.5 MeV whilst placed on a water-cooled metal bench. At this beam energy, the electron dose would be expected to be homogeneous through the thicknesses of samples grown for this paper [141]. Samples were irradiated for varying durations with the electron dose then estimated from the geometry of the system and the known current of the e^- source. Subsequent annealing of the samples to create NV centers took place in a tube furnace with samples placed in an alumina boat. After loading, the tube was evacuated to a pressure of $\sim 1\times10^{-6}\,\text{mbar}$ in order to minimize graphitization. Annealing was undertaken with the following thermal-ramp profile: 400 °C for 2 hours, 800 °C for 16 hours, 1000 °C for 2 hours and 1200 °C for 2 hours (3 °C/min ramp rate), similar to the methodology employed by Chu *et al.* [142].

Room-temperature optical absorption measurements to probe the absorption characteristics of samples in the range 240-800 nm (UV-Vis) were performed using an Analytik Jena Specord 50 Plus spectrometer. This permitted measurement of $[N_S^0]$ and estimates of the strength of absorption band features at 360 and 520 nm through spectral deconvolution and fitting of the samples post-synthesis, as described by Khan *et al.* [59]. Fourier Transform Infrared spectroscopy (FTIR) spectroscopy was also used to estimate $[N_S^0]$ as well as $[N_S^+]$ in the as-grown samples, through measurement and fitting of the absorption peaks at $1130\,\text{cm}^{-1}$ and $1344\,\text{cm}^{-1}$ for N_S^0 and $1332\,\text{cm}^{-1}$ for N_S^+; see Liggins for further details [143]. These techniques employed an aperture

of 1.6 mm.

Electron Paramagnetic Resonance (EPR) at X-band frequencies ($\sim$9.7 GHz) was used in order to quantify the level of paramagnetic defects NVH^-, N_S^0 and NV^- in samples prior to irradiation and annealing. A sample of known $[N_S^0]$ was used as a reference and the spectral fitting and deconvolution method is described elsewhere [144, 145].

Irradiated and annealed samples were examined by low-temperature (77 K) UV-Vis absorption measurements, with samples held within an Oxford Instruments Optistat DN2 cryostat and cooled to 77 K using liquid N_2. The integrated intensities under the zero-phonon-lines (ZPLs) at 575 nm and 637 nm were then used to quantify the levels of $[NV^0]$ and $[NV^-]$ respectively, using the revised calibration constants of Dale [146] (updated from those of Davies [147]). Prior to quantification of defect concentrations by the methods described, samples were exposed to UV for 2 minutes, using the Xe arc lamp excitation source of the DiamondView photoluminescence imaging instrument [136].

NV-based characterization of diamond material produced in this work employed multiple experimental setups. The first setup was designed for wide-field continuous wave optically detected magnetic resonance (CW-ODMR) imaging of mm-scale diamond samples as previously described by Kehayias *et al.* [38]. From the measured CW-ODMR spectra in each pixel, both magnetic and strain-induced shifts in the NV^- spin resonances were determined by fitting to the NV^- Hamiltonian as described in previous publications [16, 38] .

A second, photodiode-based setup utilized pulsed microwave control to mea-

sure the NV^- ensemble T_2^* by extracting the Ramsey free induction decay constant. Using an epi-illumination microscope configuration, 5–1000 mW of 532 nm laser light was focused through the sample with a beam-waist of 20 µm. A 2 mT applied bias magnetic field aligned with NV^- centers oriented along a single crystallographic axis induced a Zeeman splitting such that the $m_s = 0$ to $m_s = \pm 1$ transitions between the NV^- ground state sublevels were individually addressable with resonant MW pulses.

Ramsey-based measurements enabled determination of T_2^* for both the single and double quantum coherences. For double quantum (DQ) Ramsey measurements (immune to axial strain-induced contributions to T_2^*), two-tone MW pulses resonant with the NV^- ground state spin transitions prepared a superposition of the $m_s = \pm 1$ states during the free precession interval. Single quantum (SQ) Ramsey measurements (sensitive to axial strain-induced contributions to T_2^*) employed single-tone MW pulses to create a superposition of the $m_s = 0$ and $m_s = +1$ or $m_s = -1$ levels during the free precession interval. See Sec. 6.4.2 and Bauch *et al.* [73] for further discussion of single and double quantum coherence measurements.

Quantitative birefringence microscopy was used to assess the level of strain in samples after laser cutting and polishing of the surfaces. This was performed using a commercial Metripol system [105], with the methodology as discussed by Friel *et al.* [61] and summarized in Sec. 2.3. Images were collected through the growth face of the sample, since dislocations that thread in the growth direction are the dominant contribution to strain in CVD diamond [61, 136, 140].

6.3 Characterization of As-Grown Material and Choice of Material for Further Study

This section describes the characterization of samples across a range of growth conditions, including their UV-Vis absorption properties, resulting color, and concentration of $[N_S^0]$ and $[N_S^+]$. Samples with preferable as-grown properties were then further characterized by EPR. These initial studies were conducted with natural-abundance CH_4 gas (98.9% ^{12}C, 1.1% ^{13}C).

6.3.1 Characterizing the nitrogen and charge environment

A wide range of levels of $[N_S]$ and absorption characteristics were observed across the broad window of synthesis conditions used. The results of UV-Vis and FTIR measurements from two different processes, P_1 and P_2, are summarized in Tab. 6.1 as examples.

For the UV-Vis absorption measurements, a peak at 270 nm attributed to N_S^0 was observed [148, 149] as well as bands at 360 nm and 520 nm, which are thought to originate from clusters of vacancies and NVH^0, respectively [58]. The amplitude of the N_S^0-related UV-Vis feature was used to calculate $[N_S^0]$. For the process P_1 material, a concentration of $[N_S^0] = 9.3(5)$ ppm is determined. Meanwhile, the P_2 material has a higher concentration of $[N_S^0] = 17(1)$ ppm. However, additional FTIR measurements reveal that these two processes also exhibit dramatically varying $[N_S^+]$, with the P_1 and P_2 samples containing concentrations of 8(2) ppm and 3.0(3) ppm, respectively. Thus, the two processes contain similar $[N_S]$, but with dramatically different charge

Table 6.1: **Results from high-[N] diamond samples after CVD growth for two different processes (P_1 and P_2).** The two processes exhibit a dramatic difference in $[N_S^0]$ and $[N_S^+]$ as well as color, as evaluated by lightness (L^*). The charge balance in $[N_S]$ is defined by $[N_S^0]/[N_S]$ and is denoted by χ. Quoted results indicated the average value across 5 samples. The standard deviations are reported in parentheses.

Process	N_S^0 (ppm)	N_S^+ (ppm)	N_S^0/N_S (χ)	L^*
P_1	9.3(5)	8(2)	0.49(8)	34(10)
P_2	17(1)	3.0(3)	0.85(1)	74(2)

distributions. In the material produced by the P_1 process the levels of $[N_S^0]$ and $[N_S^+]$ are comparable. This follows the findings of previous reports of characterization of CVD material containing > 10 ppm [65], which also measured $[N_S^0] \approx [N_S^+]$. However, in the case of the P_2 process sample, $[N_S^0] \approx 6\times[N_S^+]$ despite containing a similar concentration of N_S. This suggests that the charge balance of N_S is highly variable between different processes. These results also demonstrate that UV-Vis and/or EPR measurements solely determining $[N_S^0]$ (neglecting N_S^+) in N-doped CVD diamond may poorly reflect the overall level of [N] in this class of CVD material.

It was also observed that the color of material produced using processes P_1 and P_2 differed significantly (refer to Fig. 6.1). In order to assess this in a quantitative manner, images of samples were examined in ImageJ [150] after the background was normalized to pure white, given by a lightness (L^*) value of 100 (CIELAB color space [151]) where lightness indicates the relative brightness of a color (an L^* value of 0 corresponds to pure black). The color was averaged over a circular area in the center of the samples and the L^* value for each sample was determined; in this sense L^* was used as a proxy for the degree of brown coloration.

The determined lightness L^* values for the two processes P_1 and P_2, 34(10)

and 74(2), are proportional to the N_S charge fractions, 0.49(8) and 0.85(1). This relationship further suggests that increased levels of $[N_S]$ do not necessarily imply a degradation in absorption properties (color) and higher fractions of $[N_S^+]$, related to the incorporation of parasitic defects. These factors are, instead, strongly dependent on growth conditions. It has previously been suggested in studies by Khan *et al.* that the presence of high levels of $[N_S^+]$ in CVD diamond may be indicative of significant brown color [59], but limited data was provided to illustrate any such relation. Hence, this was investigated here across the entire range of explored synthesis conditions, to elucidate any correlations that may exist between the charge fraction of N_S, the color of the samples, and the absorption features present in absorption spectra.

Fig. 6.3(a-c) depict the measured lightness, L^*, for all samples produced in this study as a function of $[N_S^0]$, $[N_S]$, and $[N_S^0]/[N_S]$. The lightness of the as-grown samples was observed to not be correlated not with the determined $[N_S^0]$ in the samples, nor with the total $[N_S]$ (re-enforcing the results in table 6.1), but was correalted with the charge fraction χ, $[N_S^0]/[N_S]$. This suggests that the level of absorption leading to brown coloration is associated with the degree of acceptor-defects present in this range of $[N_S]$.

The connection between charge fraction, color, and the presence of charge acceptors is further buoyed by measurements of the 360 nm and 520 nm bands in UV-Vis across the set of samples. As shown in Fig. 6.3(d,e) the N_S charge fraction χ also appears correlated with the strength of the 360 nm and 520 nm bands in the UV-Vis measurements originating from clusters of vacancies and NVH^0, respectively [58]. As the strength of these bands decreases, the N_S charge fraction χ increases towards

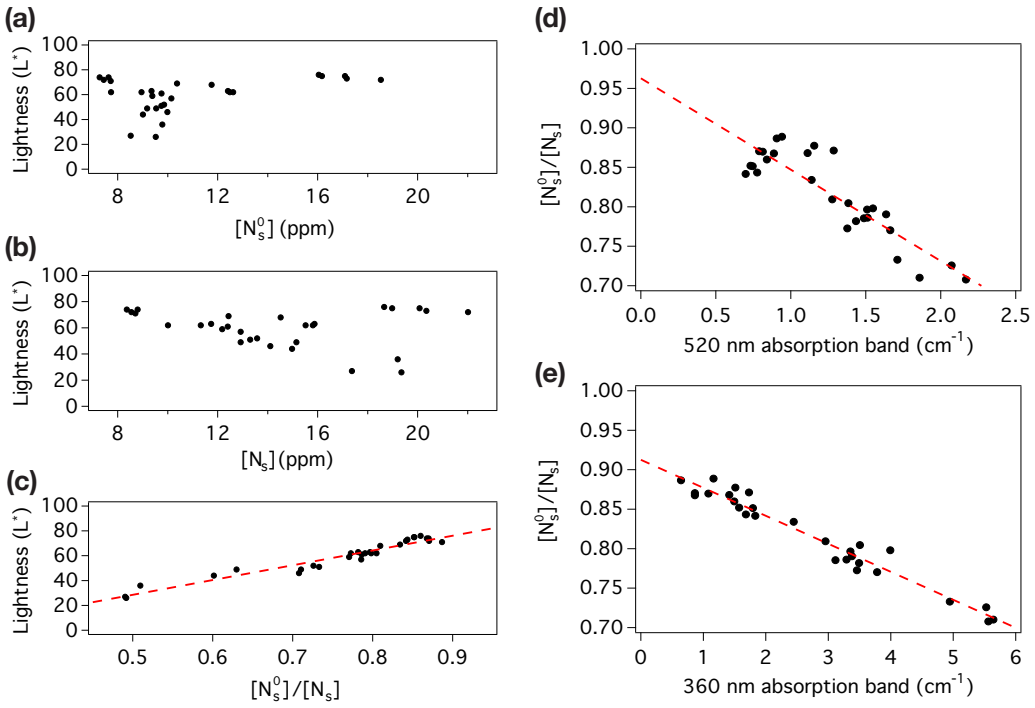

Figure 6.3: **Relationships between the N_S charge fraction and [N_S], [N_S^0], sample color (lightness), and UV-Vis absorption bands. (a)** The sample lightness (evaluated as L*) for all material produced in this study is shown as function of neutral substitutional nitrogen concentration, [N_S^0]. **(b)** Plot constructed using the same data set as (a), but as a function of total [N_S] (summing [N_S^0] and [N_S^+]) and **(c)** L* against the ratio of [N_S^0] to [N_S] (denoted by χ in the text). **(d)** Plot of the relationship between the charge fraction [N_S^0]/[N_S] (denoted by χ in the text) and the strength of the 520 nm absorption band observed in UV-Vis measurements. **(e)** Similar to **(d)** but for the the 360 nm absorption band observed in UV-Vis measurements. The linear fits serve as a guide to the eye to illustrate the link between the two parameters.

unity, particularly for 360 nm band. Thus, in the absence of the vacancy-cluster-related feature at 360 nm, the incorporated N_S defects would be expected to favor the N_S^0 charge state.

The mapping from CVD process values depends on the particular reactor design via intermediate variables such as the gas and electron temperatures and the position

Table 6.2: **Summary of as-grown N-related defect concentrations in a representative sample from the high-[N] CVD process P_3** as measured by UV-Vis and FTIR absorption spectroscopy as well as electron paramagnetic resonance (EPR).

	Concentration (ppm)		
Defect	UV-Vis	FTIR	EPR
N_S^0	13.9(7)	15(2)	16(2)
N_S^+	–	3.5(7)	–
NVH^-	–	–	1.6(2)
NV^-	0.08(1)	–	0.07(4)

of the plasma relative to the deposition area. The process conditions needed to produce given material characteristics therefore differ considerably between different reactor designs, making it difficult to generalise the findings in this work for other investigators in this field. Nevertheless, it is noted that, at a given doping level, careful simultaneous control of the CH_4 fraction (relative to total gas flow) and the substrate temperature was crucial to reducing χ whilst also maintaining a growth surface free of etch pits [152] or {100} surface twins [153].

6.3.2 Characterization of Process P_3 Samples

Based on the findings from the samples characterized in the previous section, a process denoted P_3 was developed, targeting $[N_S^0] \sim 15$ ppm. A small initial batch of 5 diamond samples resulted in $[N_S^0] \approx 14\,(1)$ ppm and $[N_S^0]/[N_S] \approx 0.81\,(2)$, and were utilized for further characterization and processing.

EPR measurements were conducted on a sample from this first batch, in order to investigate additional point defects present in this material (Sample 6A). This approach allowed $[NVH^-]$ and $[NV^-]$ to be quantified in samples grown using process

P_3 prior to treatment. Table 6.2 shows these results and summarizes the quantification of $[N_S^0]$ by three different techniques; UV-Vis and FTIR absorption measurements, as well as EPR, in order to confirm general agreement between these methods.

The concentrations $[NV^-]$ and $[NVH^-]$ can be compared to $[N_S]$ in order to assess the ratios of N-related defects in this material. $[N_S]$:$[NVH^-]$:$[NV^-]$ in the examined sample was $\sim$230:20:1, close to the previously observed values in studies of CVD material (300:30:1 [65] and 52:7:1 [86]). Hence, despite having high-[N] and a low fraction of acceptors (high χ), NVH remains a considerable fraction of the measurable N-related defects in the studied material (>10 %, given only the negative charge-state can be quantified). This likely reflects the hydrogen-rich environment that exists during the CVD growth process.

Motivated by previous reports [154–156] concerning the annealing of NV^- containing material at high temperatures, similar experiments were conducted on the P_3 samples. Annealing took place in vacuum at 1500°C for 16 hours to maximize any possible effects of treatments at this temperature. As shown in Tab. 6.3, $[NV^-]$ increased to 0.2 ppm after annealing, suggesting some residual vacancy clusters were broken up in this treatment. $[NV^0]$ was below detection limits both before and after annealing (<0.01 ppm). A straightforward N→NV conversion is likely, echoing recent findings in treatment of layers grown on {111}-oriented substrates [156]. In the results summarized in Tab. 6.3 for Sample 6B, it is also notable that the 360 nm absorption band decreased dramatically in strength (by $\sim$90 %), lending support to previous assignments of V-related defects/clusters to this feature. The 520 nm feature, associated with NVH, remained unchanged within the likely uncertainties of the

Table 6.3: **Summary of material properties before and after high temperature annealing.** Concentrations of N_S^0 and NV^- are reported along with the UV-Vis absorption spectra coefficients at 360 nm and 520 nm before and after sample annealing at 1500 °C for a representative sample from process P_3. Additionally, measurements of the NV^- ensemble Hahn echo T_2 and stress-immune $T_2^*\{DQ\}$ are included at both stages.

State	$[N_S^0]$ (ppm)	$[NV^-]$ (ppm)	360 nm (cm^{-1})	520 nm (cm^{-1})	T_2 (μs)	$T_2^*\{DQ\}$ (ns)
As-grown	13.9(7)	0.070(4)	3.0(1)	1.5(1)	5.7(3)	205(15)
Post-anneal	13.7(7)	0.20(1)	0.3(1)	1.7(1)	7.9(1)	289(9)

measurements.

Measurements the Hahn echo T_2 and double-quantum $T_2^*\{DQ\}$ for Sample 6B before and after high-temperature annealing are also documented in Tab. 6.3. Before high temperature annealing, an average $T_2 = 5.7(3)\,\mu s$ and $T_2^*\{DQ\} = 0.205(15)\,\mu s$ were observed. Based on the $T_2([N])$ and $T_2^*([N])$ scalings established experimentally in Secs. 2.2.1 and 2.2.2, we expect a sample with total nitrogen, $[N] \approx 17$ ppm, to exhibit $T_2 \approx 10.0\,\mu s$ and $T_2^*\{DQ\} \approx 0.250(30)\,\mu s$. These estimates are in reasonable agreement with the measured values.

After high-temperature annealing, the measured decay times increase to $T_2 = 7.9(1)\,\mu s$ and $T_2^*\{DQ\} = 0.289(9)\,\mu s$ in conjunction with the observed increase in $[NV^-]$ and suspected decrease in vacancy-related defects. The similar increases in T_2 and T_2^* may be the result of increasing the $[NV^-]$ by a factor of three. However, further investigation is needed to map out the extent to which vacancy-related defects (especially those associated with the 360 nm band) impact NV creation and contribute to dephasing of NV^- ensembles [73].

6.4 Characterization of Material Post-irradiation and Annealing and NV-sensing Performance

This section discusses characterization of diamond samples grown using process P_3 after electron irradiation and annealing to create $\sim$ppm levels of NV centers. Measurements of [NV], [NV^-], and [NV^0] as a function of electron irradiation dose up to $6\times10^{18}\,cm^{-2}$ are presented in Sec. 6.4.1. The success of strain-mitigation strategies on T_2^* are investigated in Sec. 6.4.2, respectively. Finally, in Sec. 6.4.2, links between measured [NV^-] and contrast and the starting material (in terms of N_S charge fraction, χ) are reviewed.

6.4.1 Nitrogen-vacancy concentration as function of irradiation dose

To optimize the fraction of [NV^-] (ψ) in the material, it is crucial to choose the irradiation dose appropriately. If the irradiation dose and hence number of vacancies introduced is too low, then the generation of NV centers will be limited. Conversely, if the material is over-irradiated, [NV] will be saturated, but at the expense of generating a large number of NV^0 centers, detrimentally affecting the value of ψ [108].

To determine the optimal dose for the process P_3 material described in the previous section with [N_S^0]≈ 14 ppm, the generation of [NV^-] and [NV^0] was characterized as a function of irradiation dose. This was conducted up to a dose of $\sim6\times10^{18}\,cm^{-2}$ and the results obtained after the samples were annealed are shown in Fig. 6.4(a). Samples were annealed using a ramped-temperature annealing recipe which has a

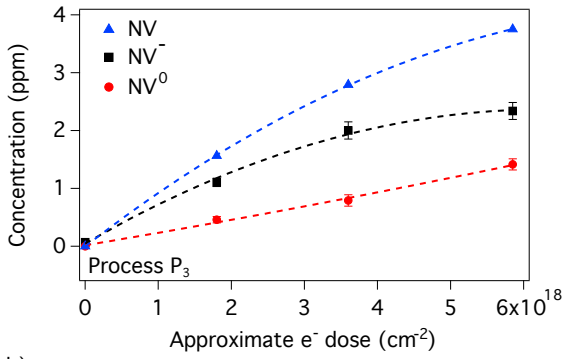

Figure 6.4: **Irradiation dose study for process P_3 samples.** Average concentrations of $[NV^-]$, $[NV^0]$ and [NV] ($[NV^-]$+$[NV^0]$) of e^- irradiated (4.5 MeV) and annealed process P_3 samples containing ≈14 ppm $[N_S^0]$ as-grown, as measured by UV-Vis absorption.

final 2 hour step at 1200 °C. Although temperatures above 1000 °C do not increase [NV] [13], higher temperatures have previously been shown to assist in annealing out multi-vacancy defects [157, 158]; an observation supported by the measurements reported in the previous section.

Over this range of irradiation doses $[NV^0]$ was observed to increase linearly, whereas $[NV^-]$ began to saturate at the highest dose. The dose was therefore not increased further and was chosen as the level of irradiation to use for the remainder of the work described in this chapter. At this chosen level of irradiation, samples were found to contain 3.7 (2) ppm [NV], comprising 2.3 (1) ppm of $[NV^-]$ and 1.4 (1) ppm of $[NV^0]$ after exposure to UV.

6.4.2 Impact on NV⁻ Sensing Parameters

In this section, the properties relevant to magnetic-field sensing of irradiated and annealed samples are studied, including T_2^* and ODMR contrast. Correlations between

the final material properties and as-grown material properties (N_S charge fraction, χ) are established by comparing process P_3 to process P_1 (see section 6.3.1) which had a similar $[N_S]$, but a dramatically lower charge fraction due to an increased concentration of parasitic defects.

As-grown ^{13}C-depleted (0.005% ^{13}C) samples grown by the P_3 process were irradiated and annealed using the selected dose of $6\times10^{18}\,\mathrm{cm}^{-2}$ identified previously in Sec. 6.4.1. Examples of these samples, post irradiation and annealing, are shown in Fig. 6.5(a). The intense purple color is a result of the high $[NV^-]$ achieved in this material. Across such a batch of 23 samples produced in the same synthesis run, the average $[N_S^0]$ was $\approx$13 ppm with a standard deviation of 1 ppm, which demonstrates the ability to achieve the same level of $[N_S^0]$ in a larger batch, as well as repeatability between separate synthesis runs (refer to Tab. 6.2 and Tab. 6.3 for measurements of $[N_S^0]$ in other runs). The measured $[NV] = 3.8(2)$ ppm ($[NV^-] = 2.3(2)$ ppm) was similarly consistent across the batch and yield a favorable average charge fraction of $\psi = 0.62\,(5)$ (uncertainty indicates one standard deviation).

Strain mitigation and T_2^* measurements

When averaging over an ensemble of NV^- centers, strain inhomogeneity can degrade the NV⁻ ensemble dephasing time, T_2^*, and ODMR contrast [38]. To mitigate potential strain issues, CVD substrates and pre-synthesis etches were carefully controlled to minimize the density of dislocations present in the high-[N] material grown, according to the methods discussed in Friel *et al.* [61]. Deposition conditions were also controlled for the duration of the run to avoid the formation of non-epitaxial crystallites.

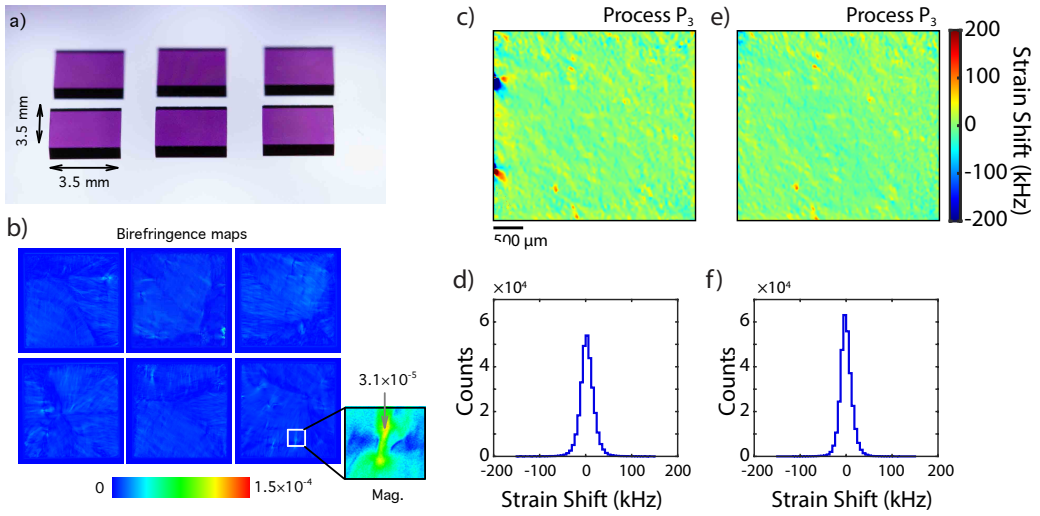

Figure 6.5: **Batch production of P_3 samples and stress characterization.** **(a)** Photograph of six process P_3 samples (0.005% ^{13}C) with approximately 900 µm thickness, after irradiation and annealing to create [NV] ≈ 3.8 ppm. **(b)** Birefringence images of the plates in (a) as measured on a Metripol microscope. **(c)** Map of extracted strain-induced NV resonance shifts for a $(3.6\times3.6\times0.1)\,\mathrm{mm}^3$ freestanding plate produced from a thicker original process P_3 sample (Sample 6C). **(d)** Map of extracted strain-induced NV resonance shifts for a second freestanding plate (Sample 6D) produced from a different portion of the sample used to produce the plate shown in (c). **(e,f)** Histograms of the strain shift values shown in (c) and (d), respectively.

The strain environment of each sample imaged in Fig. 6.5(a) was first characterized using Metripol birefringence imaging and representative images are shown in Fig. 6.5(b). In these samples, an average birefringence $\Delta n \approx 7(1) \times 10^{-6}$ was determined with peak values of $\Delta n \sim 3 \times 10^{-5}$ in isolated petal features (see inset of Fig. 6.5(b) for an example). A vast majority (>99%) of the pixel values within the birefringence image, Fig. 6.5(b), satisfy $\Delta n \lesssim 10^{-5}$, the standard for ultra-low birefringence diamond established by Friel *et al.* [61].

To further characterise the success of these simple strain mitigation strategies,

the NV^- spin properties were studied. These measurements employed two 100 µm-thick freestanding plates produced from a single process P_3 sample grown with ^{13}C depleted to 0.005 % and subsequently irradiated and annealed (Samples 6C and 6D). This thickness was chosen to improve the planar spatial resolution of CW-OMDR-based imaging and reduce inhomogeneities in the applied magnetic, optical, and MW control fields.

Stress-induced resonance shifts were extracted by fitting the measured CW-ODMR spectra pixel-by-pixel to the full NV Hamiltonian as described in Sec. 2.3 and Kehayias *et al.* [38]. Due to the thickness of the diamond substrate limiting spatial resolution [16, 38], NV strain shift measurements are only advantageous for probing the strain environment for length scales larger than the thickness of the diamond samples, 100 µm. Maps of these shifts for the Samples 6C and 6D are shown in Figs. 6.5(c,d) and histograms of the measured shifts are shown in Figs. 6.5(e,f), respectively. Both samples exhibit minimal stress inhomogeneity with a distribution in stress-induced shifts of approximately 25 kHz full-width half-maximum (FWHM). These measurements demonstrate lower levels of strain in this CVD process relative to previous thin-layer samples in the literature (see Kehayias *et al.* [38] for typical examples of N-doped CVD diamond layers, with stress-induced shifts on the order of hundreds of kHz to MHz). The shared spatial variations in the stress inhomogeneity between figure 6.5(c) and 6.5(d) are a consequence of the two samples being cut from the same original diamond sample (particularly visible along the bottom edges of the diamond plates).

For Sample 6C shown in Fig. 6.5(a), additional photodiode-based Ramsey mea-

surements of ensemble-NV T_2^* were conducted on the setup described in section 6.2 and previously established to have negligible contribution from B_0 gradients and temporal variations, and other technical inhomogeneities [73]. Measurements of the single and double quantum T_2^* in six different locations across Sample 6C yielded average values of $T_2^*\{\mathrm{DQ}\} = 0.70\,(5)\,\mu\mathrm{s}$ and $T_2^*\{\mathrm{SQ}\} = 1.12\,(6)\,\mu\mathrm{s}$ where the uncertainties indicate one standard deviation. The post-treatment average $T_2^*\{\mathrm{DQ}\}$ value is nearly three times longer than the as-grown $T_2^*\{\mathrm{DQ}\}$, which beneficial for magnetic sensitivity. However, as discussed for similar material in Sec. 5.3.6, the observed $T_2^*\{\mathrm{DQ}\}$ exceeds the expected value given the $[\mathrm{NV^-}]$ and $[\mathrm{N_S^0}]$ of about 550 ns (see proposed toy model presented in Eqn. 5.12). This discrepancy may in part be accounted for due to charge state dynamics under 532 nm optical excitation.

Comparison of the single quantum T_2^* and axial-strain-immune double quantum T_2^* provides insight into the dominant dephasing sources across the interrogated ensemble, including the strain inhomogeneity on length scales shorter than the 100 µm sample thickness. As expected when limited by magnetic dipolar interactions with the surrounding spin bath, the average $T_2^*\{\mathrm{DQ}\}$ is nearly half the average $T_2^*\{\mathrm{SQ}\}$ due to the effectively doubled gyromagnetic ratio for the double quantum sensing basis [73]. These values are moderately compatible with ensemble-NV dephasing dominated by interactions with other $\mathrm{NV^-}$ sensor spins and remaining $\mathrm{N_S^0}$ bath spins, with a residual contribution from strain inhomogeneity across the interrogated volume of approximately 50 kHz. This strain-induced contribution is similar to the 25 kHz distribution imaged in the previous section, suggesting minimal additional stress-gradients on the sub-100 µm length-scales.

Table 6.4: **Results obtained from material made by processes P_1 and P_3.** The two processes have similar starting levels of $[N_S]$, but different fractions $[N_S^0]/[N_S]$. Concentrations were determined after exposure to UV. Uncertainties indicate one standard deviation across three samples for each process.

	As-grown		Post irradiation and annealing	
Process	$[N_S]$ (ppm)	$[N_S^0]/[N_S]$ (χ)	[NV] (ppm)	$[NV^-]/[NV]$ (ψ)
P_1	17(1)	0.49(8)	3.6(1)	0.43(7)
P_3	16(2)	0.81(2)	3.8(2)	0.62(5)

The product of $[NV^-]$ and T_2^* can be used as a material figure of merit to account for the achieved density of $[NV^-]$ sensor spins. In past work [159, 160], ^{12}C-enriched (99.97 %) HPHT material containing $[N_S^0]$ of $\sim$2 ppm as-grown was treated to produce 0.4 ppm $[NV^-]$ and exhibited a T_2^* of $\sim$3.2 µs. In such samples, the product $[NV^-]\times T_2^*$ is 1.3 µs·ppm, which compares to the 2.7 µs·ppm for the process P_3 material. The reported value of 2.7 µs·ppm also compares favorably to compiled assessments of samples in the literature [2, 13, 161].

NV charge-state and contrast

The preceeding sections have focused on maximising the value of $[N_S^0]/[N_S]$ (χ), i.e., minimizing charge traps, in as-grown material with the rationale that this would be beneficial to improve the NV charge ratio ψ. Hence, it is worthwhile to examine whether the material produced in this study can elucidate the relationship between the concentration of charge-traps in as-grown CVD material and the values of ψ (and ODMR contrast) after irradiation and annealing.

To demonstrate an understanding and control of charge trap synthesis, a charge-state-detrimental process (process P_1) was used that produced $[N_S]$= 17(1) ppm with

$\chi = 0.49(8)$, compared to $[N_S]$= 16(2) ppm with $\chi = 0.81(2)$ in process P_3. Hence, in this case, the two processes had similar $[N_S]$, but with significantly different levels of acceptors. As expected, the material also had visibly different absorption properties (Sec. 6.3.1) post growth.

Three samples grown using process P_1 were irradiated to the same dose as that used for process P_3 (Sec. 6.4.1) and were annealed utilising an equivalent thermal profile. The results obtained from these processes are shown in Tab. 6.4. The NV charge fraction ψ is reduced in the process P_1 sample, suggesting that grown-in defects in CVD diamond that act as charge acceptors can have a detrimental influence on the yield of $[NV^-]$ after irradiation and annealing. Hence, a material with a higher starting χ is desirable.

ODMR contrast, which depends upon the NV charge fraction under excitation and scales inverse-linearly with magnetic sensitivity, is a critical material-based factor to optimize [2, 13, 162]. The ODMR contrast for two diamond samples, Samples 6E and 6C, produced using processes P_1 and P_3, was compared using pulsed-ODMR, as depicted in Fig. 6.6(a). Measurements were performed as a function of excitation intensity to account for changes in charge state under 532 nm illumination and T_1-related effects. A pinhole was introduced to the NV fluorescence collection path of the setup used in Sec. 6.4.2 to restrict the collection volume and ensure homogeneous illumination similar to the approach in Alsid *et al.* [77].

A 647 nm long-pass filter was introduced to the collection path to replicate realistic experimental conditions. As shown in Fig. 6.6(b), the measured pulsed-ODMR contrast for process P_3 (Sample 6C) exceeds that of process P_1 (Sample 6E) by ap-

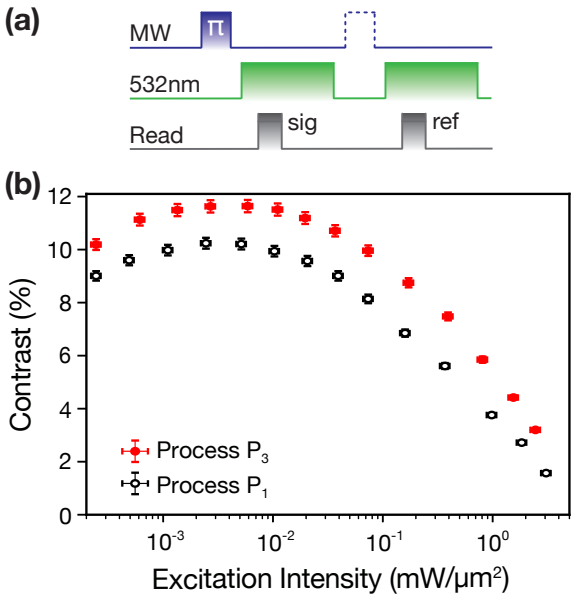

Figure 6.6: **NV pulsed-ODMR contrast measurements of Samples 6E and 6C grown with processes P_1 and P_3, respectively. (a)** Schematic of the sequence used to measure the NV contrast. Before the first 532 nm optical pulse (green), a resonant microwave (MW) pulse is applied to transfer population from the $m_s = 0$ to the $m_s = 1$ state. The black dashed pulse indicates that no MW pulse was applied before the second optical pulse. Optical pulses are 5 ms in duration and not shown to scale. **(b)** Pulsed-ODMR contrast as a function of excitation intensity for Samples 6E and 6C. Horizontal errors bars indicate an estimated 10% uncertainty in the measured intensity and vertical error bars indicate an estimated 2% uncertainty in measured contrast.

proximately 20% across a range of 532 nm excitation intensities spanning from near saturation intensity around 1–3 $\mathrm{mW}/\mu\mathrm{m}^2$ [84] (optimal for applications using pulsed measurement protocols) down to $10^{-4}\,\mathrm{mW}/\mu\mathrm{m}^2$ (similar to the intensities used for CW-ODMR applications [24]). The two samples exhibit maximum contrast for excitation intensities around $5\times10^{-3}\,\mathrm{mW}/\mu\mathrm{m}^2$ with values of 12% and 10% for processes P_3 and P_1, respectively. At higher intensities, the measured contrast decreases for both samples, likely due to reduced NV charge fraction $[NV^-]/[NV]$ with increasing

optical intensity [77, 78]. At lower excitation intensities, the measured contrast also decreases because the fraction of NV^- centers initialized into the $m_s = 0$ state depends upon the ratio of the optical pumping rate to the depolarisation rate $1/T_1$ (see the Appendix of Dréau *et al.* for further details [69]).

The largest measured pulsed-ODMR contrasts for both processes, 10% and 12% respectively, are favorable compared to the maximum contrast attainable for NV^- ensembles. Assuming a typical single NV^- contrast of 30%, an ensemble with NV^- centers along all four crystal axes has a maximum possible conventional optical readout contrast of about 15% when the excitation laser polarization optimally addresses two of the four orientations (as done in this present work). Experimentally, the observed contrast is typically less than 15% because the NV^- PL cannot be completely isolated from the NV^0 PL background due to the broad, overlapping phonon sidebands at room temperature [77, 78].

The pulsed-ODMR measurements on Samples 6C and 6E therefore imply that as-grown defects in CVD diamond that act as acceptors may impact the material properties after irradiation and annealing. The improvement in NV charge fraction, ψ, for the P_3 process simultaneously offers higher contrast across a broad range of optical excitation intensities and increased $[NV^-]$. However, while beneficial for magnetic sensitivity, the observed increase in ODMR contrast between processes P_1 and P_3 is modest compared to the difference in NV charge fraction (without illumination) for two reasons: (a) the detected PL is predominately from NV^- due to the 647 nm long-pass filter which partially isolates the NV^- PL from NV^0 PL and simulates realistic sensing conditions and (b) the conversion of NV^- to NV^0 is less detrimental to optical

contrast than expected because the NV^- charge state has a $\sim 2\times$ higher level of PL compared to NV^0 under weak 532 nm illumination [77].

Further work is required to understand how the maximum achievable NV charge fraction, ψ, scales with reduced levels of $[N_S]$, where the relative concentration of residual donors/acceptors are likely to be significantly altered. Nevertheless, the increased level of contrast and moderate reduction in absorption in this study suggests value in evaluating as-grown material in terms of its N_S charge fraction, χ, during the development of synthesis processes.

6.5 Conclusion

This study illustrates the wide range of diamond material, in terms of absorption characteristics and relative concentrations of N_S^0 and N_S^+, that may be produced with nitrogen-doped CVD processes. In the range $[N_S] \approx 10$–20 ppm strong relationships are observed between the color of the samples and the $[N_S^0]/[N_S]$ charge fraction, which is related to the incorporation of unwanted, vacancy-related defects in such samples. However, it is demonstrated here that high values of χ can be achieved independent of $[N_S]$ up to 20 ppm, hence this does not represent a major concern for production of such material by CVD.

Comparison of material grown with the same initial $[N_S]$ before and after irradiation and annealing suggests that improved χ in as-grown material increases $N_S \rightarrow NV^-$ conversion, thereby increasing the density of NV^- sensor spins and ODMR measurement contrast, which both benefit sensing applications.

The correlation of the desired material properties, such as $[NV^-]$ after irradia-

tion and annealing, with simple CVD-growth metrics, such as the color of as-grown samples, enables rapid exploration of large synthesis parameter spaces. This approach provides an efficient framework to develop future diamond material with varying defect densities tailored to specific applications.

This study also demonstrates that NV-ensemble-diamond samples with controlled levels of strain and reproducible [NV^-] and T_2^* may be produced by CVD, shown through characterization of 23 near-identical samples. The NV^- concentration was observed to vary by less than 7% with an average of 2.3(2) ppm as measured by UV-Vis absorption spectroscopy. Furthermore, birefringence, CW-ODMR strain-imaging, and Ramsey-based T_2^* measurements suggest that careful substrate surface preparation and pre-synthesis etches is sufficient to control strain inhomogeneity in the material to largely mitigate stress-gradient-induced contributions to ensemble-NV dephasing. These findings are positive for the academic and industrial efforts focused on the the production, by the CVD method, of reproducible high-[NV] material with favorable properties for magnetic-field sensing.

The material presented in this chapter would be expected to provide sensitivity improvements for current NV-ensemble devices, without the additional experimental complexity or power consumption associated with advanced spin control or readout techniques [2]. CVD processes producing diamond with this range of [N_S] therefore appears to be an area that deserves further study. This is especially true in the case of production of micron-scale, NV-rich surface layers of such material, as this would enable advances in NV-ensemble wide-field magnetic imaging applications. For growing such samples, control of additional qualities such as surface morphology and a

well-defined interface between the high-purity diamond substrate and nitrogen-doped layer will be critical.

Chapter 7

Outlook

The previous chapters have summarized recent experimental progress towards improved NV^- ensemble magnetometry via techniques to improve magnetometer performance as well as the development of an NV-based characterization toolbox used to aid in engineering diamond material tailored to NV^- ensemble applications. The benefits for magnetic sensitivity, magnetic specificity, and scalability are expected to enable both new application spaces as well as broader access to state-of-the-art NV-diamond devices.

Amongst the techniques explored, the advantages of DQ coherence magnetometry are particularly multi-faceted. Sensing using the DQ basis provides an effectively doubled gyromagnetic ratio; while simultaneously suppressing unwanted (in the context of magnetometry) vulnerability to crystal stress inhomogeneity and temperature drifts. By mitigating stress-induced dephasing, DQ Ramsey measurements commonly yield extended dephasing times and improved magnetic sensitivity. In the context of magnetic imaging applications, the DQ sensing basis also enables more homogeneous

magnetic sensitivity across a field of view. Application of DQ techniques to NV^- ensembles has historically been hampered by the requisite control field uniformity required to avoid MW pulse errors and mixing of the DQ and SQ coherences. This challenge is addressed using the 4-Ramsey protocol introduced in Sec. 3.4.1, which enabled the demonstration of volume-normalized magnetic imaging sensitivities competitive with bulk, NV-based magnetometers in Chapter 4. These advances bring envisioned applications such as imaging of magnetic activity in mammalian cells closer to reality.

However, further improvements in magnetic sensitivity are critical to continue to broaden the application space of NV-based sensors. Chapters 5 tackles this challenge using resonant control of the diamond spin bath to decouple NV-bath dipolar interactions, while remaining sensitive to DC magnetic fields common in applications. In as-grown material, extensions or the ensemble dephasing time by $16\times$ are achieved when spin bath decoupling and DQ coherence magnetometry are used together. In NV-rich diamond material, preliminary experiments suggest it is possible to use such techniques to achieve dephasing times limited by like-spin, NV-NV dipolar interactions, although additional exploration is required.

Operation in the NV-NV interaction-limited regime is desirable, but not typically achieved for current generation NV-based magnetometers. In this regime, the magnetic sensitivity "plateaus", i.e., adding additional NV^- sensor spins commensurately shortens the dephasing time such that the magnetic sensitivity remains roughly constant. Achieving NV-NV-limited T_2^* requires the identification and mitigation of all other dephasing sources. This presents a significant experimental challenge when

also attempting to retain sensitivity to DC magnetic fields. In contrast, for AC magnetic field sensing, conventional dynamical decoupling protocols such as XY8-N readily mitigate other dephasing and decoherence sources such that the observed T_2 saturates at the NV-NV-induced limited set by instantaneous diffusion [76,97–99,163].

Looking forward, once operating in the NV-NV interaction dominated regime, we can work to decouple interactions between NV^- sensor spins while retaining sensitivity to DC magnetic fields. Such decoupling protocols were recently proposed and demonstrated for AC magnetic field sensing in Refs. [164,165] using NV-rich HPHT diamonds. While similar protocols for decoupling Spin-1 interactions and retaining DC magnetic sensitivity have been proposed, experimental demonstrations have not yet been reported. Nonetheless, Osterkamp *et al.* [156] have made recent progress combining spin bath control with an WAHUHA sequence, which is designed to decouple S=1/2 like-spin interactions, to extend the dephasing time of preferentially-oriented, as-grown nitrogen-doped diamond material. Attaining similar results for the NV-rich samples (with NVs distributed along all four crystal axes as described in Chapters 5 and 6) is an immediate next research direction. Looking further into the future, we can consider protocols that do not simply decouple NV-NV interactions, but instead leverage them as a resource to improve sensitivity to external fields [166].

In addition to considering techniques to extend the NV^- ensemble T_2^*, there are exciting possibilities to improve NV^- magnetometer sensitivity by understanding and improving the charge state environment in NV-rich samples, with implications for both the ODMR contrast and number of sensor spins. In the Ramsey work described in Chapters 4 and 6, we found increasing the optical intensity lead to

severe worsening of the NV^- charge fraction, which largely mitigates the anticipated sensitivity improvement. This behavior depends on many parameters including the microscopic distribution of charge donors and acceptors as well as the particular illumination procedure, geometry, and wavelength. This both presents a complex system to understand, but also suggests there are promising avenues to tune the NV charge stability in NV-rich diamond material.

As conveyed in Chapter 6, much of our recent efforts have focused on the scalable production of diamond material with reproducible properties favorable for NV^- ensemble magnetic sensing. Particular emphasis was placed on mitigating stress inhomogeneity, consistent and uniform defect densities, as well as isotopic purity (both $^{13}C/^{12}C$ as well as $^{14}N/^{15}N$). Ultimately, these efforts will hopefully be broadly beneficial for the NV-diamond community: improving access to high-quality material is critical to inspiring new applications and making significant contributions to questions in other fields.

Appendix A

Calibration of a Ramsey-Based NV$^-$ Ensemble Magnetometer

In order to achieve optimal magnetic sensitivity in a Ramsey-based measurement the free precession interval τ and applied MW frequency or frequencies f_{AC} must be chosen appropriately (f_{AC} contains two tones for double quantum Ramsey measurements, see Chapter 3). An image of the NV$^-$ free induction decay (FID) signal as a function of both τ and detuning of f_{AC} from the center of the hyperfine-split resonances, δ is shown in Fig. A.1(b). In this data, f_{AC} is swept in order to mimic an magnetic-field-induced-shift in the NV- spin resonances. Cross-sectional slices as a function of *tau* with fixed detuning and vice-versa are shown in Fig. A.1(a) and Fig. A.1(c), respectively. In the time domain, the Ramsey FID signal exhibits fringes which oscillate at the detuning of the F_{AC} with each hyperfine population (in this case a ^{15}N-enriched diamond sample with $I = 1/2$). Changes in the detuning between the NV$^-$ spin resonances and f_{AC} also produces an oscillatory response in the NV$^-$

ODMR signal as population is projected onto the $|0\rangle$ and either of the$|\pm1\rangle$ states after phase accumulation. This response to changes in the magnetic source field is typically referred to as a DC magnetometry curve.

For optimal sensitivity to changes in applied magnetic field, the relevant figure of merit to maximize, denoted ζ, is the product of the NV- response S to changes in magnetic-field dS/dB and the factor $1/\sqrt{\tau+\tau_O}$ where τ_O accounts for measurement overhead time (e.g., initialization and readout). The maximum slope dS/dB is proportional to the product of the amplitude ($\propto C\mathrm{e}^{-(\tau/T_2^*)^p}$) and frequency of this oscillation ($\propto \tau$) such that we can express ζ as:

$$\zeta \propto \frac{C\mathrm{e}^{-(\tau/T_2^*)^p}\tau}{\sqrt{\tau+\tau_O}} \tag{A.1}$$

where C is the ODMR contrast, T_2^* is the NV- dephasing time, and p is the decay shape parameter.

The protocol to determine the optimal τ and f_{AC} required to maximize ζ depends upon two external factors. First, assuming a simple exponential decay ($p=1$) and non-negligible experimental overhead time τ_O, the optimal free precession interval is τ_2^*; instead of $\tau_2^*/2$ when τ_O is neglected. However, the Ramsey fringe beating introduced by the hyperfine splitting of the NV- spin resonances restricts the possible choices of τ to discrete values where the fringes interfere constructively. As a consequence, we must select the nearest available τ to T_2^*. This choice is dependent upon whether the diamond was synthesized using natural abundance nitrogen source gases ($>99\%$ ^{14}N) or isotopically enriched ^{15}N sources. The explicit protocol for ^{15}N samples is discussed later in this section.

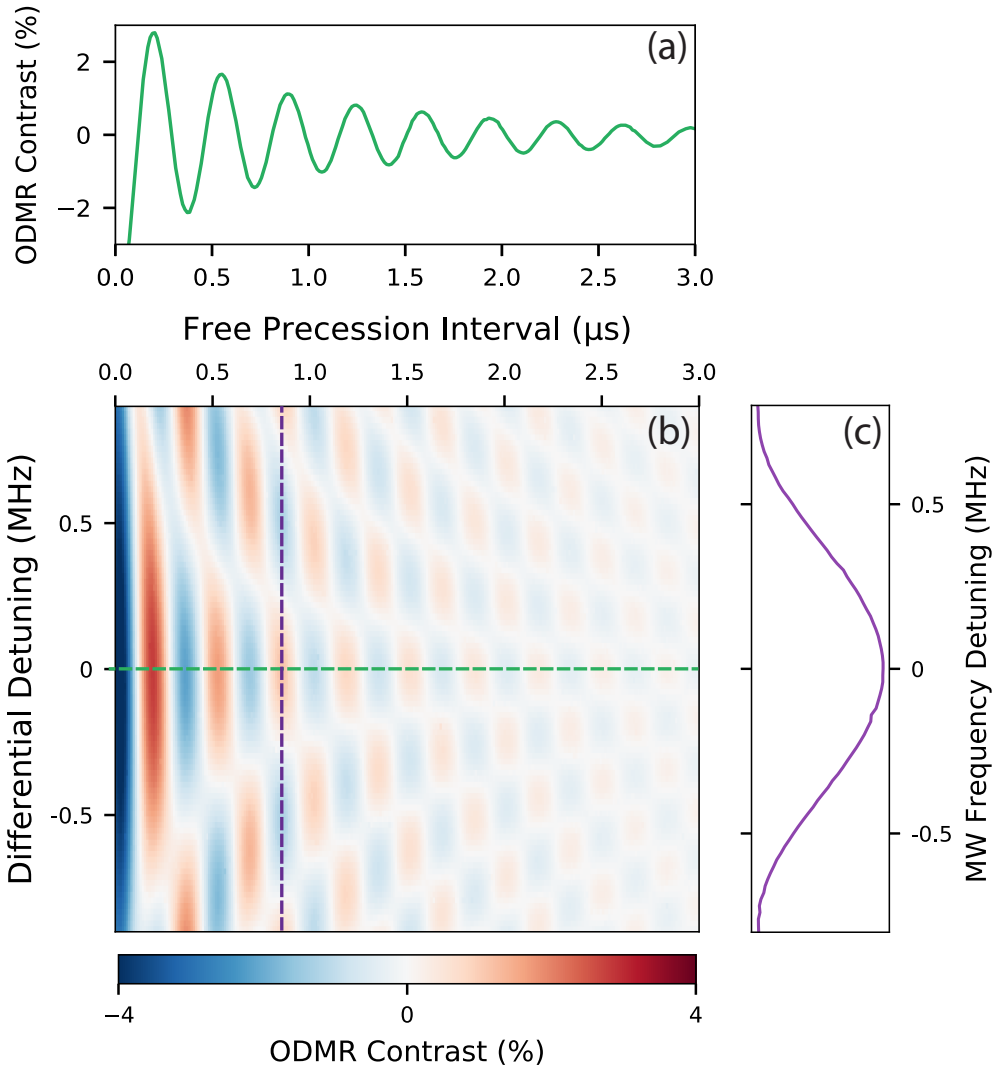

Figure A.1: **2-dimensional sweep of Ramsey free induction decay (FID) interval and detuning. (a)** Ramsey free induction decay signal in the time domain for an equal detuning of the applied MW pulse frequencies between the two ^{15}N hyperfine-split populations. **(b)** Image of the FID signal as a function of MW pulse frequency detuning. The purple and green dashed lines indicate corresponding location of data shown in (a) and (c), respectively. **(c)** OMDR contrast as a function of magnetic-field-like detuning of the MW pulse frequency. The duration of the free precession interval is fixed.

Second, in typical experimental schemes two or more Ramsey measurements (e.g., 2-Ramsey in Sec. 3.4.1) are used to modulate the NV response and suppress low-frequency noise sources such as laser intensity drift [118]. Toggling the phase of the final pulse in each Ramsey sequence by $\Delta\phi = 180°$ alternately maps to positive and negative changes in NV^- fluorescence, such that subtracting every second detection from the previous and dividing by their sum yields a rectified, normalized magnetometry signal. The choice of MW pulse phases is often expressed in terms of the Bloch sphere rotation axis (at least for SQ Ramsey sequences) such that a Ramsey sequence with phases {0°, 180°} corresponds to rotations {x,-x}. For a SQ 2-Ramsey scheme we could describe the phase choices and resulting rotations as {{x,x},{x,-x}} where there is a phase shift $\Delta\phi = 180°$ between the final MW pulses. These choices determine the phase of the DC magnetometry curve and optimal detuning δ_{opt} for maximizing ζ. For {{x,x},{x,-x}} schemes with zero detuning of f_{AC} with respect to the center frequency between the hyperfine-split resonances, the NV^- is minimally sensitive to external DC magnetic fields. This is often referred to as cosine magnetometry. As a consequence, an additional purposeful detuning must be introduced in order to operate at the point of maximum slope on the Ramsey magnetometry curve. Alternatively, the choice of {{0°,90°},{0°,-90°}} ({{x,y},{x,-y}}) shifts the phase of the magnetometry curve by 90° such that no additional detuning is required to operate at the point of maximum slope where the NV response is linearly to magnetic field changes (rendering Step 3 below unnecessary). This scheme is hereafter referred to as sine magnetometry. Although the experimental work presented in this dissertation exclusively employed cosine magnetometry schemes due to technical limitations, sine

magnetometry is favorable as a result of avoiding the additional detuning which is unequal with respect to the hyperfine-split resonances.

We now describe potential steps to calibrate a Ramsey-based NV- experimental setup for a ^{15}N diamond sample. Although each step is accomplished experimentally in the following discussion for clarity, only Step 1 requires an experimental measurement. The parameters determined in Steps 2 and 3 can be analytically estimated or numerically calculated given the results of Step 1.

Step 1 – We begin by measuring the Ramsey free induction decay (FID) in order to extract the NV ensemble T_2^* and relative spin resonance frequencies with respect to f_{AC}. A shown in Fig. A.2(1), a detuning on the order of the NV- ground-state hyperfine splitting is introduced in order to more easily determine the FID envelope and ensure each NV- spin resonance exhibits a unique fringe frequencies, as indicated by Δ_1 Δ_2 in the ODMR spectrum cartoon. The power spectrum calculated from the FID data is shown on the right and exhibits two frequency components split as expected for a ^{15}N sample.

Step 2 – Using the measured detunings from Step 1, f_{AC} can be chosen such that the applied MW pulse is equally detuned from both hyperfine split resonances. This yields a FID signal with a single frequency component at $\Delta_{\mathrm{HF}}/2$ (or Δ_{HF} for the DQ sensing basis) as shown in the calculated power spectrum on the right of Fig. A.2(2). When using cosine magnetometry, the maxima and minima of the equal-detuning Ramsey FID signal correspond to potential choices of free precession interval τ given the hyperfine-induced restrictions. Alternatively, for sine magnetometry (not shown), the zero-crossings would indicate the possible choices of τ. In Fig. A.2(2) the nearest

extrema to T_2^* ($\tau = \tau_{\text{opt}}$) is indicated with a solid, red vertical line. A dashed, red vertical line indicates $\tau = T_2^*$.

Step 3 – The resulting DC magnetometry curves for these two choices of τ are depicted on the left of Fig. A.2(3). The choice of $\tau = \tau_{\text{opt}}$ indicated by the local minima yields an oscillation with dramatically improved contrast, and hence slope/response, compared to the choice of $\tau = T_2^*$. The corresponding slopes are shown explicitly on the right of Fig. A.2(3) along with the optimal detuning δ_{opt}. If sine magnetometry had been employed, this additional detuning would not be required.

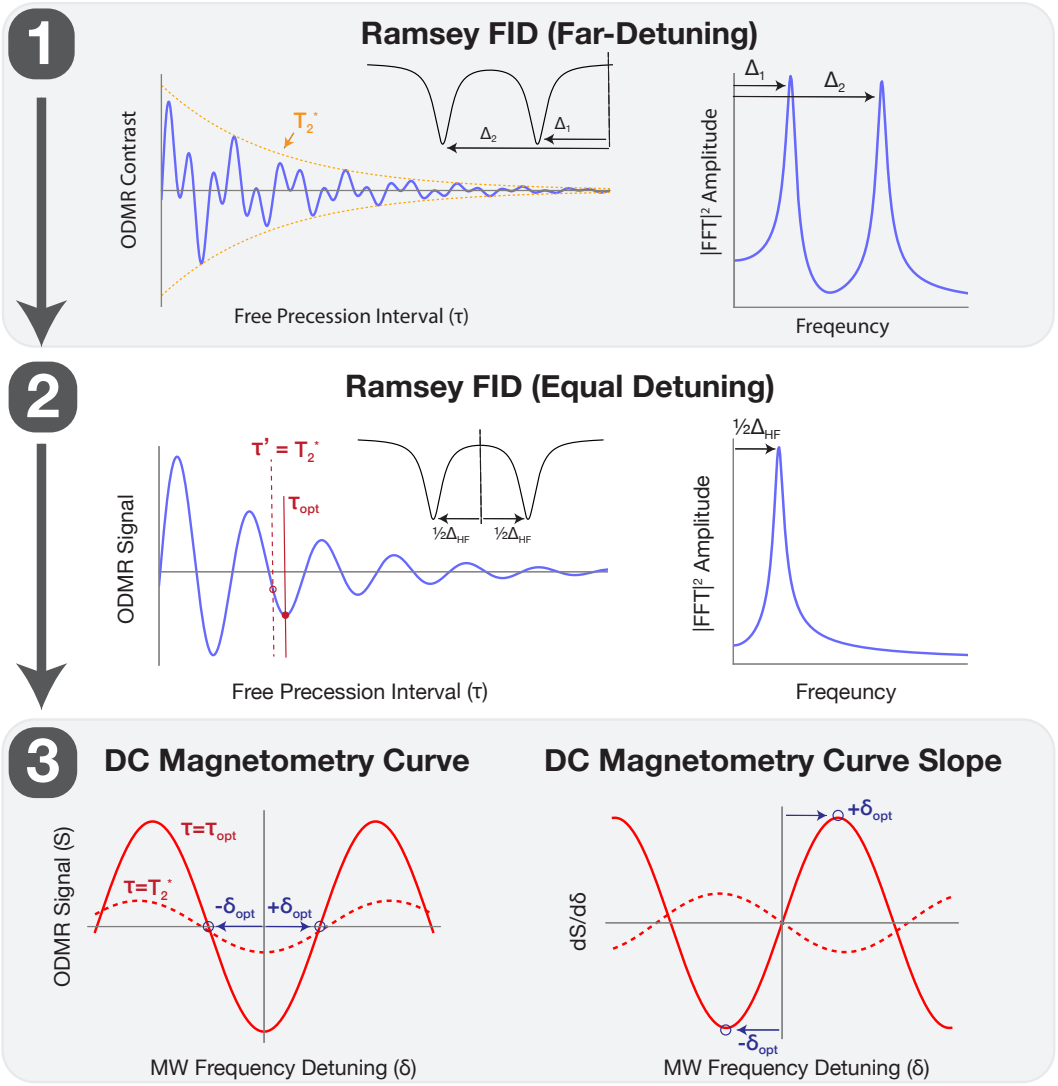

Figure A.2: **Ramsey magnetometer calibration protocol. Step 1:** Extraction of the NV ensemble T_2^* spin resonance frequencies from the Ramsey free induction decay (FID) signal with arbitrary detuning of the MW pulse frequency by Δ_1 and Δ_2. The power spectrum of the FID signal is shown on the right. This step must be performed experimentally. **Step 2:** Determination of the optimal free precession interval τ_2^* with $\Delta_1 = \Delta_2 = \Delta_{\mathrm{HF}}/2$. This step can be accomplished experimentally, numerically, or analytically. **Step 3:** Determination of the optimal detuning of the MW pulse frequency, δ_{opt}, which maximizes the slope of the DC magnetometry curve. Solid line indicates measurements using τ_{opt} instead of the T_2^* exactly (dashed line). This step can be accomplished experimentally, numerically, or analytically.

Appendix B

Bias Magnetic Field Gradient Analysis

The experimental results described throughout this dissertation employed a custom-built samarium-cobalt (SmCo) magnet assembly designed to apply a homogeneous external bias magnetic field B_0 parallel to NV^- defects oriented along the [111] diamond crystallographic axis. Mounted on an optical rail, the field strength can be varied from 2 to 20 mT by adjusting the separation between the two set os diametrically arranged ring magnets (Fig. B.1). SmCo was chosen for its low reversible temperature coefficient (-0.03 %/K). Calculations performed using the Radia software package [167] enabled the optimization of the geometry to minimize B_0 gradients across the NV fluorescence collection volume. For photodiode-based measurements, the typical collection volume is approximately cylindrical, with a measured diameter of $\approx$20 µm and a length determined by the NV layer thickness along the z-axis (1–100 µm, depending on the diamond sample).

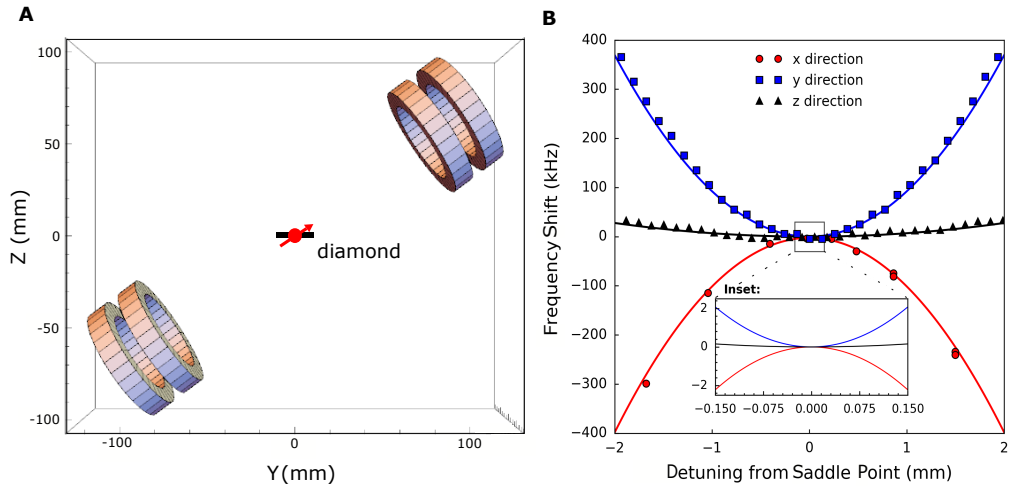

Figure B.1: **Design of homogeneous magnetic bias field. (a)** Magnet geometry used to apply an external B_0 field along one NV orientation within the diamond crystal (typically [111]). Red arrow depicts the NV orientation class interrogated in these experiments; black rectangle represents diamond sample approximately to scale. **(b)** Magnets are translated along three axes to measure the B_0 field strength (shift in ESR transition frequency) as a function of detuning from the origin (x, y, z = 0) where the origin is defined as the center of the collection volume. Solid lines depict Radia simulation results while plotted points correspond to measured values. Inset: Zoomed view for length scales relevant for NV$^-$ fluorescence collection volumes used throughout this dissertation.

To calculate the expected B_0 field strength and homogeneity projected along a target NV$^-$ orientation, the magnet assembly was simulated using Radia [167]. We find good agreement between the calculated field strength and values extracted from NV$^-$ ODMR measurements using Sample 3B, over a few millimeter length-scale. The simulation results and measured values are plotted together in Fig. B.1(b). The z-direction gradient is reduced compared to the gradient in the xy-plane due to a high degree of symmetry along the z-axis for the magnet geometry.

Using data and simulation, we calculate that the B_0-gradient at 8.5 mT induces

an NV^- ensemble ODMR linewidth broadening of less than 0.1 kHz across the collection volume of Sample 3B (100 μm, thickness). This corresponds to a T_2^*-limit on the order of 1 ms. However, due to interaction of the bias magnetic field with nearby materials and the displacement of the collection volume from the magnetic field saddle point, the experimentally realized gradient for Sample 3C was found to contribute an ODMR ESR linewidth broadening ≈ 1 kHz (implying a T_2^*-limit ≈ 320 μs), which constitutes a small but non-negligible contribution to the T_2^* values measured in Chapter 3 and Chapter 5. Ramsey measurements for Sample 3B were taken at a four times smaller bias field; we estimate therefore $\approx 4\times$ better magnetic field homogeneity. For Sample 3D, with a layer thickness of 40 μm, the contribution of the magnetic field gradient at 10 mT to T_2^* was similar to that of Sample 3C.

Appendix C

Summary of Samples

Sample	Appears in...	[N] (ppm)	[^{13}C] (%)	Geometry	Processing Stage
2A	Sec. 2.2.4	0.5, ^{14}N	1.10%	freestanding (500 µm)	AG
2B	Sec. 2.3	25, ^{14}N	<0.005%	layer (13 µm)	IA
2C	Sec. 2.3	8, ^{15}N	<0.005%	layer (40 µm)	IA
2D	Sec. 2.4	8, ^{15}N	<0.005%	layer (10 µm)	IA
3A	Sec. 3.4.1, 4	20, ^{14}N	<0.005%	layer (1 µm)	IA
3B	Sec. 3.5	<0.05, ^{14}N	<0.01%	layer (100 µm)	AG
3C	Sec. 3.5, 5.1 5.3	0.75, ^{14}N	<0.01%	layer (100 µm)	AG
3D	Sec. 3.5, 5.3	8, ^{15}N	<0.005%	layer (40 µm)	AG
5A	Sec. 5.1	16, ^{15}N	<0.005%	layer (1 µm)	AG
5B	Sec. 5.1	8, ^{15}N	<0.005%	layer (40 µm)	AG, I, IA,
5C	Sec. 5.3	16, ^{15}N	<0.005%	layer (1 µm)	IA
6A	Sec. 6.3	16, ^{14}N	<0.005%	freestanding (500 µm)	AG
6B	Sec. 6.3	16, ^{14}N	<0.005%	freestanding (500 µm)	AG, HTA
6C	Sec. 6.4.2	16, ^{14}N	<0.005%	freestanding (100 µm)	IA
6D	Sec. 6.4.2	16, ^{14}N	<0.005%	freestanding (100 µm)	IA
6E	Sec. 6.4.2	16, ^{14}N	1.1%	freestanding (100 µm)	IA

Table C.1: **Summary of Diamond Samples.** Samples are denoted by the chapter and section in which they first appear and the order in which they are introduced. The indicated properties are listed as reported by the manufacturer, Element Six Ltd. The dominant nitrogen isotope is listed along with the reported total nitrogen concentration, when available, with relevant additional information provided in the main text. Any additional processing after growth is indicated in the final column: as-grown (AG), post-irradiation (I), post-irradiation and annealing (IA), and post annealing at 1500° C (HTA).

Bibliography

[1] C. Degen, F. Reinhard, and P. Cappellaro. Quantum sensing. *Reviews of Modern Physics*, 89(3):035002, Jul 2017.

[2] J. F. Barry, J. M. Schloss, E. Bauch, M. J. Turner, C. A. Hart, L. M. Pham, and R. L. Walsworth. Sensitivity optimization for nv-diamond magnetometry. *Rev. Mod. Phys.*, 92:015004, Mar 2020.

[3] A. Grosz, M. J. Haji-Sheikh, and S. C. Mukhopadhyay. *High Sensitivity Magnetometers*. Springer, Switzerland, 2017.

[4] F. Casola, T. Van Der Sar, and A. Yacoby. Probing condensed matter physics with magnetometry based on nitrogen-vacancy centres in diamond. *Nature Reviews Materials*, 3, 2018.

[5] A. M. Zaitsev. *Optical Properties of Diamond*. Springer, Berlin, 2001.

[6] D. A. Redman, S. Brown, R. H. Sands, and S. C. Rand. Spin dynamics and electronic states of N-V centers in diamond by EPR and four-wave-mixing spectroscopy. *Physical Review Letters*, 67(24):3420–3423, 1991.

[7] A. Lenef and S. Rand. Electronic structure of the N-V center in diamond: Theory. *Physical Review B - Condensed Matter and Materials Physics*, 53(20):13441–13455, 1996.

[8] J. Wrachtrup, S. Y. Kilin, and A. P. Nizovtsev. Quantum computation using the 13C nuclear spins near the single NV defect center in diamond. *Optics and Spectroscopy*, 91(3):429–437, Sep 2001.

[9] J. M. Taylor, P. Cappellaro, L. Childress, L. Jiang, D. Budker, P. R. Hemmer, A. Yacoby, R. Walsworth, and M. D. Lukin. High-sensitivity diamond magnetometer with nanoscale resolution. *Nat. Phys.*, 4(10):810–816, 10 2008.

[10] C. L. Degen. Scanning magnetic field microscope with a diamond single-spin sensor. *Appl. Phys. Lett.*, 92(24):243111, 2008.

[11] J. R. Maze, P. L. Stanwix, J. S. Hodges, S. Hong, J. M. Taylor, P. Cappellaro, L. Jiang, M. V. G. Dutt, E. Togan, A. S. Zibrov, A. Yacoby, R. L. Walsworth, and M. D. Lukin. Nanoscale magnetic sensing with an individual electronic spin in diamond. *Nature*, 455(7213):644–647, 10 2008.

[12] G. Balasubramanian, P. Neumann, D. Twitchen, M. Markham, R. Kolesov, N. Mizuochi, J. Isoya, J. Achard, J. Beck, J. Tissler, V. Jacques, P. R. Hemmer, F. Jelezko, and J. Wrachtrup. Ultralong spin coherence time in isotopically engineered diamond. *Nat. Mater.*, 8(5):383–387, May 2009.

[13] V. M. Acosta, E. Bauch, M. P. Ledbetter, C. Santori, K.-M. C. Fu, P. E. Barclay, R. G. Beausoleil, H. Linget, J. F. Roch, F. Treussart, S. Chemerisov, W. Gawlik, and D. Budker. Diamonds with a high density of nitrogen-vacancy centers for magnetometry applications. *Phys. Rev. B*, 80:115202, Sep 2009.

[14] R. Schirhagl, K. Chang, M. Loretz, and C. L. Degen. Nitrogen-vacancy centers in diamond: Nanoscale sensors for physics and biology. *Annu. Rev. Phys. Chem.*, 65(1):83–105, 2014.

[15] Y. Wu, F. Jelezko, M. B. Plenio, and T. Weil. Diamond quantum devices in biology. *Angew. Chem. Int. Ed.*, 55(23):6586–6598, 2016.

[16] D. R. Glenn, R. R. Fu, P. Kehayias, D. Le Sage, E. A. Lima, B. P. Weiss, and R. L. Walsworth. Micrometer-scale magnetic imaging of geological samples using a quantum diamond microscope. *Geochemistry, Geophysics, Geosystems*, 18(8):3254–3267, Aug 2017.

[17] M. J. Turner, N. Langellier, R. Bainbridge, D. Walters, S. Meesala, T. M. Babinec, P. Kehayias, A. Yacoby, E. Hu, M. Lončar, R. L. Walsworth, and E. V. Levine. Magnetic field fingerprinting of integrated-circuit activity with a quantum diamond microscope. *Phys. Rev. Applied*, 14:014097, Jul 2020.

[18] I. Lovchinsky, A. O. Sushkov, E. Urbach, N. P. de Leon, S. Choi, K. De Greve, R. Evans, R. Gertner, E. Bersin, C. Muller, L. McGuinness, F. Jelezko, R. L. Walsworth, H. Park, and M. D. Lukin. Nuclear magnetic resonance detection and spectroscopy of single proteins using quantum logic. *Science*, 351(6275):836–841, Feb 2016.

[19] J. F. Barry, M. J. Turner, J. M. Schloss, D. R. Glenn, Y. Song, M. D. Lukin, H. Park, and R. L. Walsworth. Optical magnetic detection of single-neuron action potentials using quantum defects in diamond. *Proceedings of the National Academy of Sciences of the United States of America*, 113(49):14133–14138, 2016.

[20] D. R. Glenn, D. B. Bucher, J. Lee, M. D. Lukin, H. Park, and R. L. Walsworth. High-resolution magnetic resonance spectroscopy using a solid-state spin sensor. *Nature*, 555(7696):351–354, mar 2018.

[21] D. B. Bucher, D. R. Glenn, H. Park, M. D. Lukin, and R. L. Walsworth. Hyperpolarization-enhanced nmr spectroscopy with femtomole sensitivity using quantum defects in diamond. *Phys. Rev. X*, 10:021053, Jun 2020.

[22] T. Fleig and P. Frontera. IEEE/ION Position Location and Navigation Symposium : [proceedings]. pages 1107–1112. Institute of Electrical and Electronics Engineers, Apr 2018.

[23] P. Frontera, S. Alessandrini, J. Stetson, and J. Stetson. IEEE/ION Position Location and Navigation Symposium : [proceedings]. pages 497–504. Institute of Electrical and Electronics Engineers, Apr 2018.

[24] E. V. Levine, M. J. Turner, P. Kehayias, C. A. Hart, N. Langellier, R. Trubko, D. R. Glenn, R. R. Fu, and R. L. Walsworth. Principles and techniques of the quantum diamond microscope. *Nanophotonics*, 8(11):1945–1973, 2019.

[25] D. A. Simpson, J. P. Tetienne, J. M. McCoey, K. Ganesan, L. T. Hall, S. Petrou, R. E. Scholten, and L. C. Hollenberg. Magneto-optical imaging of thin magnetic films using spins in diamond. *Scientific Reports*, 6(March):1–8, 2016.

[26] J. M. McCoey, M. Matsuoka, R. W. de Gille, L. T. Hall, J. A. Shaw, J. P. Tetienne, D. Kisailus, L. C. Hollenberg, and D. A. Simpson. Quantum Magnetic Imaging of Iron Biomineralization in Teeth of the Chiton Acanthopleura hirtosa. *Small Methods*, 4(3), 2020.

[27] J.-P. Tetienne, N. Dontschuk, D. A. Broadway, A. Stacey, D. A. Simpson, and L. C. L. Hollenberg. Quantum imaging of current flow in graphene. *Science Advances*, 3(4):e1602429, Apr 2017.

[28] M. J. H. Ku, T. X. Zhou, Q. Li, Y. J. Shin, J. K. Shi, C. Burch, L. E. Anderson, A. T. Pierce, Y. Xie, A. Hamo, U. Vool, H. Zhang, F. Casola, T. Taniguchi, K. Watanabe, M. M. Fogler, P. Kim, A. Yacoby, and R. L. Walsworth. Imaging viscous flow of the Dirac fluid in graphene. *Nature*, 583(7817):537–541, Jul 2020.

[29] D. Le Sage, K. Arai, D. R. Glenn, S. J. DeVience, L. M. Pham, L. Rahn-Lee, M. D. Lukin, A. Yacoby, A. Komeili, and R. Walsworth. Optical magnetic imaging of living cells. *Nature*, 496(7446):486–9, 2013.

[30] D. R. Glenn, K. Lee, H. Park, R. Weissleder, A. Yacoby, M. D. Lukin, H. Lee, R. L. Walsworth, and C. B. Connolly. Single-cell magnetic imaging using a quantum diamond microscope. *Nature Methods*, 12(8):736–738, 2015.

[31] J. M. Schloss, J. F. Barry, M. J. Turner, and R. L. Walsworth. Simultaneous Broadband Vector Magnetometry Using Solid-State Spins. *Physical Review Applied*, 10(3):1, 2018.

[32] B. J. Maertz, A. P. Wijnheijmer, G. D. Fuchs, M. E. Nowakowski, and D. D. Awschalom. Vector magnetic field microscopy using nitrogen vacancy centers in diamond. *Appl. Phys. Lett*, 96:92504, 2010.

[33] C. Zhang, H. Yuan, N. Zhang, L. Xu, J. Zhang, B. Li, and J. Fang. Vector magnetometer based on synchronous manipulation of nitrogen-vacancy centers in all crystal directions. *Journal of Physics D: Applied Physics*, 51(15):155102, Apr 2018.

[34] F. Camps, S. Harasse, and A. Monin. Numerical calibration for 3-axis accelerometers and magnetometers. In *2009 IEEE International Conference on Electro/Information Technology*, pages 217–221. IEEE, Jun 2009.

[35] H. S. Ousaloo, G. Sharifi, J. Mahdian, and M. T. Nodeh. Complete Calibration of Three-Axis Strapdown Magnetometer in Mounting Frame. *IEEE Sensors Journal*, 17(23):7886–7893, Dec 2017.

[36] J. Kitching. Chip-scale atomic devices. *Applied Physics Reviews*, 5(3), 2018.

[37] P. C. Maurer, G. Kucsko, C. Latta, L. Jiang, N. Y. Yao, S. D. Bennett, F. Pastawski, D. Hunger, N. Chisholm, M. Markham, D. J. Twitchen, J. I. Cirac, and M. D. Lukin. Room-temperature quantum bit memory exceeding one second. *Science (New York, N.Y.)*, 336(6086):1283–6, Jun 2012.

[38] P. Kehayias, M. J. Turner, R. Trubko, J. M. Schloss, C. A. Hart, M. Wesson, D. R. Glenn, and R. L. Walsworth. Imaging crystal stress in diamond using ensembles of nitrogen-vacancy centers. *Phys. Rev. B*, 100(17):174103, November 2019.

[39] A. M. Edmonds, C. A. Hart, M. J. Turner, P.-O. Colard, J. M. Schloss, K. Olsson, R. Trubko, M. L. Markham, A. Rathmill, B. Horne-Smith, W. Lew, A. Manickam, S. Bruce, P. G. Kaup, J. C. Russo, M. J. DiMario, J. T. South, J. T. Hansen, D. J. Twitchen, and R. L. Walsworth. Generation of nitrogen-vacancy ensembles in diamond for quantum sensors: Optimization and scalability of CVD processes. Apr 2020.

[40] M. W. Doherty, N. B. Manson, P. Delaney, F. Jelezko, J. Wrachtrup, and L. C. Hollenberg. The nitrogen-vacancy colour centre in diamond. *Phys. Rep.*, 528(1):1–45, 2013.

[41] M. L. Goldman, M. W. Doherty, A. Sipahigil, N. Y. Yao, S. D. Bennett, N. B. Manson, A. Kubanek, and M. D. Lukin. State-selective intersystem crossing in nitrogen-vacancy centers. *Phys. Rev. B*, 91:165201, Apr 2015.

[42] M. L. Goldman, A. Sipahigil, M. W. Doherty, N. Y. Yao, S. D. Bennett, M. Markham, D. J. Twitchen, N. B. Manson, A. Kubanek, and M. D. Lukin. Phonon-induced population dynamics and intersystem crossing in nitrogen-vacancy centers. *Phys. Rev. Lett.*, 114:145502, Apr 2015.

[43] G. Thiering and A. Gali. Theory of the optical spin-polarization loop of the nitrogen-vacancy center in diamond. *Phys. Rev. B*, 98:085207, Aug 2018.

[44] V. M. Acosta, E. Bauch, M. P. Ledbetter, A. Waxman, L.-S. Bouchard, and D. Budker. Temperature Dependence of the Nitrogen-Vacancy Magnetic Resonance in Diamond. *Physical Review Letters*, 104(7):070801, Feb 2010.

[45] N. B. Manson, X.-F. He, and P. T. H. Fisk. Raman heterodyne detected electron-nuclear-double-resonance measurements of the nitrogen-vacancy center in diamond. *Optics Letters*, 15(19):1094, Oct 1990.

[46] N. B. Manson, X.-F. He, and P. T. Fisk. Raman heterodyne studies of the nitrogen-vacancy centre in diamond. *Journal of Luminescence*, 53(1):49 – 54, 1992.

[47] E. Van Oort, P. Stroomer, and M. Glasbeek. Low-field optically detected magnetic resonance of a coupled triplet-doublet defect pair in diamond. *Physical Review B*, 42(13):8605–8608, 1990.

[48] J. Michl, J. Steiner, A. Denisenko, A. Bülau, A. Zimmermann, K. Nakamura, H. Sumiya, S. Onoda, P. Neumann, J. Isoya, and J. Wrachtrup. Robust and Accurate Electric Field Sensing with Solid State Spin Ensembles. *Nano Letters*, 19(8):4904–4910, Aug 2019.

[49] A. Barfuss, M. Kasperczyk, J. Kölbl, and P. Maletinsky. Spin-stress and spin-strain coupling in diamond-based hybrid spin oscillator systems. *Phys. Rev. B*, 99:174102, May 2019.

[50] M. S. J. Barson, P. Peddibhotla, P. Ovartchaiyapong, K. Ganesan, R. L. Taylor, M. Gebert, Z. Mielens, B. Koslowski, D. A. Simpson, L. P. McGuinness, J. McCallum, S. Prawer, S. Onoda, T. Ohshima, A. C. Bleszynski Jayich, F. Jelezko, N. B. Manson, and M. W. Doherty. Nanomechanical sensing using spins in diamond. *Nano Letters*, 17(3):1496–1503, Mar 2017.

[51] H. Kanda. Large diamonds grown at high pressure conditions. *Brazilian Journal of Physics*, 30(3):482–489, 2000.

[52] J. C. Angus, H. A. Will, and W. S. Stanko. Growth of Diamond Seed Crystals by Vapor Deposition. *Journal of Applied Physics*, 39(6):2915–2922, May 1968.

[53] A. Tallaire, V. Mille, O. Brinza, T. N. Tran Thi, J. Brom, Y. Loguinov, A. Katrusha, A. Koliadin, and J. Achard. Thick CVD diamond films grown on high-quality type IIa HPHT diamond substrates from New Diamond Technology. *Diamond and Related Materials*, 77:146–152, Aug 2017.

[54] K. Ohno, F. Joseph Heremans, L. C. Bassett, B. A. Myers, D. M. Toyli, A. C. Bleszynski Jayich, C. J. Palmstrøm, and D. D. Awschalom. Engineering shallow spins in diamond with nitrogen delta-doping. *Applied Physics Letters*, 101(8):082413, Aug 2012.

[55] C. A. McLellan, B. A. Myers, S. Kraemer, K. Ohno, D. D. Awschalom, and A. C. Bleszynski Jayich. Patterned Formation of Highly Coherent Nitrogen-Vacancy Centers Using a Focused Electron Irradiation Technique. *Nano Letters*, 16(4):2450–2454, Apr 2016.

[56] N. Fujita, R. Jones, S. Öberg, and P. Briddon. Large spherical vacancy clusters in diamond – Origin of the brown colouration? *Diamond and Related Materials*, 18(5-8):843–845, May 2009.

[57] L. S. Hounsome, R. Jones, P. M. Martineau, D. Fisher, M. J. Shaw, P. R. Briddon, and S. Öberg. Origin of brown coloration in diamond. *Physical Review B*, 73(12):125203, mar 2006.

[58] R. U. A. Khan, P. M. Martineau, B. L. Cann, M. E. Newton, and D. J. Twitchen. Charge transfer effects, thermo and photochromism in single crystal CVD synthetic diamond. *Journal of Physics: Condensed Matter*, 21(36):364214, Sep 2009.

[59] R. U. A. Khan, B. L. Cann, P. M. Martineau, J. Samartseva, J. J. P. Freeth, S. J. Sibley, C. B. Hartland, M. E. Newton, H. K. Dhillon, and D. J. Twitchen. Colour-causing defects and their related optoelectronic transitions in single crystal CVD diamond. *Journal of Physics: Condensed Matter*, 25(27):275801, Jun 2013.

[60] J. Baker. Deducing atomic models for point defects in diamond: The relevance of their mechanism of formation. *Diamond and Related Materials*, 16(2):216 – 219, 2007.

[61] I. Friel, S. L. Clewes, H. K. Dhillon, N. Perkins, D. J. Twitchen, and G. A. Scarsbrook. Control of surface and bulk crystalline quality in single crystal diamond grown by chemical vapour deposition. *Diamond and Related Materials*, 18(5-8):808–815, jan 2009.

[62] P. M. Martineau, M. P. Gaukroger, K. B. Guy, S. C. Lawson, D. J. Twitchen, I. Friel, J. O. Hansen, G. C. Summerton, T. P. G. Addison, and R. Burns. High crystalline quality single crystal chemical vapour deposition diamond. *Journal of Physics: Condensed Matter*, 21(36):364205, Sep 2009.

[63] U. F. D'Haenens-Johansson, K. S. Moe, P. Johnson, S. Y. Wong, R. Lu, and W. Wang. Near-Colorless HPHT Synthetic Diamonds from AOTC Group. *Gems & Gemology*, 50(1), May 2014.

[64] R. Burns, V. Cvetkovic, C. Dodge, D. Evans, M.-L. T. Rooney, P. Spear, and C. Welbourn. Growth-sector dependence of optical features in large synthetic diamonds. *Journal of Crystal Growth*, 104(2):257–279, Jul 1990.

[65] A. M. Edmonds, U. F. S. D'Haenens-Johansson, R. J. Cruddace, M. E. Newton, K.-M. C. Fu, C. Santori, R. G. Beausoleil, D. J. Twitchen, and M. L. Markham. Production of oriented nitrogen-vacancy color centers in synthetic diamond. *Physical Review B*, 86(3):035201, 2012.

[66] R. R. Fu, B. P. Weiss, E. A. Lima, P. Kehayias, J. F. Araujo, D. R. Glenn, J. Gelb, J. F. Einsle, A. M. Bauer, R. J. Harrison, G. A. Ali, and R. L. Walsworth. Evaluating the paleomagnetic potential of single zircon crystals using the bishop tuff. *Earth and Planetary Science Letters*, 458:1 – 13, 2017.

[67] I. Fescenko, A. Jarmola, I. Savukov, P. Kehayias, J. Smits, J. Damron, N. Ristoff, N. Mosavian, and V. M. Acosta. Diamond magnetometer enhanced by ferrite flux concentrators. *Physical Review Research*, 2(2):023394, Jun 2020.

[68] Z. Kazi, I. M. Shelby, H. Watanabe, K. M. Itoh, V. Shutthanandan, P. A. Wiggins, and K.-M. C. Fu. Mitigation of sensor inhomogeneities to speed up diamond-based wide-field magnetic imaging. *arXiv:2002.06237*, 2020.

[69] A. Dréau, M. Lesik, L. Rondin, P. Spinicelli, O. Arcizet, J. F. Roch, and V. Jacques. Avoiding power broadening in optically detected magnetic resonance of single NV defects for enhanced dc magnetic field sensitivity. *Physical Review B - Condensed Matter and Materials Physics*, 84(19):1–8, 2011.

[70] N. F. Ramsey. A Molecular Beam Resonance Method with Separated Oscillating Fields. *Physical Review*, 78(6):695–699, 1950.

[71] Ł. Cywiński, R. M. Lutchyn, C. P. Nave, and S. Das Sarma. How to enhance dephasing time in superconducting qubits. *Physical Review B - Condensed Matter and Materials Physics*, 77(17):1–11, 2008.

[72] E. Bauch, S. Singh, J. Lee, C. A. Hart, J. M. Schloss, M. J. Turner, J. F. Barry, L. Pham, N. Bar-Gill, S. F. Yelin, and R. L. Walsworth. Decoherence of dipolar spin ensembles in diamond. *arXiv:1904.08763*, 2019.

[73] E. Bauch, C. A. Hart, J. M. Schloss, M. J. Turner, J. F. Barry, P. Kehayias, S. Singh, and R. L. Walsworth. Ultralong dephasing times in solid-state spin ensembles via quantum control. *Phys. Rev. X*, 8:031025, Jul 2018.

[74] V. V. Dobrovitski, A. E. Feiguin, D. D. Awschalom, and R. Hanson. Decoherence dynamics of a single spin versus spin ensemble. *Physical Review B*, 77(24):245212, Jun 2008.

[75] D. Hopper, H. Shulevitz, and L. Bassett. Spin Readout Techniques of the Nitrogen-Vacancy Center in Diamond. *Micromachines*, 9(9):437, Aug 2018.

[76] G. Kucsko, S. Choi, J. Choi, P. Maurer, H. Zhou, R. Landig, H. Sumiya, S. Onoda, J. Isoya, F. Jelezko, E. Demler, N. Yao, and M. Lukin. Critical Thermalization of a Disordered Dipolar Spin System in Diamond. *Physical Review Letters*, 121(2):023601, 2018.

[77] S. T. Alsid, J. F. Barry, L. M. Pham, J. M. Schloss, M. F. O'Keeffe, P. Cappellaro, and D. A. Braje. Photoluminescence Decomposition Analysis: A Technique to Characterize N - V Creation in Diamond. *Physical Review Applied*, 12(4):044003, Oct 2019.

[78] D. Aude Craik, P. Kehayias, A. Greenspon, X. Zhang, M. Turner, J. Schloss, E. Bauch, C. Hart, E. Hu, and R. Walsworth. Microwave-Assisted Spectroscopy Technique for Studying Charge State in Nitrogen-Vacancy Ensembles in Diamond. *Physical Review Applied*, 14(1):014009, Jul 2020.

[79] H. J. Mamin, M. H. Sherwood, M. Kim, C. T. Rettner, K. Ohno, D. D. Awschalom, and D. Rugar. Multipulse double-quantum magnetometry with near-surface nitrogen-vacancy centers. *Physical Review Letters*, 113(3):1–5, 2014.

[80] K. Fang, V. M. Acosta, C. Santori, Z. Huang, K. M. Itoh, H. Watanabe, S. Shikata, and R. G. Beausoleil. High-sensitivity magnetometry based on quantum beats in diamond nitrogen-vacancy centers. *Physical Review Letters*, 110(13):2–4, 2013.

[81] A. Angerer, T. Nöbauer, G. Wachter, M. Markham, A. Stacey, J. Majer, J. Schmiedmayer, and M. Trupke. Subnanotesla quantum-interference magnetometry with a single spin in diamond. *Arxiv preprint 1509.01637*, Sep 2015.

[82] G. de Lange, T. van der Sar, M. Blok, Z.-H. Wang, V. Dobrovitski, and R. Hanson. Controlling the quantum dynamics of a mesoscopic spin bath in diamond. *Scientific reports*, 2(9):382, 2012.

[83] H. S. Knowles, D. M. Kara, and M. Atatüre. Observing bulk diamond spin coherence in high-purity nanodiamonds. *Nature materials*, 13(1):21–5, 2014.

[84] T. L. Wee, Y. K. Tzeng, C. C. Han, H. C. Chang, W. Fann, J. H. Hsu, K. M. Chen, and E. C. Yu. Two-photon excited fluorescence of nitrogen-vacancy centers in proton-irradiated type Ib diamond. *Journal of Physical Chemistry A*, 111(38):9379–9386, 2007.

[85] S. Felton, A. M. Edmonds, M. E. Newton, P. M. Martineau, D. Fisher, and D. J. Twitchen. Electron paramagnetic resonance studies of the neutral nitrogen vacancy in diamond. *Physical Review B*, 77(8):081201, Feb 2008.

[86] C. B. Hartland. *A Study of Point Defects in CVD Diamond Using Electron Paramagnetic Resonance and Optical Spectroscopy*. PhD thesis, University of Warwick, 2014.

[87] C. Glover, M. E. Newton, P. Martineau, D. J. Twitchen, and J. M. Baker. Hydrogen Incorporation in Diamond: The Nitrogen-Vacancy-Hydrogen Complex. *Physical Review Letters*, 90(18):185507, may 2003.

[88] C. Glover, M. E. Newton, P. M. Martineau, S. Quinn, and D. J. Twitchen. Hydrogen Incorporation in Diamond: The Vacancy-Hydrogen Complex. *Physical Review Letters*, 92(13):135502, Mar 2004.

[89] B. Myers, A. Ariyaratne, and A. B. Jayich. Double-Quantum Spin-Relaxation Limits to Coherence of Near-Surface Nitrogen-Vacancy Centers. *Physical Review Letters*, 118(19):197201, May 2017.

[90] J. A. Van Wyk, E. C. Reynhardt, G. L. High, and I. Kiflawi. The dependences of ESR line widths and spin - spin relaxation times of single nitrogen defects on the concentration of nitrogen defects in diamond. *Journal of Physics D: Applied Physics*, 30(12):1790–1793, 1997.

[91] R. de Sousa. *Electron Spin as a Spectrometer of Nuclear-Spin Noise and Other Fluctuations*, pages 183–220. Springer Berlin Heidelberg, Berlin, Heidelberg, 2009.

[92] L. T. Hall, J. H. Cole, and L. C. L. Hollenberg. Analytic solutions to the central-spin problem for nitrogen-vacancy centers in diamond. *Physical Review B*, 90(7):075201, Aug 2014.

[93] L. I. Childress. *Coherent manipulation of single quantum systems in the solid state*. PhD thesis, Harvard University, 2007.

[94] L. M. Pham. *Magnetic Field Sensing with Nitrogen-Vacancy Color Centers in Diamond*. PhD thesis, Harvard University, 2013.

[95] A. Abragam. *The principles of nuclear magnetism*. Clarendon Press, 1983.

[96] F. Dolde, I. Jakobi, B. Naydenov, N. Zhao, S. Pezzagna, C. Trautmann, J. Meijer, P. Neumann, F. Jelezko, and J. Wrachtrup. Room-temperature entanglement between single defect spins in diamond. *Nature Physics*, 9(3):139–143, mar 2013.

[97] A. E. Dementyev, D. Li, K. MacLean, and S. E. Barrett. Anomalies in the NMR of silicon:Unexpected spin echoes in a dilute dipolar solid. *Physical Review B*, 68(15):153302, Oct 2003.

[98] C. D. Ridge, L. F. O'Donnell, and J. D. Walls. Long-lived selective spin echoes in dipolar solids under periodic and aperiodic π -pulse trains. *Physical Review B*, 89(2):024404, jan 2014.

[99] M. B. Franzoni and P. R. Levstein. Manifestations of the absence of spin diffusion in multipulse NMR experiments on diluted dipolar solids. *Physical Review B*, 72(23):235410, Dec 2005.

[100] D. Farfurnik, Y. Horowicz, and N. Bar-Gill. Identifying and decoupling many-body interactions in spin ensembles in diamond. *Physical Review A*, 98(3):033409, Sep 2018.

[101] D. A. Broadway, B. C. Johnson, M. S. J. Barson, S. E. Lillie, N. Dontschuk, D. J. McCloskey, A. Tsai, T. Teraji, D. A. Simpson, A. Stacey, J. C. McCallum, J. E. Bradby, M. W. Doherty, L. C. L. Hollenberg, and J.-P. Tetienne. Microscopic Imaging of the Stress Tensor in Diamond Using in Situ Quantum Sensors. *Nano Letters*, 19(7):4543–4550, Jul 2019.

[102] On topographically identifiable sources of cathodoluminescence in natural diamonds. *Philosophical Transactions of the Royal Society of London. Series A, Mathematical and Physical Sciences*, 284(1324):329–368, Feb 1977.

[103] A. Crisci, F. Baillet, M. Mermoux, G. Bogdan, M. Nesládek, and K. Haenen. Residual strain around grown-in defects in CVD diamond single crystals: A 2D and 3D Raman imaging study. *Physica Status Solidi (a)*, 208(9):2038–2044, Sep 2011.

[104] L. T. M. Hoa, T. Ouisse, D. Chaussende, M. Naamoun, A. Tallaire, and J. Achard. Birefringence Microscopy of Unit Dislocations in Diamond. *Crystal Growth & Design*, 14(11):5761–5766, Nov 2014.

[105] A. Glazer, J. Lewis, and W. Kaminsky. An automatic optical imaging system for birefringent media. *Proceedings of the Royal Society of London. Series A: Mathematical, Physical and Engineering Sciences*, 452(1955):2751–2765, Dec 1996.

[106] N. Manson and J. Harrison. Photo-ionization of the nitrogen-vacancy center in diamond. *Diamond and Related Materials*, 14(10):1705–1710, Oct 2005.

[107] N. Aslam, G. Waldherr, P. Neumann, F. Jelezko, and J. Wrachtrup. Photo-induced ionization dynamics of the nitrogen vacancy defect in diamond investigated by single-shot charge state detection. *New Journal of Physics*, 15(1):013064, Jan 2013.

[108] Y. Mita. Change of absorption spectra in type-Ib diamond with heavy neutron irradiation. *Physical Review B*, 53(17):11360–11364, May 1996.

[109] Y. Doi, T. Makino, H. Kato, D. Takeuchi, M. Ogura, H. Okushi, H. Morishita, T. Tashima, S. Miwa, S. Yamasaki, P. Neumann, J. Wrachtrup, Y. Suzuki, and N. Mizuochi. Deterministic Electrical Charge-State Initialization of Single Nitrogen-Vacancy Center in Diamond. *Physical Review X*, 4(1):011057, mar 2014.

[110] B. Grotz, M. V. Hauf, M. Dankerl, B. Naydenov, S. Pezzagna, J. Meijer, F. Jelezko, J. Wrachtrup, M. Stutzmann, F. Reinhard, and J. A. Garrido. Charge state manipulation of qubits in diamond. *Nature communications*, 3:729, mar 2012.

[111] M. Turner. *Quantum Diamond Microscopes for Biological Systems and Integrated Circuits*. PhD thesis, Harvard University, 2020.

[112] M. Loretz, H. Takahashi, T. F. Segawa, J. M. Boss, and C. L. Degen. Optical hyperpolarization of nitrogen donor spins in bulk diamond. *PHYSICAL REVIEW B*, 95:64413, 2017.

[113] D. J. Twitchen, M. E. Newton, J. M. Baker, T. R. Anthony, and W. F. Banholzer. Electron-paramagnetic-resonance measurements on the divacancy defect center R4/W6 in diamond. *Physical Review B*, 59(20):12900–12910, May 1999.

[114] T. Wolf, P. Neumann, K. Nakamura, H. Sumiya, T. Ohshima, J. Isoya, and J. Wrachtrup. Subpicotesla diamond magnetometry. *Physical Review X*, 5(4):1–10, 2015.

[115] P. Udvarhelyi, V. O. Shkolnikov, A. Gali, G. Burkard, and A. Pályi. Spin-strain interaction in nitrogen-vacancy centers in diamond. *Phys. Rev. B*, 98:075201, 2018.

[116] J. J. J. J. Sakurai and J. Napolitano. *Modern quantum mechanics*. Addison-Wesley, 2011.

[117] D. M. Toyli, C. F. de las Casas, D. J. Christle, V. V. Dobrovitski, and D. D. Awschalom. Fluorescence thermometry enhanced by the quantum coherence of single spins in diamond. *Proceedings of the National Academy of Sciences of the United States of America*, 110(21):8417–21, May 2013.

[118] N. Bar-Gill, L. M. Pham, A. Jarmola, D. Budker, and R. L. Walsworth. Solid-state electronic spin coherence time approaching one second. *Nature communications*, 4:1743, 2013.

[119] P. Jamonneau, M. Lesik, J. P. Tetienne, I. Alvizu, L. Mayer, A. Dréau, S. Kosen, J. F. Roch, S. Pezzagna, J. Meijer, T. Teraji, Y. Kubo, P. Bertet, J. R. Maze, and V. Jacques. Competition between electric field and magnetic field noise in the decoherence of a single spin in diamond. *arXiv*, 024305(1511.08175):1–8, 2015.

[120] A. Przybylski, B. Thiel, J. Keller-Findeisen, B. Stock, and M. Bates. Gpufit: An open-source toolkit for gpu-accelerated curve fitting. *Scientific Reports*, 7(1), 2017.

[121] D. Le Sage, L. M. Pham, N. Bar-Gill, C. Belthangady, M. D. Lukin, A. Yacoby, and R. L. Walsworth. Efficient photon detection from color centers in a diamond optical waveguide. *Physical Review B*, 85(12):121202, 2012.

[122] M. Bal, C. Deng, J. L. Orgiazzi, F. R. Ong, and A. Lupascu. Ultrasensitive magnetic field detection using a single artificial atom. *Nature Communications*, 3:1–8, 2012.

[123] R. S. Schoenfeld and W. Harneit. Real time magnetic field sensing and imaging using a single spin in diamond. *Physical Review Letters*, 106(3):1–4, 2011.

[124] J. S. Hodges, N. Y. Yao, D. Maclaurin, C. Rastogi, M. D. Lukin, and D. Englund. Timekeeping with electron spin states in diamond. *Physical Review A - Atomic, Molecular, and Optical Physics*, 87(3), 2013.

[125] S. Rajendran, N. Zobrist, A. O. Sushkov, R. Walsworth, and M. Lukin. A method for directional detection of dark matter using spectroscopy of crystal defects. *Physical Review D*, 96(3):1–9, 2017.

[126] A. A. Schweiger and G. Jeschke. *Principles of pulse electron paramagnetic resonance*. Oxford University Press, 2001.

[127] A. Cox, M. E. Newton, and J. M. Baker. 13C, 14N and 15N ENDOR measurements on the single substitutional nitrogen centre (P1) in diamond. *Journal of Physics: Condensed Matter*, 6(2):551–563, Jan 1994.

[128] W. V. Smith, P. P. Sorokin, I. L. Gelles, and G. J. Lasher. Electron-Spin Resonance of Nitrogen Donors in Diamond. *Physical Review*, 115(6):1546–1552, Sep 1959.

[129] R. J. Cook and D. H. Whiffen. Electron Nuclear Double Resonance Study of a Nitrogen Centre in Diamond. *Proceedings of the Royal Society A: Mathematical, Physical and Engineering Sciences*, 295(1441):99–106, Nov 1966.

[130] V. Stepanov and S. Takahashi. Determination of nitrogen spin concentration in diamond using double electron-electron resonance. *Physical Review B*, 94(2):024421, Jul 2016.

[131] G. de Lange, Z. H. Wang, D. Ristè, V. V. Dobrovitski, and R. Hanson. Universal dynamical decoupling of a single solid-state spin from a spin bath. *Science (New York, N.Y.)*, 330(6000):60–63, 2010.

[132] E. R. MacQuarrie, T. a. Gosavi, a. M. Moehle, N. R. Jungwirth, S. a. Bhave, and G. D. Fuchs. Coherent control of a nitrogen-vacancy center spin ensemble with a diamond mechanical resonator. *Optica*, 2(3):233, mar 2015.

[133] G. Davies, S. C. Lawson, A. T. Collins, A. Mainwood, and S. J. Sharp. Vacancy-related centers in diamond. *Physical Review B*, 46(20):13157–13170, Nov 1992.

[134] S. C. Lawson, D. Fisher, D. C. Hunt, and M. E. Newton. On the existence of positively charged single-substitutional nitrogen in diamond. *Journal of Physics: Condensed Matter*, 10(27):6171–6180, Jul 1998.

[135] F. Dolde, H. Fedder, M. W. Doherty, T. Nöbauer, F. Rempp, G. Balasubramanian, T. Wolf, F. Reinhard, L. C. Hollenberg, F. Jelezko, and J. Wrachtrup. Electric-field sensing using single diamond spins. *Nature Physics*, 7(6):459–463, Jun 2011.

[136] P. M. Martineau, S. C. Lawson, A. J. Taylor, S. J. Quinn, D. J. F. Evans, and M. J. Crowder. Identification of Synthetic Diamond Grown Using Chemical Vapor Deposition (CVD). *Gems & Gemology*, 40(1):2–25, Apr 2004.

[137] R. U. A Khan, P. M. Martineau, B. L. Cann, M. E. Newton, H. K. Dhillon, and D. J. Twitchen. Color Alterations in CVD Synthetic Diamond with Heat and UV Exposure: Implications for Color Grading and Identification. *Gems and Gemology*, 46(1), 2010.

[138] B. Willems, A. Tallaire, and J. Achard. Optical study of defects in thick undoped CVD synthetic diamond layers. *Diamond and Related Materials*, 41:25–33, Jan 2014.

[139] A. Tallaire, J. Achard, F. Silva, O. Brinza, and A. Gicquel. Growth of large size diamond single crystals by plasma assisted chemical vapour deposition: Recent achievements and remaining challenges. *Comptes Rendus Physique*, 14(2-3):169–184, Feb 2013.

[140] M. Gaukroger, P. Martineau, M. Crowder, I. Friel, S. Williams, and D. Twitchen. X-ray topography studies of dislocations in single crystal CVD diamond. *Diamond and Related Materials*, 17(3):262–269, Mar 2008.

[141] B. Campbell, W. Choudhury, A. Mainwood, M. Newton, and G. Davies. Lattice damage caused by the irradiation of diamond. *Nuclear Instruments and Methods in Physics Research Section A: Accelerators, Spectrometers, Detectors and Associated Equipment*, 476(3):680–685, Jan 2002.

[142] Y. Chu, N. de Leon, B. Shields, B. Hausmann, R. Evans, E. Togan, M. J. Burek, M. Markham, A. Stacey, A. Zibrov, A. Yacoby, D. Twitchen, M. Loncar, H. Park, P. Maletinsky, and M. Lukin. Coherent Optical Transitions in Implanted Nitrogen Vacancy Centers. *Nano Letters*, 14(4):1982–1986, Apr 2014.

[143] Stephanie Liggins. *Identification of point defects in treated single crystal diamond*. PhD thesis, University of Warwick, 2010.

[144] A. M. Edmonds, M. E. Newton, P. M. Martineau, D. J. Twitchen, and S. D. Williams. Electron paramagnetic resonance studies of silicon-related defects in diamond. *Physical Review B*, 77(24):245205, Jun 2008.

[145] A. Tallaire, A. Collins, D. Charles, J. Achard, R. Sussmann, A. Gicquel, M. Newton, A. Edmonds, and R. Cruddace. Characterisation of high-quality thick single-crystal diamond grown by CVD with a low nitrogen addition. *Diamond and Related Materials*, 15(10):1700–1707, Oct 2006.

[146] M. W. Dale. *Colour Centres on Demand in Diamond*. PhD thesis, University of Warwick, 2015.

[147] G. Davies. Current problems in diamond: towards a quantitative understanding. *Physica B: Condensed Matter*, 273-274:15–23, Dec 1999.

[148] H. B. Dyer, F. A. Raal, L. Du Preez, and J. H. N. Loubser. Optical absorption features associated with paramagnetic nitrogen in diamond. *Philosophical Magazine*, 11(112):763–774, Apr 1965.

[149] R. M. Chrenko, H. M. Strong, and R. E. Tuft. Dispersed paramagnetic nitrogen content of large laboratory diamonds. *Philosophical Magazine*, 23(182):313–318, Feb 1971.

[150] C. A. Schneider, W. S. Rasband, and K. W. Eliceiri. NIH Image to ImageJ: 25 years of image analysis. *Nature Methods*, 9(7):671–675, Jul 2012.

[151] K. McLaren and B. Rigg. XII-The SDC Recommended Colour-difference Formula: Change to CIELAB. *Journal of the Society of Dyers and Colourists*, 92(9):337–338, Oct 2008.

[152] J. Achard, A. Tallaire, R. Sussmann, F. Silva, and A. Gicquel. The control of growth parameters in the synthesis of high-quality single crystalline diamond by CVD. *Journal of Crystal Growth*, 284(3-4):396–405, Nov 2005.

[153] C. Wild, R. Kohl, N. Herres, W. Müller-Sebert, and P. Koidl. Oriented CVD diamond films: twin formation, structure and morphology. *Diamond and Related Materials*, 3(4-6):373–381, Apr 1994.

[154] J. O. Orwa, C. Santori, K. M. C. Fu, B. Gibson, D. Simpson, I. Aharonovich, A. Stacey, A. Cimmino, P. Balog, M. Markham, D. Twitchen, A. D. Greentree, R. G. Beausoleil, and S. Prawer. Engineering of nitrogen-vacancy color centers in high purity diamond by ion implantation and annealing. *Journal of Applied Physics*, 109(8):083530, Apr 2011.

[155] J.-P. Tetienne, R. W. de Gille, D. A. Broadway, T. Teraji, S. E. Lillie, J. M. McCoey, N. Dontschuk, L. T. Hall, A. Stacey, D. A. Simpson, and L. C. L. Hollenberg. Spin properties of dense near-surface ensembles of nitrogen-vacancy centers in diamond. *Physical Review B*, 97(8):085402, Feb 2018.

[156] P. Balasubramanian, C. Osterkamp, Y. Chen, X. Chen, T. Teraji, E. Wu, B. Naydenov, and F. Jelezko. dc Magnetometry with Engineered Nitrogen-Vacancy Spin Ensembles in Diamond. *Nano Letters*, 19(9):6681–6686, sep 2019.

[157] B. Naydenov, F. Reinhard, A. Lämmle, V. Richter, R. Kalish, U. F. S. D'Haenens-Johansson, M. Newton, F. Jelezko, and J. Wrachtrup. Increasing the coherence time of single electron spins in diamond by high temperature annealing. *Applied Physics Letters*, 97(24):242511, Dec 2010.

[158] T. Yamamoto, T. Umeda, K. Watanabe, S. Onoda, M. L. Markham, D. J. Twitchen, B. Naydenov, L. P. McGuinness, T. Teraji, S. Koizumi, F. Dolde, H. Fedder, J. Honert, J. Wrachtrup, T. Ohshima, F. Jelezko, and J. Isoya. Extending spin coherence times of diamond qubits by high-temperature annealing. *Physical Review B*, 88(7):075206, Aug 2013.

[159] F. M. Stürner, A. Brenneis, J. Kassel, U. Wostradowski, R. Rölver, T. Fuchs, K. Nakamura, H. Sumiya, S. Onoda, J. Isoya, and F. Jelezko. Compact integrated magnetometer based on nitrogen-vacancy centres in diamond. *Diamond and Related Materials*, 93:59–65, Mar 2019.

[160] C. Grezes, B. Julsgaard, Y. Kubo, W. L. Ma, M. Stern, A. Bienfait, K. Nakamura, J. Isoya, S. Onoda, T. Ohshima, V. Jacques, D. Vion, D. Esteve, R. B. Liu, K. Mølmer, and P. Bertet. Storage and retrieval of microwave fields at the single-photon level in a spin ensemble. *Physical Review A*, 92(2):020301, Aug 2015.

[161] T. Nöbauer, K. Buczak, A. Angerer, S. Putz, G. Steinhauser, J. Akbarzadeh, H. Peterlik, J. Majer, J. Schmiedmayer, and M. Trupke. Creation of ensembles of nitrogen-vacancy centers in diamond by neutron and electron irradiation. *arXiv:1309.0453*, Sep 2013.

[162] D. Budker and M. Romalis. Optical magnetometry. *Nat. Phys.*, 3(4):227–234, 04 2007.

[163] A. M. Tyryshkin, S. Tojo, J. J. L. Morton, H. Riemann, N. V. Abrosimov, P. Becker, H.-J. Pohl, T. Schenkel, M. L. W. Thewalt, K. M. Itoh, and S. A. Lyon. Electron spin coherence exceeding seconds in high-purity silicon. *Nature Materials*, 11(2):143–147, Feb 2012.

[164] J. Choi, H. Zhou, H. S. Knowles, R. Landig, S. Choi, and M. D. Lukin. Robust Dynamic Hamiltonian Engineering of Many-Body Spin Systems. *Physical Review X*, 10(3):031002, Jul 2020.

[165] H. Zhou, J. Choi, S. Choi, R. Landig, A. M. Douglas, J. Isoya, F. Jelezko, S. Onoda, H. Sumiya, P. Cappellaro, H. S. Knowles, H. Park, and M. D. Lukin. Quantum Metrology with Strongly Interacting Spin Systems. *Physical Review X*, 10, 2020.

[166] S. Choi, N. Y. Yao, and M. D. Lukin. Quantum metrology based on strongly correlated matter. *arXiv:1801.00042*, Dec 2017.

[167] J. C. O. Chubar, P. Elleaume. Radia software package, 2017.